Clinical and anatomical consequences of impaired cerebrovascular reserve as detectable by quantitative functional MR imaging

Jorn Fierstra

Clinical and anatomical consequences of impaired cerebrovascular reserve as detectable by quantitative functional MR imaging
PhD thesis, Utrecht University, The Netherlands

ISBN:	978-90-393-5726-2
Cover:	Jorn Fierstra & Julien Poublanc
Cover Image:	Axial image of BOLD-MRI cerebrovascular reactivity map of patient with unilateral impaired cerebrovascular reserve (indicated in blue) related to steno-occlusive disease.
Lay-out:	Jorn Fierstra
Printed by:	Proefschriftmaken.nl

Clinical and anatomical consequences of impaired cerebrovascular reserve as detectable by quantitative functional MR imaging

Klinische en anatomische consequenties van gestoorde cerebrovasculaire reserve detecteerbaar met kwantitatieve functionele MR beeldvorming

(*met een samenvatting in het Nederlands*)

Proefschrift

ter verkrijging van de graad van doctor aan de Universiteit Utrecht op gezag van de rector magnificus, prof.dr. G.J. van der Zwaan, ingevolge het besluit van het college voor promoties in het openbaar te verdedigen op donderdag 1 maart 2012 des middags te 4.15 uur

door

Jorn Fierstra

geboren op 15 mei 1983 te Leeuwarden

Promotoren:	Prof.dr. L.P.E. Regli
	Prof.dr. M. Tymianski
Co-promotoren:	Dr. D.J. Mikulis
	Dr. J.A. Fisher

Oer ús skynt deselde sinne,
hwer’t wy op de wrâld ek binne

Upon us shines the same sun,
wherever we are in the world

For my family

Table of Contents

Part 2: Experimental animal models

Addendum

Abstract

Brain areas exhibiting impaired cerebrovascular reserve are believed to be at higher risk of ischemic tissue injury under circumstances in which cerebral blood flow is insufficient to meet metabolic demand. Other than for acute ischemia, which results in apparent (irreversible) loss of brain tissue and function, the consequences of chronic intermittent hemodynamic failure are not well understood. In these instances, perfusion of brain tissue may be just sufficient to prevent gross ischemia but may fail to respond adequately to increases in demand such as those normally seen during neuronal activation. To date, there are no studies published on the anatomical and clinical consequences of non-ischemic chronic intermittent hypoperfusion in humans. However, experimental animal models simulating a state of non-ischemic chronic hypoperfusion show a decline in neuronal structure and viability.

To investigate whether chronic hypoperfusion is present, the integrity of the cerebrovascular flow response system can be assessed by measures of cerebrovascular reactivity (CVR), a measure of the change in cerebral blood flow in response to a vasodilatory stimulus. Reductions in CVR can range from a blunted increase in blood flow in response to a stimulus in mild cases, to "paradoxical" reduction in regional blood flow indicating steal physiology, in severe cases. Existing imaging methods for spatially measuring cerebrovascular reserve, such as ^{133}Xe-CT and Single Photon Emission Computed Tomography (SPECT), have drawbacks, including cost and limited clinical availability.

In this thesis, I extensively use a non-invasive quantitative MR-based method to infer the anatomical and clinical consequences of impaired cerebrovascular reserve. This method employs functional acquisitions of blood oxygen-level dependent (BOLD) MR contrast with standardized iso-oxic changes in end-tidal PCO_2 as the vasoactive stimulus.
Specifically, I will investigate the adverse effects of chronically compromised blood flow control on the health of brain tissue to associate this with the onset of clinical symptoms in patients with severe chronic steno-occlusive cerebrovascular disease and brain arteriovenous malformations.

Where MRI-CVR measurements require precise changes in end-tidal pCO_2, I will also study the translation of the standardized PCO_2 stimuli for patients that require mechanical ventilation (i.e. positive inspiratory pressure), using an animal model.
This method may open up future research avenues for critically ill patients such as those who suffer from traumatic brain injuries or a subarachnoid hemorrhage due to aneurysmal rupture, who may benefit from MRI-CVR studies.

Organisation of thesis

The background is based on:

Fierstra J, Mikulis DJ. Neurovascular uncoupling in functional MR imaging; chapter 20 in "Functional Neuroradiology: Principles and Clinical Applications" By Faro S, Mohamed F. 1st ed. 2011. Springerlink Verlag

Fierstra J, Mikulis DJ, Regli L, Tymianski M, Fisher JA. Measuring cerebrovascular reactivity: a review of various functional imaging methods and vasoactive stimuli. *Submitted for publication*

The chapters are based on:

Chapter 2: Fierstra J, Pucci O, Battisti-Charbonney A, Duffin J, Poublanc J, Crawley, AP, Regli L, Rinkel GJ Van Dijk JMC, Mandell DM, Tymianski M, Mikulis DJ, Fisher JA. Sequential standardized fMRI assessment of cerebrovascular reserve in chronic intracranial steno-occlusive disease with two illustrative case studies. *Submitted for publication*

Chapter 3: Fierstra J, Poublanc J, Han JS, Silver F, Tymianski M, Crawley AP, Fisher JA, Mikulis DJ. Steal physiology is spatially associated with cerebral cortical thinning. J Neurol Neurosurg Psychiatry 2010;81(3):290-3

Chapter 4: Fierstra J, MacLean DB, Fisher JA, Han JS, Mandell DM, Conklin J, Poublanc J, Crawley AP, Regli L, Mikulis DJ, Tymianski M. Surgical revascularization reverses cerebral cortical thinning in patients with severe cerebrovascular steno-occlusive disease. Stroke 2011;42(6):1631-7

Chapter 5: Fierstra J, Conklin J, Krings T, Slessarev M, Han JS, Fisher JA, Terbrugge K, Wallace MC, Tymianski M, Mikulis DJ. Impaired peri-nidal cerebrovascular reserve in seizure patients with brain arteriovenous malformations. Brain 2011;134(Pt 1):100-9

Chapter 6: Fierstra J, Machina M, Battisti-Charbonney A, Duffin J, Fisher JA, Minkovich L. End-inspiratory rebreathing reduces the end-tidal to arterial PCO_2 gradient in mechanically ventilated pigs. Intensive Care Med 2011;37(9):1543-50

Chapter 7: Fierstra J, Winter JD, Machina M, Lukovich J, Duffin J, Kassner A, Fisher JA. Non-invasive accurate measurement of $PaCO_2$ in a pediatric animal model. *Submitted for publication*

Addendum chapter I: Conklin J, Fierstra J, Crawley AP, Han JS, Poublanc J, Mandell DM, Silver F, Tymianski M, Fisher JA, Mikulis DJ. Impaired cerebrovascular reactivity with steal phenomenon is associated with increased diffusion in white matter of patients with moyamoya disease. Stroke 2010;41(8):1610-6

Addendum chapter II: Conklin J, Fierstra J, Crawley AP, Han JS, Poublanc J, Mandell DM, Silver F, Tymianski M, Fisher JA, Mikulis DJ. Mapping white matter diffusion and cerebrovascular reactivity in carotid occlusive disease. Neurology 2011;77)5):431-8

Incorporated in the Discussion are:
Fierstra J, Spieth S, Tran LE, Conklin J, Tymianski M, Terbrugge K, Fisher JA, Mikulis DJ, Krings T. Severely impaired cerebrovascular reserve in patients with cerebral proliferative angiopathy. J Neurosurg Pediatr 2011;8(3):310-5

MacLean DB, Fierstra J, Pucci O, Battisti-Charbonney A, Conklin J, Fisher JA, Mikulis DJ. Restriction of cerebral venous outflow decreases cerebrovascular reserve in healthy subjects. *Submitted for publication*

Winter JD, Fierstra J, Dorner S, Fisher JA, St-Lawrence KS, Kassner A.Feasibility and precision of cerebral blood flow and cerebrovascular reactivity MRI measurements using a computer-controlled gas delivery system in an anesthetised juvenile animal model. J Magn Reson Imaging 2010;32(5):1068-75

Mandell DM, Han JS, Poublanc J, Crawley AP, Fierstra J, Tymianski M, Fisher JA, Mikulis DJ. Quantitative measurement of cerebrovascular reactivity by blood oxygen level-dependent MR imaging in patients with intracranial stenosis: preoperative cerebrovascular reactivity predicts the effect of extracranial-intracranial bypass surgery. AJNR Am J Neuroradiol 2011;32(4):721-7

The background will start with an overview of basic brain anatomy and physiology with specific attention to cerebral blood flow and cerebral blood flow control (i.e. cerebro-vascular autoregulation). I will also set out how chronic cerebrovascular diseases may affect this flow control mechanism, i.e. the cerebrovascular reserve capacity, to maintain brain tissue perfusion. Furthermore, I will explain how the integrity of this flow control mechanism can be evaluated with various imaging techniques using various vasoactive stimuli. The focus will be specifically on functional MR imaging employing a standardized global PCO_2 stimulus for quantitative measures of the cerebrovascular reserve (the BOLD MRI-sCVR exam). Following the background, in the introduction I will elucidate the rationale leading to the main hypothesis.
In chapter 2, I will introduce and describe various analysis methods that can be derived from the standardized BOLD-MRI sCVR exam. Such methods may find their use investigating (subclinical) fluctuations in cerebrovascular reserve over time in patients with severe chronic steno-occlusive disease whom may be neurologically asymptomatic and without brain tissue loss on structural imaging but that are still at risk to develop ischemia. These analysis methods are illustrated in two patients with chronic steno-occlusive intracranial disease in one subject with, and one subject without surgical revascularization to restore brain tissue perfusion.

Further elaborating on the cerebrovascular reserve in severe chronic steno-occlusive disease, I will investigate whether normal appearing brain tissue exhibits ultrastructural tissue injury when autoregulation cannot maintain sufficient perfusion, as spatially identified as brain tissue with impaired cerebrovascular reserve associated with steal physiology by BOLD-MRI sCVR examinations ('gray matter changes are described in chapter 3, whereas white matter changes are described in addendum chapters I & II). Following these investigations, I will test whether surgical revascularization, restoring cerebrovascular reserve capacity, may reverse such ultrastructural changes (chapter 4).

In chapter 5, I will investigate whether MRI-sCVR can identify differences in cerebrovascular reserve to distinguish similar appearing brain arteriovenous malformations on structural MR imaging, however with a different clinical presentation: with or without epileptic seizures.

With a more experimental approach for future applications of the BOLD-MRI sCVR exam, I will investigate the applicability of the standardized vasoactive CO_2 stimulus (as utilized in the MRI sCVR exam) for positive inspiratory pressure, i.e. comatose (intubated) adult patients (chapter 6), and pediatric patients (chapter 7). This work based on animal models, may function as a foundation to elaborate on MRI sCVR studies in more critically ill patients with a variety of neurovascular diseases, such as aneurysmal subarachnoid hemorrhage and traumatic brain injury.

The whole body of work in this thesis is integrated by a brief rationale and interpretation of results between consecutive chapters. In the discussion (chapter 8), I will summarize the findings and will provide an integrated interpretation of the results, along with significant limitations, and future avenues to arrive at the conclusions resulting from this work.

Definition of terms

Terms referring to cerebrovascular autoregulation are often used interchangeably and have been assigned different meanings according to different users and research groups. Although I am not claiming to be the final authority on this issue, I would like to establish the following definitions to inform the reader in order to minimize uncertainty while reading this thesis.

Cerebrovascular autoregulation refers to the mechanism that maintains constant blood flow in the brain under varying day-to-day physiological changes in blood pressure. Superimposed on this are the metabolic based responses to changes in arterial carbon dioxde partial pressure ($PaCO_2$). It also accounts for neuroglial mediated increases in regional cerebral blood flow (= perfusion) during neuronal activity (1,2), while maintaining baseline perfusion for the remaining parts of the brain. This is achieved through control of resistance in pre-capillary blood vessels (either by relaxation or contraction of smooth muscle). Cerebrovascular reserve is the capacity to augment blood flow from a baseline level, by decreasing vascular resistance (vasodilatation).

Cerebrovascular reactivity (CVR) can be used as an indicator of how much cerebrovascular reserve is left in a given vascular bed. CVR is defined as the percent change in cerebral blood flow/percent change in flow stimulus. For Blood Oxygen Level-Dependent MR imaging (BOLD-MRI), CVR is the percentage change in BOLD signal per mmHg change in end-tidal PCO_2 ($P_{ET}CO_2$). Standardization of the global vasodilatory stimulus, in this case CO_2, results in quantitative measures of CVR (standardized CVR; sCVR).

With severe chronic cerebrovascular disease (i.e. a vascular occlusion or high-grade stenosis), this reserve capacity can reach its limit. The vascular bed downstream of the affected vessel is maximally dilated in order to maintain sufficient blood flow to the brain tissue at baseline. Here the autoregulatory mechanism is still intact (vasodilatation occurred) but is approaching its maximum endpoint. The reserve capacity for additional augmentation of blood flow is, therefore, exhausted.

Arterial “steal” physiology or arterial “steal” phenomenon refers to a brain region where blood flow paradoxically drops when a vasodilatory stimulus is applied.

Two conditions must be met for this to happen. The first is that cerebrovascular reserve must be, or become, exhausted. The second is that sufficient reserve capacity exists in surrounding tissue such that flow resistance can drop in response to the vasoactive stimulus. The net result is a diversion of blood flow from the vascular bed with exhausted vasodilatory reserve, to that which continues to dilate.

Chapter 1

Background & Introduction

1.1 Brain anatomy

Macroscopically, the brain can be separated into the cerebrum, diencephalon, brainstem, and the cerebellum. The cerebrum consists of a left and right hemisphere that individually can be divided into a frontal, temporal, parietal, occipital lobe, and the insula. Contained within each lobe and cerebellum is tissue that is composed predominantly of cell bodies (gray matter) and of axonal fiber tracts (white matter).

The gray matter is composed of the neuronal cell bodies, along with their dense network of dendrites, unmyelinated axons plus associated neuroglia cells. The gray matter includes the center of the spinal cord and the thin outer layer of the cerebral hemispheres, commonly known as the cortex. The thickness of the cortex, as measured in healthy subjects, varies from approximately 2 mm in the calcarine cortex to approximately 4 mm in the pre-central gyrus (motor cortex), (3) where the left hemisphere is considered thicker. (4)

Neuroglia cells are considered to embody supporting scaffolding for optimal functioning of the neurons. Four types of neuroglia cells can be distinguished in the central nervous system: Astrocytes, which play a role in coordinating the capillary tone with neuronal function. Microglia cells are considered a special type of macrophage protecting the neuronal system by engulfing invading microorganisms and dead neuronal tissue. Oligodendrocytes produce insulating coverings and myelin sheets, over large neuron fibers. Last of all, there are ependymal cells that form a fairly permeable barrier between the cerebrospinal fluid and brain tissue. The cilia found on the surface of these cells also help to circulate the cerebrospinal fluid.

White matter consists predominantly of myelinated axons of these same neurons bundled into fiber tracts, to enable them to conduct nerve impulses more rapidly. The volume of the white matter is approximately 60% of the total brain tissue volume.

1.2 Brain vasculature

The blood vessels of the brain consist of a dense arterial and venous system. These two systems are connected through a capillary network, arterioles. Furthermore, functional collateral anastomoses exist within the systems as well as between the systems for sufficient blood flow to and from the brain.

Cerebral arteries

A dense network of arteries exists to provide sufficient blood flow and nutrients for normal functioning of the brain. The blood supply to the brain can be divided into an anterior circulation and a posterior circulation that communicate with each other through the posterior communicating arteries, establishing the Circle of Willis.

Anterior arterial circulation

The anterior part of the brain, as well as the scalp and the face receive their blood supply through the common carotid arteries that divide into an external carotid artery branch that supplies the scalp and face, and an internal carotid artery branch dividing into several arteries on the skull base. The first branch is the ophthalmic artery, followed by the posterior communicating arteries, whereas on the level of the carotid artery bifurcation the anterior and middle cerebral arteries originate, supplying the frontal, parietal, parts of the temporal lobes (temporal pole), and the middle brain with exemption of the pituitary (receives its blood supply directly from the internal carotid artery). (5) The left and right anterior circulation is connected via the anterior communicating artery, an anastomosis between the left and right anterior cerebral artery.

Anterior cerebral artery

The anterior cerebral artery (ACA) branches directly from the internal carotid artery. The ACA courses below the anterior cerebral hemispheres and ramifies over the cortical surface at the front of the brain. The ACA also extends along the longitudinal sulcus between the two hemispheres on each side and continues up the medial aspect of the hemisphere giving off penetrating branches supplying the interior of the respective hemisphere.

Each anterior cerebral artery principally supplies:

- The frontal pole of the hemisphere, and
- The whole medial surface of the frontal and parietal lobes to the parieto-occipital sulcus, where it then anastomoses with the posterior cerebral artery.

Middle cerebral artery

The middle cerebral artery (MCA) is a direct continuation of the main branch of the internal carotid artery coursing in a horizontal plane, laterally and slightly anterior; they are the predominant arteries in the brain. Proximal vessels that branch of the MCA are the lenticulo- striate arteries, supplying the deep white matter. These vessels are considered end-arteries, since they cannot benefit from direct collateral anastomoses.

The middle cerebral artery principally supplies

- The insula,
- The inferior and middle frontal gyri,
- Two thirds of the precentral and postcentral gyri,
- The superior and inferior parietal lobes, and
- The superior and middle temporal gyri

Posterior arterial circulation

The posterior circulation commences with the left and right vertebral arteries that originate from the respective subclavian artery. Two major branches originate from the vertebral arteries, the superior spinal arteries supplying the anterior part of the spinal cord and the posterior inferior cerebellar arteries supplying the inferior dorsal part of the cerebellum and lower brainstem, before merging into the basilar artery. The basilar artery gives rise also to

several branches going to the cerebellum, the anterior inferior cerebellar artery and the superior cerebellar artery. At the tip, the basilar artery divides into the left and right posterior cerebral arteries supplying the remaining part of the temporal lobes, the occipital lobes, splenium, corpus callosum, the caudal part of the thalamus, and the internal capsula. (5) There are anatomical variations known where the posterior cerebral artery originates directly from the internal carotid artery, known as a fetal posterior cerebral artery, excluding the basilar artery as a supplier of the circle of Willis.

Posterior cerebral artery
The left and right posterior cerebral arteries are a direct continuation of the basilar artery. The posterior cerebral artery is primarily responsible for supplying blood flow to the medial and inferior surfaces of the occipital lobe, the inferior surface of the gyrus of the temporal lobe, and part of the superior parietal lobule and the entire calcarine cortex

Functional collateral anastomoses
Functional anastomoses may not be patent when blood flow is sufficiently delivered to the brain. They may act as functional collaterals delivering blood of re-direct blood flow for sufficient perfusion when the primarily responsible vessel(s) fail. Such anastomoses include:

- The posterior and anterior communicating arteries

The anterior communicating artery connects the left and right anterior circulation, while the posterior communicating arteries connect the anterior with the posterior circulation.

- Lepto-meningeal anastomoses:

Located on the surface of the brain, these collaterals develop between the cortical branches of the anterior, middle and posterior cerebral arteries.

- Dural anastomoses

These collaterals occur between meningeal branches of the ICA, ECA and the vertebral arteries.

Cerebral veins
Basically, two major venous draining systems can be distinguished; the superficial venous drainage and the deep venous drainage. The superficial veins over the cortex all come together in the superior sagittal sinus, present over de longitudinal axis between the two hemispheres, and the straight sinus, both draining into the left and right transverse sinus, via the sigmoid sinus to the internal jugular veins. The deep venous drainage all collects

into the Vein of Galen. Both venous systems are interconnected via anastomoses that are prone to more anatomical variation than the arterial collateral system.

1.3 Physiology

Cerebral blood flow

Twenty percent of the baseline cardiac output is directed towards the brain, which in contrast only accounts for 2% of the body weight, underscoring the high metabolic requirements of neurons and glia. In addition, a considerable increase in regional cerebral blood flow (CBF) occurs during neuronal activation. (6) This high demand for blood flow is associated with a flow control pathway that is not fully understood but appears to act through the same final common effector as the cerebrovascular autoregulatory mechanism. This effector is arterial vascular resistance mediated by smooth muscle tone of the pre-capillary sphincter in arteries and arterioles, under influence of intraluminal pressure (autoregulation) or changes in pH/CO_2 (chemoregulation). (1,2,7,8) The manner in which active neurons signal for augmentation of blood flow, and the reason that such a considerable flow increase is needed involves complex mechanisms and continues to be actively investigated.

Control of cerebral blood flow

Modulation of vascular resistance is the mechanism for controlling cerebral blood flow at the pre-capillary level. CBF is modulated via control of the luminal diameter of the supplying arteries and arterioles. Smooth muscle tone in these vessels directly affects blood vessel diameter and therefore vascular resistance. Also, vascular resistance can be affected by capillary bed outflow resistance. Therefore resistance in sinovenous outflow pathways can also have an impact on capillary blood flow. Modulation of arterial vascular resistance is the underlying mechanism responsible for the brain's ability to control blood flow and has been termed cerebrovascular autoregulation. This mechanism is responsive to many different physiological stimuli. The first of these is a pressure responsive mechanism that maintains constant blood flow in the microcirculation through a wide range of cerebral perfusion pressures (CPP). (7,8) It is a smooth muscle reflex mechanism where an increase in pressure produces a rapid reflex increase in smooth muscle tone increasing vascular resistance and vice versa. The second is a response to metabolic vasoactive molecules such as CO_2, O_2, potassium, calcium, serotonin, and endothelin. (9) The third is a vasoactive response to local neuronal activity, termed the neurovascular unit. (10,11) As indicated previously, the final common response pathway to these stimuli is thought to be smooth muscle tone in the arterial system, including the pre-capillary arterioles, where the pre-capillary sphincter is thought to reside. (1,2) The sphincter represents a 'valve' at the interface between the arterioles and capillary bed. All intra-cranial blood vessels have myogenic control of their vascular tone: i.e. the greater the intraluminal pressure, the greater the smooth muscle tone. The major intracranial blood vessels normally have little

smooth muscle tone; they have little myogenic gain with changes in intraluminal pressure. Arterioles and end-arteries, however, use their smooth muscle tone to keep their luminal diameter constricted for about 75% during resting state, keeping a large reserve for to augment blood flow when needed. The cerebrovascular autoregulation serves to maintain metabolic homeostasis by ensuring adequate blood flow, and thus constant delivery of oxygen and glucose to the brain. The mechanism also serves to remove metabolic 'waste' products, under varying physiological conditions and states of neuronal activity.

1.4 Chronic cerebrovascular diseases

The structure and the intraluminal diameter of brain blood vessels may get compromised under various pathological neurovascular conditions resulting in hemodynamic failure in severe cases, when collateral flow recruitment is also inadequate. On the other hand, malformation of cerebral blood vessels may also alter cerebral blood flow without apparent loss of intraluminal diameter. In fact, pathological vasodilatation may cause symptoms/tissue abnormalities in these instances. Deformities of brain blood vessels may occur as soon as in the embryonic developmental stage, whereas obliteration of blood vessel lumen may occur over decades. Although, the pathophysiology of the majority of these diseases remains not fully understood, I have aimed to give an up-to-date overview of intracranial cerebrovascular diseases as investigated in this thesis.

Chronic cerebrovascular steno-occlusive disease

Chronic cerebrovascular steno-occlusive diseases can alter cerebral hemodynamics, up to a critical point where brain tissue perfusion becomes insufficient (chronic hypoperfusion). The spectrum of diseases varies from extracranial, and intracranial focal stenosis or occlusion to more progressive obliterative vasculopathies that affect multiple vessels/vascular territories (Figure 1). The result is an adaptation of the autoregulatory flow control mechanism by lowering the vascular resistance downstream, and providing blood flow to brain tissue through collateral pathways, up to a point where these compensatory mechanisms fail and tissue injury occurs. These processes will be discussed in greater detail later.

In this thesis, I have mainly studied patients with severe chronic cerebrovascular disease, where the autoregulatory flow mechanism is altered, including focal stenosis/occlusion of the major cerebral arteries (mainly carotid artery disease), and more widespread vasculopathy (moyamoya disease), but also shunting lesions, such as brain arteriovenous malformations.

Figure 1: *Spectrum of cerebrovascular steno-occlusive disease*

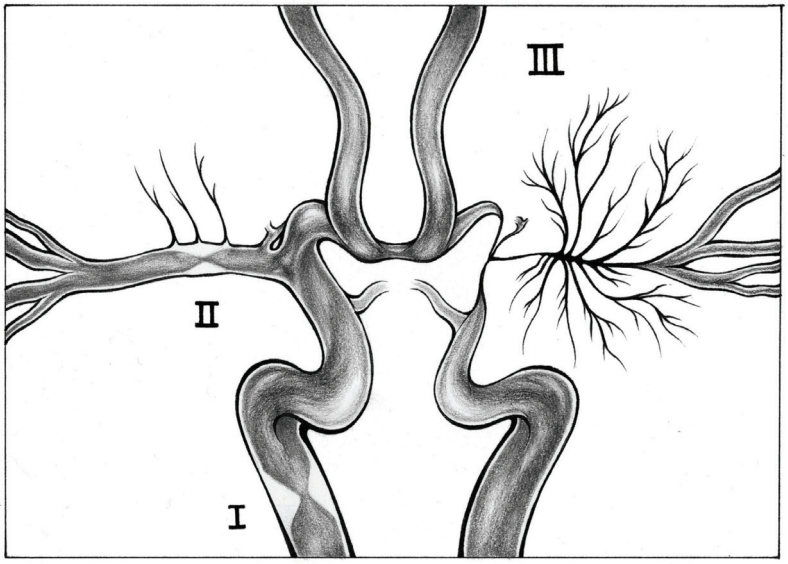

Caption figure 1: *Illustration of cerebrovascular steno-occlusive diseases. (I) Focal stenosis of the internal carotid artery. (II) Focal stenosis of the middle cerebral artery. (III) Moyamoya vasculopathy with obliteration of the ICA termination and formation of collaterals. The location and distribution of the disease determines whether and which collateral pathways can still be functional in order to maintain sufficient brain tissue perfusion.*

Extracranial and intracranial focal steno-occlusive disease in a major cerebral artery

Cerebrovascular disease is the third leading cause of mortality in western countries, with an annual stroke rate of approximately 2-4% of the population. Moreover, it is the leading cause of adult disability. Carotid occlusive disease is responsible for about 25% of these strokes. Extracranial stenoses of the intracranial carotid artery often produce no hemodynamic effect due to autoregulatory flow compensation downstream and/or enroachment of collateral blood supply. Even a total occlusion of the internal carotid artery, unilateral but also bilateral, may remain unnoticed due to sufficient collateral blood flow through the circle of Willis and pial collateralization. A stenosis may reach a more critical point earlier when it occurs in the intracranial cerebral circulation, e.g. the MCA. Here, a vascular territory may become isolated from the circle of Willis collateral supply, and depending on the presence of functional collateral pathways, hemodynamic compromise may occur. Hemodynamic failure in patients with carotid artery disease has been extensively studied, with most pioneering work done by the Washington and Pittsburg group. For instance, landmark papers by Powers et al. (12) have introduced the staging system for hemodynamic failure (see section: *Classifying severity of hemodynamic compromise)*, and thereby shown that an elevated oxygen extraction fraction (OEF), as

measured with Positron Emission Tomography (PET), is an independent marker for future stroke. (12,13) In the same line, Yonas et al. (14,15) have demonstrated the significance of impaired cerebrovascular reserve, measured with ^{133}Xe-CT, to indicate brain tissue at risk for stroke.
However, there is ongoing debate whether current imaging techniques and markers are robust enough to select those patients with severe hemodynamic failure that may benefit from surgical revascularization, regardless of being symptomatic or asymptomatic. This impasse is further highlighted in the discussion section of the thesis.

Carotid revascularization procedures
The main indication for surgical revascularization is to prevent irreversible injury to brain tissue (ischemia, or in selected cases hemorrhage). Historically, carotid endarterectomy has been the most effective treatment to reduce stroke risk in symptomatic (16,17) in appropriately selected asymptomatic (18-20) patients with carotid artery disease. During carotid endarterectomy the 'plaque' that is responsible for the intraluminal narrowing is removed, basically immediately restoring blood flow through the treated carotid artery. This procedure can only be carried out for an extracranial focal stenosis of the carotid artery. In the last couple of years some major trials have also investigated whether endovascular carotid stenting would be as an effective treatment as carotid endarterectomy. (21-23) For intracranial stenoses, an endovascular balloon angioplasty with or without stent placing (for vessel lumen reconstruction) can be preferred. The current outcome is that for both asymptomatic and symptomatic patients, both procedures do not differ significantly for 4-year rate of stroke and death (4.7% for endarterectomy versus 6.4% for stenting; p=0.03). (21)
With respect to age, studies have shown that carotid stenting is slightly more favorable in younger patients (<70 years of age), whereas carotid endarterectomy would be preferred in older patients (>70 years of age). (22,23) Ongoing evolution of revascularization procedures, in particular endovascular techniques, may improve patient outcome. However, appropriate patient selection for either medical or surgical therapy will remain the most critical link to improve clinical outcome.

Moyamoya vasculopathy
Moyamoya vasculopathy is a disease of unknown etiology exhibiting unilateral or more frequently bilateral progressive narrowing of the supraclinoid intracranial carotid artery termination including its proximal branches resulting in (chronic) brain ischemia. (24) Typical in moyamoya is the formation of compensatory collaterals arising mainly from the anterior circulation, leptomeningeal and the external carotid, with the appearance of 'a puff of smoke' as seen on angiography. The pathophysiology of the disease remains unclear and includes a process of progressive lumen obliteration in the larger vessels caused by a diverse collection of genetic and acquired conditions. (24) As opposed to a focal (carotid) stenosis, moyamoya vasculopathy is a more widespread disease where progressive obliteration of vessels minimizes the efficacy of collateral pathways (Figure 2). Symptoms

result from acute discrepancies between brain oxygen requirements and blood supply or from acute bleeding from a ruptured fragile collateral vessel. Clinically, patients may present acutely with brain infarction, transient ischemic attacks, hemorrhage, but sometimes also with epilepsy. (25) It is important to note that children most frequently present with ischemic attacks whereas adults present with either ischemic attacks or hemorrhage. (26) Cognitive deficits like mental retardation and attention disorders seem to be more severe in children than in adults, although little research regarding cognitive function in moyamoya in the absence of ischemia is available. (27,28) The only effective procedure to augment brain blood flow in patients with moyamoya vasculopathy is surgical revascularization, by performing an indirect bypass (for example pial synangiosis and encephaloduromyoarteriosynangiosis), a direct extracranial-to-intracranial (EC-IC) bypass or a combination of the two mentioned techniques.

Historically, moyamoya vasculopathy was considered a disease solely affecting the Asian demographic, however, a more widespread demographic has been observed, including Western populations. (29) Two incidence peaks prevail in the age groups around 5 years of age and the mid-40's, (30,31) mostly affecting women. (26) The highest prevalence of moyamoya vasculopathy is found amongst the Japanese population, (26) about 3 cases per 100.000 children. (32) The prevalence in the western world would be $1/10^{th}$ of that from Japan, (33,34) and mostly affecting children and Caucasian women in their mid-40's. Moyamoya has been associated with conditions such as Down's syndrome, Neurofibromatosis I, MEN-II and radiotherapy, in which the vasculopathy is called moyamoya syndrome. (24)

Surgical revascularization procedures for moyamoya vasculopathy

Currently, the only effective procedure to augment brain blood flow in patients with moyamoya vasculopathy is an EC-IC bypass. Such a bypass can be indicated when the vessel obliteration due to moyamoya has been that far progressed such that brain tissue perfusion becomes inadequate and the patient experiences ischemic symptoms (e.g transient ischemic attacks). EC-IC bypass revascularization procedures are either direct, indirect, or combined anastomoses to distal brain vessels, using various techniques. A bypass may have a great benefit in sub-acutely restoring sufficient perfusion but there is disagreement as to which patients with progressive hemodynamic failure might benefit from such a procedure. The problems encountered with surgical revascularization and controversial findings will be further debated in the discussion chapter.

Figure 2: *Illustration of moyamoya vasculopathy*

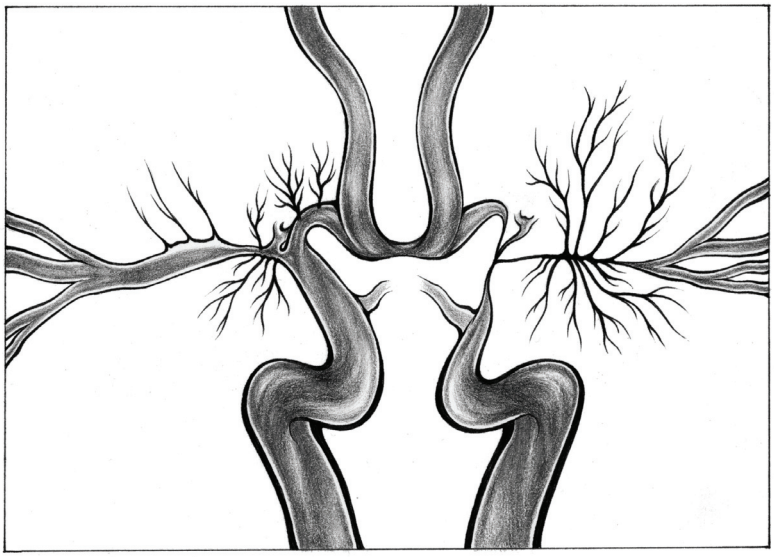

Caption figure 2: *Illustration of moyamoya vasculopathy in different stages of the disease. Shown on the right is an example of a mild case; progressive narrowing of the ICA termination and its major branches with formation of moyamoya-type collaterals. Sufficient brain tissue perfusion may still be present since the affected vessels can drop their vascular resistance and there is a "lumen" left to receive collateral flow. On the left side is a severe condition of the disease shown with complete obliteration of the ICA termination as well as the left A1 and M1 segment, leaving no "lumen" for collaterals to supply blood to the affected vascular territories. Performing bypass revascularization (direct and indirect) in such conditions may therefore only be effective in restoring perfusion more downstream the anterior and middle cerebral vascular territory (mostly the gray matter). The deep white matter for instance will be totally reliant on the fragile so-called moyamoya 'puff-of-smoke" collateral formation since the M1 is occluded.*

Brain arteriovenous malformations

Arteriovenous malformations of the brain (bAVM) are a rare neurovascular disease with an incidence of less than 1% in the general population. They can occur in people of all races and sexes in almost equal proportions. The typical time of discovery is between the ages of 20 and 40 years. The two most devastating symptoms that bAVM patients present with are intracranial hemorrhage (4/100 AVM patients per year), and seizures (45-60% of patients). The risk of hemorrhage is high, for example a young AVM patient will have over 70% risk of an intracranial hemorrhage over 30 years, and the chance of re-bleeding of a ruptured AVM is 25% in 4 years. (35)

A bAVM can be considered as a nidus consisting of abnormal tortuous and tangled cerebral arteries directly connected to dilated veins due to absence of an intervening capillary

vascular bed (Figure 3). The etiology is largely unknown where traditionally the deformity of blood vessels was assumed to occur in the embryonic stage with dynamic changes over time in angioarchitecture (‘*vascular remodeling’*) and hemodynamics possibly acting as the trigger for onset of symptoms. (36) This theory was mostly supported by the presence of a higher incidence of bAVMs in association with syndromes, e.g. ataxia telangiectasia, Sturge-Weber syndrome, and Osler-Weber-Rendu syndrome. (37) Today this concept has been challenged with more comprehensive pathophysiological arguments that bAVMs occur as a result of an active angiogenic and inflammatory response to some post-natal inciting vascular event. (38-40) The natural history is mostly unknown since AVMs are treated soon after diagnosis. (37) In a large series from the Brain Vascular Malformation group of the University of Toronto (41) it was shown that AVMs in the occipital region have a more benign nature than AVM in other locations. Large trials, such as the A Randomized trial of Unruptured Brain AVMs (ARUBA) (42) are underway to address this question more precisely. Currently, Hereditary Hemangio-Telangieectasia (HHT) is the only known disease with a genetic predisposition for AVM development. (36)

The absence of capillaries, and therefore smooth muscle tone for cerebrovascular autoregulation of blood flow, creates a low resistance environment in the abnormal tortuous and directly connected arteries to veins. High volumes of blood flow can shunt through an AVM nidus, (37,43) possibly re-directing blood away from normal surrounding blood vessels. (43-45) Also, the high inflow into the nidus might alter outflow as venous vessels may not have the capacity to cope with high volumes of blood flow. This may lead to venous outflow restriction (venous congestion), and redirection of venous outflow, all together called a “pseudophlebitic pattern”. (46,47) The hemodynamic concepts in relationship to seizures are further investigated in Chapter 5 of this thesis with an extensive evaluation and debate in the discussion section.

Clinical management

There are three treatment options that, either alone or combined, can be indicated to obliterate or reduce an AVM nidus. Surgical removal of the nidus provides the most definitive and direct removal of an AVM and remains the mainstay of treatment in patients with a Spetzler-Martin grade 1 or 2 AVMs with a very low complication rate in experienced hands. (48) Surgical procedures, however, are limited to anatomical location, nidus angioarchitecture, and size. Therapy aimed at embolization of the arterial feeder(s), can disconnect an AVM from the cerebral vasculature, or with larger and more complex AVMs reduce nidal size or eliminate shunts that may be a high risk for hemorrhage. All approaches have the major objective to reduce the risk of future hemorrhage. Stereotactic radiosurgery represents one of the main established therapeutic modalities in the treatment of intracranial AVMs and can be indicated for complex AVMs that are located deep in the brain. Within that paradigm, the Cyberknife represents a more recent and robot-based technique to deliver stereotactic radiation as compared with gamma knife or Linear Accelerator-based radiosurgery. The intervention, despite multiple procedures and long

"lagtime' before success of obliteration can be determined, is relatively quick and good clinical outcome has been reported in a large patient series. (49)

Figure 3: *Illustration of a brain arteriovenous malformation*

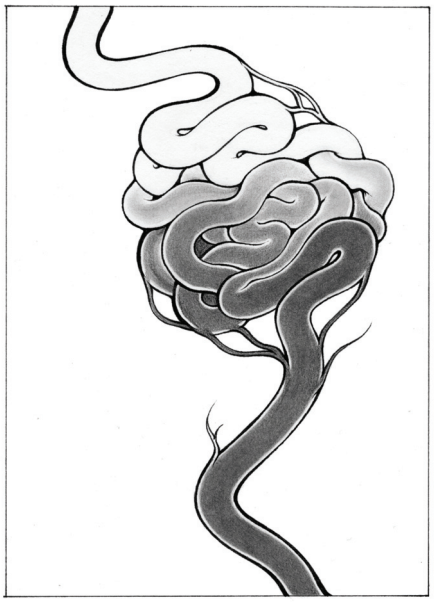

Caption figure 3: *Illustration of a classic appearing brain AVM with one arterial feeder (dark vessel) and one draining vein (white vessel). Note that the compact nidus does not contain internidal brain tissue*

Cerebrovascular autoregulation in chronic cerebrovascular disease

In general, vascular diseases impair the ability of the feeding vasculature to deliver adequate flow to the microcirculation. Cerebrovascular autoregulation can compensate for supply deficits through vasodilatation by decreasing the vascular resistance of the vessels downstream of the affected artery(-ies). This pressure drop occurs by reduction of the smooth muscle tone in the capillary bed, i.e. relaxation of the pre-capillary sphincter. Also, the presence of functional collateral flow pathways plays an important compensatory role to maintain adequate perfusion of brain tissue.

However, in severe chronic cases of cerebrovascular disease the flow control mechanism may reach its limits, and is not able to further decrease the vascular resistance by vasodilatation. In other words, the vascular beds have already responded to proximal vascular stenosis with maximal smooth muscle relaxation, i.e. the vascular beds are already

operating at the extreme vasodilatory endpoint of the autoregulatory reserve capacity. The flow control mechanism becomes "exhausted".

In effect, these vascular beds are unable to respond to day-to-day physiological changes in blood pressure and CO_2, as well as a neuronal signal for augmentation of blood flow. However, normal surrounding vascular beds are still able to lower vascular resistance. The overall effect is a diversion of blood towards the lower resistance vascular bed. Under these conditions a flow stimulus such as carbon dioxide will increase flow to the normal territory and "paradoxically" decrease flow to the territory with exhausted autoregulatory reserve. This condition is termed arterial "steal physiology" (Figure 4).

On the other hand, outflow restrictions in the venous system might also alter the flow control mechanism. In this instance, arterial inflow is sufficient but the venous system cannot drain the inflowing blood from the brain tissue sufficiently, possibly leading to high pressures in the arterioles, affecting the pre-capillary sphincter tone. Furthermore, the inability to drain the blood away from brain tissue may prohibit effective removal of harmful metabolites, and heat generated by neuronal activation that all can lead to tissue injury.

Classifying severity of hemodynamic compromise

Severity of hemodynamic compromise in cerebrovascular disease can be classified* using lower limits of vascular and metabolic reserve which function as a compensatory system to preserve cerebral oxygen metabolism towards the reduction of cerebral perfusion pressure (CPP). This classification is according to the landmark papers by Powers et al. (12,50)

In Stage I, there is maintenance of CBF due to autoregulatory compensation leading to a lower vascular resistance; the net result is a decrease of cerebovascular reserve. In Stage II the brain exhibits a decrease of CBF since the cerebrovacular autoregulation cannot lower the vascular resistance anymore; the cerebrovascular reserve is 'exhausted'. The decrease in CBF results in an increased OEF, there is no surplus of oxygen delivered to brain tissue anymore (decrease of metabolic reserve), preserving $CMRO_2$. Whereas minimum cerebral blood flow (CBF) found with normal neurological function is 19 ml/100 g-min, the minimal flow required to maintain tissue viability is 15 ml/100 g-min. In stage 2 impairment, CBF can be reduced to 15 ml/100 g-min whereas the cerebral metabolic rate of O_2 ($CMRO_2$) is maintained constant at a level near that of healthy brain (1.3 ml/100 g-min). Important to note is that CBV *increases* under these conditions, possibly related to the maximum vasodilatation.

Figure 4: *Concept of arterial steal physiology*

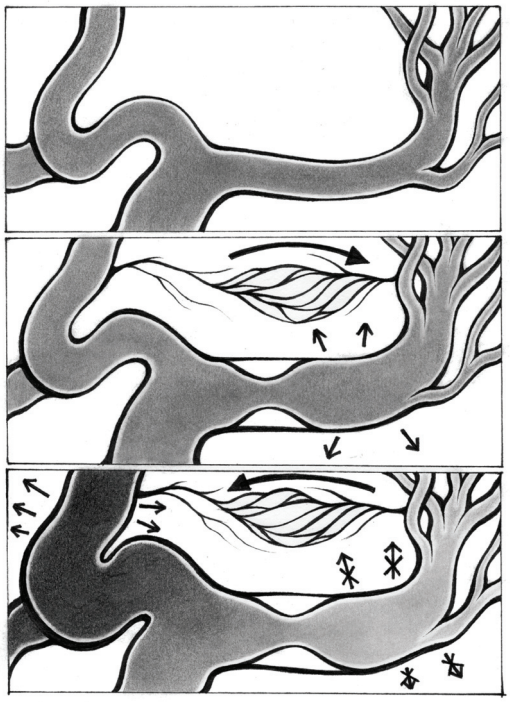

Caption figure 4: *Illustration of the mechanism of 'steal physiology'. The upper box shows a normal cerebral vasculature with blood flow distributed in sufficient means to all major cerebral arteries. The middle box shows vasodilatation of the middle cerebral artery in response to a focal stenosis in this vessel (small arrows) resulting in a drop in vascular resistance. Also collateral pathways open up from the anterior cerebral artery (large arrow). The lower box shows vasodilatation of the anterior cerebral artery territory in response to a vasoactive stimulus, and the inability of the middle cerebral artery to further drop the vascular resistance, since the autoregulatory flow control mechanism is exhausted here due to the stenosis (arrows with cross through them). Effectively the anterior cerebral artery territory drops its vascular resistance to a greater degree than the middle cerebral artery territory with subsequently redirection of blood flow towards the unaffected vascular territory (darker shade in anterior cerebral artery and reversed large arrow). This process is called "steal physiology".*

This initial classification was extended with a third stage when studies found decreased CBF, and $CMRO_2$, with near normal OEF in patients that were considered in stage II of hemodynamic compromise. (13,15) Ischemic neuronal damage was present in these patients, leading to less oxygen consumption ($CMOR_2$) by the tissue, returning OEF to 'normal' despite the decrease in CBF. Figure 5 in the paper by Derdeyn et al. (13) outlines the interplay of decreasing blood flow on following parameters: CBF, cerebral blood volume (CBV), cerebral metabolic rate of oxygen ($CMRO_2$), oxygen extraction fraction (OEF), and CPP, illustrating the three stages.

If we can assume that the final common pathway for blood flow modulation occurs through vascular resistance and arterial smooth muscle tone, than there are clinically relevant issues that arise in patients with chronic cerebrovascular disease, i.e. a vascular stenosis, occlusion, or a significant shunt. Assessing the cerebrovascular reserve can act as a functional assessment that represent not only the degree of vessel lumen narrowing, but also the extent of collateral vascular supply and overall, the ability to augment/maintain sufficient blood flow to brain tissue.

**Important to note is that the classification of hemodynamic failure is based on atherosclerotic carotid artery disease. In this thesis, as outlined in section "chronic cerebrovascular diseases", I investigate a wider spectrum of chronic steno-occlusive disease, including non-atherosclerotic intracranial diseases such as idiopathic middle cerebral artery occlusion and moyamoya vasculopathy. I would like to emphasize that the pathophysiolgical processes underlying these diseases may behave differently than for carotid artery disease. For instance, the cerebral vessels downstream of an occluded internal carotid artery are assumingly unaffected (normal intraluminal diameter), preserving the possibility for collateral pathways such as the posterior and anterior communicating artery and even surgical revascularization to reperfuse the downstream vascular territory, since the MCA lumen is still patent. Considering moyamoya vasculopathy, the main anterior vascular supply is affected (from supraclinoid ICA to proximal MCA and ACA), often bilateral) resulting in narrowing or even obliteration of multiple vessel segments. Absence of sufficient intraluminal diameter causes a major obstruction for successful collateral supply, either intrinsically or by surgical means.*

1.5 Examining the integrity of the cerebrovascular flow control mechanism

The integrity of the flow control mechanism is indicated by the cerebrovascular reserve, the measure of how much a given vascular territory can vasoconstrict or vasodilate to maintain sufficient blood flow or to augment blood flow during neuronal activity. The cerebrovascular reserve can be assessed by measures of cerebrovascular reactivity (CVR), which is the measure of the change in cerebral blood flow in response to a global vasodilatory stimulus. Assessment of CVR requires a vasodilatory stimulus and a technique for measuring the resulting change in cerebral blood flow.

Arterial PCO_2 as vasoactive stimulus

Carbon dioxide (CO_2) is the most widely used vasodilatory stimulus for CVR examinations since it can induce a rapid and potent response of the vascular system. More specifically, the change in the partial pressure of arterial CO_2 ($PaCO_2$) values is the independent stimulus to induce a vascular response. Furthermore, $PaCO_2$ is the independent variable of interest for control of cerebral blood flow (CBF). Changes in CBF in response to vasoactive provocative stimuli (i.e. CVR) are important for the assessment of the autoregulatory capacity.

Increases in $PaCO_2$ are easily reversed with hyperventilation and changes in CBF are predictable at about 3% per mmHg change in $PaCO_2$. (51) However, $PaCO_2$ remains an invasive measure. Therefore, the partial pressure of end-tidal CO_2 ($P_{ET}CO_2$) has been advocated as a surrogate for $PaCO_2$, as this measure can be obtained non-invasively. (52)

1.5.1 Vasoactive stimuli

Below is a brief overview of the various methods for manipulating $PaCO_2$ along with the advantages and disadvantages of each method.

Acetazolamide

Acetazolamide (ACZ; diamox) has been administered to induce increases in $PaCO_2$ in CVR studies. ACZ is a competitive inhibitor of the carbonic anhydrase. Carbonic anhydrase is a zinc containing enzyme that catalyzes the following reversible reaction:

$CO_2 + H_2O \leftrightarrow HCO_3^- + H^+$

In the presence of ACZ the carbonic anhydrase is inhibited from catalyzing the aforementioned reaction resulting in an increase in $PaCO_2$. (53,54)

Advantages

- Administration does not alter the systemic blood pressure making it a good surrogate for measuring CVR in the presence of hypotension
- Maximal vasodilatation achieved
- Safe agent to use

Disadvantages

- Must be injected intravenously rendering its use somewhat invasive.
- The time course of response to oral administration is highly variable
- $PaCO_2$ changes in response to changes in ventilation are superimposed on those of ACZ.
- The mechanism of affect of ACZ does not allow a quantifiable measure of change in $PaCO_2$ to be made, thereby making each application an independent stimulus that is non-standardized.

Breath holding

Breath holding is another method of inducing changes in $PaCO_2$. This method works by eliminating the flux of both O_2 and CO_2 in the lung allowing for the alveolar PO_2 and PCO_2 to equilibrate with those in the mixed venous blood. Once the alveolar and mixed venous PO_2 and PCO_2 are equilibrated then any changes that occur will do so only according the metabolic production of CO_2. (55)

Advantages

- No external gas sources are needed
- Relatively safe

Disadvantages

- Cannot measure $P_{ET}CO_2$ and $P_{ET}O_2$
- The rates of change in PaO_2 and $PaCO_2$ are relatively slow and vary from subject to subject, as well as the circulation time required for blood to travel from the lungs to the tissues and then back to the lungs.
- The CO_2 capacitances of the body are very large relative to metabolic changes resulting in a buffering of end tidal partial pressure changes relative to content changes and thereby limiting the change in $PaCO_2$ from those at steady state.
- The $PaCO_2$ and PaO_2 change continuously in opposite direction.
- The changes in $PaCO_2$ and PO_2 are not linear therefore very sensitive to time of breath hold.
- The length of the stimulus is limited by the subject's ability to hold his breath.

Direct CO_2 administration by inhalation

- Manipulation of $PaCO_2$ can also be achieved by administration of 5– 7% CO_2 by inhalation. However the inconvenience of shortness of breath and relatively high rate of adverse effects such as nausea, tachycardia, and hypertension make CO_2 inhalation not an ideal method. Furthermore, most of the aforementioned disadvantages for the other techniques also apply for CO_2 inhalation, as it cannot measure $PaCO_2$ (the true independent variable) and PaO_2. the changes in $PaCO_2$ and PaO_2 depend not just on the inspired concentration, but also on the ventilatory response, which may vary between subjects and within a single subject on

consecutive examinations. The $PaCO_2$ and PaO_2 change continuously in opposite direction with ventilation. In summary, a fixed inspired PCO_2 does not result in a fixed vasoactive stimulus.

A standardized method to control $PaCO_2$

Several problems arise with these methods that prohibit precise control of $PaCO_2$ and therefore standardization of the technique to examine cerebrovascular reserve. $PaCO_2$ and the partial pressure of arterial O_2 (PaO_2) were long assumed to both have a physiologically inseparable effect on CBF (i.e. CVR). For instance, raises in arterial PCO_2 content would lower the PO_2 content in arterial blood. Although the cerebral vasculature is more sensitive to changes in $PaCO_2$, PaO_2 can act as a confounder. For example, a higher PaO_2 content (i.e. hyperoxia) is known to induce vasoconstriction in cerebral arteries. (56)

Despite the physiological limitations, changes in $PaCO_2$ are considered a safe and easy way to induce a global response in the cerebral vasculature for CVR examinations. In particular, the use of the partial pressure of end-tidal CO_2 ($PETCO_2$) to provoke changes in $PaCO_2$ is often used as a suitable surrogate. However, a gradient exist between alveolar-arterial PCO_2 (A-a gradient) that might be insignificant in young healthy subjects with no cardio-pulmonary disorders –on average, but generate an unreliable relationship between $PETCO_2$ and $PaCO_2$ in even a healthy individual, and certainly patients, and elderly.

The two major limitations: The inseparable physiological effect of $PaCO_2$ and PaO_2 on CBF and the unreliable relationship between $PETCO_2$ and $PaCO_2$ have been addressed with a method that allows prospective and independent control of $PETCO_2$ and the end-tidal partial pressure of O_2 ($PETO_2$). Controlled changes in $PETCO_2$ can be implemented with a custom-built automated gas blender and breathing circuit combination (RespirAct™, Thornhill Research Inc., Toronto, Canada). The technique applies an end-inspiratory rebreathing method to precisely control $PETCO_2$ and $PETO_2$ independently of each other. This method has been precisely described by Slessarev et al. (57) and reduces the A-a gradient of CO_2 within clinical acceptable range (0.5 ± 1.7 mmHg; p=0.53) in healthy sitting subjects. (58)

An automated computer feedback method for controlling $PETCO_2$ and $PETO_2$

Various methods aimed at manipulation of arterial CO_2 and O_2 levels have been extensively used to study CBF. Previously, precise and independent control of arterial gases has usually been achieved by adjusting inspired gas concentrations on a breath-by-breath basis to attain target end-tidal values of CO_2 and O_2. However, breath-by-breath variations in respiratory frequency and tidal volume in spontaneously breathing subjects result in an increased variability in end-tidal gas concentrations. This problem has been addressed by some creating highly sophisticated feed-back algorithms and rapid gas analyzers to improve the performance of these techniques and minimize the variations in end-tidal gas concentrations, the so called end-tidal forcing method. (59,60) Significant

drawbacks remain, such as the requirement of high inspiratory flows and the complexity and bulkiness of the technique, making it a very expensive method and unsuitable for the clinical setting

A method based on end-inspiratory rebreathing (a sequential rebreathing method)
A simpler method of partial end-inspiratory rebreathing may have more clinical utility. The use of a simple re-breathing circuit that is self-regulating (Hi-Ox-80; Viasys Healthcare, Yorba Linda, Calif, USA) enables normal levels of CO_2 and O_2 independent of ventilation and tidal volume. Adding the algorithms of model-based prospective end-tidal targeting, that tightly controls CO_2 and O_2 concentrations flowing into the re-breathing mask (57), $P_{ET}CO_2$ and $P_{ET}O_2$ levels can be prospectively controlled and targeted.
Furthermore, with this partial end-inspiratory rebreathing technique, the end-tidal PCO_2 and O_2 values approaches the arterial PCO_2 and O_2 concentrations. (58) This is an important feature for studies investigating cerebral blood flow.

For CVR examinations, robust iso-oxic near-square wave changes in $P_{ET}CO_2$ can be induced with end-inspiratory rebreathing. However, the actual measurement of CVR requires an imaging technique that can display the changes in cerebral blood flow.

Imaging modalities for examining cerebrovascular reserve
As mentioned previously, cerebrovascular autoregulatory compensation fails when smooth muscle in the pre-capillary sphincter cannot either further relax or constrict in response to a vasoactive stimulus. The ability to interrogate the existing "setpoint" of smooth muscle tone would be very useful in determining how much of an additional response is present within the vascular system. This "reactivity" assessment can be performed by determining how much of an increase or decrease in blood flow occurs in response to a given vasoactive stimulus. This is termed cerebrovascular reactivity (CVR), and is defined as the percent change in cerebral blood flow/percent change in flow stimulus.

There are numerous imaging methodologies available for making CVR measurements including Transcranial Doppler ultrasound (TCD), xenon enhanced computed tomography (Xe-CT), single photon emission CT (SPECT), ^{15}O-positron emission tomography (^{15}O-PET), and magnetic resonance imaging (MRI) using different stimuli and different imaging contrast agents.

Transcranial Doppler ultrasound
TCD was first used to measure CVR by Ringelstein et al. (51) The Doppler effect depends on change in frequency of sound waves reflecting from moving objects. In this case, the moving objects are red blood cells flowing in the middle cerebral artery (MCA). The proximal segment of the MCA is insonated in the temple area in front of the ears by a transmitter-receiver the size of a small microphone. The beam can be focused to a depth of about 45-55 mm to optimize the signal. As there is little change in MCA diameter with

changes in blood pressure and PCO_2, (61,62) the changes in velocity of the blood in the artery in response to a stimulus are proportional to those of flow. (63) The relationship of middle cerebral artery velocity (MCA_V) to blood flow has been validated against CBF as measured using ^{133}Xenon Computed Tomography (^{133}Xe-CT) by Bishop et al. (64) and Dahl et al. (65) and used clinically to measure CVR. (66) As discussed above, the change in MCA_V as an index of CBF in response to a vasoactive stimulus has since been shown to be strongly predictive of cerebrovascular reserve. Nevertheless, MCA_V may be useful when comparing pulsatility on one side to the other, the side with the carotid artery lesion acting as a low pass filter, reducing the pulsatility on the ipsilateral side. (67) TCD is inexpensive, non-invasive, and free of ionizing radiation. Although a TCD examination is inexpensive, the technique has low spatial resolution, and solely covers a single middle cerebral artery territory at the most proximal part of the MCA, rather than a spatial acquisition of reactivity for the brain. It is also technically not feasible in about 10% of patients due to lack of an acoustic window, and the measured value is highly operator dependent.

CT-based imaging methods

The ^{15}O-PET technique has been extensively used to gather quantitative CBF data in patients with hemodynamic failure. With this technique, various metabolic parameters, such as oxygen extraction fraction (OEF) and regional metabolic rate of oxygen ($CMRO_2$) can be measured (12,13,68-70) Information about regional CBF, cerebral blood volume, OEF, and $CMRO_2$ can be used to assess the severity and classification of hemodynamic failure in chronic cerebrovascular disease (see section "*Classifying severity of hemodynamic compromise*"), (12,13,50) where elevated OEF by itself has been put forward as a powerful parameter for increased future risk for ischemia in patients with symptomatic carotid artery occlusion. (12,71-73) Yet in clinical practice, PET studies may be difficult to implement for routine use. The required ^{15}O-gas studies are expensive, and access to the instable and rapidly decaying oxygen isotope needed for cerebral hemodynamic studies requires an on-site cyclotron. Furthermore, derivation of quantitative data requires repeat exams, often on separate days, with low reproducibility and only moderately coverage of the brain. Finally, as for all CT-techniques, the examination will introduce ionizing radiation and may be invasive when ACZ is injected as a vasoactive stimulus.

With Xenon enhanced CT quantitative measures of CBF can be derived. With relevance to hemodynamic failure, Xe-CT in combination with ACZ has clearly demonstrated that impaired CVR associated with steal phenomenon is an indicator for a future ischemic event. (66) Measurement of CBF with the stable ^{133}Xe gas (68) is, however, expensive, radioactive, and inhalation of stable xenon can have undesirable side effects. Xe-CT has a good resolution but cannot cover the whole brain; only one brain region at a time can be measured. (69,74) In contrast, stable Xe-CT (66,75) provides a good resolution and quantitative capacity and therefore is considered the gold standard for CVR measurements in combination with an ACZ challenge in between two consecutive scans. As for PET and SPECT, the Kety-Schmidt equation is used to calculate the change in CBF. (76) The major

drawback is that Xe-CT is not widely available in hospitals around the world. Studies with the stable xenon gas are very expensive and, with relevance to North America, currently not approved by the Food and Drug Administration. Also, the subject examinations will involve the use of ionizing radiation and an intravenous injection of ACZ making it an invasive exam.

A third CT-based technique is SPECT, which has a relatively widespread use for mapping CVR when used in combination with an ACZ challenge and Xenon and has shown that impaired CVR is a predictor of future ischemia in patients with symptomatic internal carotid artery and middle cerebral artery occlusion (77,78) A major limitation is that SPECT studies are typically performed over two days due to the radio-pharmaceutical kinetics (the repeat scan is usually performed three days later), allowing for many potentially confounding variables. It is possible to perform the study over a single day, but this requires much higher activity for the second scan, increasing the radiation dose to the patient, and estimations of input parameters only generate semi-quantitative data, with moderate reproducibility. Related to that is the scatter of x-rays that may act as a potential confounder of the CVR measurements.

In fact all of these techniques are not fully standardized, and with the exception of TCD, are expensive, invasive, exposing patients to ionizing radiation and carry a certain complexity that prohibits clinical implementation.

Improvements should be made to create a non-invasive, standardized and therefore quantitative (input independent), functional test with high spatial resolution providing information of the cerebrovascular reserve over the whole brain. Such a technique may add information over current existing functional imaging modalities, and may provide additional information over conventional structural imaging methods. The next section will elaborate on the role of MR imaging for CVR examinations and will introduce a standardized test that addresses aforementioned problems and may have a practical clinical application.

1.6 Structural versus functional neurovascular MR imaging in chronic cerebrovascular disease

Structural MR imaging

Overview of magnetic resonance imaging principles

To create clinical images, magnetic resonance imaging (MRI) utilizes the nuclei of hydrogen (^{1}H). The hydrogen nucleus carries one proton that possesses spin, basically resembling a tiny magnet that is sensitive to magnetic fields and electromagnetic waves, varying these atoms between low and high energy states. Protons can be induced to change from low to high energy states using radio waves with frequency that is proportional to the energy difference between the two states. The frequency in angular terms in given by the Larmor equation which underpins the whole of magnetic resonance:

$$\omega = \gamma B_0$$

,where ω represents the frequency of the precession of the nuclear magnetic moment, γ is the gyromagnetic ratio, and B_0 is the strength of the externally applied magnetic field. The frequency of the radio wave required to induce the change from a low to high energy state is therefore equal to ω.

Once in the high energy state, nuclei begin to revert back to a more stable low energy state. This process is referred to as T1 recovery. The repetition time (TR) is the time span between two successive excitations of the same slice. A short TR will generate a high T1 weighting on MR images, as structures with a short T1 will appear bright. As mentioned previously nuclei act as tiny spinning magnets.

The rotation of the nucleus' magnet moment around direction of the externally applied magnetic field is called precession. Following application of a radio frequency pulse at the Larmor frequency, the axes of precession of individual nuclei become aligned. The process of dispersion between these alignments is called T2 relaxation. Echo Time (TE) is time between excitement and measurement of MR signal. Long TE results in strong T2-weighting with structures with high water content, such as cerebrospinal fluid, appear bright. This can be explained as tissues with short TE lost most of their signal strength while tissues with long TE will show considerable signal strength. The relaxation times T1 and T2 are very important in imaging, as they have the greatest effect in determining contrast.

Lastly, in addition to T2 weighting, two other factors can cause magnetic moments to go out of phase. Nuclei acting as tiny magnets, cause local haphazard fluctuation of the magnetic field by interacting with each other. This results in small inhomogeneities in applied magnetic field thereby reducing the MR signal. Moreover, differences in the magnetization of neighboring tissues (susceptibility effects) will also cause phase

dispersion of the MR signal. This property underlies the BOLD imaging principle (discussed further on in section "BOLD-MRI"). The haphazard field inhomogeneities, variations in B_0, and T2 weighting can be used to produce T2* (dephasing) contrast, which can be defined in following equation:

$$1/T2^* = 1/T2 + 1/T2_{inhomogeneous}$$

Structural MR imaging for chronic cerebrovascular disease

Magnetic Resonance Imaging (MRI) techniques may provide useful information about hemodynamic alterations due to chronic cerebrovascular diseases. Structural volumes acquired with MR imaging can provide a comprehensive and non-invasive assessment of diseases affecting brain tissue and cerebral blood vessels, as a single observation at one time point or over different points in time. Continuing advances such as development of higher field strength MR-systems and further expansion of tailored sequences with high spatial resolution make MR exams increasingly utilized for clinical and research purposes.

An example of a specific structural MR acquisition is magnetic resonance angiography (MRA), a sequence that can provide a comprehensive overview of the cerebral vasculature, and vessel patency. Generally, these images can be obtained after administration of a contrast agent (contrast enhanced) or with the Time-of-Flight technique, where direction and blood flow velocity instead of contrast, are used as parameters to visualize blood vessels. Here, a short TE and flow compensation is used to make flowing blood much brighter than stationary tissue. This acquisition can also be carried out for imaging of the cerebral veins by magnetic resonance venography (MRV). Fluid-attenuated inversion recovery (FLAIR) is a special sequence with long T1 to remove the effect of fluid on the acquired images, therefore enhancing detection of brain lesions. Inversion recovery prepared fast spoiled gradient recalled (IR-FSPGR) images generate detailed spatial anatomical information of the brain. A final example is diffusion weighted imaging (DWI) a sequence sensitive as to the diffusion of water molecules. For instance, in brain areas with restricted diffusion (indicative for (future) ischemia) the MR signal loss is less intense resulting in a brighter display on imaging.

However, these image acquisitions are typically static images, meaning these acquisitions cannot provide information about dynamic processes in the brain, such as changes in neuronal activity and cerebral blood flow. Also, depending on the signal-to-noise ratio of the sequence, input parameters, and field-strength of the MR system, anatomical information might be lost or neglected spatially. Finally, structural images may fail to correlate to clinical presentation where, for example, a patient with moyamoya vasculopathy may have neurological symptoms but may demonstrate intact appearing vessels on MR angiography while another patient with the same condition can be asymptomatic with poorly appearing vessels on MRA (Figure 5). The same accounts for

patients with brain arteriovenous malformation, as similar appearing bAVMs can present, for instance, either with or without epileptic seizures (Figure 6).

Functional MR imaging

Functional acquired MR volumes (fMRI) further elaborate on understanding 'real-time' processes in the brain, such as changes in cerebral blood flow and activation of neurons in different areas of the brain. Unfortunately, the functional MRI exams are currently not very well integrated for clinical use. Generally, functional acquisitions are straightforward to obtain, though post-processing and analysis of the functional data may be cumbersome therefore preventing its utilization as a practical clinical test. Though, by further development and clinical implementation of functional MR imaging techniques more may be learned about the natural history and pathophysiology of chronic cerebrovascular diseases altering CBF and therefore the functioning of neurons (integrity of the brain tissue). One sequence in particular may assist in this learning process: Blood Oxygen-Level Dependent (BOLD) contrast.

Blood Oxygen-Level Dependent MRI

The first application of functional MR imaging (fMRI) with Blood Oxygen Level-Dependent (BOLD) acquisitions generated by T2* weighted contrast, was demonstrated in an animal model by Ogawa et al. (79) in 1990, followed by Kwong et al. (80) in humans in 1992. Their work reported that changes in the activity of the brain affected the local MR signal and provided an intrinsic mechanism for detecting brain activation. The change in signal occurs due to changes in local magnetic field strength induced by the paramagnetic effects of deoxyhemoglobin. Application of this effect using BOLD-functional MR imaging (fMRI) has revolutionized the detection and analysis of neuronal networks. Blood flow in the brain is tightly coupled to local tissue metabolism. (81,82) Change in metabolism due to neuronal activity produce marked increases in local cerebral blood flow in those activated areas. (6,81,82) The net result is a washout of deoxyhemoglobin (dHb) in that brain area which in turn affects the BOLD signal. Changes in BOLD signal in response to local metabolism (neuronal activity) underlies the basis of functional MR imaging, which can be used to map changes in local blood flow response to various tasks, such as fingertapping and (relevant for this thesis) a vasoactive CO_2 stimulus. Note that BOLD measures are only an indirect representation of changes in cerebral blood flow. The true utility of BOLD contrast can be used to study CVR, the measure of how much cerebrovascular reserve is present in a given vascular bed.

Figure 5: *Structural versus functional neurovascular imaging*

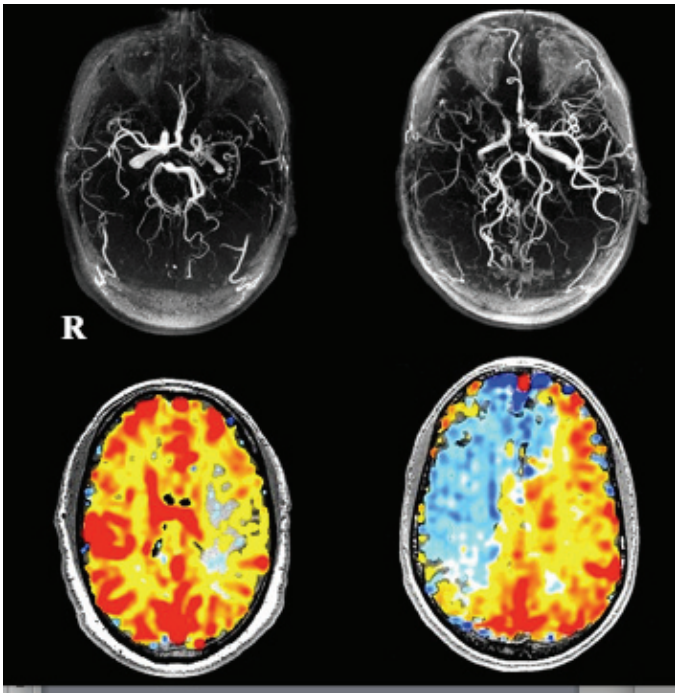

Caption figure 5: *Illustration of structural versus functional imaging in two subjects with chronic cerebrovascular steno-occlusive disease. The subject on the left demonstrates an occlusion of the left ICA and MCA on MR angiography but with a near normal appearing (functional MRI) CVR map indicating sufficient collateral flow to maintain brain tissue perfusion. The subject on the right demonstrates a similar MR angiographic image with an occlusion of the right ICA and MCA, however in this instance collateral pathways are insufficient to maintain sufficient brain tissue perfusion as shown by the blue appearing region in the right hemisphere on the (functional MRI) CVR map (the blue colour indicates severely impaired cerebrovascular reserve associated with steal physiology; see also figure 6 for color grading scale).*

Figure 6: *Structural versus functional imaging in brain arteriovenous malformations*

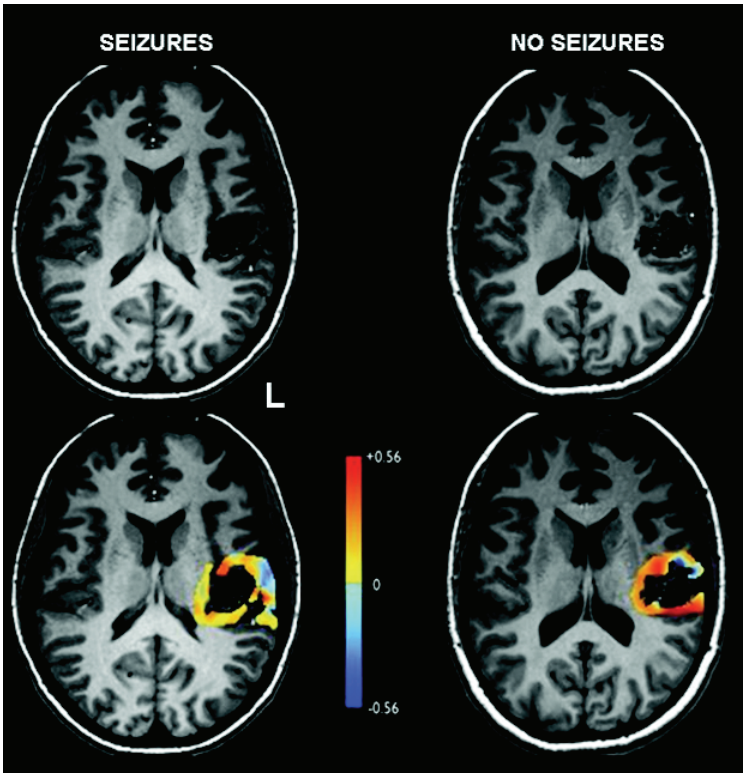

Caption figure 6: *Axial anatomical images and CVR in adjacent tissue. An anatomical acquisition of a seizure prone patient with bAVM (top left) and a bAVM in a patient with no history of seizures (top right). Note that the bAVMs appear in the same location and demonstrate similar features on structural MR imaging. Below each scan is the corresponding CVR map, masked to show CVR for only peri-nidal tissue, overlaid on the anatomical images in the bottom row The peri-nidal CVR of the bAVM patient with seizures (bottom left) shows decreased CVR ($p<0.001$) compared to that of the bAVM patient without seizures.*

BOLD-MR imaging to examine the cerebrovascular reserve

BOLD MRI depends on an adequate response of the cerebrovascular autoregulatory mechanism to augment blood flow when a vasodilatory stimulus is applied. The increase in blood flow results in washout of deoxyhemoglobin that can be detected in the BOLD signal. In chronic cerebrovascular disease, with progressive stenosis, cerebrovascular reserve gets progressively smaller resulting in a parallel decrease in BOLD signal eventually leading to a paradoxical (negative) BOLD signal in severe cases when the autoregulatory reserve becomes “exhausted” due to failure of collateral flow pathways

(Figure 4). Under these conditions, augmentation of blood flow under any stimulus including neuronal activation is theoretically not possible.

Several limitations, however, are inherent to BOLD CVR imaging. The MRI signal contains an intrinsic baseline drift requires multiple comparative measurements to be made between two steady-state conditions in order to improve statistical matching. This dramatically influences reliability of CVR measures as the vasoactive stimulus, either CO_2 or acetazolamide, is not standardized (see section "*Arterial PCO_2 as vasoactive stimulus*"). Furthermore, changes in $PaCO_2$ influences the PaO_2 level resulting in confounding effects on the BOLD signal. A high arterial PO_2 level may cause vasoconstriction (56) thereby decreasing CBF, increasing venous dHb levels (assuming constant $CMRO_2$) resulting in *decreasing* BOLD signal intensity. Moreover, high levels of PaO_2 also increase arterial oxygen content by increasing the O_2 saturation of hemoglobin and the fraction of O_2physically dissolved in the plasma. For a given brain $CMRO_2$ and cerebral blood flow, the increase in PaO_2 content will decrease venous dHb levels, thereby *increasing* the BOLD signal. (83)

BOLD MRI sCVR examination to quantitatively measure cerebrovascular reserve

Aiming to improve these matters, a practical and quantitative MR-based test has been developed at the University of Toronto where BOLD acquisitions are obtained during a standardized iso-oxic PCO_2 stimulus to test the reactivity of the brain blood vessels (standardized CVR; sCVR). (57,84) CVR is defined as percent change in BOLD signal/mmHg change in $PETCO_2$. The iso-oxic steps in PCO_2 are near-square wave changes, employed with the previously described end-inspiratory rebreathing method, (57) resulting in a robust response in BOLD signal. When the change in $PETCO_2$ is applied by the method of Slessarev et al. (57) it has been shown to be equal to the $PaCO_2$, allowing the exact stimulus to CBF to be known. (85) The sCVR measured in a single voxel provides a measure of the vascular reserve of the voxel. The sCVR of the voxels superimposed on the anatomical image indicate the range and distribution of vascular reserve in the brain.

The ability to maintain normal levels of PaO_2 prevents that a subject becomes hypoxic, and minimizes alterations in the BOLD response, such as a T1-inflow effect. (86,87) Yet, the BOLD signal depends to an unknown extent on factors other than CBF, e.g. CBV, $CMRO_2$, and hematocrit. Recent investigations in different medical centers, by Goode et al. (88) and Kassner et al. (89) have shown good inter-subject and intra-subject reproducibility of the BOLD sCVR, providing empirical evidence that such factors are not major confounders. Another concern might be that BOLD MR does not provide a direct measurement of changes in CBF, but is more so a measure of the existing cerebrovascular reserve in a given vascular bed. Nonetheless, BOLD sCVR may act as a suitable surrogate for changes in CBF as a comparative study for direct blood flow measurement, i.e. arterial spin labeling (ASL) and where the standardized end-inspiratory rebreathing method was used for altering $PaCO_2$ for both studies, demonstrated good agreement. (90) The high signal-to-noise ratio

that can be generated for this sCVR exam allows for spatial mapping of CVR over the whole brain that can be color-coded on with according to an intensity scale (Figure 7).

Figure 7: *BOLD-MRI cerebrovascular reserve map of a healthy subject*

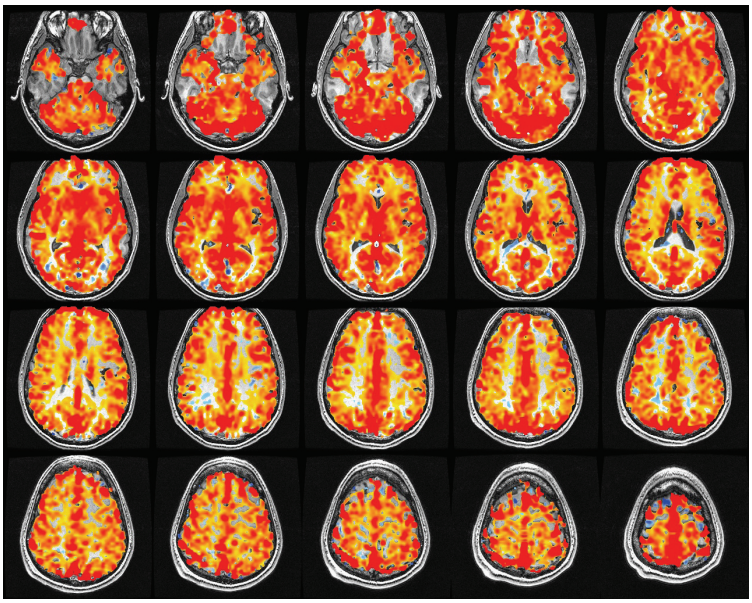

Caption figure 7: *Example of a BOLD-MRI sCVR map in a healthy subject. The red color indicates normal cerebrovascular reactivity (see also figure 6 for color grading scale).*

Translating sCVR to clinical operation, data acquisition takes fifteen minutes with the possibility to acquire structural imaging, such as MRA, DWI, and FLAIR acquisitions, during the same MR exam. The sCVR test for clinical purposes has been successfully utilized in patients with moyamoya vasculopathy, (91,92) steno-occlusive disease in adults (90) and pediatric patients, (93) and vasculitis. (94)

MRI protocol for sCVR examination

An axial 3-D T1 weighted Inversion Recovery-prepped Fast Spoiled Gradient Recalled (IR-FSPGR) volume (voxel size 0.78 x 0.78 x 1.0 mm) is acquired for spatial co-registration of the BOLD signal variation associated with CO_2 induced changes in blood flow using BOLD–EPI (echoplanar) acquisitions (EPI gradient echo with TR 2000, TE 25, 3.75 x 3.75 x 5 mm voxels) on a 3.0-Tesla HDX MRI system (GE Healthcare, Wis, USA). During the BOLD signal acquisitions sCVR studies are performed using an iso-oxic change

in $P_{ET}CO_2$as the vasoactive stimulus. The $P_{ET}CO_2$ and $P_{ET}O_2$ in all subjects are adjusted to baseline values of 40 mmHg and 100 mmHg respectively. Subjects then undergo two iso-oxic near-square wave increases in $P_{ET}CO_2$ to 50 mmHg. The first increase is of 45 s duration, followed by a return to baseline for 90 s and then a second increase for 130 s followed by a return to baseline. All $P_{ET}CO_2$ plateaus are maintained within ±1 mmHg.

Data analysis

The acquired MRI and $P_{ET}CO_2$ data are imported to the Analysis of Functional Neuroimages software. (95) BOLD images are co-registered to the T1-weighted anatomical dataset, (96) and are volume registered and slice-time corrected to the point of maximum correlation with the whole-brain average BOLD signal to compensate for temporal offset between end-tidal gas sampling and the BOLD signal acquisition (circulatory delay). The $P_{ET}CO_2$ data is time shifted to the point of maximum correlation with the whole brain average BOLD signal. Next, a linear least-squares fit of the BOLD-signal data series to the $P_{ET}CO_2$ data series is then performed voxel-by-voxel. CVR is calculated as the percent change in BOLD signal per mmHg change in $P_{ET}CO_2$. The correlation is color-coded and superimposed on the corresponding voxel of the anatomical volume to generate a color-coded CVR map.

1.7 Introduction

Determining the severity of hemodynamic failure in patients with cerebrovascular steno-occlusive disease resulting from an arterial stenosis, occlusion and/or failure of collateral flow recruitment is of great value for predicting subsequent risk for irreversible brain tissue loss. Whereas acute ischemia can be considered the end-stage of severe hemodynamic failure resulting in irreversible brain tissue damage and function, the consequences of so-called non-ischemic chronic intermittent hemodynamic failure are less well understood. In such instances, perfusion of brain tissue may be just sufficient to prevent gross ischemia but may fail to respond adequately to increases in demand such as those normally occurring during neuronal activation. The integrity of this flow response system can be assessed by measures of cerebrovascular reactivity (CVR), a measure of the change in cerebral blood flow in response to a vasodilatory stimulus. Reductions in CVR can range from a blunted increase in blood flow in response to a stimulus in mild cases, to "paradoxical" reduction in regional blood flow indicating steal physiology, in severe cases.

Brain areas exhibiting impaired cerebrovascular reserve with steal physiology are at high risk for developing a future acute ischemic event. (66,97,98) However, steal physiology can occur episodically and may exist over a long period of time without ictal signs of acute ischemia, but may still affect the integrity of both gray and white matter. Experimental animal models simulating a state of non-ischemic chronic hypoperfusion (99,100) demonstrate a decline in neuronal structure and viability. In humans, vascular cognitive impairment is associated with the loss of cortical gray matter, (101-104) whereas steno-occlusive disease without stroke has been associated with neurocognitive decline. (105-107) These studies indicate that a pathophysiological association may exist among cerebrovascular impairment, structural changes in the brain, and neurocognitive dysfunction. Furthermore, clinical symptoms may derive from hemodynamic alterations. In arteriovenous lesions, low-pressure shunts may redirect blood flow from normal perilesional tissue (steal physiological mechanism) where the high shunting volume load may overwhelm the venous outflow passage. These alterations lead to a higher risk for hemorrhage, but may affect the health of brain tissue as well.

In this thesis I extensively use the previously described quantitative BOLD-MRI sCVR method to infer the anatomical and clinical consequences of impaired cerebrovascular reserve. Specifically, I will investigate the adverse effects of chronically compromised blood flow control on the health of brain tissue to associate this with the onset of clinical symptoms in patients with severe chronic steno-occlusive cerebrovascular disease and brain arteriovenous malformations.

Where MRI-CVR measurements require precise changes in end-tidal pCO_2, I will also study the translation of the standardized PCO_2 stimuli for patients that require mechanical ventilation (i.e. positive inspiratory pressure), using an animal model. This method may open up future research avenues for critically ill patients who may benefit from MRI-CVR

studies, such as patients who suffer from traumatic brain injuries or a subarachnoid hemorrhage due to aneurysmal rupture.

1.7.1 Main hypothesis

Impaired cerebrovascular reserve results in chronic intermittent ischemic insults that are deleterious to brain tissue structure with adverse clinical consequences.

Sub-hypotheses

-Impaired cerebrovascular reserve associated with steal physiology leads to structural changes of brain tissue that cannot be detected by conventional imaging modalities. (*Chapter 3 & Addendum chapters I and II*)

-Cerebral surgical revascularization restoring cerebrovascular reserve can reverse deleterious structural changes in the brain. (*Chapter 4*)

-Impaired cerebrovascular reserve is associated with seizure onset in patients with brain arteriovenous malformations. (*Chapter 5*)

-The standardized vasoactive PCO_2 stimulus, employed for BOLD-MRI sCVR examinations, is also compatible for non-spontaneously breathing subjects. (*Chapter 6 &7)*

Part 1

MRI studies in human subjects

Chapter 2

Sequential standardized fMRI assessment of cerebrovascular reserve in chronic intracranial steno-occlusive disease with two illustrative case studies

Abstract

Introduction

The rate and extent of development of ischemic symptoms from chronic intracranial vascular steno-occlusive conditions depend on the balance between the reduction in perfusion pressure distal to the stenos is and the compensatory reduction in downstream vascular resistance and recruitment of collateral blood vessels. This interplay can be assessed with quantitative measures of cerebrovascular reserve obtained with functional magnetic resonance imaging during standardized changes in partial pressure of arterial CO_2.

Methods

We used this standardized method to follow voxel-by-by voxel changes of the cerebrovascular reserve over time. Each scan was compared to previous scans in the same subject over time and to that of a cohort of young healthy subjects whose cerebrovascular reserve scans were co-registered to form a "normal atlas".

Conclusions

Here we describe such 'secondary analysis' methods derived from the standardized MRI method to measure cerebrovascular reserve. These methods are illustrated in two patients with chronic cerebrovascular steno-occlusive disease to demonstrate the fluctuating course of the balance between blood supply and demand over a two year period.

Introduction

Chronic intracranial arterial steno-occlusive diseases occur in both children and adults. Most are of unknown etiology, and some cases are associated with diseases such as Down's syndrome, sickle cell disease and moyamoya vasculopathy. (24) In a given patient, the development of ischemic symptoms depends on the balance between the reduction in perfusion pressure distal to the stenosis and the compensatory reduction in downstream vascular resistance, increase in oxygen extraction fraction, and recruitment of collateral blood flow. (12,13) Neither structural imaging nor angiographic imaging have been able to assess the adequacy of perfusion relative to demand. (12) Patients with intracranial steno-occlusive disease have been followed clinically, with structural imaging and angiography" (108) but no studies to date have documented the changing balance, over time, between progressive large vessel stenosis and regional hemodynamic compensation.

Assuming constant cerebral metabolic rate for oxygen ($CMRO_2$) in resting brain tissue, deoxyhemoglobin concentration would be inversely proportional to the cerebral blood flow (CBF). The blood oxygen level dependent (BOLD) T2* weighted MRI signal is attenuated in direct proportion to the changes deoxyhemoglobin concentration, making the magnitude of the BOLD signal change proportional to a change in CBF. (90,109) The response of the BOLD MR signal (in percent change) to a vasodilatory stimulus such as an increase in the arterial partial pressure of CO_2 ($PaCO_2$), termed cerebrovascular reactivity (CVR), can then be an indicator of the cerebrovascular perfusion reserve. Standardizing the change in $PaCO_2$ (57) enables a voxel-by-by voxel comparison of the BOLD signal change between subjects, between a subject and a cohort, (110) and in serial studies in the same subject over time. (89) In this communication we report on the results of secondary analyses that we applied to serial BOLD-MRI CVR tests performed with the same vasodilatory stimulus (standardized CVR; sCVR). We report on the use of these images to follow the changing balance of tissue perfusion in two patients with intracranial arterial steno-occlusive disease.

Methods

Ethics approval

After obtaining approval from the institutional research ethics board of the University Health Network, we searched our research database of patients with chronic cerebro-vascular disease (n= 325) for patients with intracranial steno-occlusive disease who underwent 4 or more sCVR examinations. Two cases were found that underwent 6 and 5 sCVR examinations over a time period of 2.5 and 2 years respectively. All patients and subjects enrolled in the studies from which the database was formed had given prior written informed consent for the study and use of data. This included the thirty healthy subjects whose data was used to generate normal values for the reference atlas.

sCVR generation

Gas control methods described by Slessarev et al. (57) applied by a computer-controlled gas blender (RespirAct™, Thornhill Research Inc., Toronto, Canada) were used to attain

and maintain repeatable iso-oxic changes in the end tidal (end expired) partial pressure of CO_2 ($P_{ET}CO_2$) from 40 mmHg (resting value) up to 50 mmHg (hypercapnia) in a near-square wave fashion. (111) $P_{ET}CO_2$ implemented with this method has been shown to be equal to $PaCO_2$, (58) the independent variable affecting brain blood flow. (76,86) Henceforth we refer to $PaCO_2$ as the stimulus affecting CBF and $P_{ET}CO_2$ as our measured variable.

Thirty healthy subjects (12 females) without known brain pathology and taking no medication were recruited as control subjects for the generation of the atlas. Subjects were asked to refrain from caffeine and heavy exercise on the day of the scan. Most increases in $P_{ET}CO_2$ and the main part of the reductions in $P_{ET}CO_2$ occurred within 1-3 breaths minimizing the time spent in transition. Other parameters in the generation of the atlas are listed in Table 1.

Table 1: *Subject demographics*

		# of subjects
Age Range	20-30	18
	30-40	5
	40-50	3
	50-60	3
	60-70	1
Sex	F	12
	M	18
Mean PCO_2 Changes during BOLD-MRI exam	9.21±0.71	

MR imaging consisting of BOLD acquisitions using an echo planar imaging (EPI) gradient echo sequence (TR 2000, TE 30 ms, 3.75 x 3.75 x 5 mm voxels). The acquired MRI and $P_{ET}CO_2$ data were analyzed using AFNI software. (95) $P_{ET}CO_2$ data was time shifted to the point of maximum correlation with the whole brain average BOLD signal. A linear least-squares fit of the BOLD signal data series to the $P_{ET}CO_2$ data series was then performed voxel-by-voxel. The slope of the relation between the BOLD signal and the $P_{ET}CO_2$ was color-coded to a spectrum of colors corresponding to the direction (positive or negative) and the magnitude of the correlation s 8b and 10b). BOLD images were then volume registered and slice-time corrected and co-registered to an axial 3-D T1-weighted Inversion-Recovery prepared Fast Spoiled Gradient-Echo (IR-FSPGR) volume (voxel size 0.86 x 0.86 x 1.0 mm) that was acquired in the same session. (96) This method has been described in greater detail in the background section of this thesis.

Secondary analysis:

Construction of normal atlas

Thirty healthy subjects (range 20-65 years) underwent a CVR imaging protocol with the same cerebrovasodilator stimulus described above resulting in a standardized CVR test (sCVR). Analytical processing software (SPM5; Wellcome Department of Imaging Neuroscience, University College, London, UK), was used to co-register each individual brain volume into MNI standard space using a 12-parameter affine transformation (112) followed by nonlinear deformations to warp the brain volume of interest into an MNI template of identical weighting contrast. The T1-weighted FSPGR volume was used to estimate the transformation normalization into standard space, as defined by a T1-weighted MNI152 standard template. (113) Finally, the mean sCVR ($\bar{r}$) and the standard deviation (σ_r) was calculated for each voxel (AFNI software).

Construction of 'z-maps'

The spatial sCVR information was further analyzed by comparing the direction and magnitude of the change in BOLD signal of each voxel to that of the corresponding voxel in the 'atlas'. This consisted of three steps. First, the patient's sCVR distribution was spatially normalized using the same MNI152 SPM template. Second, each voxel's sCVR value (r) was expressed in terms of the sd of the distribution of sCVR scores for the corresponding voxel in the atlas, $z = \frac{r - \bar{r}}{\sigma_r}$. Where ($\bar{r}$) is the mean sCVR and ($\sigma_r$) the standard deviation.

Finally, each z value was color coded to indicate its magnitude and direction of difference from the corresponding voxel atlas mean. Positive scores were colored with 15 shade gradations of green between the values of 0 to 3.0. Negative scores were colored purple with 15 shade gradations of purple between 0 and -3. The z-scores were superimposed on the corresponding normalized anatomical volume. Maps with thresholds for z-score < 0.5 provide highest sensitivity while those > 2.0 greatest specificity (Figures 8c and 10c).

Frequency distribution histograms

All images were normalized by mapping them into the same number of voxels. We were then able to construct frequency distribution histograms (FDH) (110) that were comparable to one another. We used FDH to compare the patterns of sCVR distributions between tests and to that of the normal cohort. FDH were made for whole brain, white matter (WM), gray matter (GM)) and segmented into regions of interest (ROI) according to vascular territory (SPM5; Wellcome Department on Imaging Neuroscience, University College, London, UK). ROI for each vascular territory (left and right anterior, middle, and posterior cerebral artery, ACA, MCA and PCA, respectively) were drawn manually. Since the pathology of the presented cases affect primarily the MCA territories, we will present only these territory specific FDH in our case studies.

Case presentations

Case A: Bilateral Moyamoya vasculopathy with surgical revascularization for progression of symptoms

A 37 year old woman presented with transient right hemibody weakness diagnosed as transient ischemic attacks (TIAs). The patient was otherwise asymptomatic, taking no medication and had no significant findings on physical examination. The patient's mother had previously had a subarachnoid bleed from a ruptured aneurysm.

MR angiography demonstrated severe bilateral narrowing of the supraclinoid internal carotid arteries (ICAs), with the proximal ACA and MCA segments relatively intact, and formation of 'Moyamoya-type' collateral vessels (Figure 8, top line). Given the lack of ischemic changes on structural MR imaging the patient was prescribed anti-platelet therapy. The patient returned six months later with an acute onset of bilateral TIAs and increasing, now bilateral, neurological deficits. MR angiography at this time showed progressive bilateral narrowing at the carotid termination. The patient underwent left direct superficial temporal artery to middle cerebral artery (STA-MCA) surgical bypass revascularization and a similar procedure on the right side 2 months later, after which her symptoms ceased. At follow-up examinations 3 months, 6 months, and 1 year after the second bypass, the patient remained asymptomatic. Sequential MR angiograms at these visits showed progressive bilateral narrowing at the carotid termination and at the proximal segments of ACA and MCA.

Description of sCVR examinations

The sCVR investigations (Figure 8, series 2) were performed at the same sessions as the structural MRA acquisitions. The left hemisphere and the deep white matter in the right hemisphere exhibited severely impaired cerebrovascular reserve (paradoxical reduction in sCVR, or vascular 'steal') on the 1st pre operative sCVR examination. Z-maps (Figure 8, series 3) revealed extensive areas of reduced sCVR in the left ACA and MCA territories and right ACA territory. Remaining areas in the right hemisphere had normal (colorless) or increased (green) sCVR. Noteworthy is that some of the extent of impairment of sCVR, particularly in the left MCA territory exceeded 2 sd. The distribution of sCVR in the left MCA (black bars, Figure 9a1) showed a marked shift to the left as compared the distribution of mean values in the normal population (dotted line). The right MCA territory (Figure 9b1) showed a distribution more towards that of the normal reference population (dotted line). This shift may represent reduced sCVR voxels in the deep white matter as indicated in the z-maps.

Progression to bilateral TIA-like symptoms were accompanied by an extension of severely impaired sCVR to the right ACA and MCA territory on the z-maps. The FDH (Figure 9b1, crosshatched bars) showed a shift to the left in the right MCA territory (corresponding to

the deep purple voxels in the z-maps) and a greater number of voxels in the left MCA territory became less reactive overall (Figure 9a1, crosshatched bars).

Figure 8: *Structural and functional axial images of cae A*

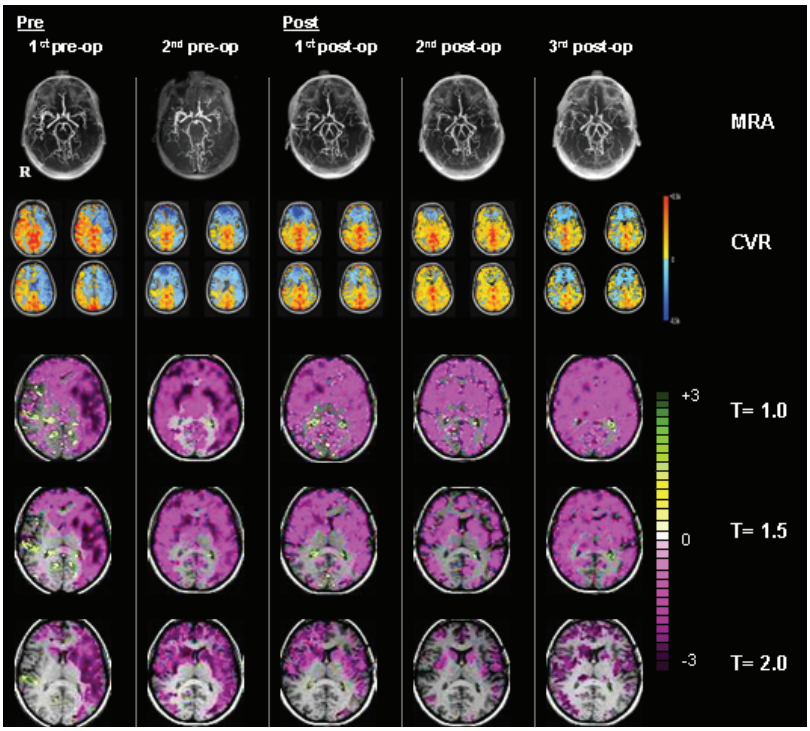

Caption figure 8: *Sequential structural and functional MR images with z-maps over 2 years in a patient with moyamoya vasculopathy (Patient A). The first set is the sequential MR angiographic studies demonstrating progressive bilateral vessel obliteration of the supraclinoid ICA and its proximal major branches, ACA and MCA. The second set shows, in two rows, the complimentary functional sCVR examinations. The third set shows the corresponding z-maps at z value thresholds of 1.0, 1.5, and 2.0. These thresholds illustrate progressively increasing specificity for the most compromised brain areas.*

Post-operative sCVR examinations and z-map profiles at 3 and 6 months after the second bypass (bilateral bypass revascularization) demonstrate progressive improvement in cerebrovascular reserve (Figure 8 and 10, lines b and c). The FDH demonstrate a right shift towards more positive CVR values for both MCA territories (Figures 9a2 and 9b2, the pre-operative crosshatched bars versus the 2nd post-operative white bars). On the first two postoperative examinations, both bypasses appeared patent on quantitative MR

angiography, and there is a progressive reduction in the number of voxels with poor sCVR. Surprisingly, the third post-operative sCVR examination at one year after the second bypass procedure shows worsening of the cerebrovascular reserve, despite the patient being neurologically asymptomatic. Z-maps show a marked (>2 sd) impairment in bilateral cortical sCVR, accompanied by a left shift towards more negative sCVR values in the FDH (Figures 9a3 and 9b3, the grey bars representing the final sCVR examination).

Figure 9: *Frequency distribution histograms of case A*

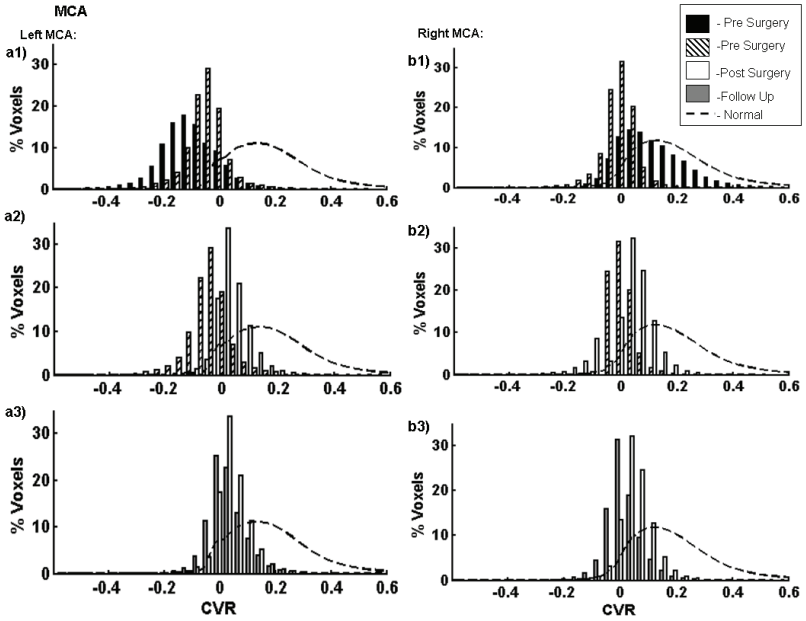

Figure 9: *Frequency distributions histograms of sequential sCVR examinations for the left and right MCA territory in patient A. The BOLD MRI CVR protocol covering the entire brain provides the same number of voxels per patient allowing comparability of data from examination to examination and to a normal cohort. FDHs show transient shift of sCVR to the right following surgery and then a progressive 'shift' of CVR to the left with a narrowing of the range of sCVR.*

Case B: Progressive middle cerebral artery occlusion with regression of symptoms over time without surgical revascularization

A 21 year old woman presented with a history of transient episodes of left motor and sensory deficits involving the left face and arm. For the previous three years she had received antithymocyte globulin and cyclosporine therapy for aplastic anemia. There was no history of smoking, use of alcohol, and non-prescription drugs. The rest of her history and physical examination were unremarkable. On investigation, the structural imaging was normal, but CT angiography showed a narrowed lumen in the right MCA (Figure 10, series 1). The patient's symptoms improved while in hospital. She was prescribed anti-platelet therapy and followed clinically without further treatment. The patient underwent periodic MR angiography and sCVR studies. Over the following two years MRA studies showed increasing stenosis of the right MCA with eventual total occlusion. The patient, however, remained asymptomatic.

Description of sCVR examinations

The first sCVR study shows paradoxical reduction in sCVR ('steal') in the right MCA territory (Figure 11, series 2). The z- maps show extensive areas of impaired sCVR in these territories that are more than 2 sd below that of the healthy cohort (Figure 11, series 3). The successive sCVR scans (each with a 6-month time intervals between successive scans) show progressive improvement up to examination 4 with the z- maps in studies 2-6 showing extensive areas of increased reactivity in the left hemisphere. We interpret this as indicating that a vasodilatory stimulus results in a paradoxical redistribution of blood flow to areas with retained vascular reactivity at the expense of the areas with reduced vascular responsiveness ('steal physiology'). After improvement of sCVR in the left MCA between studies 1 and 4, there was a trend towards worsening sCVR in the remaining studies. The FDH (Figure 11, a1, b1, and c1) indicate the marked improvement in sCVR between examinations 1, when the patient was symptomatic, and examination 4 (the time between scan 1 and 4 was two years). The graphs on the right of Figure 11 (a2, b2, and c2) indicate the worsening of sCVR in right MCA between examination 4 and 6 (1 year between scan 4 and 6). It also shows that the changes in sCVR occur in both the GM and WM. We attribute these differences in sCVR to the shifting balance between the primary progressive occlusion of the right MCA and the development of collateral blood flow.

Figure 10: *Structural and functional axial images of case B*

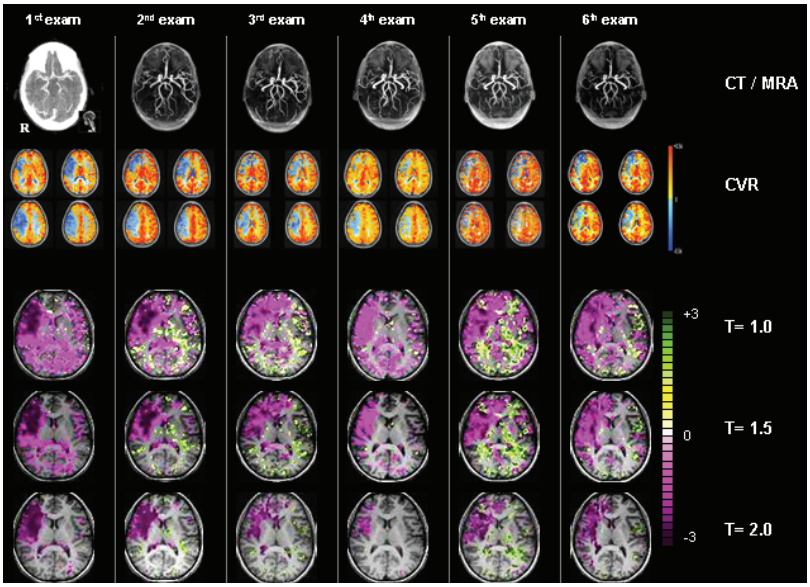

Caption figure 10: *Sequential structural and functional MR images with z-maps over 2.5 years in a patient with aplastic anemia and right-sided idiopathic MCA occlusion (Patient B). The first set is the sequential MR angiograms demonstrating progressive obliteration of the supraclinoid MCA. The second set shows, in two rows, the complimentary functional sCVR examinations. The third set shows the corresponding z-maps at z-value thresholds of 1.0, 1.5, and 2.0, increasingly illustrating the most compromised brain areas.*

Discussion

We derived secondary analysis methods of a standardized MR-based assessment of cerebrovascular reserve, sCVR, to measure fluctuations in brain tissue perfusion over time that can be present without a clinical indicator (i.e. ischemic symptoms). Comparison of the sCVR to that of the normal reference atlas enabled the quantitation of the deviation of the subject's cerebrovascular reserve of the corresponding voxel from that of the reference cohort, in absolute values. Practically, as demonstrated with the two cases, this method was used to follow the changes in brain perfusion over the course of progressive stenosis of large intracranial vessels. When the patients were symptomatic, the sCVR examination showed marked reduction in cerebrovascular reserve. Nevertheless, the total blood flow in both patients apparently remained above the threshold required to sustain neuronal function and cellular integrity preventing an acute stroke as gauged by the absence of ischemia and absence symptoms during follow-up examination.

Figure 11: *Frequency distribution histograms of case B*

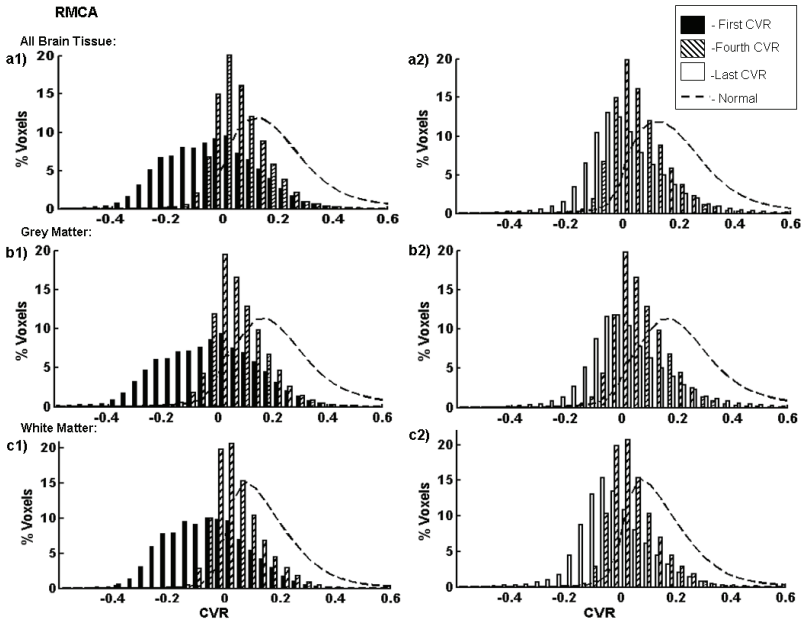

Caption figure 11: *Frequency distribution histograms of sequential sCVR examinations for right MCA territory for all brain tissue and for gray and white matter separately. The dotted line represents the frequency distribution of sCVR for the normal atlas. Each pattern of bars represents a single sCVR examination.*

Bypass revascularization surgery transiently improved cerebrovascular reserve (but not to normal values) in case A (Figure 8 & 9). Thereafter, the degree and extent of cerebrovascular reserve progressively deteriorated on the final follow-up scan, while the patient remained asymptomatic. This may be the consequence of the progressive nature of the bilateral moyamoya vasculopathy where blood flow provided by the bypass and extent of collateralization may fall short over time due to the progressive vessel obliteration. The fact that the patient remained asymptomatic at this point may be explained as follows: 1) The decrease in cerebrovascular reserve, although deteriorating, was not severe enough at that time point to cause ischemic symptoms (there are no 'dark purple' areas on the 3rd postoperative z-map series in Figure 9 which would indicate severe hemodyamic compromise). 2) The patient may have developed so-called 'ischemic tolerance' where the chronically hypoperfused neurons are operating on the lower end of blood flow requirements. There is a possibility that, future follow-up examinations will demonstrate further deterioration of cerebrovascular reserve with recurrence of ischemic symptoms. The sCVR examinations may therefore detect subclinical deterioration of brain tissue perfusion.

These are speculations that are not currently supported by our data but could be explored in ongoing similar investigations.
The course of disease as revealed by sCVR scans in patient B was that of progressive improvement of the cerebrovascular reserve up until the fourth examination followed by progressive deterioration in studies 5 and 6. During asymptomatic periods, the balance of vascular reserve as indicated by the functional imaging was not ascertainable from structural imaging and clinical examination alone. Over two years while the patient was followed, there was progressive occlusion of the right MCA on structural imaging, while the patient remained totally asymptomatic. The functional data from the sCVR exam (CVR map and z-map series in Figure 9 & Figure 11) revealed a more fluctuating balance between progression of vascular stenosis and the rate of recruitment of collateral blood flow. During examination 5 and 6 this balance seemed to have shifted towards deterioration of cerebrovascular reserve again but as in case A, not to a degree that resulted in ischemic symptoms. The development of 'darker purple' areas (i.e. severe hemodynamic failure) in the right hemisphere on scan 6 (z-map series Figure 11), suggests that without the timely recruitment of additional collateral blood flow the patient may become symptomatic again in this territory.

Functional neurovascular imaging may be performed with modalities such as ^{15}O-Positron Emission Tomography (^{15}O –PET), Single-Photon Emission Computed Tomography (SPECT), or perfusion CT/MRI measuring changes to acetazolamide challenge. These tests have been used to provide information about the cerebral hemodynamics that may address indications for surgical revascularization and predict prognosis. (114) However, they are invasive and carry a degree of complexity that precludes their use in routine clinical assessment. Also, the use of acetazolamide as a safe stimulus for hemodynamic studies has recently been challenged. (115) In contrast, BOLD CVR MRI is non-invasive and the BOLD sequence is available for every MR system. Standardization of the vasodilatory provocation allows for comparability of MR signal values from follow-up examinations whereas the high spatial resolution of the MR data indicates more accurately the extent of the brain tissue at risk.

Standardization of the BOLD CVR signal
Blood flow signal. The dependent variable, BOLD signal, was normalized for signal strength by calculating percent change from baseline. This facilitated the comparability of signal intensity without regression analysis. (110) The effects of signal drift were minimized by incorporating the two separate hypercapnic and normocapnic exposures over 8 minutes. The normocapnic exposures were used for linear detrending of the signal over the scan time. These measures provide good test-retest reliability. (89) The standardization of the provocative stimulus and the signal response allowed the comparison of results between examinations performed over the span of 2.5 years. Although the concept of a voxel-by-voxel comparison of the intensity of an image to that of a normal cohort has been extensively explored (116-118) the novel aspects of our approach are (a) that this is the first

application to brain vascular reactivity using a standardized PCO_2 stimulus in combination with BOLD MRI signal, (b) the entire range of z-values is mapped giving maximum sensitivity, while using several thresholds improving spatial resolution of the magnitude of the deficit, (c) and standardizing the number of voxels in each scan enabling direct comparison of FDH in a subject over time, as well as in a subject to a designated cohort.

Control of $PaCO_2$

Comparison of studies over time and between patients, as well as the compilation of ensemble data for the reference atlas, was enabled by employing a standardized vasodilatory stimulus in conjunction with a surrogate measure of regional cerebral blood flow. (90) Other known means of implementing a vasodilatory stimulus such as infusing CO_2 into a face mask, (119) inhaling a fixed concentration of CO_2, (120) or simply breath holding (121) are not reproducible, and cannot even provide a reliable measure of the change in the $PaCO_2$ (85,87,122,123) which is the independent variable affecting cerebral blood flow. (76) In addition, these methods result in variations in the arterial partial pressure of O_2, (122,123) which also affects the BOLD signal. (87) As a consequence, the changes in BOLD signal cannot be related to a stimulus (i.e., normalized) and therefore cannot be compared. In this study we used a computer-controlled gas blender to prospectively target $P_{ET}CO_2$, which has equilibrated with the $PaCO_2$. (58) This allowed us to repeatedly administer a standardized stimulus consisting of a change in $PaCO_2$ from 40 to 50 mmHg. In our subjects, the baseline $P_{ET}CO_2$ was 40.2 ± 1.1 (sd) mmHg and the hypercapnic stimulus was 49.9 ± 1.5 mmHg.

In summary, standardization of measures of cerebrovascular reserve, in this instance with BOLD MRI, allow for analysis methods where fluctuations in brain tissue perfusion can be followed over time and compared to a normal reference cohort. In two illustrative cases with steno-occlusive disease these sequential sCVR examinations showed a fluctuating degree and distribution of vasodilatory reserve in the face of progressive large vessel occlusion. sCVR examinations may provide information about the dynamic balance between progressive intracranial vessel occlusion and the rate of recruitment of collateral blood flow. Changes in sCVR may provide an assessment of the balance of vascular reserve than is not ascertainable by clinical examination, with or without angiography.

Chapter 3

Steal physiology is spatially associated with cerebral cortical thinning

Data presented in chapter 2 demonstrated that changes in brain tissue perfusion may occur even in the absence of clinical symptoms and signs of ischemia. Such chronic subclinical changes in perfusion, however, may have a deleterious effect on brain tissue structure. From the literature it is known that brain areas demonstrating severely impaired cerebrovascular reserve with steal physiology are at high risk for developing a future acute ischemic event. (66,97,98) Although, steal physiology may occur episodically and exist over a long period of time without ictal signs of ischemia it may still lead to brain tissue injury. The question of whether chronic episodic oligemia can produce pathological effects short of frank infarction in humans has been a longstanding question and difficult to document. Various animal models (99,100) have mimicked sublethal hypoperfusion, mostly by creating a permanent shunt to reduce CBF by 50%, to study the consequences on neuronal activity, and neurocognitive performance. These studies revealed that neuronal signaling decreased, and that the animals' neurocognitive performance was declined.

As a first step in the investigation of these possible scenarios in humans with severely impaired cerebrovascular reserve (chronic intermittent hypoperfusion) we investigated the integrity of the cortex in patients with severe chronic cerebrovascular steno-occlusive disease exhibiting 'steal' physiology.

Abstract

Introduction

The physiological impact of severely impaired cerebral auto-regulatory vascular reactivity on cortical integrity is unknown. The purpose of this study is to determine the relationship between severe impairment of auto-regulatory flow control associated with steal phenomenon and its impact on cortical thickness.

Methods

Two hundred and fifty BOLD-MRI cerebrovascular reactivity (CVR) studies were reviewed in order to identify subjects with severe unilateral exhausted cerebrovascular reserve demonstrating steal physiology, but with normal appearing cortex on FLAIR imaging. Seventeen patients meeting the inclusion criteria were identified. A reconstructed inflated cortical surface map was created for every subject using Freesurfer software. The region of interest (ROI) reflecting the steal physiology was determined by overlaying the subject's CVR map on to the cortical surface map. This ROI was compared to the corresponding area in the healthy hemisphere which provided control cortical thickness measurement in each subject.

Results

The hemisphere with steal physiology showed an 8% thinner cortex (2.23 mm +/- 0.28) than the corresponding healthy hemisphere (2.42 mm +/- 0.23) ($p = 0.0005$).

Conclusions

Our findings indicate that a spatial correspondence exists between impairment of auto-regulatory capacity with steal physiology and cortical thinning.

Introduction

Investigation of cerebral blood flow has revealed three important adaptations of the flow control mechanism. The first is a pressure responsive mechanism that maintains constant blood flow in the microcirculation through a wide range of perfusion pressures. (7) The second is a response to metabolic vasoactive molecules such as CO_2, O_2, and endothelin. The third is a vasoactive response to local neuronal activity. (10,11) The final common pathway in these adaptive perfusion mechanisms is smooth muscle tone in the arterial system, predominantly at the level of pre-capillary arterioles. (2)

Patients with severe large artery stenosis or occlusion, associated with exhausted auto-regulation and steal phenomenon, are at higher risk of ischemic injury than in those with intact auto-regulation. (66,97,98) This may be because lowering of blood pressure reduces the perfusion distal to the stenosis. As well, in the case of vascular steal, increases in arterial PCO_2 dilate normal vessels, resulting in a redistribution of blood flow away from the vascular impaired brain areas. Blood pressure variation and hypercarbia are common events in day to day living particularly during sleep. These "normal" decreases in blood pressure can be a potential risk in patients with vascular stenoses risking hypoperfusion in areas supplied by the stenotic vessel. We considered that repetitive transient non-lethal ischemic events may, over time, lead to neuronal damage and loss. (124-126)

The purpose of this study is to determine the relationship between severe impairment of auto-regulatory flow control sufficiently severe to cause steal phenomenon, and cortical thickness, an indicator of neuronal density. We identified 17 subjects with steno-occlusive cerebrovascular disease (but normal appearing cortex on conventional MRI) and unilateral paradoxical cerebrovascular reactivity (CVR) to hypercarbia (steal phenomenon). We then compared the cortical thickness in the impaired area to the corresponding region in the opposite hemisphere in which auto regulation was preserved.

Methods

Subjects

After approval from our institutional ethics review board, 250 consecutive BOLD-MRI CVR studies, conducted between March 2003 and October 2008, were reviewed to identify subjects with areas of unilateral paradoxical CVR, but with normal appearing cortex on FLAIR imaging (Figure 12b). 'Steal physiology' is defined as a reduction in BOLD-signal during hypercarbia. The reduction of BOLD signal has previously been shown to represent blood flow reduction. (90) Subjects with lacunar infarcts in the white matter were excluded (loss of axons). Subjects with small foci of T2 hyperintensity in the white matter were included in the study. Although these hyperintense foci represent ischemic demyelination, the axons are still preserved, as is cortical integrity. Seventeen patients with a mean age of 42.3 years (range 12-75, 9 females) meeting the inclusion criteria were identified (table 2).

Table 2: *Clinical characteristics of subjects*

Subject	Age	Sex	Etiology	Duration*
1	30	F	Bilateral Moyamoya disease	26
2	42	F	Unilateral Moyamoya syndrome	8
3	14	F	Unilateral Moyamoya disease	1
4	22	M	Sickle cell anemia; unilateral MCA disease	120
5	37	F	Unilateral MCA occlusion	1
6	71	M	Unilateral Moyamoya disease	1
7	50	F	Unilateral carotid artery occlusion	36
8	39	M	Unilateral Moyamoya disease	296
9	12	F	Unilateral Moyamoya disease	1
10	26	M	Neurofibromatosis type 1; Unilateral Moyamoya syndrome	18
11	48	M	Unilateral MCA occlusion	22
12	54	M	Unilateral carotid artery occlusion	4
13	38	F	Bilateral Moyamoya disease	48
14	75	M	Unilateral carotid artery stenosis	4
15	71	M	Unilateral Moyamoya disease	2
16	53	F	Unilateral Moyamoya syndrome	1
17	38	F	Unilateral Moyamoya disease	80
Mean (SD)	42 (18.8)			40 (74)

**Interval patient recall of onset of symptoms to CVR study (in months) SD= standard deviation*

MRI data acquisition

An axial 3D T1 weighted (anatomical acquisition FSPGR) volume (voxel size 0.78 x 0.78 x 2.2 mm) was acquired for spatial co-registration of the blood oxygen level dependent (BOLD) signal variation associated with CO2 induced changes in blood flow using BOLD–EPI (echoplanar) acquisitions (EPI gradient echo with TR 2000, TE 25, 3.75 x 3.75 x 5 mm voxels on a 3.0-Tesla HDX MRI system in 15 cases, and EPI gradient echo with TR 2000, TE 40, 3.75 x 3.75 x 5 mm voxels on a 1.5-Tesla HD MRI system in 2 cases (GE Healthcare, Milwaukee, Wis). During the BOLD signal acquisitions CVR studies were performed using a change in end-tidal partial pressure of CO_2 ($P_{ET}CO_2$) as the vasoactive stimulus. Subjects were fitted with an airtight sequential gas delivery mask (127) (Hi-Ox-80; Viasys Healthcare, Yorba Linda, Calif, USA). A custom-built computer-controlled gas blender (RespirAct; Thornhill Research Institute, Toronto, Canada) was programmed using the algorithms from Slessarev et al. (57) to deliver set concentrations of O_2, N_2, and CO_2 to

the mask in order to attain and clamp targeted levels of $P_{ET}CO_2$. The subjects underwent two prospective iso-oxic (87) pseudo-square wave increases in end-tidal partial pressure of CO_2 ($P_{ET}CO_2$) of 10 mmHg from a baseline of 40 mmHg. (84)

Figure 12: *Functional and structural MR images of illustrative subject*

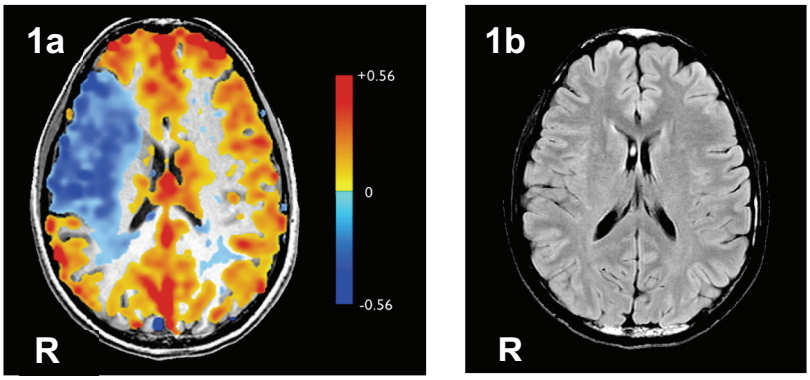

Caption figure 12: *Axial image of BOLD-MRI CVR map and FLAIR image of subject 10. (A) The axial BOLD CVR map of subject 10. The negative change in BOLD signal during hypercarbia, related to steal physiology, is delineated in blue. (B) The axial FLAIR image of the same subject is normal in appearance, and has no signs of infarction or volume loss.*

MRI data analysis

The acquired anatomical acquisition FSPGR volume was analyzed for cortical thickness using Freesurfer software (http://surfer.nmr.mgh.harvard.edu/), a method for automated surface reconstruction and accurate cortical thickness measurement. (128) Briefly, software reconstruction of the brain creates an inflated 3-D brain surface image (129,130) which facilitates interpretation of functional MRI data across the entire cortical surface without the interference from cortical folding. (131)

The MRI and $P_{ET}CO_2$ data were imported into, and analyzed with, AFNI software. (95) The BOLD-MR signal was regressed against the $P_{ET}CO_2$ on a voxel-by-voxel basis. The slope of the regression of the percentage change in MR signal intensity vs. mmHg change in $P_{ET}CO_2$ is referred to as CVR. The CVR was color-coded on a spectrum from grey to red for positive correlations and from grey to blue for negative correlations, and overlaid voxel-by-voxel on the anatomical scan to generate a CVR map (Figure 13a). The CVR map was then overlaid on the inflated cortical surface map to determine a region of interest (ROI) encompassing the region of negative BOLD response (area showing steal physiology) within the affected hemisphere. The corresponding region on the hemisphere

showing normal CVR was then identified (Figure 13). Mean cortical thickness between the left and right hemisphere ROI's for each subject was calculated by Freesurfer software. Cortical thickness was then compared by a paired t-test.

Figure 13: *Functional and cortical thickness overlay on inflated brain surface area*

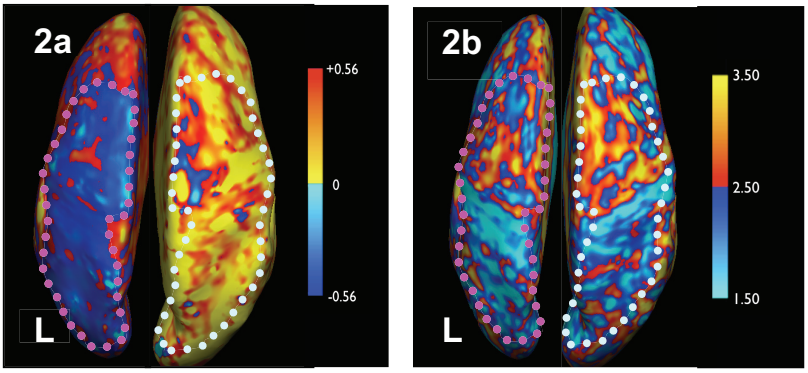

Caption figure 13: *The relationship between the spatial extent of impaired CVR and the spatial extent of cortical thinning in subject 10. Figure A shows an axial view of the same BOLD CVR map as seen in figure 12a, overlaid on the inflated cortical surface map in 3-D. Unilateral steal physiology is delineated in blue. The ROI was drawn around the blue area (pink dotted line, left hemisphere). Light blue dotted line outlines ROI in the corresponding area of hemisphere with normal CVR. Figure B shows the cortical thickness map overlaid on the inflated cortical surface map in 3-D, with the same ROI projected on top of it. Light blue designates the thinnest cortex and red the thickest. The scale is in mm.*

Results

Nine of the 17 subjects showed steal physiology in the left hemisphere. Mean cortical thickness was 2.23 mm ± 0.28 (SD) mm in the ROI encompassing paradoxical CVR (figure 13a), and 2.42 mm ± 0.23 mm in the corresponding contra lateral side ($p = 0.0005$) (table 3), a difference of 8%. One subject, with steal physiology in the left hemisphere had thinner cortex in the hemisphere showing normal CVR.

Discussion

To our knowledge this is the first study relating reduced vascular reactivity with thinning of cerebral cortex, an indication of neuronal loss.

The limit of smooth muscle relaxation response to a decrease in blood pressure is the point of exhausted autoregulation. This can occur in a specific vascular territory in a normotensive subject when a severe vascular stenosis or occlusion results in a drop in

downstream perfusion pressure. In this scenario steal physiology occurs primarily because the drop in flow resistance in the normally supplied tissue exceeds any additional drop in flow resistance in the tissue supplied by narrowed vessels. If these territories are connected by collateral vessels (through the circle of Willis or pial collateral vessels), then steal physiology becomes manifest. (90)

The normal appearing cortex on FLAIR imaging shows that there is still enough perfusion to maintain cellular neuronal function. However, repeated periods of hypo-perfusion may not be sufficient for immediate cell death, but over time may lead to apoptosis or involution of cells, resulting in neuronal fallout. This concept of "selective neuronal loss" is similar to that proposed by others. (124-126) The exact nature of this tissue loss requires further investigation.

Table 3: *Cortical thickness measurements*

Subject		Mean Cortical thickness*		
	voxels (1.34 mm3) in ROI	Hemisphere with normal CVR	Hemisphere with paradoxical CVR	Thickness difference
1	4818	2.622	2.488	0.134
2	4171	2.477	2.26	0.217
3	10582	2.785	2.762	0.023
4	14646	2.366	1.73	0.636
5	19469	2.31	2.28	0.03
6	27396	2.433	2.061	0.372
7	2557	2.494	2.082	0.412
8	29298	2.524	2.123	0.401
9	42705	2.461	2.369	0.092
10	42413	2.356	2.207	0.149
11	10823	2.558	2.615	-0.057
12	6994	2.743	2.408	0.326
13	56052	2.419	2.231	0.188
14	8909	2.17	2.057	0.113
15	13604	2.009	1.906	0.103
16	30396	2.534	2.525	0.009
17	10060	1.925	1.839	0.086
Mean	19699	2.42	2.23	0.19
SD	15309	0.23	0.28	0.18

** Thickness in mm ROI= region of interest CVR= cerebrovascular reactivity; SD= standard deviation*

We carefully selected this cohort of subjects that represent the most severe end of the hypoperfusion spectrum, to examine our hypothesis. Because cortical thinning is a gross measure of neuronal number, (132) changes in cortical thickness would only be seen with severe neuronal loss. As cortical thickness may vary from person to person, we used the thickness of the cortex in the patient's own unaffected cortex for control values. The retrospective design of this study was necessary, as unilateral steal physiology cannot be prospectively identified without a CVR study. The retrospective review method provided a large pool of patients (250) that provided a sufficiently large cohort with the specific inclusion criteria (n= 17) we required to test our hypothesis.

It is possible that at least part of the thinning of the cortex was due to reduced blood volume and not due to a loss of cells. This however is unlikely since cerebral blood volume should be at a normal level or even elevated (due to compensatory vasodilation) in areas of reduced perfusion pressure with no signs of ischemia. (13) Another confounding mechanism may be the presence of cortical dehydration with loss in cell volume. This is unlikely as a limitation in blood flow is generally associated with decreased cellular energy resources leading to cell swelling. This therefore leaves loss of neuroglial tissue as the most likely explanation for the regional cortical thinning that we observed.

Interestingly, 9 of our cases had left sided steal physiology with 8 showing thinner left hemispheric cortex compared to the right hemisphere. This hemispheric difference is therefore more significant in that it occurred in the typically thicker left hemisphere. (133,134) We note that handedness has no significant effect on cortical (hemispheric) asymmetry. (135) However, one subject measured a slightly thicker cortex in the hemisphere with the paradoxical CVR, the left hemisphere in this case. Luders et al. (133) reported that the left hemisphere is thicker (left vs right; 2.42 (0.14) versus 2.36 (0.13)); given these robust standard deviations, the cortex on the left side could still have undergone thinning without the overall thickness being reduced below the normally thinner right hemisphere.

The interval from onset of symptoms to time of CVR study was 39.4 (SD+/-73.9; median 8) months. We attempted to draw a correlation with first report of symptoms and degree of cortical thinning in order to determine the annual rate of cortical thinning in the area of brain with steal phenomenon. The calculated rate was 0.023 mm per annum. However, the reliability of patient recall in determining symptom onset is questionable and the outcome was mainly supported by two pints (subject 8 and 10; table 2). Further data will be required for confirmation of this correlation. Furthermore, the association with symptom onset may not be coincident with the development of steal physiology. These issues preclude accurate determination of the magnitude of cortical thinning per unit time in the small sample of patients studied. Serial CVR studies may allow for more accurate quantification of this result and provide insight as to whether medical intervention can have an impact on the

cortical integrity. Future research should also explore the relationship between cortical thinning due to steal physiology and neurocognitive functioning.

Our findings indicate that a spatial correspondence exists between impairment of auto-regulatory capacity with steal physiology and cortical thinning.

Chapter 4

Surgical revascularization reverses cerebral cortical thinning in patients with severe cerebrovascular steno-occlusive disease

In addition to the cortical thinning, a subsequent paper by our group also demonstrated white matter injury in normal-appearing brain tissue exhibiting severely impaired cerebrovascular reserve with steal physiology. (136,137; see also Addendum chapters I & II). These manuscripts are included as addendum chapters in this thesis. Briefly, MRI investigation of the white matter revealed elevated apparent diffusion coefficient (ADC) in white matter areas that exhibited severely impaired cerebrovascular reserve associated with steal physiology. A higher ADC value indicates more free-moving water in white matter tissue, which would imply that fewer cells are present (a lesser cell density) as compared to brain areas with preserved cerebrovascular reserve.

Both findings that of cortical thinning and elevated ADC in white matter demonstrate that normal appearing brain tissue on structural MR imaging affected by steal physiology, as spatially identified by BOLD-MRI sCVR imaging, exhibits tissue injury. In this chapter I investigate whether this process of tissue injury would be reversible after successful restoration of cerebral blood flow, i.e. normalizing the cerebrovascular reserve, to the affected cortex.

Abstract

Introduction

Chronic deficiencies in regional blood flow lead to cerebral cortical thinning without evidence of gross tissue loss, while potentially negatively impacting on neurological and cognitive performance. This is most pronounced in patients with severe occlusive cerebrovascular disease in whom affected brain areas exhibit "steal physiology", a paradoxical reduction of cerebral blood flow in response to a global vasodilatory stimulus intended to increase blood flow. We tested whether surgical brain revascularization that eliminates steal physiology can reverse cortical thinning.

Methods

We identified 29 patients from our database who had undergone brain revascularization with pre- and post-operative studies of cerebrovascular reactivity (CVR) using BOLD MRI and whose pre-operative study exhibited steal physiology without MRI-evident structural abnormalities. Cortical thickness in regions corresponding to steal physiology, and where applicable corresponding areas in the normal hemisphere, were measured using Freesurfer software.

Results

At an average of 11 months after surgery, cortical thickness increased in every successfully revascularized hemisphere (n=30). Mean cortical thickness in the revascularized regions increased by 5.1% (from 2.40 mm ±0.03 to 2.53 mm ±0.03; $p<0.0001$).

Conclusions

Successful regional revascularization and reversal of steal physiology is followed by restoration of cortical thickness.

Introduction

Chronic deficiencies in regional cerebral blood flow lead to thinning of the cerebral cortex (138) even without evidence of gross tissue loss on conventional MR imaging. In such instances, perfusion of brain tissue may be just sufficient to prevent gross ischemia but fails to respond adequately to increases in demand such as those normally occurring during neuronal activation. The integrity of this flow response system can be assessed by measures of cerebrovascular reactivity (CVR), a measure of the change in cerebral blood flow in response to a vasodilatory stimulus. Reductions in CVR can range from a blunted increase in blood flow in response to a stimulus in mild cases, to "paradoxical" reduction in regional blood flow indicating steal physiology, in severe cases.

Patients, in whom neuronal activity is no longer met with a commensurate augmentation of cerebral blood flow, are believed to be at a higher risk of an acute ischemic stroke,[2] even in the absence of acute ischemia. Experimental animal models simulating a state of non-ischemic chronic hypoperfusion demonstrate a decline in neuronal structure and viability. (99,100) In humans, vascular cognitive impairment (VCI) is associated with the loss of cortical grey matter, (102-104) while steno-occlusive disease without stroke has been associated with neurocognitive decline. (105-107) On the other hand, neurodegenerative disorders such as Alzheimer's disease (139) and Huntington's disease (101,140) are associated with reduced vascular function. These studies indicate that there may well be a pathophysiological association between vascular impairment, structural changes in the brain and neurocognitive dysfunction.

Our aim was to study the association between vascular dysfunction in the form of steal phenomenon and cerebral cortical thinning. (138) We hypothesized that the reduction of vascular reserve was etiologically connected to the cortical thinning. We therefore investigated whether restoring CVR by surgical revascularization could arrest or reverse cortical thinning.

Methods

Subjects

The study was approved by the research ethics board of the University Health Network (REB, UHN). Subjects were identified from a prospectively maintained database of patients who underwent cerebrovascular reactivity (CVR) BOLD MR imaging as part of a series of REB-approved studies at the Toronto Western Hospital (n= 262). All subjects provided signed informed consent for the CVR study. Selection criteria for this study were (a) Patients who had undergone a surgical revascularization procedure (extracranial-intracranial (EC-IC) bypass or carotid endarterectomy) performed for reducing stoke risk in the affected hemisphere; (b) the presence of 'steal physiology' on the pre-revascularization CVR map, (c) with normal appearing brain tissue on structural MR imaging pre and post operatively (small hyperintense T2 foci in the white matter were considered acceptable);

(d) availability of post operative CVR-MRI maps. The selection process is described in Figure 14.

Figure 14: *Flow chart with selection criteria*

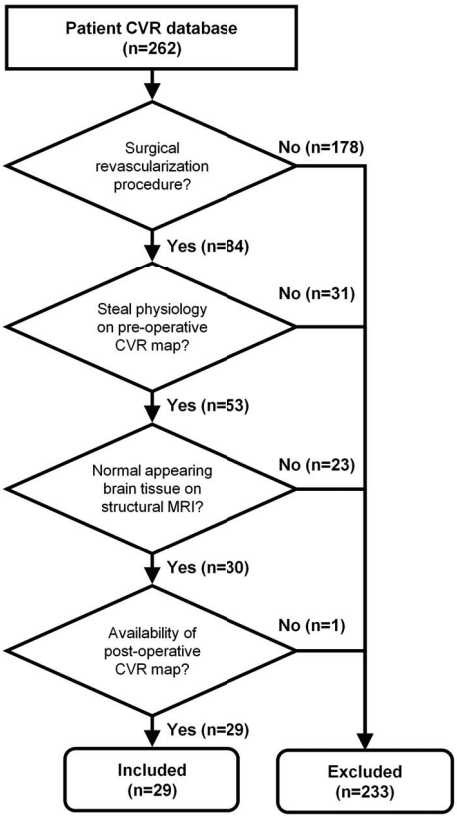

Imaging protocol and analysis

A customized gas blender with a sequential rebreathing mask (RespirAct™, Thornhill Research Inc., Toronto, Canada) was used to apply a precise, repeatable series of vasodilatory stimuli consisting of iso-oxic pseudo-square wave changes in end-tidal CO_2 ($P_{ET}CO_2$) from 40 mmHg up to 50 mmHg. (57) The precise repeatability of the target $P_{ET}CO_2$ sequence and consistent MR sequence enabled the direct comparisons of the CVR in a subject over time, and the comparison of CVR between subjects. (89) CVR maps were obtained with MR imaging consisting of BOLD acquisitions with echo planar imaging (EPI) gradient echo (TR 2000, TE 30 ms, 3.75 x 3.75 x 5 mm voxels). The acquired MRI and $P_{ET}CO_2$ data were analyzed using AFNI software. (95) BOLD images were volume

registered and slice-time corrected and co-registered to an axial 3-D T1-weighted Inversion-Recovery prepared Fast Spoiled Gradient-Echo (IR-FSPGR) volume (voxel size 0.86 x 0.86 x 1.0 mm) that was acquired at the same time. (96) The acquired $P_{ET}CO_2$ data was time shifted to the point of maximum correlation with the whole brain average BOLD signal. Next, a linear least-squares fit of the BOLD signal data series to the $P_{ET}CO_2$ data series was performed voxel-by-voxel. CVR is calculated as the percent change in BOLD signal per mmHg change in $P_{ET}CO_2$. The correlation was color-coded and superimposed on the corresponding voxel of the anatomical volume to generate a color-coded CVR map.

Cortical thickness analysis

Cortical thickness measurements were derived from the acquired anatomical volume data using Freesurfer software (http://surfer.nmr.mgh.harvard.edu/), a method for automated surface reconstruction and accurate cortical thickness measurement. (128) In brief, the software reconstruction of the brain creates an inflated 3-D brain surface image, (129,130) which facilitates interpretation of functional MRI data across the entire cortical surface after accounting for cortical folding. (131) The generated cortical thickness maps are not restricted to the voxel resolution of the original data therefore allowing detection of sub millimeter differences between examinations.

The region of interest (ROI) comprised of cortical regions exhibiting 'steal physiology' was indicated by the CVR map overlaid on the inflated pre-operative cortical surface (a paradoxically negative BOLD response to hypercapnia depicted in blue on CVR maps in Figures 15a and 15c). All cortical thickness measurements were confined to these ROIs, and the results were automatically generated by the software. To enable comparisons of pre-and post-operative cortical thickness, the ROI was automatically copied onto the post-revascularization cortical surface (Figures 15b and 15d). In cases where steal physiology was not bilateral, additional cortical thickness comparisons were performed with the non-revascularized contralateral hemisphere (n=20 hemispheres) by reflecting the ROI encompassing the brain area with 'steal physiology' onto the healthy contralateral hemisphere on both the pre and post revascularization CVR map (Figure 15b).

Results

Patient demographics

Of the 29 patients (15 female) included in this study, 21 had moyamoya disease and 8 had other carotid or large intracranial vessel occlusive disease (Table 6). Mean age was 41 years (range 13-66 years). Four of the 29 subjects exhibited continuing 'steal physiology' on the post-operative CVR study, indicating that the surgical revascularization was unsuccessful. These 4 patients (two of which had bilateral procedures, and therefore provided 6 hemispheres) were therefore counted as 'sham operated' controls. Of the 25 patients that showed normalization of CVR (i.e. successful revascularization), 5 patients had bilaterally affected hemispheres, and underwent bilateral surgeries, for a total of 30 hemispheres with successful revascularization.

Cortical thickness was measured in each ROI (Table 4 and Table 5). An independent sample *t*-test was used to evaluate significant differences in cortical thickness before and after surgical revascularization. Fisher's exact test was used to determine whether the thickness changes were directly related to the successful revascularization or over time. A p-value <0.05 was considered significant.

Figure 15: *Pre and post revascularization CVR maps overlaid on inflated cortical thickness surface and regions of interest*

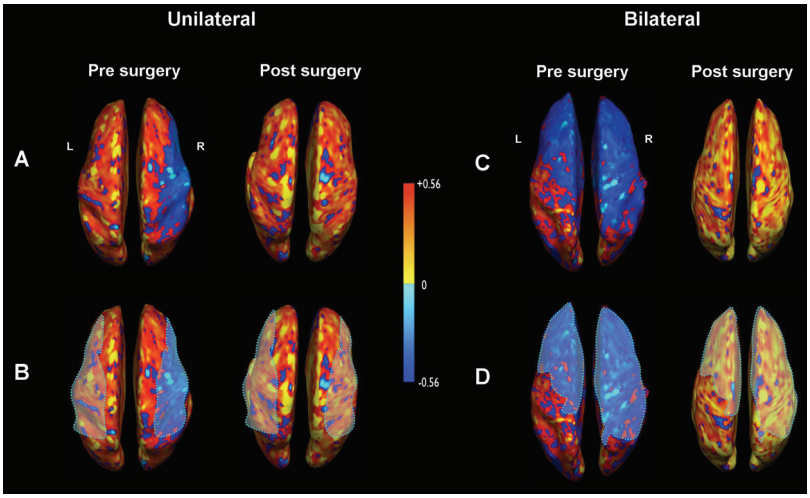

Caption: *Figure 15 demonstrates the spatial CVR maps overlaid on the inflated cortical surface for the hemispheres that were successfully revascularized. Figure A and C are examples of a patient with unilateral and bilateral steal physiology (blue brain area) on the pre revascularization CVR map. The post revascularization maps show absence of steal physiology in the same area. Figure B and D show the same CVR maps, this time with a ROI drawn around the brain area with steal physiology (blue brain area). This ROI was reflected on the post revascularization CVR map for cortical thickness comparison. Figure B also demonstrates the same ROI reflected on the contralateral unaffected hemisphere for pre and post revascularization cortical thickness comparison (left hemisphere in this case).*

Intervention and follow-up time

Surgical revascularization was in the form of an EC-IC bypass for 34 hemispheres, and carotid endarterectomy in 2 hemispheres (Table 6). Surgery was successful in eliminating all evidence of 'steal physiology' in 30 hemispheres (Figures 15a and 15c). Mean duration between surgery and post-operative CVR study was 11 months (median 8 months). There

was no correlation between follow-up time and cortical thickness changes (r^2= 0.0004). The mean time between pre- and post-operative CVR studies was 16 months (Table 4).

Revascularization increases cortical thickness in brain areas exhibiting steal physiology
Analyses of cortical thickness were conducted using methods that corrected for interference from cortical folding (Methods). The region of interest (ROI) comprised cortical regions exhibiting 'steal physiology' as indicated by the pre-operative CVR map (Figures 15a and 15c). All post-operative measurements were made in the same ROI as the pre-operative measurement (Fig 15b and 15d). Compared to pre-operative values, cortical thickness increased by 5.1% (mean ± SEM) from 2.40 mm ±0.03 to 2.53 mm ±0.03 ($p<0.0001$; Table 4, Fig 16) in the ROI in successfully revascularized hemispheres.

In contrast, the six hemispheres in which revascularization was unsuccessful, as gauged by persistent steal physiology on the post operative CVR study, there was progression of cortical thinning (mean ± SEM) from 2.48 mm ±0.04 to 2.37 mm ±0.04, ($p<0.03$; Table 4, Fig 16). Thus, successful revascularization improves cortical thickness.

Changes in cortical thickness in affected vs. contralateral, non-revascularized hemisphere
We compared the cortical thickness in the ROI within the brain areas with steal physiology to the corresponding area in the contralateral, non-revascularized hemisphere (Fig 15b) to control for the accuracy of the cortical thickness measurements. Cortical thickness in the 20 subjects with unilateral steal physiology showed a mean cortical thickness increase of 1.9% (mean ± SEM) 2.44 mm ±0.009 to 2.49 mm ±0.002 ($p<0.001$; Table 5, Fig 16) in the ROI in non-revascularized hemispheres.
Unlike in the revascularized hemispheres, which all showed increases in cortical thickness, not every non-revascularized hemisphere exhibited a thickness increase (Table 5). This may be due to variations in vascular collateral blood flow (e.g., incomplete Circle of Willis) between patients. A significant thinner cortex was also found when comparing the pre-operative cortical thickness between the revascularized hemisphere exhibiting steal physiology versus the non-revascularized hemisphere ($p<0.05$, Fig 16). There was no significant difference in cortical thickness between the post-operative revascularized hemisphere and non-revascularized hemisphere ($p=0.65$, Fig 16).

Furthermore, cortical thickness comparison in the 20 subjects with unilateral steal physiology showed a mean cortical thickness increase of 0.13 mm (±0.05) in the revascularized hemispheres versus 0.05 mm (±0.08) in the non-revascularized, contralateral hemispheres ($p<0.002$).

Table 4: *Cortical thickness changes and time to follow-up in revascularized hemispheres*

Hemisphere	Thickness pre†	ROI volume††	Thickness post†	ROI volume††	Thickness difference	Follow -up 1*	Follow -up 2**
1	2.52 (0.80)	44404	2.53 (0.64)	45263	0.01	27	23
2	2.54 (0.90)	84845	2.61 (0.87)	101987	0.07	14	16
3	2.56 (0.78)	22104	2.70 (0.78)	23886	0.14	10	3
4	2.19 (0.72)	14136	2.36 (0.73)	14806	0.17	7	4
5	2.38 (1.22)	2983	2.52 (0.79)	3480	0.14	8	5
6	2.41 (0.61)	10531	2.61 (0.60)	11091	0.2	42	37
7	2.32 (0.75)	14366	2.39 (0.57)	13341	0.07	27	5
8	2.40 (0.72)	46839	2.58 (0.64)	50248	0.18	8	4
9	2.39 (0.69)	19007	2.57 (0.64)	20418	0.18	20	19
10	2.40 (0.61)	26674	2.57 (0.60)	25975	0.17	4	3
11	2.45 (0.75)	52622	2.48 (0.74)	49335	0.03	18	14
12	2.32 (0.71)	47429	2.44 (0.70)	50360	0.12	11	9
13	2.77 (0.95)	16256	2.92 (0.77)	17942	0.15	14	12
14	2.18 (0.65)	22169	2.29 (0.62)	23592	0.11	34	29
15	2.53 (0.77)	20901	2.66 (0.66)	38467	0.13	20	10
16	2.46 (0.76)	36344	2.57 (0.67)	37813	0.11	20	4
17	2.45 (0.67)	125368	2.52 (0.66)	128402	0.07	15	8
18	2.48 (0.69)	74665	2.57 (0.68)	77592	0.09	15	7
19	2.14 (0.54)	27989	2.21 (0.53)	28636	0.08	7	5
20	2.49 (0.82)	11134	2.80 (0.85)	11151	0.31	11	5
21	1.91 (0.64)	49855	2.13 (0.65)	53602	0.22	16	13
22	2.19 (0.64)	61047	2.36 (0.66)	62436	0.17	13	4
23	2.33 (0.72)	18966	2.46 (0.73)	20041	0.13	32	30
24	2.59 (0.97)	19139	2.74 (0.94)	18942	0.15	35	32
25	2.47 (0.76)	96001	2.62 (0.77)	115781	0.15	8	6
26	2.46 (0.89)	94376	2.56 (0.90)	96545	0.1	5	5
27	2.46 (0.71)	71904	2.58 (0.60)	77097	0.12	22	18
28	2.56 (0.74)	68500	2.65 (0.65)	73648	0.09	22	22
29	2.41 (0.64)	20001	2.49 (0.63)	20321	0.08	4	2
30	2.33 (0.66)	36475	2.44 (0.62)	36300	0.11	10	1

31	2.17 (0.70)	50376	2.05 (0.66)	47813	-0.12	13	6
32	2.54 (0.55)	44607	2.27 (0.60)	40110	-0.27	13	10
33	2.71 (0.68)	50347	2.70 (0.63)	49321	-0.01	2	1
34	2.74 (0.73)	73298	2.65 (0.75)	71399	-0.09	9	8
35	2.55 (0.71)	72231	2.42 (0.82)	69032	-0.13	15	11
36	2.22 (0.64)	45094	2.15 (0.65)	42867	-0.07	15	8

† pre = cortical thickness pre revascularization; post = cortical thickness post revascularization
†† Number of voxels in ROI (voxel volume is 1.33 mm^3)
** Follow-up 1 = time between pre revascularization CVR-MRI study and post revascularization CVR-MRI study (months).*
*** Follow-up 2 = time between surgical revascularization and post revascularization CVR-MRI study (months).*
Note that hemispheres 31-36 are the non-succesfully revascularized hemispheres.

Abbreviations: ROI, region-of-interest; Values are depicted in mm (mean ± sd).

Caption table 4: *Pre and post-operative cortical thickness measurements and volume of the region of interest for the successfully revascularized hemispheres (hemisphere 1-30), and unsuccessfully revascularized hemispheres (hemisphere 31-36).*

Figure 16: *Changes in cortical thickness*

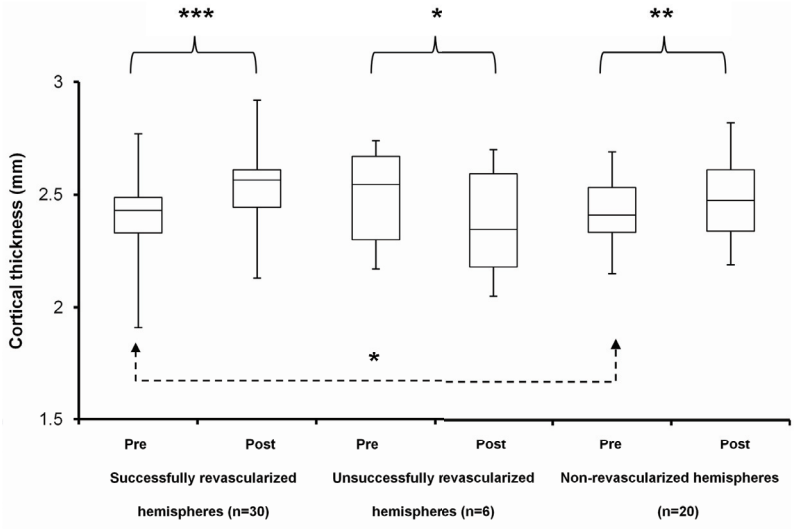

Statistical significant differences in cortical thickness:
** p<0.05*
*** p<0.001*
**** p<0.0001*

Caption: *Figure 16 shows the pre versus postoperative changes in cortical thickness for the successfully, non-successfully, and non-revascularized hemispheres. Horizontal line in the box is median, box is interquartile range (25-75%), and the whiskers represent the minimum and maximum values.*

Table 5*: Cortical thickness changes in non-revascularized hemispheres*

Hemisphere	Thickness pre†	ROI volume††	Thickness post†	ROI volume††	Thickness difference
1	2.61 (0.76)	12865	2.61 (0.66)	11916	0
2	2.58 (0.76)	4668	2.62 (0.76)	4610	0.04
3	2.15 (0.73)	10983	2.21 (0.75)	11367	0.06
4	2.31 (0.72)	43897	2.49 (0.70)	52221	0.18
5	2.69 (0.75)	8920	2.82 (0.77)	9340	0.13
6	2.21 (0.76)	18977	2.23 (0.74)	19002	0.02
7	2.43 (0.69)	22715	2.61 (0.58)	17875	0.18
8	2.69 (0.91)	10452	2.65 (0.90)	10611	-0.04
9	2.48 (0.79)	31517	2.42 (0.78)	30894	-0.06
10	2.38 (0.78)	13467	2.30 (0.80)	12304	-0.08
11	2.37 (0.65)	15976	2.36 (0.57)	14071	-0.01
12	2.53 (0.82)	17851	2.76 (0.74)	15064	0.24
13	2.39 (0.74)	18648	2.46 (0.76)	16461	0.07
14	2.21 (0.53)	20478	2.26 (0.53)	17057	0.05
15	2.54 (0.72)	20446	2.60 (0.65)	19275	0.06
16	2.51 (0.62)	27819	2.58 (0.64)	24294	0.07
17	2.34 (0.67)	56502	2.36 (0.74)	54284	0.02
18	2.51 (0.68)	13156	2.50 (0.65)	13431	-0.01
19	2.35 (0.57)	64003	2.35 (0.61)	63871	0
20	2.21 (0.74)	34031	2.19 (0.77)	33615	-0.02

† pre = cortical thickness pre revascularization; post = cortical thickness post revascularization
†† Number of voxels in ROI (voxel volume is 1.33 mm^3)
Abbreviations: ROI, region-of-interest; Values are depicted in mm (mean ± sd).

Caption table 5: *Pre and post-operative cortical thickness measurements and volume of the region of interest for the non-revascularized hemispheres.*

Discussion

To our knowledge, this is the first report of a surgical therapy resulting in a reversal of cortical thinning in patients with steno-occlusive disease. Each of the successfully revascularized hemispheres showed an increase in cortical thickness post revascularization, with a mean cortical thickness increase of 5.1% ($p<0.0001$, Table 4, Fig 16), while the 6 unsuccessfully revascularized hemispheres showed progressive cortical thinning of 4.4% ($p<0.01$). Furthermore, the contralateral non-revascularized hemispheres also exhibited some increases in thickness (1.9%, $p<0.001$, Table 5, Fig 16), although this was smaller and less consistent.

The mechanism of restoration of cortical thickness requires further investigation. Increased cortical density has been described in patients with bipolar disorder treated with lithium, which is attributed to an increased neuropil. (141) Certainly, animal studies after acute ischemia confirm that neuropil can be made to increase after stroke by rehabilitation, (142) by strategies that enhance neurogenesis using endogenous or exogenous stem cells, (143-145) or other mechanisms that may lead to enhanced dendritic arborization or synaptogenesis. (146) Although in such studies the ischemia produced acute tissue loss, the proposed mechanisms of restoration might be applicable to brain tissue with the chronic ischemia imposed by impaired vascular reserve and steal physiology, where cortical thinning occurs more slowly.

If the observed changes in cortical thickness are indeed caused by the loss and gain of neuroglial tissue, these structural changes may have direct consequences on brain function, especially in the pathophysiology of vascular insufficiency-induced cognitive impairment (VCI). Mandell et al. (147) have demonstrated that in young healthy subjects (age range 22-42) presence of steal physiology in the deep white matter, precisely matches with frequency maps of leukoaraiosis. (148) Furthermore, Conklin et al. (136) have shown an increase in Apparent Diffusion Coefficient (ADC) in normal-appearing white matter underlying the cortex with steal physiology. Like cortical thinning, leukoaraiosis, and elevated ADC values in white matter tissue have been associated with VCI. (149,150) The distributions of the cortical changes elucidated in the present studies correspond anatomically to those involved in VCI. Furthermore, a steno-occlusive etiology causing oligemia (chronic hypoperfusion) has been related to a decline in neurocognitive performance in humans. (106-107)

Other than loss and gain of neuroglial tissue, other changes can have affected the cortical thickness. One possibility is changes in cortical blood volume. A decrease in cerebral blood volume (CBV) in the brain region with steal physiology could potentially account for reduced cortical blood volume. However, studies have shown that although these brain areas are hypoperfused in the presence of steno-occlusive disease in the feeding vessels, CBV is increased (12,13) and should normalize when blood flow is restored. In this case, the expected effect on the pattern thickness change is opposite to that observed in this

study, and to that in our previous publication (138) in which we demonstrated cortical thinning in brain areas despite elevated CBV.

Table 6: *Patient demographics*

subject	sex	age	etiology	Steal †	Intervention†	Intervention
1	F	38	Unilateral Moyamoya disease	L	L	STA-MCA bypass
2	M	17	Unilateral Moyamoya disease	R	R	STA-MCA bypass
3	M	49	Unilateral MCA stenosis	L	L	STA-MCA bypass
4	F	49	Unilateral Moyamoya syndrome	R	R	STA-MCA bypass
5	F	40	Unilateral Moyamoya disease	L	L	STA-MCA bypass
6	F	51	Unilateral ICA occlusion	R	R	CCA-M2 bypass
7	M	26	Bilateral Moyamoya disease	R	R	STA-MCA bypass
8	F	54	Unilateral Moyamoya disease	R	R	STA-MCA bypass
9	F	20	Bilateral Moyamoya disease	L	L	STA-MCA bypass
10	M	44	Unilateral MCA stenosis	L	L	STA-MCA bypass
11	F	34	Bilateral Moyamoya disease	Bi	Bi	STA-MCA bypass
12	F	50	Unilateral MCA stenosis	R	R	STA-MCA bypass
13	M	13	Unilateral Moyamoya disease	L	L	STA-MCA bypass
14	M	40	Bilateral Moyamoya disease	Bi	L	STA-MCA bypass
15	F	35	Bilateral Moyamoya disease	Bi	Bi	STA-MCA bypass
16	F	39	Bilateral Moyamoya disease	Bi	Bi	STA-MCA bypass
17	M	51	Unilateral ICA occlusion	L	L	STA-MCA bypass
18	M	27	Unilateral Moyamoya disease	L	L	STA-MCA bypass
19	F	42	Bilateral Moyamoya disease	Bi	Bi	STA-MCA bypass
20	F	39	Bilateral Moyamoya disease	Bi	Bi	STA-MCA bypass
21	M	14	Bilateral Moyamoya disease	R	R	STA-MCA bypass
22	M	53	Unilateral ICA occlusion	R	R	STA-MCA bypass
23	F	66	Bilateral Moyamoya disease	Bi	R	STA-MCA bypass
24	M	59	Unilateral ICA stenosis	R	R	Endarterectomy
25	F	60	Bilateral ICA stenosis	L	L	Endarterectomy
26	M	58	Bilateral Moyamoya disease	Bi	Bi	STA-MCA bypass
27	F	32	Bilateral Moyamoya disease	R	R	STA-MCA bypass
28	M	41	Unilateral Moyamoya disease	L	L	STA-MCA bypass
29	M	62	Bilateral Moyamoya disease	Bi	Bi	STA-MCA bypass

† Left (L), right (R), or bilateral (Bi) hemisphere

Abbreviations: MCA, middle cerebral artery; ICA, intracranial carotid artery; STA-MCA, superficial temporal artery to middle cerebral artery; CCA-M2, common carotid artery to second segment of middle cerebral artery.

It is also possible that hyperperfusion after revascularization could have generated increased CBV, potentially causing cortical thickening. This too seems unlikely since a potential hyperperfusion syndrome, if present, would occur in the acute setting whereas our post revascularization CVR-MRI studies were conducted months after the surgical intervention (mean= 11 ± 9.4 months), when such changes could be expected to have subsided. CBV measurements were not performed in our cohort as this parameter is difficult to quantify with MR imaging without the use of intravenous contrast agents. (151) However, a sub-analysis of 6 patients from the Japanese EC-IC Bypass Trial, (152) which suggested progressive loss of brain volume in EC-IC patients despite revascularization suggested a decrease in CBV. However, the reasons for this were not elucidated. Future work, using other imaging modalities such as Positron Emission Tomogaphy (PET), may provide a more definitive answer to this potentially important issue.

Another possible mechanism accounting for cortical volume loss and recovery is changes in extracellular fluid (ECF) volume. However, dehydration is known to cause a reduction in brain volume. (153) We are not aware of any studies suggestive of reduced cortical ECF volume in chronic steno-occlusive disease.

Selective neuronal loss has been observed in the penumbra of acute ischemic stroke. It is plausible that in patients with severe steno-occlusive disorders, a chronic penumbra-like state exists resulting in progressive tissue loss. Whereas reversal of neuronal loss is unlikely, it is conceivable that the "effective volume" of neurons operating in areas of steal physiology shrink in size with decreases in synaptic density and dendritic arborization. (154) Alternatively, there may be a reduction in the numbers or volumes of glial cells. (155) Lastly, the changes in thickness may be due to reversal of myelin loss in the cortex. (156) Our data do not address any of these possibilities.

Summary

Our data provide the first evidence that surgical brain revascularization can reverse cerebral cortical thinning. Given the potential for profound implications to neurological and cognitive function, these relationships and the mechanisms underlying this phenomenon warrant further study.

Chapter 5

Impaired peri-nidal cerebrovascular reserve in seizure patients with brain arteriovenous malformations

In the previous chapters it became evident that brain tissue with a normal appearance on structural imaging may still suffer injury in areas that exhibit severely impaired cerebrovascular reserve associated with steal physiology. The question arose whether the BOLD-MRI exam could also add important clinical information for other (non-ischemic) neurovascular diseases on top of information derived from structural imaging. In this chapter I investigated whether brain arteriovenous malformations with a similar presentation on structural imaging, but with a different clinical presentation (seizures or no seizures) could be distinguished with BOLD-MRI sCVR investigations.

Abstract

Introduction

Epileptic seizures are a common presentation in patients with newly diagnosed brain arteriovenous malformations, but the pathophysiological mechanisms causing the seizures remain poorly understood. We used magnetic resonance imaging – based quantitative cerebrovascular reactivity mapping to determine whether seizure-prone patients with brain arteriovenous malformations exhibit impaired cerebrovascular reserve or morphological angiographic features predictive of seizures.

Methods

Twenty consecutive patients with untreated brain arteriovenous malformations were recruited (10 with and 10 without epileptic seizures) along with 12 age-matched healthy controls. Blood oxygen level-dependent-magnetic resonance imaging was performed while applying iso-oxic step changes in end-tidal PCO_2 to obtain quantitative cerebrovascular reactivity measurements. The brain arteriovenous malformation morphology was evaluated by angiography, to determine to what extent limitations of arterial blood supply or the presence of restricted venous outflow and tissue congestion correlated with seizure susceptibility.

Results

Seizure patients harboring brain arteriovenous malformations, and none of the brain arteriovenous malformation patients without seizures, exhibited impaired peri-nidal cerebrovascular reactivity by magnetic resonance imaging (0.11 ± 0.10 versus 0.25 ± 0.07, respectively; $p<0.001$) and venous drainage patterns suggestive of tissue congestion on angiography. However, cerebrovascular reactivity changes were not of a magnitude suggestive of arterial steal, and were likely compatible with venous congestion in etiology.

Conclusions

Our findings demonstrate a strong association between impaired peri-nidal cerebrovascular reserve and epileptic seizure presentation in brain arteriovenous malformation patients. The impaired cerebrovascular reserve may be associated with venous congestion. Quantitative measurements of CVR using BOLD-MRI appear to correlate with seizure susceptibility in bAVM patients.

Introduction

Epileptic seizures are a common presentation in patients with newly diagnosed brain arteriovenous malformations (bAVMs). (35) They may be disabling and patients may require life-long medication use. However, the etiology by which bAVMs cause seizures remains poorly understood, and cannot easily be explained by their morphology as similar appearing bAVMs can present either with, or without seizures. Thus additional pathophysiological mechanisms may be involved.

Previous reports suggest that bAVMs located in the frontal and temporal lobe are more seizure-prone, (17,158) or that mass effect (159) and cerebral hemorrhage (160-161) in brain tissue surrounding bAVMs can be responsible for triggering seizure activity. Also, hemodynamic alterations caused by the bAVMs complex angioarchitecture have been suggested as playing an etiological role, though with varying results. For example, large AVM size and high flow through the arterial feeding vessels of the bAVM have been related to seizure susceptibility on the assumption that the large nidus creates a low resistance vascular bed redirecting blood away from the surrounding brain tissue, with higher vascular resistance, towards the bAVM. This is considered the classical definition of arterial "steal physiology". (43-45) However, the actual existence of steal physiology has been questioned, as it has been difficult to demonstrate quantitatively. (159,162,163) Perhaps a more provocative component, like a vasoactive stimulus (e.g. hypercarbia), has to be in place to for steal physiology to occur. Others raised the possibility that seizures are more often related to a disrupted venous outflow pattern rather than to an inadequacy of arterial blood supply. (164-167) Such studies were generally based on retrospective chart reviews or case reports and, while correlating the proposed risk factors to seizures, did not provide the mechanism.

Cerebrovascular reactivity (CVR), a measure of the existing cerebro-vascular autoregulatory reserve in a vascular bed, (89,90) can be measured as the change in Blood Oxygen Level-Dependent-Magnetic Resonance Imaging (BOLD-MRI) signal in response to precise alterations in end-tidal PCO_2 ($P_{ET}CO_2$). (57,84)

Here, we used this technique to determine whether seizure-prone bAVMs exhibit impaired cerebrovascular reserve in tissue surrounding the bAVM. Also, we examined the angiographic bAVM morphology to determine to what extent limitations of arterial blood supply or the presence of restricted venous outflow and tissue congestion correlated with seizure susceptibility.

Methods

Subject Enrollment

Patients were recruited from the neurovascular clinic at the University Health Network (UHN). The study protocol was approved by the UHN Research Ethics Board. We aimed to recruit 10 bAVM patients with seizures and 10 bAVM patients without seizures.

Twenty-six bAVM patients met the inclusion criteria of whom 5 patients declined to sign informed consent (3 patients declined because of claustrophobia for an MRI exam, and 2 patients declined since the traveling distance was too far). One patient could not be studied due to intolerance for the applied CO_2 stimulus during the MRI exam. The following inclusion criteria were used: the bAVM had to be untreated and the nidus had to measure 3 or more cm in size to maximize the possibility of that arterial steal physiology may be occurring due to high flow shunting through the large nidus. Seizure patients with a prior history of brain hemorrhage were not enrolled to exclude patients with seizure activity that is unrelated to hemodynamic factors, such as prior cortical scarring or gliosis. Twelve age-matched healthy control subjects were also recruited for comparison of CVR patterns in the brain. These controls did not have a history of brain pathology. The investigators performing the BOLD-MRI CVR, and morphological analyses were blinded to the patients' past history of seizures.

MRI Study Protocol

All 32 subjects underwent MRI imaging consisting of 3-D T1-weighted Inversion-Recovery prepared Fast Spoiled Gradient-Echo (IR-FSPGR) acquisition (voxel size 0.86 x 0.86 x 1.0 mm) on a 3.0-Tesla HDX MRI system (Signa, GE Healthcare, Milwaukee, Wis). CVR was then evaluated using BOLD echo planar (EPI) gradient echo imaging (TR 2000, TE 30 ms, 3.75 x 3.75 x 5 mm voxels) and iso-oxic step changes in $P_{ET}CO_2$ as the vasoactive stimulus.

Control of $P_{ET}CO_2$

Controlled changes in $P_{ET}CO_2$ were implemented with a custom-built automated gas blender and breathing circuit combination (RespirAct™, Thornhill Research Inc., Toronto, Canada). The technique applies an end-inspiratroy rebreathing method to precisely control $P_{ET}CO_2$ and end-tidal PO_2 ($P_{ET}O_2$) independently of each other. (57) The $P_{ET}CO_2$ and $P_{ET}O_2$ in all subjects were adjusted to baseline values of 40 mmHg and 100 mmHg respectively. Subjects then underwent two iso-oxic near-square wave increases in $P_{ET}CO_2$ to 50 mmHg.

Morphological characterization of bAVMs on angiography

All bAVM patients underwent 6 vessel cerebral angiograms that are used for detection of neurovascular abnormalities in and around the brain by injecting contrast into the internal and external carotid and vertebral arteries. The angiograms were evaluated by a neuroradiologist (TK) who was blinded as to the patient's seizure history and CVR findings. The specific morphological evaluations were for:

1. The bAVMs nidal type: either glomus type, fistulous type or combined. (36)
2. Venous congestion: a pseudophlebitic pattern, (46,47) as shown in Figure 17. This pattern is usually caused by rerouting of venous flow due to venous outflow restriction (i.e.thrombosis or stenosis), resulting in dilated cortical veins.

3. Morphological flow features of feeding arteries and draining veins: Presence or absence of dilated arterial feeder(s) indicating high flow shunting of blood through the bAVM and susceptibility to venous congestion, and flow related aneurysms that may indicate high flow through the arterial feeder(s) and possibly venous congestion.

MRI data analysis

MRI and $P_{ET}CO_2$ data were imported to the AFNI software. BOLD images images were automatically co-registered to the T1-weighted anatomical dataset. (96) $P_{ET}CO_2$ data was time-shifted to the point of maximum correlation with the whole brain average BOLD signal to compensate for temporal offset between end-tidal gas sampling and the BOLD signal acquisition (circulatory delay). To minimize the effect of head motion, the BOLD time series at each voxel was orthogonalized to 6 rigid body motion parameters estimated from the volume registration procedure. A linear least-squares fit of the BOLD signal data series to the $P_{ET}CO_2$ data series was then performed. The CVR value was calculated as the percent change in BOLD signal per mmHg change in $P_{ET}CO_2$. Anatomical images and co-registered CVR maps were fitted to a 1 mm isotropic grid to facilitate subsequent analysis.

Figure 17: *Angiographic signs of venous congestion in brain arteriovenous malformations in a seizure-prone patient.*

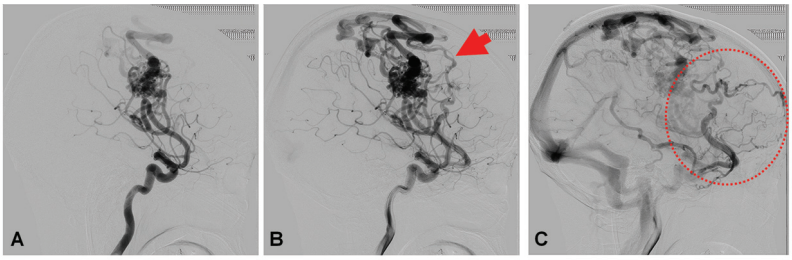

Caption figure 17: *(A) Angiogram of bAVM nidus (contrast injected in the right internal carotid artery). (B) The venous phase showing enlarged veins (indicating outflow obstruction) and absence of opacification of the cortical veins, indicating outflow obstruction-related retrograde flow (red arrow). (C) Pseudophlebitic pattern due to rerouting of venous flow to adjacent vascular territories (encircled in red).*

Tissue Classification and Regions-of-Interest

Tissue probability maps for white matter (WM) and gray matter (GM) were generated from the anatomical images (SPM5; Wellcome Department of Imaging Neuroscience, University College, London, UK) with a threshold at a probability of 0.9 to construct categorical tissue masks for GM, WM, and 'brain tissue' (defined as either WM or GM). The AVM was excluded from the WM, GM and 'brain tissue' masks (Figure 18).

To construct a 3-D region-of-interest containing the bAVM a single rater blinded to the patient's clinical history manually outlined the nidus of the AVM on all slices of the anatomical dataset in which the AVM was visible (Figure 18d). The same rater then traced a 2 mm thick region of interest (ROI) around the bAVM nidus, that was automatically expanded by stepwise margins of approximately 2 mm, up to a maximum expansion of 30 mm. (Matlab, Image Processing Toolbox; Mathworks, Natick, MA) (Figure 18g). These ROIs were then combined with the previously generated WM, GM, and 'brain tissue' masks to categorize each voxel by both tissue class (WM, GM, or non-brain) and distance from the AVM nidus. Mean CVR was computed separately for GM, WM, and brain tissue, for each successive 2mm ROI.

Figure 18: *Illustration of axial anatomical and cerebrovascular reactivity images, tissue segmentations and concentric expansion of peri-nidal region of interest*

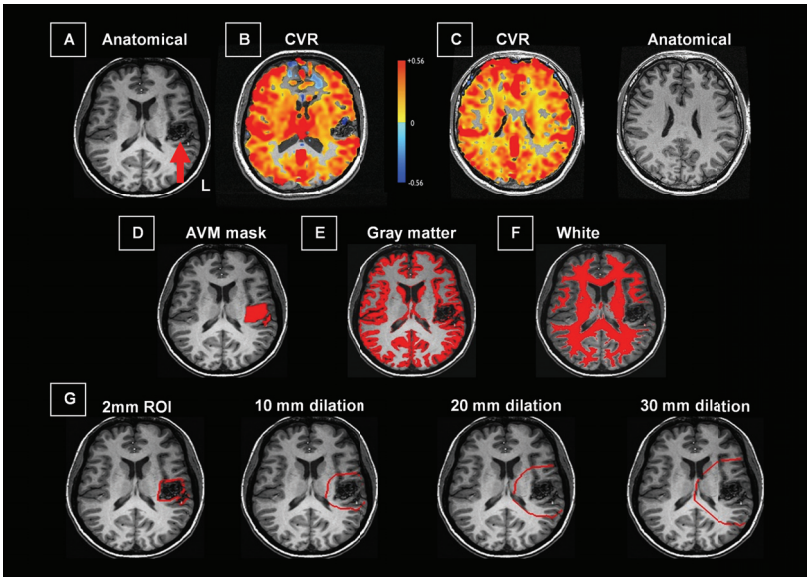

Caption figure 18: *(A) An axial anatomical image of a bAVM (red arrow) located in the posterior sylvian region. (B) The CVR map overlaid on the same anatomical brain image. CVR is calculated as the percent change in BOLD signal per mmHg change in* $P_{ET}CO_2$*. (C) An axial anatomical and CVR map from a healthy volunteer. (D) CVR analysis in bAVM patients, with the area overlying the AVM masked out in order to avoid partial volume averaging from the lesion. (E) Further segmentation for calculation of CVR in gray matter and in white matter (F). (G) Expansion of the ROI around the AVM nidus in concentric individual rings of 2 mm diameter each up to a maximum expansion of 30 mm from the lesion.*

Statistical Analysis

Demographic data and CVR were compared between two patient groups (those with seizures and those without seizures) using independent sample *t*-tests and Fisher's Exact test ($p<0.05$ was considered significant; $t_{(30)} = 2.04$). Mean CVR values for WM, GM, and brain tissue in each consecutive ring were compared in patients with and without seizures using an independent samples *t*-test ($p<0.05$ was considered significant; $t_{(18)} = 2.10$). A multi-variate exact logistic regression was performed using the binary variable '*seizures*' as the dependent variable, and CVR of adjacent brain tissue (0 to 6mm) as the independent variable (LogXact 9.0, Cytel Software, Cambridge, MA). Age and seizure prone bAVM location (i.e., a frontal or temporal lobe component to the bAVM) were included as co-variates in the regression model.

Table 7: *Patient demographics & general AVM characteristics*

			Feeding artery						
Patient	**Age (yrs)**	**Sex**	**ACA**	**MCA**	**PCA**	**size (cm)**	**Grade †**	**Location**	**Presentation**
1	22	F		+		>6	4	Right temporal	GTCS
2	48	F		+	+	3	4	Right temporal-occipital	Headaches
3	25	M	+	+	+	>6	5	Left fronto-parietal	GTCS
4	54	F		+		3	2	Left temporal	Headaches
5	40	M	+			3	2	Left occipital	Headaches
6	25	F		+		3	3	Left fronto-temporal	Hemorrhage
7	41	F		+		3	3	Left fronto-temporal	Hemorrhage
8	44	M		+		5	4	Left parietal	GTCS
9	38	F	+		+	3	2	Left parietal	Headaches
10	48	F		+		4	3	Right fronto-parietal	Seizures (unknown)
11	21	F			+	>6	4	Left fronto-temporal	GTCS
12	37	M	+	+		4	3	Right fronto-parietal	GTCS
13	14	M			+	5	3	Left thalamic	Headaches
14	24	M		+		3	3	Left frontal	Headaches
15	50	M		+		3	3	Right parietal	GTCS
16	47	M		+		3	2	Right frontal	GTCS
17	53	M			+	5	3	Left temporal-occipital	Focal seizures
18	62	M		+		3	3	Right frontal	Headaches
19	42	F	+	+		3	2	Left frontal	Focal seizures
20	49	F		+		5	3	Right occipital	Headaches

† Grading according to the Spetzler-martin grading scale.

Abbreviations: F= Female, M= Male, GTCS = Generalized tonic clonic seizures. ACA= Anterior cerebral artery, MCA= Middle cerebral artery, PCA= Posterior cerebral artery

Results

Potential confounders affecting CVR in the current patient cohort

We evaluated in our patients co-morbidities that could potentially impact on CVR findings. Evaluating the following co-morbidities; smoking, diabetes, COPD, asthma, hypercholesteremia, and hypertension, did not reveal significant differences in CVR readings between healthy subjects and bAVM patients ($p=0.73$) nor between seizure and no-seizure bAVM patients ($p=0.88$).

CVR findings between healthy subjects and bAVM patients

In order to determine whether the presence of a bAVM impacted on cerebral vascular reserve, we compared CVR maps obtained from 12 age-matched healthy subjects (mean age 37 y, range (20-52); 6 females) with those of the 20 subjects harboring a bAVM (mean age 39.2 y, range (14-62); 9 females, Figure 18 and Table 7). Differences in CVR were calculated as the percent change in BOLD signal per mmHg change in $P_{ET}CO_2$ (Methods). There were no global differences in mean CVR (as calculated from all voxels included in the 'brain tissue' mask) between bAVM patients and healthy subjects (0.231 ± 0.084 versus 0.210 ± 0.064, respectively; $p= 0.538$). This suggests that bAVMs do not produce hemodynamic effects sufficient to modify CVR throughout the whole brain.

CVR findings between bAVM patients with and without seizures

Further CVR analysis was performed between bAVM patients with seizures and those without seizures. There were no differences in age ($p=0.582$) and sex ($p=0.637$) between the two groups. The mean CVR values calculated from the entire brain volume did not exhibit a difference between the bAVM patients with seizures and bAVM patients without seizures (0.220 ± 0.086 versus 0.244 ± 0.087, respectively; $p=0.928$). More detailed analyses were undertaken in which the brain volume was further segmented by hemisphere, by GM only, and by WM only. None of these additional analyses of the data revealed any differences in mean CVR between patients with and without seizures.

These findings suggest that, if CVR differences exist between these patient populations, they are not present across these entire brain segments and seemingly independent of seizure characteristics.

Figure 19: *Mean cerebrovascular reactivity versus distance from brain arteriovenous malformation nidus in patients with and without seizures*

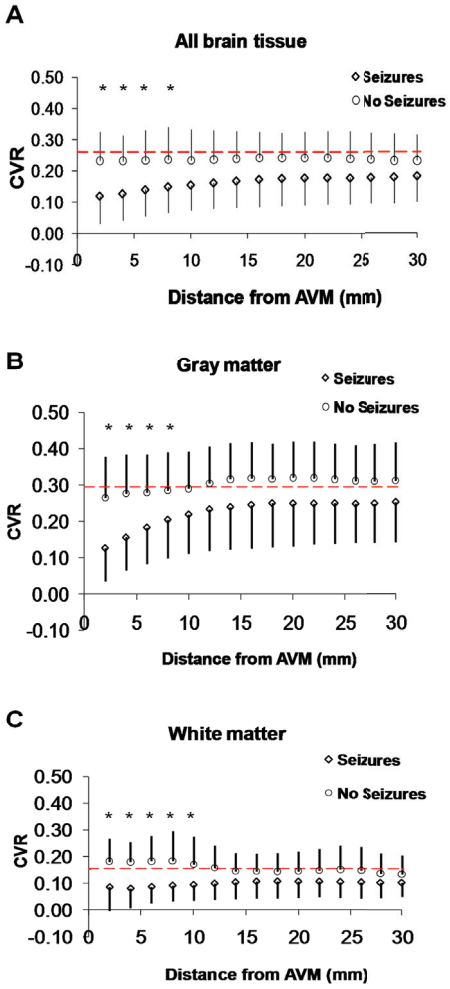

**Statistical significant individual ROI measurements; †Red line indicates normal mean CVR*

Caption: *Figure 19 shows the difference in mean CVR versus distance from the bAVM (mm) between the seizure and no seizure group. Data points indicate the mean CVR for each individual ROI, and error bars indicate the standard deviation computed cross patients within each group. The first 4 ROIs (0-8mm) show a statistically significant difference in mean CVR (*) for all brain tissue (GM plus WM; A) and GM (B). WM (C) exhibits a statistically significant difference in mean CVR up to 10mm.*

CVR in brain tissue adjacent to the bAVM distinguishes patients with and without seizures
Because bAVM-related seizures are thought to originate focally in the brain, differences in CVR might appear in closer approximation to the bAVM. Therefore, CVR analysis was performed in concentric 2 mm thick regions of interest (ROI) drawn around the bAVM nidus (Methods; Figure 18g). Analysis of the ROI immediately adjacent to the AVM revealed that seizure-prone patients showed a markedly impaired peri-nidal CVR as compared with those without seizures (0.11 ±0.10 versus 0.25 ±0.07, respectively; $p<0.001$; Figure 6). In a further analysis this 2 mm ROI was expanded in concentric rings with steps of 2 mm up to a maximum expansion of 30 mm. The difference in CVR was greatest in the 2 mm closest to the bAVM and became smaller at each more distal ROI. (Table 8; Figure 19). Analyses of CVR changes in gray and white matter separately within the same individual concentric ROIs revealed that CVR differences for both tissue types exist between seizure-prone and non-seizure prone AVMs. Also, the method of concentric ROIs was applied to the contralateral brain region mirroring that encompassing the bAVM and the same analysis repeated for all brain tissue, GM and WM in every individual concentric ROI. This additional analysis only revealed a significant CVR difference in the first 4mm for the contralateral versus ispilateral CVR comparison in the seizure group (all brain tissue and GM).

Table 8: *Cerebrovascular reactivity findings in the concentric regions of interest in brain tissue surrounding the brain arteriovenous malformation*

Distance from AVM nidus (mm)	2	4	6	8	10	20	30	0-30
S^+ CVR	0.120 (0.08)	0.127 (0.08)	0.140 (0.09)	0.149 (0.08)	0.155 (0.09)	0.178 (0.08)	0.183 (0.08)	0.166 (0.006)
S^0 CVR	0.232 (0.09)	0.231 (0.07)	0.233 (0.09)	0.236 (0.09)	0.234 (0.09)	0.242 (0.08)	0.232 (0.08)	0.247 (0.01)
p-value	**p< 0.01**	**p< 0.01**	**p< 0.05**	**p< 0.05**	p = 0.06	p = 0.10	p = 0.20	p=0.07

Abbreviations: CVR= cerebrovascular reactivity, S^+ = seizure group, S^0= non seizure group. Values depicted as mean (±sd)

CVR calculated for every individual concentric ring and the mean CVR for the overall ROI (0-30 mm). Statistical significant p-values are highlighted in bold.

Finally, using the exact logistic regression model with "seizures" being the dependent variable and adjacent CVR (0-6mm) being the independent variable, the CVR of adjacent brain tissue demonstrated a significant effect on seizures ($p= 0.03$). The effect of the other co-variates (seizure-prone location and age) did not reach significance, although there was a trend towards a positive association between seizure-prone bAVM location and seizures

(p= 0.08). Finally, two similar models were calculated by confining the CVR measurements to WM only, and GM only. CVR of both WM and GM within 6 mm of the AVM were both significantly associated with seizures (p=0.045 and p= 0.022, respectively). Also, a bAVM nidal size of >3cm showed a difference between the two groups (p= 0.02). This may comprise a reason for hemodynamic differences between the groups.
Considering the seizure patients with a bAVM, the frequency of seizures (p= 0.86), duration of seizures (p= 0.61), seizure medication (p= 0.61), and whether the seizures were medically refractory or controlled (p= 0.93) did not demonstrate a significant effect on the CVR readings.

Our CVR measurements indicate that cerebrovascular reserve is reduced in brain tissue adjacent to bAVMs of seizure-prone patients. However, peri-nidal cerebrovascular reserve in this bAVM patient cohort was not so impaired as to reach negative values, which would have implied arterial steal from the affected tissue.

Table 9: *Morphological brain arteriovenous malformation features evaluated on angiography*

	Seizures (n=10)	**No seizures (n=10)**
Venous congestion	***10***	***0***
Pseudophlebitic pattern	10	0
outflow restriction draining vein	10	0
outflow restriction remote	0	0
Nidus		
Glomus	3	8
Fistulous	0	0
Both	7	2
Feeding Arteries		
Significant dilatation	4	0
Moderate dilatation	6	4
Flow related aneurysm	2	0

Caption: *Table 9 shows the difference in morphological features between brain arteriovenous malformations presenting with, and without seizures.*

Morphological evaluation of bAVMs on angiography
Since our CVR results did not reveal changes compatible with peri-nidal steal physiology, other bAVM features may be associated with seizure susceptibility. Therefore, morphological evaluation of the angiographic features of each bAVM was undertaken by a blinded neuroradiologist. In the seizure group all bAVMs exhibited venous congestion by

the criteria listed in Table 9, whereas the bAVMs in patients without seizure susceptibility did not. Seven bAVM lesions in the seizure group and two in the no seizure group had fistulous components, indicating a high blood flow shunting through the nidus. Other bAVM characteristics that would indicate shunting of blood flow are dilated arterial feeder(s) and flow related aneurysms, and were mainly found in the seizure group (Table 9). Morphological characterization of the bAVM lesions revealed venous congestion in all seizure- prone bAVMs.

Discussion

Our study highlights a strong association between impaired cerebrovascular reserve in brain immediately surrounding the bAVM nidus and the tendency for epileptic seizures, a finding that was also closely associated with venous congestion in all seizure-prone bAVM patients. By contrast, patients without seizures did not show impaired cerebrovascular reserve in the tissue surrounding the bAVM and did not have concomitant venous congestion. The observed impairment in CVR implies that venous congestion impairs reserve capacity for microvascular autoregulation in brain tissue surrounding bAVMs in patients with seizures.

The CVR in the seizure-prone group was smaller than that observed in bAVM patients without seizures and in controls, but still exhibited an increase in BOLD signal in response to hypercapnia. Whereas the CVR technique, by its nature, does not measure arterial flows and therefore is not a direct measure of steal physiology. Nonetheless, if steal were present, CVR could not exhibit an increase in BOLD signal but would have demonstrated a "paradoxical" decrease in BOLD signal in response to hypercarbia. (138) For this reason, it is unlikely that seizures in these bAVM patients can be explained based in arterial steal physiology, as was suggested by Taylor and Spetzler in patients with large bAVMs. (43,44) Although our study includes a relatively small number of patients, we do not believe that our inability to demonstrate arterial steal is due to methodological limitations of the CVR technique, as this quantitative method has proven itself capable of identifying even subtle reductions in cerebral blood flow to a vasodilatory stimulus. (90) Our findings, however, are more in keeping with the suggestion first proposed by Kosnik et al. in 1974, (164) that venous congestion, not arterial steal physiology, adversely affects neuronal function in the tissue surrounding bAVMs.

Several studies have reported the association between venous congestion and seizures in bAVMs, (167) dural AVMs, (164-166) as well as in relation to venous sinus thrombosis. (168) Although association does not imply causation, the consistent findings of venous congestion and peri-nidal impaired cerebrovascular reserve in seizure-prone bAVM patients indicate a possible pathophysiological association.

The role of venous congestion in the impaired CVR might be explained as follows: The area of impaired cerebrovascular reserve being present in a shell surrounding the lesion

rather than confined to a specific arterial territory (such as the territory of the feeding artery) indicates that the impaired CVR is not entirely related to an increased flow through the artery into the bAVM since different vascular territories (such as deep and superficial arteries) were involved in the supply of the tissue surrounding the bAVM. High arterial inflow through the bAVM nidus may overwhelm the venous drainage capacity leading to venous congestion. The accordingly high intravascular pressures in the venous system then limit the ability of arterioles in the peri-nidal tissue to vasodilate, thus limiting CVR. This pressure-related inability to respond to a vasoactive stimulus (CO_2) would be detectable as decrease in CVR. The association between peri-nidal impaired cerebrovascular reserve and seizures will require further investigation.

From a clinical perspective it is well known that seizures are associated with venous congestion. Detection of venous congestion, however, is based on subjective criteria set out by the neuroradiologist and requires an invasive angiographic assessment, whereas CVR measurements are quantitative and non-invasive.

Other methods may also be used for measuring CVR in relation to bAVMs including, for example, dynamic single photon emission computed tomography (D-SPECT), Xenon CT, and positron emission tomography (PET). A similar finding of regionally impaired cerebrovascular reserve in seizure patients with a bAVM was done by Van Roost and Schramm in a Xe-CT study. (169) This finding, however, did not reach statistical significance in the 12 non-hemorrhagic epilepsy patients studied which might have been related to the non-quantitative imaging technique used. Some of the reasons we have chosen BOLD-MRI include the wide availability and relatively high spatial resolution of MRI. Furthermore, prior work has validated BOLD-MRI CVR as a surrogate of cerebral blood flow changes using arterial spin labeling. (90) The use of the end-inspiratory rebreathing method also enabled precise and reproducible $P_{ET}CO_2$ changes permitting quantification of CVR. A second advantage of our gas control method is that it maintains iso-oxia while changing $P_{ET}CO_2$ thus preventing the T1 effects of PO_2 from influencing the BOLD signal. (87) Finally, only with end-inspiratory rebreathing does the subjects' $P_{ET}CO_2$ equal the arterial PCO_2 which is the independent stimulus affecting the CBF. (58)

Although the CVR findings appear to discriminate between bAVM patients with seizures and bAVM patients without seizures, possible confounders as co-morbidities, and bAVM and seizure characteristics, might have influenced CVR readings. Even though these influences did not demonstrate a statistically significant effect, these analyses are under-powered in this cohort, with a relatively small sample size of 20 patients, to reveal possible statistical differences. Also, the effect of age, pulmonary disease and a history of chronic cigarette smoking which may ordinarily increase the arterial to end-tidal gradient in spontaneously breathing subjects might influence the CVR readings. However, Ito et al. (58) have argued that with the end-inspiratory rebreathing method, the gradient will

nevertheless be small, even in the presence of lung disease, over a large range of induced $P_{ET}CO_2$ and $P_{ET}O_2$. Finally, the significant difference of larger nidus size in the seizure group may have contributed to more pronounced changes of the local blood flow and hemodynamics as evaluated by BOLD-MRI CVR. However, the difference in nidus size is anticipated to be an underlying cause of hemodynamic changes (43-45) and thus does not contradict our conclusions that CVR can demonstrate those alterations in cerebral hemodynamics that make epilepsy more likely.

In summary, seizure-prone bAVM patients exhibit impaired peri-nidal cerebrovascular reserve and concomitant venous congestion. There was no evidence for arterial steal physiology in our patient cohort. Therefore venous congestion is the likely factor associated with the pathophysiology of seizures. Quantitative measurements of CVR using BOLD-MRI appear to correlate with seizure susceptibility in bAVM patients and may provide an objective test to detect bAVMs with seizure susceptibility in the future. Further studies in this regard may yield clinically useful predictive criteria for seizure propensity in treated and untreated patients with bAVMs.

Part 2

Experimental animal models

For quantitative measures of cerebrovascular reserve obtained with BOLD-MRI imaging, I have employed the standardized CO_2 delivery method as described by Slessarev et al. (57) This method is based on end-inspiratory rebreathing (127) but has only been used and validated in spontaneously breathing subjects. From a clinical perspective it would be very interesting to obtain measures of cerebrovascular reserve in a population of severely ill patients that require mechanical ventilator support, e.g. patients that suffer from traumatic brain injury, and aneurysmal subarachnoid hemorrhage.

However, translating the end-inspiratory rebreathing technique from negative inspiratory pressure (i.e. spontaneous breathing) to a condition of positive inspiratory pressure (i.e. mechanical ventilation) is not straightforward as different conditions apply. In an intubated patient, positive inspiratory pressure drives the ventilation leading to various physiological and anatomical differences in the respiratory system. Furthermore, the necessity for mechanical ventilation denotes that the patient is in a critical condition with possible lung pathology.

In the following two chapters, I will examine the compatibility of the end-inspiratory rebreathing model with a modified re-breathing circuit, compatible with that of positive inspiratory pressure, in an adult and pediatric swine model.

Chapter 6

End-inspiratory rebreathing reduces the end-tidal to arterial PCO_2 gradient in mechanically ventilated pigs

Abstract

Introduction

Non-invasive monitoring of the arterial partial pressures of CO_2 ($PaCO_2$) of critically ill patients by measuring their end-tidal partial pressures of CO_2 ($PETCO_2$) would be of great clinical value. However, the gradient between $PETCO_2$ and $PaCO_2$ ($PET\text{-}aCO_2$) in such patients typically varies over a wide range. A reduction of the $PET\text{-}aCO_2$ gradient can be achieved in spontaneously breathing healthy humans using an end-inspiratory rebreathing technique. We investigated whether this method would be effective in reducing the $PET\text{-}aCO_2$ gradient in a ventilated animal model.

Methods

Six anesthetized pigs were ventilated mechanically. End tidal gases were systematically adjusted over a wide range of $PETCO_2$ (30-55 mmHg) and $PETO_2$ (35-500 mmHg) while employing the end-inspiratory rebreathing technique and measured the $PET\text{-}aCO_2$ gradient. Duplicate arterial blood samples were taken for blood gas analysis at each set of gas tensions.

Results

$PETCO_2$ and $PaCO_2$ remained equal within the error of measurement at all gas tension combinations. The mean ± SD $PET\text{-}aCO_2$ gradient (0.13 ± 0.12 mmHg, 95% CI: -0.36, 0.10) was the same ($p = 0.66$) as that between duplicate $PaCO_2$ measurements at all $PETCO_2$ and $PETO_2$ combinations (0.19 ± 0.06, 95% CI: -0.32, -0.06).

Conclusions

The end-inspiratory rebreathing technique is capable of reducing the $PET\text{-}aCO_2$ gradient sufficiently to make the non-invasive measurement of $PETCO_2$ a useful clinical surrogate for $PaCO_2$ over a wide range of $PETCO_2$ and $PETO_2$ combinations in mechanically ventilated pigs. Further studies in the presence of severe V/Q mismatching will be required to identify the limitations of the method.

Introduction

The partial pressure of CO_2 in arterial blood ($PaCO_2$) is an indicator of the adequacy of alveolar ventilation, and an aid to diagnosing such diseases as respiratory acid-base disorders, pneumonia, and pulmonary embolism. Nevertheless, $PaCO_2$ remains an invasive measure available only intermittently, even using indwelling arterial catheters. End-tidal partial pressure of CO_2 ($P_{ET}CO_2$) might give some information about changes of $PaCO_2$ and is a standard noninvasive monitoring tool readily available in ER, OR, and ICU. Although $P_{ET}CO_2$ has been advocated as a surrogate for $PaCO_2$ in spontaneously breathing healthy adults, (170) its accuracy varies with age, (171) gravitational effects, (172) size of breath, (173) presence of lung disease (174,175) and other conditions. (170,176) In intensive care units, ventilated patients with a variety of respiratory failures, (177-180) exhibit differences between $P_{ET}CO_2$ and $PaCO_2$ (P_{ET}-aCO_2); these gradients vary between patients, and over time in individual patients, making $P_{ET}CO_2$ an unreliable surrogate of $PaCO_2$, or even its trend. (181-183) A technique that estimated $PaCO_2$ from $P_{ET}CO_2$ would allow continuous noninvasive measurement of $PaCO_2$ using standard capnography and hence might be of great benefit in intensive care.

Attempts to find such a technique have been based on the idea that rebreathing equilibrates end-tidal, alveolar arterial and venous PCO_2 tensions. (184) Bowie et al (185) showed in healthy anesthetized dogs, that introducing rebreathed gas near the end of an inspiration via a Mapleson D anesthetic circuit reduced the P_{ET}-aCO_2 gradient in proportion to the amount rebreathed, but they only tested this idea at a single $P_{ET}CO_2$. Ito et al. (58) reported that in healthy, spontaneously breathing humans, introduction of rebreathed gas at the end of inspiration via a sequential gas delivery circuit, (57) further reduced the P_{ET}-aCO_2 gradient to within the error of arterial tension measurement (0.5 ± 1.7 mmHg) over a range of $P_{ET}CO_2$ tensions between 35 and 50 mmHg and end-tidal partial pressures of O_2 ($P_{ET}O_2$) between 70 and 300 mmHg. However, the efficacy of the end-inspiratory rebreathing technique has not been tested under conditions of positive pressure ventilation and associated alterations of PO_2. Since these conditions affect cardiac output, pulmonary shunt and deadspace (186-188) they may obviate the technique. Our aim was therefore to test the end-inspiratory rebreathing technique by measuring the P_{ET}-aCO_2 gradient over a wide range of $P_{ET}CO_2$ and $P_{ET}O_2$ tensions in ventilated animals.

Methods

This study was approved by our institutional animal care committee, and all procedures were conducted according to the guidelines of the Canadian Council on Animal Care.

Animal preparation

Swine (Table 10) were pre-medicated with an intramuscular bolus of 30 mg/kg of ketamine and 0.04 mg/kg of atropine. Anesthesia was then deepened by administering 5% isoflurane through a veterinary cone mask. When the animals were at sufficient anesthetic depth, judged by a loss of eyelash reflexes and jaw tone, the trachea was intubated with a 7 mm

ID cuffed endotracheal tube. Mechanical ventilation (Surgivet, Smiths Medical PM Inc, Waukesha, WI, USA), was instituted at a frequency of 20-28 breaths/min, with an inspiratory:expiratory ratio of 1:3, tidal volumes between 300-350 mL, and a PEEP of 0 cmH_2O. We adjusted tidal volume to keep peak inspiratory pressure under 24 cmH_2O to prevent barotrauma and thereafter maintained tidal volumes and frequency constant while control of $P_{ET}CO_2$ and $P_{ET}O_2$ tensions was achieved by changing inspired gas concentrations. (57) Anesthesia was maintained with propofol infusion at a rate of 0.5- 1.0 ml/kg/h, adjusted according to clinical signs of depth of anesthesia (absence of movement, eye lash reflex, heart rate, ventilatory efforts, blood pressure). Indwelling arterial catheters were placed in the internal carotid artery under ultrasound guidance (Acuson, Computed Sonography, Mountain View, CA, USA) for continuous pressure monitoring and access to blood sampling. Tidal volume, respiratory frequency, airway pressure, electrocardiography (ECG), rectal temperature, pulse oximetry, and arterial pressure wave forms were monitored continuously (Datex AS/3, Finland).

Table 10: *Swine characteristics and baseline measurements*

Swine	Weight (kg)	$\dot{V}CO_2$ (ml/min)	Baseline $PaCO_2$	PaO2 (FIO_2 0.21)	PA-a O_2 (FiO_2 1.0)
1	40	400	**40.5**	91	164
2	40	420	**36.1**	53	324
3	38	430	**34.6**	85	124
4	40	420	**37.1**	65	243
5	41	430	**35.7**	94	98
6	38	410	**41.4**	92	84

Computer-controlled gas delivery system

To control $P_{ET}CO_2$ and $P_{ET}O_2$ tensions and implement the end-inspiratory rebreathing technique without changing ventilator parameters we placed a sequential gas delivery circuit, (127) in a rigid container to form a functional "bag in box" secondary circuit (Figure 20). This assembly was interposed between the ventilator and the animal's endotracheal tube. The breathing circuit delivered the gas output by the RespirAct™ followed by rebreathed gas similar to spontaneous breathing subjects. (57) Ventilation was controlled at 6-7 L/min and remained constant. The flow from the computer-controlled gas blender was set less than minute ventilation so that rebreathing of previously exhaled gas, 'neutral' with respect to gas exchange, occurred at the end of inspiration. Under these conditions the flow from the blender was equal to alveolar ventilation and changes in $P_{ET}CO_2$ and $P_{ET}O_2$ were implemented by changing the concentrations of CO_2 and O_2 flowing into the circuit (57) from the computerized gas blender (RespirAct™, Thornhill Research Inc., Toronto Canada).

Figure 20: *The secondary sequential gas delivery circuit*

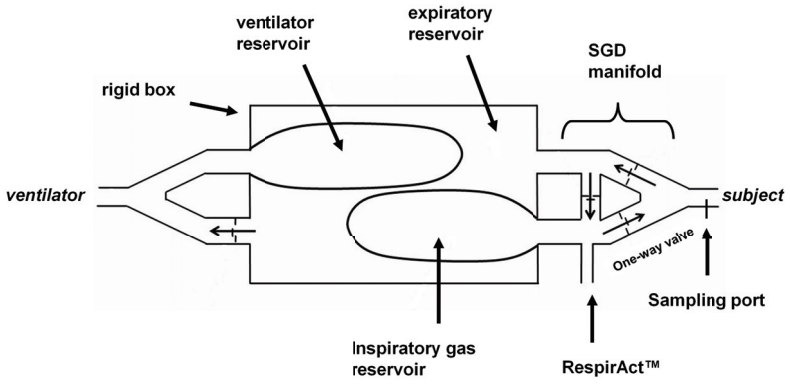

Caption figure 20: *The secondary sequential gas delivery (SGD) circuit is interposed between the ventilator and the subject, with the SGD manifold part of the rigid box that acts as the expiratory gas reservoir and contains the inspiratory gas reservoir. During exhalation, gas from the RespirAct™ enters the inspiratory gas reservoir and exhaled gas enters the rigid container. During inspiration, the box is pressurized. The relative opening pressure of the one-way valves assures that the gas from the inspiratory gas reservoir is first displaced into the inspiratory limb of the SGD. Once the inspiratory gas reservoir empties the valve in the cross-over limb opens and the ventilator displaces previously exhaled gas to the subject.*

During the inspiratory phase, the ventilator pressurizes the box containing the valve manifold and the gas reservoirs, displacing gas first from the inspiratory reservoir, and after its collapse, from the expiratory reservoir. End-inspiration rebreathing was confirmed by observing an increase in the PCO_2 at the end of the inspiratory phase. $\dot{V}O_2$ and $\dot{V}CO_2$ were measured as the product of the alveolar ventilation and the difference between inspired and expired fractional concentration of O_2 and CO_2 respectively (189) (e.g., $\dot{V}O_2$ = $\dot{V}A$ ($FEO_2 - FIO_2$). Alveolar ventilation is equal to the gas flow into the sequential gas delivery circuit (57) (known) and the differences in inspired and expired gas concentrations are as measured by the respective gas sensors. Additionally, functional residual capacity was estimated to be 2 L. These values were input variables for the calculation of inspired concentrations of CO_2 and O_2 to attain target $PETCO_2$ and $PETO_2$. (57,58) Sequential gas delivery allowed both variations of inspired gas concentrations to target various combinations of $PETCO_2$ and $PETO_2$, as well as implementation of rebreathing at the end of each breath. Simpler devices can be used to implement end-inspiratory rebreathing alone; Figure 21 illustrates one example.

Tidal gas was sampled continuously from the endotracheal tube connector and analyzed for PCO_2 and PO_2 (RespirAct™). These data were recorded and analyzed on-line for $P_{ET}CO_2$ and $P_{ET}O_2$ using custom data acquisition software (LabVIEW; National Instruments Corporation, Austin, Texas). The end-tidal values were confirmed manually post hoc.

Figure 21: *Conceptual simplified circuit*

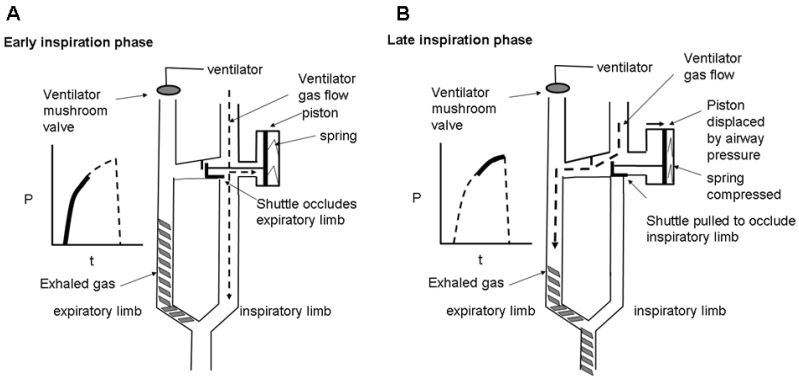

Caption figure 21: *A conceptual drawing of a simple, passive shuttle-valve that provides rebreathing at end inspiration. In early inspiration (Figure A) the mushroom valve closes the expiratory limb, and pressure rises as tidal volume is delivered to the subject (accentuated bold line in pressure-time curve on left of Figure A). The expiratory limb contains gas exhaled in the previous breath. Rising airway pressure presses on the piston and is resisted by a spring. In late inspiration (Figure B), rising airway pressure (accentuated bold line in pressure-time curve on left of Figure B) is sufficient to overcome the spring and the piston latches to the right. The shuttle-valve occludes the inspiratory limb and directs ventilator flow down the expiratory limb, displacing previously exhaled gas into the subject's lung. On exhalation, the mushroom valve opens the expiratory limb to atmosphere, the spring re-expands and the shuttle-valve is reset.*
Figure A shows a conceptual model of passive rebreathing shuttle-valve (early inspiration). The airway pressure (P) curve is indicated on the left, where t is time.
Figure B shows the passive rebreathing shuttle-valve at late inspiration. Again, the airway pressure curve is indicated on the left.

Figure 22: *Study protocol*

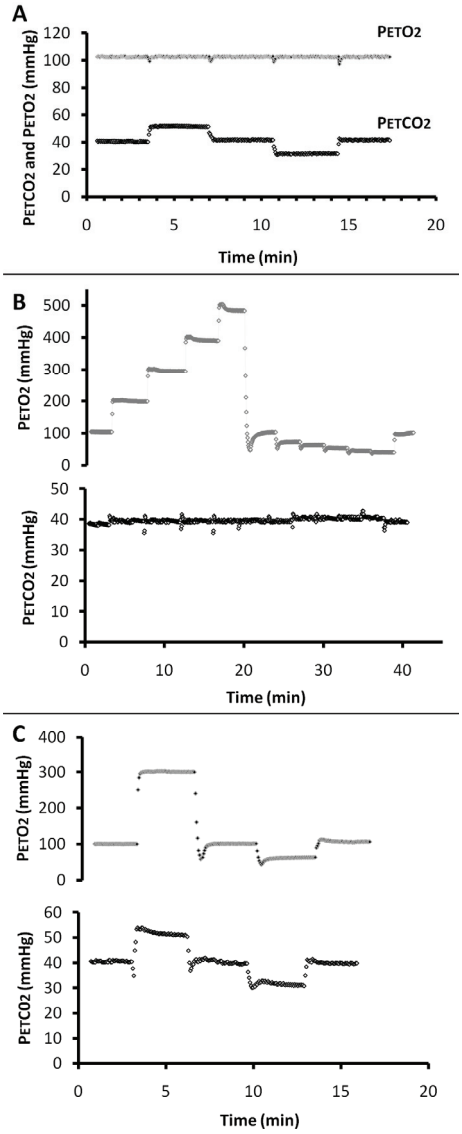

Caption figure 22: *Example data for the test protocols from a single representative pig. A) Protocol 1: iso-oxic Δ PCO_2, B) Protocol 2: isocapnic Δ PO_2, C) Protocol 3: Δ PCO_2 / Δ PO_2*

Study protocol

Three study protocols were designed to measure the P_{ET}-aCO_2 gradient at a variety of $P_{ET}CO_2$ and $P_{ET}O_2$ tensions (Figure 22).

a) Protocol 1: iso-oxic Δ PCO_2 . From a control baseline ($P_{ET}CO_2$ = 40 mmHg, $P_{ET}O_2$ 100 mmHg) 10 mmHg iso-oxic step increases and decreases in $P_{ET}CO_2$ were executed in random order, returning to baseline after each step change.

b) Protocol 2: isocapnic Δ PO_2. From control baseline, isocapnic step increases in $P_{ET}O_2$ to 500 mmHg, and step decreases in $P_{ET}O_2$ to 35 mmHg, were executed.

c) Protocol 3:Δ PCO_2 / Δ PO_2. From control baseline, combinations of $P_{ET}O_2$ and $P_{ET}CO_2$ tensions were executed in a block fashion: PCO_2 50 and PO_2 300 mmHg, and PCO_2 30 mmHg and PO_2 60 mmHg, returning to baseline between steps.

Each step was maintained for 3 minutes to ensure equilibrium in partial pressures of gases between the alveoli and the capillaries had been reached. Two consecutive arterial blood samples were drawn for analysis during the last 30 seconds of each step (Figure 22).

Data analysis

$P_{ET}CO_2$ was taken as the average $P_{ET}CO_2$ of all breaths during the last minute of every step. The consecutively drawn arterial blood samples were analyzed for blood gases (ABL 700, Radiometer Copenhagen, Denmark) within 30 minutes of collection.

Statistical analysis

Statistical analysis was performed using the SAS System v.9.1.3 (SAS Institute Inc, USA). A series of mixed-effect repeated measures models (MMRMs) was performed to determine whether differences in $P_{ET}CO_2$ and $PaCO_2$ values were significantly larger than zero, and whether the magnitude of these differences varied across step sequences, and across combinations of PCO_2 and PO_2 tensions. A subject identifier was included as a random effect in each of these models to account for the relatedness of observations taken on the same subject.

Two separate model analyses were conducted: the first to examine PCO_2 gradients as a function of sequence, and the second to examine PCO_2 gradients as a function of the targeted $P_{ET}CO_2$. Bonferroni-adjusted pairwise comparisons were used to examine whether differences between $P_{ET}CO_2$ and $PaCO_2$ tensions were significantly smaller in step sequences where both $P_{ET}CO_2$ and $P_{ET}O_2$ were varied vs. those in which $P_{ET}O_2$ tensions were constant ($p = 0.01$). Bland–Altman analysis (190) was used to calculate the limits of agreement between $P_{ET}CO_2$ (averaged over the last minute of each condition) and average $PaCO_2$ from the two blood samples. The magnitudes of the P_{ET}-aCO_2 differences were compared to the magnitudes of the differences between consecutive blood samples, and used as our outcome measure of the interchangeability of end-tidal and arterial values. (58)

Results

Several pigs had upper respiratory tract symptoms prior to the study; pigs #2 and #4 (Table 10) were particularly ill. Figure 23 illustrates the necropsy findings. Nevertheless, in the statistical analysis of each of the protocols, which included a subject identifier, we could not find any effect of subject on P_{ET}-aCO_2 gradient so pigs #2 and #4 were included in the analysis.

Figure 23: *Necropsy findings*

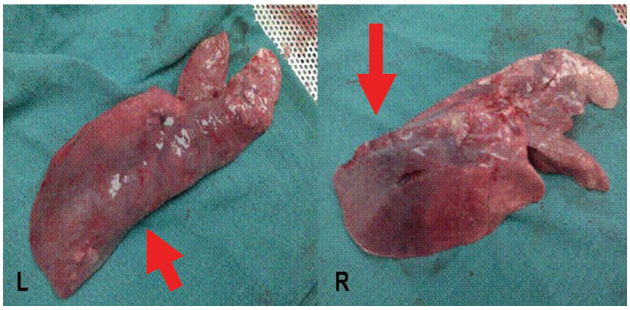

Caption figure 23: *illustrates gross specimens of lungs taken from swine #4 showing extensive bilateral lung consolidation (red arrows). Lung biopsies send for pathology confirmed acquired pneumonia ("actinobacillus pleuropnemonia" infection) Note the only normal appearing lung is at the apices*

On average, over all animals and all protocols, there was a small but consistent ($p < 0.0001$) difference between the targeted $P_{ET}CO_2$ (P_TCO_2) and the measured $P_{ET}CO_2$ (-1.08 ± 0.19 mmHg, mean ± SEM, Table 11). The average P_{ET}-aCO_2 gradient across all protocols (mean ± SE) was -0.13 ± 0.12 (95% CI: -0.36, 0.10), not significantly different from zero ($p = 0.3$). This gradient was not affected by the direction or magnitude of change of $P_{ET}CO_2$ or PaO_2. Moreover it was not significantly different ($p = 0.66$) from the difference in $PaCO_2$ between duplicate arterial blood samples (-0.19 ± 0.06 mmHg, 95% CI: -0.32, -0.06) (Figure 24).

Figure 24: *Bland-Altman plots*

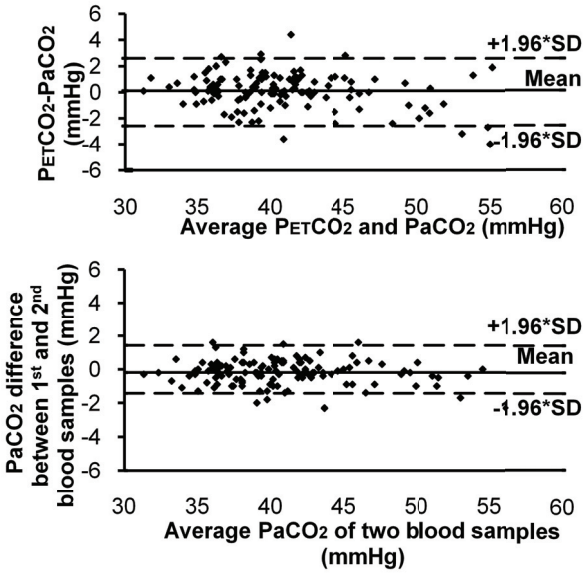

Caption figure 24: *The limits of agreement between $P_{ET}CO_2$ and $PaCO_2$ (A) and between repeat measurements of $PaCO_2$ (B).*

Discussion

$P_{ET}CO_2$ was found to be interchangeable with $PaCO_2$ throughout the full range of PCO_2 and PO_2 tensions, regardless of the $\dot{V}/\dot{Q}$ (measured by A-a O_2 gradient) of the animals and regardless of the magnitude or direction of change of PCO_2, PO_2, or both. The P_{ET}-aCO_2 gradients (mean ± SD -0.13 ± 0.12 mmHg) are an order of magnitude smaller than those previously reported in either sick or healthy humans and animals. (191-192) The interchangeability of $PaCO_2$ and $P_{ET}CO_2$ measures in these ill, ventilated animals is a unique finding.

The P_{ET}-aCO_2 gradients in these ventilated pig experiments are in marked contrast to those from human studies. Large P_{ET}-aCO_2 differences are found in healthy ventilated patients undergoing surgery, (193) and in patients on ventilator support—both children (194,195) and adults. (180,183) The magnitudes of P_{ET}-aCO_2 gradients are affected by the type and severity of primary pulmonary disease, the presence of other organ failure, (180,183,194,195) or a history of trauma. (183) They are also related to alveolar deadspace, (180) hemoglobin concentration and saturation, (196) level of positive end-expiratory pressure (PEEP), (183) respiratory frequency, fractional inspiratory concentration of O_2, pH, blood pressure, level of left-to-right shunt, and type of surgery, both singly and in combination. (183)

Table 11: *Differences between targeted end-tidal PCO_2 and measured end-tidal PCO_2 and measured arterial PCO_2 tensions for all 3 protocols*

Protocol	Target $PetCO_2$ (mmHg)						Combined Results
	30*	35	40	45	50*	55	
			1: iso-oxic Δ PCO_2				
$PetCO_2$	1.20 (n=2)	0.02 ± 1.27 (-1.55 , 1.59)	-2.18 ± 1.34 (-3.59 , -0.77)	-2.05 ± 1.49 (-3.00 , -1.10)	-2.70 ± 2.26 (-2.30 , 1.76)	-3.40 ± 0.52 (-4.23 , -2.57)	-1.85 ± 1.71 (-2.49 ,-1.21)
$PaCO_2$	2.30 (n=2)	-0.02 ± 1.38 (-1.73 , 1.69)	-1.53 ± 1.84 (-3.46 , 0.40)	-2.14 ± 1.85 (-3.32 , 0.97)	-3.55 ± 4.45 (-4.36 ,3.6.5)	-4.83 ± 0.91 (-6.27 ,-3.38)	-1.97 ± 2.35 (-2.85 ,-1.09)
			2: isocapnic Δ PO_2				
$PetCO_2$	n/a	n/a	-1.16 ± 2.23 (-1.71 , -0.61)	n/a	n/a	n/a	-1.16 ± 2.23 (-1.71 ,-0.61)
$PaCO_2$	n/a	n/a	-0.79 ± 2.32 (-1.36 , -0.22)	n/a	n/a	n/a	-0.79 ± 2.32 (-1.36 ,-0.22)
			3: Δ PCO_2 / Δ PO_2				
$PetCO_2$	3.90 ± 0.85 (-3.72 , 11.52)	-0.18 ± 2.43 (-3.20 , 2.84)	-0.33 ± 1.22 (-1.61 , 0.94)	-0.68 ± 2.68 (-2.38 , 1.03)	-0.20 ± 0.28 (-2.74 , 2.34)	-0.65 ± 2.21 (-2.97 , 1.67)	-0.23 ± 2.33 (-1.05 , 0.60)
$PetO_2$	3.80 ± 0.28 (1.26 , 6.34)	0.02 ± 2.11 (-2.60 , 2.64)	-0.38 ± 1.29 (-1.74 , 0.97)	-0.26 ± 2.75 (-2.01 , 1.49)	-1.90 ± 1.27 (-1.33 , 0.95)	-1.72 ± 1.87 (-3.68 , 0.25)	-0.36 ± 2.37 (-1.20 , 0.48)
			Combined Results				
$PetCO_2$	3.00 ± 1.67 (-1.15 , 7.15)	-0.08 ± 1.83 (-1.39 , 1.23)	-1.18 ± 2.13 (-1.66 , -0.70)	-1.36 ± 2.23 (-2.31 , -0.42)	-1.45 ± 1.95 (-4.56 , 1.66)	-1.75 ± 2.20 (-3.32 , -0.18)	-1.08 ± 2.20 (-1.47 ,-0.70)
$PetO_2$	3.33 ± 0.89 (1.09 , 5.51)	0.00 ± 1.68 (-1.20 , 1.20)	-0.81 ± 2.22 (-1.31 , -0.31)	-1.20 ± 2.49 (-2.25 , -0.15)	-2.73 ± 2.84 (-7.24 , 1.79)	-2.96 ± 2.19 (-4.53 , -1.39)	-0.95 ± 2.39 (-1.37 ,-0.53)

Abbreviations: n/a = not applicable

Caption table 11: *Differences between target end-tidal PCO_2 ($PTCO2$) and measured end-tidal PCO_2 ($PETCO_2$) and measured arterial PCO_2 ($PaCO_2$) tensions for all three protocols (varying CO_2, varying O_2 and varying both CO_2 and O_2) combined. Values are in mmHg as mean ± SD, 95% Confidence Interval (CI) is given in brackets. The $PaCO_2$ is the average $PaCO_2$ from the duplicate blood samples.*

$PETCO_2$ values of 30 and 50 mmHg were only targeted in two pigs (#1 & 6, table 10), since the high $\dot{V}CO_2$ and $\dot{V}O_2$ requirements and maximal limits of ventilatory support (see discussion section 'the animal model') required us to target values that were 5 mmHg higher (35 and 55 respectively) in the other pigs. Some of the Confidence intervals are very wide under these two conditions ($PETCO_2$ 30 and 50 mmHg), due to the small sample size in this particular sequence/PetCO2 target combination (i.e. n=2).

Russell et al. (183) found in multitrauma patients there was great variability in P_{ET}-aCO_2 gradients, with large discrepancies in 27% of cases, trending in opposite directions in 31% of successive samples. McDonald et al. (182) also found $P_{ET}CO_2$ in critically ill children was insensitive for detecting hypocapnia and hypercapnia; in only 74% of samples did $P_{ET}CO_2$ and $PaCO_2$ change in the same direction. Indeed, Grenier et al. (181) concluded that even in healthy patients undergoing non-pulmonary surgery, it is clinically inappropriate to use $P_{ET}CO_2$ as an indicator of $PaCO_2$ because of large inter-patient variability and inter-patient scatter of the P_{ET}-aCO_2 gradient over time: In 11% of 2 successive samples, P_{ET}-aCO_2 exceeded 5 mmHg, often (25%) in opposite directions.

Previous use of the end-inspiratory rebreathing technique was shown to reduce P_{ET}-aCO_2. In the study by Bowie et al. (185) the rebreathed gas was exhaled gas diluted by fresh gas during exhalation and once more during inspiration. Nevertheless, they showed that the P_{ET}-aCO_2 gradient was progressively reduced in the healthy animals as rebreathing extent increased. Ito et al.'s (58) subjects rebreathed gas more closely matching the previously exhaled gas, and observed a further reduction of P_{ET}-aCO_2 gradient such that $P_{ET}CO_2$ was interchangeable with $PaCO_2$.

However, it was not clear this method would remain robust with positive pressure ventilation, which causes increased intra-thoracic pressure, changes in alveolar deadspace (186,197) and affects the distribution of pulmonary blood flow. (198) Furthermore, Bowie et al. (185) studied their animals at one $P_{ET}CO_2$ and one $P_{ET}O_2$ and it was unknown whether P_{ET}-aCO_2 would remain small over a wide range of $P_{ET}O_2$ and $P_{ET}CO_2$, both of which affect $\dot{V}/\dot{Q}$ matching. (187,188)

In our animal model, we found that end-inspiratory rebreathing with positive pressure ventilation resulted in a low P_{ET}-aCO_2 over a wide range of combinations of $P_{ET}CO_2$ and $P_{ET}O_2$, (187) despite the potentially confounding presence of widespread severe lung pathology resulting in left to right shunt as indicated by the widened A-a O_2 gradient (197) Two pigs (pigs # 2 and 4, Table 10) had apparent upper respiratory tract infections; with runny noses and mild lethargy. On gross examination of their lungs these two animals showed severe bilateral consolidation (Figure 24). We included these animals in the study because the statistical tests did not detect that their P_{ET}-aCO_2 differed from the rest of the cohort.

Mechanism of reduction in P_{ET}-aCO_2 by end-inspiratory rebreathing

To the extent that rebreathed gas enters dead space alveoli, it limits the reduction of alveolar PCO_2. As a result, the PCO_2 in alveoli with high $\dot{V}/\dot{Q}$ approach the same value as that in the perfused alveoli. (185) Once the PCO_2 in the lung is uniform, the $P_{ET}CO_2$ will not be affected by alveolar deadspace and $PaCO_2$ will not be affected by the distribution of perfusion—i.e., $PaCO_2$ and $P_{ET}CO_2$ will equalize. (58) In principle, areas of low $\dot{V}/\dot{Q}$

('shunt') tend to make the P_{ET}-aCO_2 gradient more negative. (179,196) In practical terms, except for perhaps large right-to-left shunts such as in congenital heart disease, (196) pulmonary shunts would have little effect on P_{ET}-aCO_2 gradient because the difference in CO_2 content in the mixed venous and arterial blood is small compared to the total CO_2 content. (199) Indeed, in our study, P_{ET}-aCO_2 was small regardless of the extent of the shunt indicated by the A-a O_2 gradient (Table 10, Figure 25).

Figure 25: *PA-aCO_2 as a function of SaO_2*

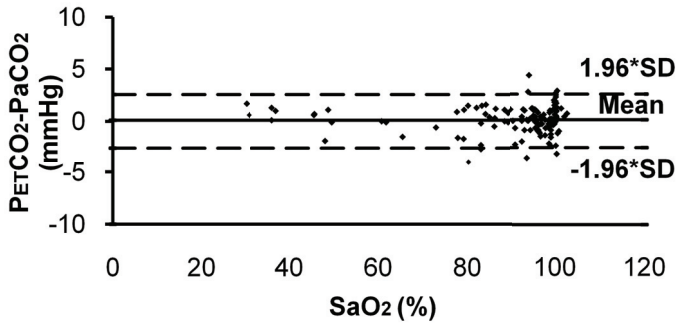

Limitations

Range of lung pathology in subjects. In this proof of concept study we included all subjects, even those with gross lung pathology. This pathology may differ from that commonly seen in patients in an ICU, who often have a component of obstructive lung disease and inflammation such as acute respiratory distress syndrome (ARDS). Our subject cohort was too small, and the extent of lung disease was insufficiently investigated for us to comment about the robustness of our method beyond the observations in this study. However, statistical analysis indicated that our results were independent of subject. Nevertheless, the ability of the end-inspiratory rebreathing technique to reduce the P_{ET}-aCO_2 gradient in various lung pathologies will require further investigation.

Protocol. A limitation of our protocol is that all $P_{ET}CO_2$ and $PaCO_2$ pairs were tested only with end-inspiratory rebreathing. Ideally, testing would be performed with end-inspiratory rebreathing and without (control test) to allow a better assessment of the specific effects of the technique. However, achieving such a comparison is impractical. It entails setting different ventilatory parameters between control tests and end-inspiratory rebreathing tests producing unavoidable differences in inspired gas concentrations, tidal volumes and airway pressures between ventilator and secondary circuit modes, all of which would confound direct comparisons. Furthermore, the passage of time between tests may further reduce the comparability of the data in unstable subjects.

Thus, while our study protocol does not prove that the end-inspiratory rebreathing technique reduces the P_{ET}-aCO_2 gradient, it does demonstrate that when the technique is used, the P_{ET}-aCO_2 gradient remains small under a wide variety of ventilations, $P_{ET}CO_2$ and $P_{ET}O_2$ combinations. Assessing the technique in a clinical setting would require the same complex implementation as used here, with the inherent control vs. test comparison difficulties mentioned above.

Extent of rebreathing required for minimizing P_{ET}-aCO_2. As discussed above, the P_{ET}-aCO_2 gradient theoretically is further reduced by increasing the extent of rebreathing. We did not control the extent of rebreathing so it likely varied throughout the protocol. The small P_{ET}-aCO_2 gradient regardless of testing conditions, suggests that the threshold for the effective extent of end-inspiratory rebreathing is low. However, this threshold is likely to vary with the underlying lung pathology, ventilator settings, type of subject (animal, child, adult) and from person to person. Therefore we emphasise that this study was designed to show proof of concept, and further experimentation is needed.

Implementation of end-inspiratory rebreathing in humans:
Reducing the P_{ET}-aCO_2 in human studies requires only end-inspiratory rebreathing. The device shown in Figure 21 is a simple passive shuttle valve interposed in an ICU ventilator circuit or a circle anesthetic circuit. It can be adjusted to give a fixed amount of end-inspiratory rebreathing with each breath. This amount can theoretically be titrated to provide an optimum reduction in the P_{ET}-aCO_2 gradient, while still controlling $P_{ET}CO_2$ by adjusting ventilator tidal volume and frequency. Indeed, careful ventilator adjustments may allow end-inspiratory rebreathing to be employed even in patients with increased intra-cranial pressures. We also anticipate that it may still be possible to implement the end-inspiratory rebreathing technique in patients ventilated with low tidal volume strategies, albeit at the expense of increases in $PaCO_2$.

Summary
In our animal model using the end-inspiratory rebreathing technique, the P_{ET}-aCO_2 gradient was an order of magnitude less than the P_{ET}-aCO_2 gradients reported for ill or healthy animals, children and adults. The precision of $P_{ET}CO_2$ as a surrogate for $PaCO_2$ was independent of the $PaCO_2$, PaO_2, SaO_2 and the extent of lung disease. $P_{ET}CO_2$ continued to track $PaCO_2$ over a wide range of $PaCO_2$ and PaO_2 tensions. This technique may allow precise, non-invasive monitoring of $PaCO_2$, in ventilated patients. Further studies in the presence of severe V/Q mismatching will be required to identify the limitations of the method.

Chapter 7

Non-invasive accurate measurements of $PaCO_2$ in a pediatric animal model

Abstract

Introduction

The PCO_2 in arterial blood ($PaCO_2$) is the best parameter for monitoring ventilation and acid-base changes in ventilated patients, but its measurement is invasive and difficult to obtain in children. Attempts have been made to use the partial pressure of CO_2 in end-tidal gas ($P_{ET}CO_2$), as a noninvasive surrogate for $PaCO_2$. Unfortunately, studies have revealed that the differences between $P_{ET}CO_2$ and $PaCO_2$ are too variable to be clinically useful. We hypothesized that end-inspiratory rebreathing, previously shown to equalize $P_{ET}CO_2$ and $PaCO_2$ in spontaneously breathing humans, would also be effective with positive pressure ventilation.

Methods

Eight newborn Yorkshire pigs were mechanically ventilated via a partial rebreathing circuit to implement end-inspiratory rebreathing. Arterial blood was sampled and tested for $PaCO_2$. A variety of alveolar ventilations resulting in different combinations of end-tidal PCO_2 (30 to 50 mmHg) and PO_2 (35 to 500 mmHg) were tested for differences between $P_{ET}CO_2$ and $PaCO_2$ (P_{ET}-aCO_2).

Results

The P_{ET}-aCO_2 of all samples was (mean ± 1.96SD) 0.4 ± 2.7 mmHg.

Conclusions

End-inspiratory rebreathing maintains P_{ET}-aCO_2 to what would be a clinically useful range in ventilated juvenile animals. If verified clinically, this approach could open the way for non-invasive monitoring of arterial PCO_2 in critically ill patients.

Introduction

During critical care, monitoring acid-base balance and the adequacy of ventilation, requires repeated invasive measurements of the partial pressure of CO_2 in arterial blood ($PaCO_2$) especially during weaning from mechanical ventilatory support. Repeated blood sampling places critically ill patients at risk for such associated complications as anemia**,** (194) infection, (182) arterial catheter blockage, and vascular endothelial injury and thrombosis. These risks are especially high in pediatric patients in whom the circulatory blood volumes, arteries and arterial catheters are smaller than in adults. In addition, drawing, transporting, and analyzing the samples consume considerable health care resources. (194,195)

By contrast, the partial pressure of CO_2 in end-tidal gas ($P_{ET}CO_2$) is a non-invasive, inexpensive measurement as a surrogate for $PaCO_2$, but in most studies there are large and variable differences between $P_{ET}CO_2$ and $PaCO_2$. (182,198) Even after a measurement of a baseline partial pressure gradient of CO_2 between end-tidal gas and arterial blood (P_{ET}-aCO_2), the reliability of assuming changes in $PaCO_2$ from serial $P_{ET}CO_2$ measurements does not improve. (183,198)

A more successful strategy has been to reduce the PCO_2 gradient between exhaled gas and the arterial blood. Ito et al. (58) administered exhaled gas at end inspiration in healthy seated spontaneously breathing volunteers and demonstrated that the P_{ET}-aCO_2 was reduced to within the range of error of measurement of $PaCO_2$. However, it is not known whether the effect would be maintained under the conditions of positive pressure ventilation, supine position, and the presence of lung pathology, which in turn affect cardiac output, pulmonary shunt and deadspace. (186-188) To test our supposition, we used a ventilated pediatric animal model to determine the effect of end-inspiratory rebreathing on P_{ET}-aCO_2 and hypothesized that end-inspiratory rebreathing would reduce P_{ET}-aCO_2 at each combination of $P_{ET}CO_2$ and $P_{ET}O_2$.

Methods

The study was approved by our institutional animal care committee, and all procedures were conducted according to the guidelines of the Canadian Council on Animal Care. We studied 8 Yorkshire newborn pigs, 3-4 weeks of age with a mean weight of 3.6 kg (table 12) in an animal operating room setting.

Animal preparation

Anesthesia was induced with a 0.2 ml/kg mixture of ketamine 58.8 mg/ml, acepromazine 1.18 mg/ml, and atropine 90 μg/ml administered by intramuscular injection, followed by 3 % isoflurane in O_2 to deepen anesthesia for surgical preparation. A catheter was inserted into the ear vein for continuous intravenous infusion anesthesia (22 mg/kg/h ketamine and 1 mg/kg/h midazolam). A 4 mm i.d. uncuffed pediatric endotracheal tube and a catheter for

gas and pressure sampling were placed in the trachea via a tracheotomy. A catheter for arterial blood sampling was inserted into the carotid artery via surgical cut-down.

Table 12: *Piglet baseline measurements, and necropsy findings*

Piglet #	Weight (kg)	$\dot{V}CO_2$ (ml/min)	PaO_2 (mmHg) (FiO_2 0.21)	PA-aO_2 (mmHg) (FiO_2 1.0)	Anatomical shunt†	Lung pathology†
1	3.1	75	87	137	PDA, PFO	severe bilateral atelectasis
2	3.6	90	95	74	PDA, PFO	severe bilateral atelectasis
3	3.8	100	65	301	PDA	severe unilateral atelectasis
4	3.4	95	88	178	PDA	bilateral atelectasis
5	3.5	90	71	418	PFO	mild bilateral atelectasis
6	3.5	90	84	271	PDA	severe unilateral atelectasis
7	3.8	95	81	304	PFO	None
8	4.2	90	75	430	none	None

† *Findings at necropsy*

Abbreviations: PDA, patent ductus arteriosus; PFO, patent foramen ovale; $\dot{V}CO_2$*, minute* CO_2 *production; PA-*aO_2*, alveolar (end-expired) to arterial* O_2 *partial pressure gradient;* FIO_2*, inspired fractional concentration of* O_2*.*

Piglets were initially mechanically ventilated with an O_2 and air mixture in pressure control mode with peak inspiratory pressures between 15-20 cmH_2O, PEEP 0 cmH_2O, frequency of 25-30/min, and inspiration:expiration ratio of 1:3. A sequential gas delivery circuit similar to that used for spontaneous ventilation (57,58) was placed in a rigid container to form a functional "bag in box" secondary circuit (Figure 21) interposed between the ventilator and the endotracheal tube. This circuit was used both to change the end-tidal gas values as well as to apply end-inspiratory rebreathing. The gas input to the circuit was provided by a computerized gas blender (RespirAct™, Thornhill Research Inc., Toronto, Canada). The blender calculated inspired concentrations of CO_2 and O_2 administered in the non-rebreathing portion of the breath to attain various target $P_{ET}CO_2$ and $P_{ET}O_2$. (57) In this way, the tidal volume, extent of rebreathing, and ventilatory frequency remained constant. During the inspiratory phase, the ventilator displaced gas first from the inspiratory reservoir, and after its collapse, from the expiratory reservoir (rebreathing). An intra-

tracheal catheter was used to monitor airway pressures and sample tidal gas. After the piglets were stabilized on the ventilator and secondary circuit, pancuronium bromide 0.2 mg/kg was administered intravenously as a bolus followed by an infusion at 0.1 mg/kg/h for the duration of the experiment. Tidal gas was sampled continuously and analyzed for PCO_2 and PO_2 (RespirAct™, Thornhill Research Inc. Toronto, Canada) from which $P_{ET}CO_2$ and $P_{ET}O_2$ were identified using specialized data acquisition software (LabView; National Instruments Corporation, Austin, TX). All monitors measuring physiologic parameters were sampled at 20 Hz and recorded using the same data acquisition software.

Study protocol

PCO_2 and PO_2 tensions of the inspired gas were varied systematically in the following three phases of the experiment (Figure 26):

1. Isoxic ΔPCO_2: From the baseline condition ($P_{ET}CO_2$ = 40 mmHg, $P_{ET}O_2$ 100 mmHg), concentrations of CO_2 and O_2 in the inspired gas were systematically altered to produce 10 mmHg isoxic step increases and decreases of $P_{ET}CO_2$ in random order, returning to baseline after each step change.
2. Isocapnic ΔPO_2. From the baseline condition, concentrations of CO_2 and O_2 in the inspired gas was systematically altered to produce an isocapnic step increase in $P_{ET}O_2$ to 500 mmHg (protocol 2a, Figure 28) and a step decrease in $P_{ET}O_2$ to 35 mmHg (protocol 2b, Figure 26).
3. $\Delta PCO_2 + \Delta PO_2$. From baseline, concentrations of CO_2 and O_2 in the inspired gas were systematically altered to produce $P_{ET}CO_2$ 50 mmHg + $P_{ET}O_2$ 300 mmHg, and $P_{ET}CO_2$ 30 mmHg + $P_{ET}O_2$ 60 mmHg in a block fashion, returning to baseline between steps.

Each step change was maintained for 3 min, and $P_{ET}CO_2$ was taken as the average $P_{ET}CO_2$ of all breaths during the last minute of each step. An arterial blood sample was drawn during the last minute of each step and analyzed within 30 min of collection (ABL 700, Radiometer Copenhagen, Denmark).

Ordinarily it may take many minutes to develop a new steady state $P_{ET}CO_2$ and $PaCO_2$ after a change in ventilation. The advantage of the RespirAct™ system is that the inspiratory gas concentrations take into account the $\dot{V}CO_2$ and $\dot{V}O_2$ and so establish a new steady state equilibrium between alveolar and capillary gas partial pressures, within 1 or 2 breaths (Figure 26).

Statistics

Statistical analysis of the data was performed using the SAS System v.9.1.3 (SAS Institute Inc, Cary NC, USA). A series of mixed-effect repeated measures models was performed to determine whether differences in $P_{ET}CO_2$ and $PaCO_2$ values were significantly greater than zero, and whether the magnitude of these differences varied across sequences, and across

PCO_2 and PO_2 tensions. A subject identifier was included as a random effect in each of these models to account for the relatedness of observations taken on the same subject.

Two separate model analyses were conducted, the first to examine P_{ET}-aCO_2 as a function of sequence, and the second to examine P_{ET}-aCO_2 as a function of $P_{ET}CO_2$. Bonferroni-adjusted pairwise comparisons were used to examine whether P_{ET}-aCO_2 was significantly smaller in the sequence in which both $P_{ET}CO_2$ and $P_{ET}O_2$ were varied than in the sequence when $P_{ET}O_2$ was maintained constant. A Bland–Altman analysis (190) was used to calculate the limits of agreement between $P_{ET}CO_2$ and $PaCO_2$. Data are presented as means ± sd.

Figure 26: *Study protocol*

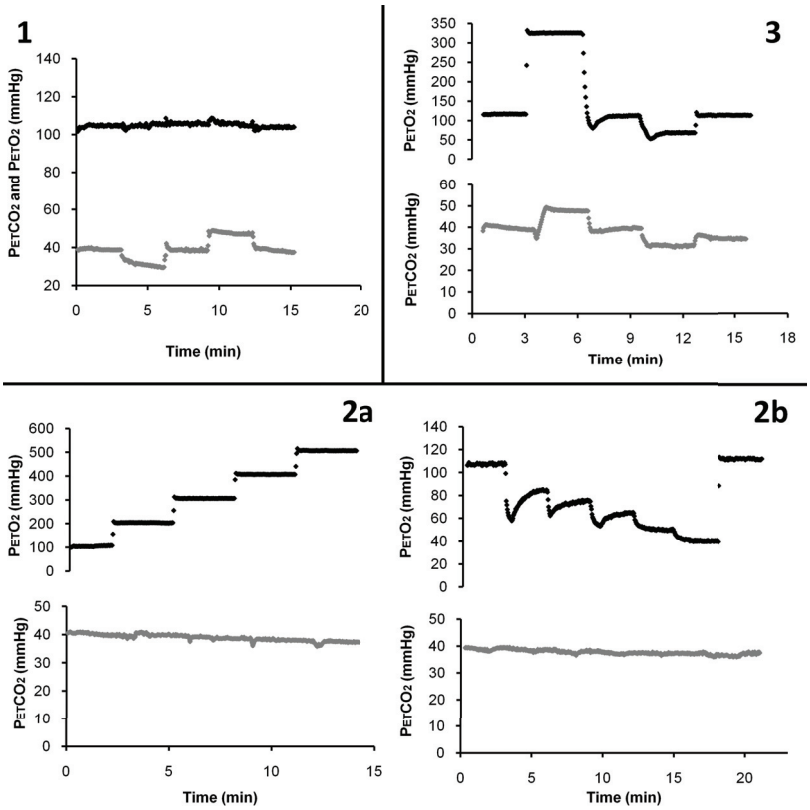

Caption figure 26: *Data for the test protocols from a representative piglet. Protocol 1) isoxic ΔPCO_2, 2a & 2b) isocapnic ΔPO_2, 3) $\Delta PCO_2/\Delta PO_2$. Protocol 2 was divided into isocapnic hyperoxic step changes in $P_{ET}CO_2$ (2a) and isocapnic hypoxic step changes in $P_{ET}CO_2$ (2b). The protocol could not be carried out as a single protocol since the*

transition from hyperoxia (500 mmHg) back to baseline (100 mmHg) was not possible within the required 3 min mainly because of the small tidal volumes employed.

Results

Animal status

The study was performed in the autumn and many of the animals in the research facility had flu-like symptoms; although the animals assigned to this experiment seemed clinically healthy, necropsy revealed them to be otherwise. Most had visible pulmonary infiltration in at least one of their lungs on gross examination (Table 12). A virology examination was not performed. Of the 8 animals in the study, 4 had a patent foramen ovale and 5 had a patent ductus arteriosus. Baseline PaO_2 tensions when breathing spontaneously (with some intermittent ventilatory assistance as required to prevent hypoventilation while titrating the level of anesthesia) on room air and on 100% O_2 (indicating A-a O_2 gradients) are also presented in Table 12. Data from a single representative piglet for each of the test protocols are presented in Figure 26.

Controlling $P_{ET}CO_2$ and $PaCO_2$:

Table 13 lists the differences between the target $P_{ET}CO_2$ (P_TCO_2) and measured $P_{ET}CO_2$ and $PaCO_2$ for all three protocols, and Figure 27a, 27b illustrate these results. There was a small but consistent difference between P_TCO_2 and measured $P_{ET}CO_2$ ($p = 0.005$), which was marginally greater at a P_TCO_2 of 30 mmHg, compared to those at 40 and 50 mmHg ($p < 0.01$ for both).

P_{ET}-aCO_2

Table 14 lists the differences between measured $P_{ET}CO_2$ and $PaCO_2$ for all three protocols, and Figure 28a and 28b illustrate these results. The average P_{ET}-aCO_2 difference was small but consistent ($p = 0.034$). Within each protocol, there were no significant differences between $P_{ET}CO_2$ and $PaCO_2$ but when the data across protocols were pooled, there was sufficient power to detect a difference. P_{ET}-aCO_2 was greater at P_TCO_2 of 30 mmHg ($p<0.0001$) than at 40 mmHg or 50 mmHg ($p<0.0001$) in each case. In every instance, $P_{ET}CO_2$ moved in the same direction as $PaCO_2$.

Table 13: *Differences between target end-tidal PCO_2 (P_TCO_2) and measured end-tidal PCO_2 ($P_{T\text{-}ET}CO_2$) and measured arterial PCO_2 ($P_{T\text{-}a}CO_2$) values for each of the 3 protocols at each of the 3 targets in mmHg*

Protocol	P_TCO_2	$P_{T\text{-}ET}CO_2$		$P_{T\text{-}a}CO_2$	
		Mean ± SD	**95% CI**	**Mean ± SD**	**95% CI**
1	30	2.8 ± 3.0	(0.0 , 5.6)	4.0 ± 2.9	(1.4 , 6.7)
1	40	-0.8 ± 2.2	(-1.6 , 0.1)	-1.3 ± 2.7	(-2.3 , -0.3)
1	50	-1.0 ± 1.7	(-2.4 , 0.5)	-1.4 ± 1.9	(-3.0 , 0.1)
	combined	-0.1 ± 2.6	(-0.9 , 0.7)	-0.5 ± 3.2	(-1.5 , 0.4)
2	30				
2	40	-1.5 ± 3.4	(-2.2 , -0.8)	-1.9 ± 3.2	(-2.6 , -1.2)
2	50				
	combined	-1.5 ± 3.4	(-2.2 , -0.8)	-1.9 ± 3.2	(-2.6 , -1.2)
3	30	4.0 ± 4.9	(-0.5 , 8.6)	4.7 ± 3.7	(1.3 , 8.1)
3	40	-0.4 ± 3.2	(-1.9 , 1.1)	-1.3 ± 2.8	(-2.5 , -0.0)
3	50	-0.8 ± 2.9	(-3.5 , 1.9)	-1.8 ± 4.1	(-5.6 , 1.9)
	combined	0.4 ± 3.9	(-0.9 , 1.8)	-0.2 ± 4.0	(-1.6 , 1.2)
combined	30	3.4 ± 4.0	(1.2 , 5.7)	4.4 ± 3.2	(2.5 , 6.2)
combined	40	-1.2 ± 3.2	(-1.7 , -0.7)	-1.7 ± 3.0	(-2.2 , -1.2)
combined	50	-0.9 ± 2.3	(-2.1 , 0.4)	-1.6 ± 3.0	(-3.3 , 0.0)
	combined	-0.7 ± 3.4	(-1.3 , -0.2)	-1.2 ± 3.5	(-1.7 , -0.7)

Table 14: *Differences between measured end-tidal PCO_2 and measured arterial PCO_2 (P_{ET}-aCO_2) values for each of the three protocols at each of the three target $P_{ET}CO_2$*

Protocol	P_TCO_2 (mmHg)	P_{ET}-aCO_2 (mmHg)	
		Mean ± SD	**95% CI**
1	30	-1.2 ± 1.5	(-2.7 , 0.2)
1	40	0.5 ± 2.0	(-0.2 , 1.3)
1	50	0.5 ± 0.8	(-0.2 , 1.1)
	combined	0.41 ± 2.03	(-0.2 , 1.0)
2	30		
2	40	0.4 ± 2.6	(-0.2 , 0.9)
2	50		
	combined	0.4 ± 2.6	(-0.2 , 0.9)
3	30	-0.7 ± 3.6	(-4.0 , 2.6)
3	40	0.9 ± 3.5	(-0.7 , 2.5)
3	50	1.1 ± 3.9	(-2.5 , 4.6)
	combined	0.6 ± 3.6	(-0.6 , 1.8)
combined	30	-0.9 ± 2.7	(-2.5 , 0.6)
combined	40	0.5 ± 2.6	(0.1 , 0.9)
combined	50	0.7 ± 2.6	(-0.7 , 2.2)
	combined	0.4 ± 2.7	(0.0 , 0.9)

Abbreviations: P_TCO_2= Target PCO_2; SD = Standard deviation; CI = Confidence Interval

Figure 27

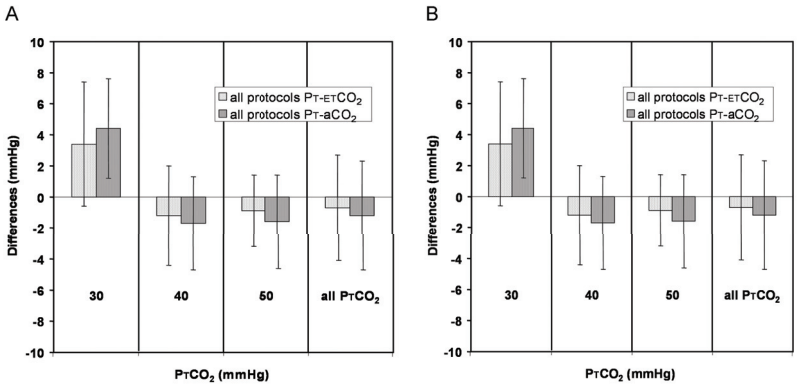

Caption figure 27: *(A) Mean ± SD gradients for each of the 3 protocols at each of the 3 desired PETCO2 tensions ($PTCO_2$). The gradients were between $PTCO_2$ and the measured $PETCO_2$ ($PT\text{-}ETCO_2$), and between PTCO2 and the measured $PaCO_2$ ($PT\text{-}aCO_2$). (B) Mean ± SD gradients for the 3 protocols combined at each of the 3 desired PETCO2 tensions ($PTCO_2$). The gradients were between $PTCO_2$ and measured $PETCO_2$ ($PT\text{-}ETCO_2$) and between PTCO2 and measured $PaCO_2$ ($PT\text{-}aCO_2$) values*

Figure 28

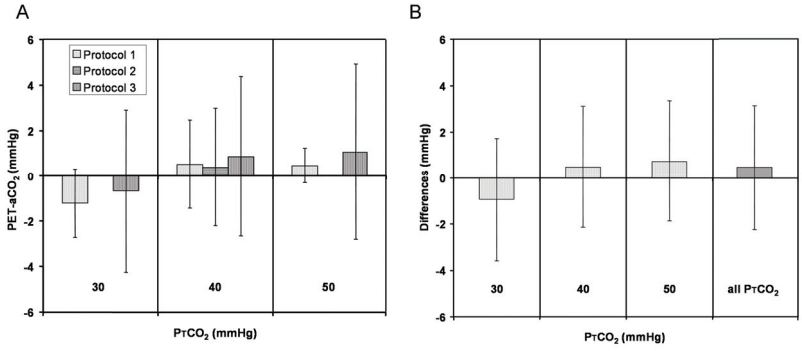

Caption figure 28: *(A) Mean ± SD gradient between measured $PETCO_2$ and measured $PaCO_2$ ($PET\text{-}aCO_2$) for each of the 3 protocols at each of the 3 desired $PETCO_2$'s tensions. (B) Mean ± SD gradient between measured $PETCO_2$ and measured $PaCO_2$ ($PET\text{-}aCO_2$) for all 3 protocols combined at each of the 3 desired $PETCO_2$ tensions.*

Figure 29: The limits of agreement between $P_{ET}CO_2$ and $PaCO_2$

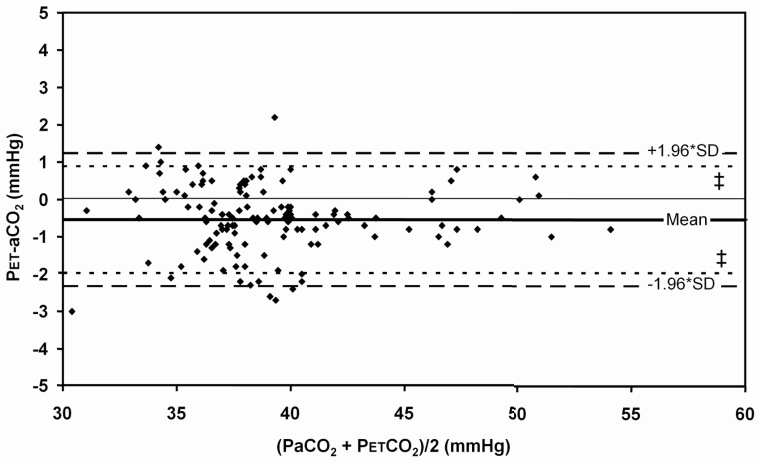

Caption figure 29: *‡ The fine dotted lines give the magnitude of the range of the P_{ET}-aCO_2 gradient due to the $PaCO_2$ measurement error alone, as calculated in a pilot study examining the P_{ET}-aCO_2 gradient in 40kg pigs; 132 test-retest samples were analyzed with the same blood gas machine used in the current study.*

Discussion

Our study in a pediatric animal model demonstrated a P_{ET}-aCO_2 gradient within the clinical error of measurement. This was achieved despite conditions, such as fetal cardiac shunts and changes in cardio-pulmonary pathophysiology as result of the severe hypoxia, hypercarbia, and hypocarbia induced in protocol 3 that are known to increase the difference in P_{ET}-aCO_2. A Bland-Altman analysis of our data indicated that the agreement between $P_{ET}CO_2$ and $PaCO_2$ was 0.4 ± 2.7 mmHg (Figure 29); an agreement not due to chance ($p < 0.0001$). (200)

The consistently small P_{ET}-aCO_2 in our study contrasts with those of most other studies in which P_{ET}-aCO_2 varies widely between subjects and in the same subjects over time. McDonald (182) studied 1708 sample pairs of $P_{ET}CO_2$ and $PaCO_2$ in 129 children in an intensive care unit; P_{ET}-aCO_2 ranged between 0 to > -30 mmHg and only 74% of samples changed in the same direction. Tobias and Meyer (195) reported a range of P_{ET}-aCO_2 of 5 to -22 mmHg in 100 sample sets in 25 infants and toddlers. Nevertheless, both studies suggested that even the broad P_{ET}-aCO_2 in their studies of -4.7 ± 8.2 mmHg and - 6.8 ± 5.1 mmHg respectively were still within a “clinically acceptable” range.

Others too have found poor, or no, correlations between $P_{ET}CO_2$ and $PaCO_2$ in adults with multi-system disease, (201) trauma, (183) undergoing neurosurgery, (202,203) as well as in dogs with healthy lungs (191) or lungs with oleic acid-induced ARDS. (192)

That our findings differ from those in the literature is likely due to the simple expedient of administering previously exhaled gas at the end of each inspiration, thereby reducing mean ± 1.96SD P_{ET}-aCO_2 to 0.4 ± 2.7 mmHg despite considerable pulmonary and circulatory pathology. End-inspiratory rebreathing has previously been shown to reduce P_{ET}-aCO_2. In the study by Bowie and group, (185) the exhaled gas was diluted with fresh gas during exhalation and once more during inspiration. Nevertheless, the authors showed that the extent of reduction of the P_{ET}-aCO_2 was related to the degree of rebreathing. In the study by Ito, (58) spontaneously breathing subjects rebreathed gas with PCO_2 that matched previously exhaled gas more closely. The result was a reduction in P_{ET}-aCO_2 to that of the difference in $PaCO_2$ between two successively drawn blood samples.

However, it was not clear that this method would remain robust with positive pressure ventilation, which causes increased intra-thoracic pressure, changes in alveolar deadspace (186,197) and affects the distribution of pulmonary blood flow. (198) Furthermore, Bowie et al. (185) studied animals at only one $P_{ET}CO_2$ and one $P_{ET}O_2$. Whether P_{ET}-aCO_2would remain small over a wide range of $P_{ET}O_2$ and $P_{ET}CO_2$ tensions, both of which affect $\dot{V}/\dot{Q}$ matching (187,188) was unknown. In our animal model, we found that with positive pressure ventilation, end-inspiratory rebreathing resulted in low P_{ET}-aCO_2 differences over a wide range of combinations of $P_{ET}CO_2$ and $P_{ET}O_2$, despite the potentially confounding presence of widespread severe lung pathology and cardiac shunting. (179)

Why end-inspiratory rebreathing reduces P_{ET}-aCO_2

The concept of rebreathing previously exhaled gas to bring the $P_{ET}CO_2$ towards the $PaCO_2$ is well established. The rebreathing methods of Read (184) and Duffin (204,205) for measuring ventilatory response are based on the premise that rebreathing eliminates the gradient between $P_{ET}CO_2$, $PaCO_2$ and mixed venous PCO_2. Rebreathing has also been used to reduce the P_{ET}-aCO_2 for monitoring purposes (185) and for controlling end-tidal gases. (58) Our study is the first to demonstrate that end-inspiratory rebreathing, first described by Sommer, (206) or its rebreathing equivalen, (207) maintains a P_{ET}-aCO_2 gradient to within the error of measurement (Figures 27 & 28) in a ventilated neonatal animal model.

Requirement for testing in a pediatric animal model

For the most part, lung ventilation, perfusion and gas exchange issues in humans can be faithfully modeled in animals. Although the pathological conditions in unselected newborn piglets (mostly seasonal pneumonia) differ from those in critically ill children; who tend to commonly suffer from conditions such as bronchiolitis, cystic fibrosis, and bronchopulmonary dysplasia. (194,195,207) Nevertheless, the pathophysiology of these

diseases (reduced lung compliance, increased pulmonary and cardiac shunting of blood and increases in alveolar deadspace) are similar in our animal model.

Other issues that are particular to the care of children should also be included in the model. The small tidal volumes relative to apparatus deadspace in infants make it difficult to accurately sample tidal gas and measure PCO_2 with clinical infrared CO_2 sensors. (193,195,209) In children, the increase of physiological deadspace with obliteration of alveolar vessels by underlying pulmonary disease (207) is exacerbated by positive pressure ventilation (210) as well as by any cardiac right-to-left shunt. (196) The presence of patent foramen ovale and persistent ductus arteriosus in newborns (211) may reduce pulmonary artery pressuresand thereby increase alveolar deadspace. Alternatively, the pulmonary artery pressure in newborns often remains close to systemic pressures (212) right-to-left shunting of blood and thereby the P_{ET}-aCO_2 gradient. (179) Finally, in the presence of right-to-left shunt, P_{ET}-aCO_2 may be affected by mixed venous CO_2 content, which is dependent on the mixed venous PO_2, pH, and the left shift of the O_2 dissociation curve resulting from the presence of fetal hemoglobin F.

Study limitations

Animal model. We found that the piglets in our study were ventilated near their ventilatory capacity. Increasing peak airway pressures risked pneumothorax, and greater ventilatory frequencies risked breath stacking.

We note that piglets are bred specifically for rapid muscle growth to reduce their time to market (http://www.thepigsite.com/stockstds/17/growth-rate), which markedly increases their CO_2 production to 2-5 times that of a human of comparable weight, but their ventilatory capacity remains proportional to their body size. Further reducing their ventilatory reserve was the presence of extensive atelectasis. PEEP was not used in this study in order to isolate the effects of our intervention (end-inspiratory rebreathing) and to maintain a "worst case scenario".

Protocol. A limitation of our protocol was that all $P_{ET}CO_2$ and $PaCO_2$ pairs were tested only with end-inspiratory rebreathing, leaving the P_{ET}-aCO_2 gradient before rebreathing unknown. It is presumed from numerous extensive investigations published in the literature that P_{ET}-aCO_2 gradients are otherwise considerably greater than those shown in this study. As a follow-up study it will be important to measure the effect of rebreathing on $PaCO_2$ and $P_{ET}CO_2$. One would adjust ventilator settings to achieve a target $PaCO_2$then note the effect of end-inspiratory rebreathing on $P_{ET}CO_2$ and $PaCO_2$. We predict that the $P_{ET}CO_2$ will move toward the $PaCO_2$. A small reduction in alveolar ventilation induced by substituting previously exhaled gas for fresh gas may also raise the $PaCO_2$ to some extent. In any event, when $P_{ET}CO_2$ is equal to $PaCO_2$, further adjustments of the ventilator can be made to target the $PaCO_2$ required clinically. The drawback of that approach for a study would be that for each subject each $PaCO_2$ would have unique tidal volume and frequency settings, and P_{ET}-aCO_2 may vary over time, making it more difficult to isolate the effects

of rebreathing. It would also be more difficult to collect more than one or two data points from a single subject. Nevertheless, this is the approach that would most suit clinical studies.

Quantifying the extent of rebreathing. Only the presence, rather than the extent, of end-inspiratory rebreathing could be identified in these experiments by observing a rise in the recorded PCO_2 trace at the end of the inspiratory phase. As a result, the extent of end-inspiratory rebreathing likely varied across the protocols. Despite this variation, the measured P_{ET}-aCO_2 gradients remained uniformly small. This finding implies that the threshold for effective end-inspiratory rebreathing is low. Nevertheless, there may be identifiable thresholds for rebreathing that vary with the underlying lung pathology, and ventilator settings.

Sampling from the trachea vs. from the proximal endotracheal tube. Small tidal volumes, high respiratory frequencies, and high ratios of equipment deadspace to tidal volume contribute to the sampling error with sidestream capnography. Badgewell (177,213) studied this issue in considerable detail and concluded that for children less than 12 kg, accurate end-tidal measurements can only be obtained from the distal endotracheal tube. We placed the gas sampling catheter beside, rather than inside, the endotracheal tube in order to provide the least resistance for the high minute ventilations required to ventilate piglets compared to those required to ventilate humans of the same weight (see above).

Summary

We found that end-inspiratory rebreathing results in a small P_{ET}-aCO_2 gradient in a newborn pig model over a wide range of $P_{ET}CO_2$ and $P_{ET}O_2$. Our findings therefore demonstrate that a non-invasive surrogate test for $PaCO_2$ may be feasible. Nevertheless, this technique must be verified clinically.

Chapter 8

Discussion

The main findings resulting from this thesis are: 1) normal appearing brain tissue on structural MR imaging exhibiting severely impaired cerebrovascular reserve associated with steal physiology reveals cortical thinning, a process that can be reversed with successful surgical revascularization. 2) Patients with severe chronic cerebrovascular steno-occlusive disease, as gauged by brain tissue exhibiting impaired cerebrovascular reserve with steal physiology on BOLD-MRI, demonstrate subclinical fluctuations in cerebrovascular reserve (i.e. brain tissue perfusion), even after successful surgical revascularization. 3) Seizure-prone brain arteriovenous malformations exhibit peri-nidal impaired cerebrovascular reserve and venous congestion. 4) With a modified re-breathing circuit, compatible with positive inspiratory pressure, the method of end-inspiratory rebreathing is also compatible with mechanical ventilation.

1) Normal appearing brain tissue on structural MR imaging exhibiting severely impaired cerebrovascular reserve associated with steal physiology reveals cortical thinning, a process that can be reversed with surgical revascularization

By measuring cerebrovascular reserve with BOLD-MRI in patients with chronic steno-occlusive disease we were able to demonstrate, for the first time in humans, brain tissue injury related to chronic ischemia without signs of gross tissue loss on conventional brain imaging. This chronic ischemia occurs due to chronic intermittent insults of hypoperfusion by the mechanism of steal physiology. In selected patients exhibiting unilateral severely impaired cerebrovascular reserve with steal physiology, thinning of the cortex occurs as compared to the contralateral hemisphere with preserved cerebrovascular reserve. A mean cortical thinning of eight percent was measured; however, the rate of thinning over time could not be assessed since it was a cross-sectional study design. We note that handedness has non-significant effect on cortical (hemispheric) asymmetry, (135) One subject measured a slightly thicker cortex in the hemisphere with the paradoxical CVR, the left hemisphere in this case. Luders et al. (4) reported that the left hemisphere is thicker (left versus right 2.42 (0.14) versus 2.36 (0.13)); given these robust standard deviations, the cortex on the left side could still have undergone thinning without the overall thickness being reduced below the normally thinner right hemisphere.

At this point it is not clear whether the observed changes in cortical thinning are indeed caused by the loss of neuroglial tissue. Chronic exposure of neurons to sublethal episodic flow insufficiency during activation may result in a loss of synaptic density and decreased dendritic arborization. Under these conditions neurons divert metabolic resources toward survival over function. (215,216) Another possible mechanism is that these episodes of hypoperfusion during activation may cause inhibition of protein synthesis resulting in delayed neuronal death. (125)

Other than loss of neuroglial tissue, other changes could have affected the cortical thickness. It is possible that at least part of the thinning of the cortex was due to reduced blood volume and not loss of cells. This however is unlikely as cerebral blood volume should be at a normal level or even elevated (due to compensatory vasodilation) in areas of reduced perfusion pressure with no signs of ischemia. (13) Another confounding mechanism may be the presence of cortical dehydration with loss in cell volume. This is unlikely as a limitation in blood flow is generally associated with decreased cellular energy resources leading to cell swelling. This therefore leaves loss of neuroglial tissue as the most likely explanation for the regional cortical thinning that we observed. Interestingly, nine of the studied cases in chapter 3 had left-sided steal physiology with eight showing a thinner left hemispheric cortex compared with the right hemisphere. This hemispheric difference is therefore more significant in that it occurred in the typically thicker left hemisphere. (3,4)

Follow-up work (Chapter 4) has been performed employing cortical thickness measurements inpatients previously identified with cortical thinning, who underwent successful surgical revascularization (i.e. normalization of cerebrovascular reserve). In this study, 30 out of 30 hemispheres showed increased cortical thickness, indicating that revascularization reverses cortical thinning. This observation would favor a reversible cause of neuroglial injury, as selective neuronal necrosis would not be expected to recover. Perhaps restoration of flow augmentation following revascularization restored metabolic balance and reversed degeneration in the neural networks and supporting cells.

A decrease in cerebral blood volume (CBV) in the brain region with steal physiology could potentially account for reduced cortical blood volume. However, studies have shown that although these brain areas are hypoperfused in the presence of steno-occlusive disease in the feeding vessels, CBV is increased (12,13) and should normalize when blood flow is restored. In this case, the expected effect on the pattern thickness change is opposite to that observed in this study and to that in our previous publication in which we demonstrated cortical thinning in brain areas despite elevated CBV. CBV measurements were not performed in our cohort because this parameter is difficult to quantify with MRI without the use of intravenous contrast agents. (151) However, a subanalysis of 6 patients from the Japanese Extracranial–Intracranial Bypass Trial, (152) which demonstrated progressive loss of brain volume in extracranial–intracranial patients despite revascularization and suggested a decrease in CBV. However, the reasons for this were not elucidated. Future work, using other imaging modalities such as positron emission tomography, may provide a more definitive answer to this potentially important issue. Another possible mechanism accounting for cortical volume loss and recovery is changes in extracellular fluid volume. However, dehydration is known to cause a reduction in brain volume. (153) We are not aware of any studies suggestive of reduced cortical extracellular fluid volume in chronic steno-occlusive disease. Selective neuronal loss has been observed in the penumbra of acute ischemic stroke. It is plausible that in patients with severe steno-occlusive disorders, a chronic penumbra-like state exists resulting in progressive tissue loss. Whereas reversal

of neuronal loss is unlikely, it is conceivable that the "effective volume" of neurons operating in areas of steal physiology shrink in size with decreases in synaptic density and dendritic arborization. (154) Alternatively, there may be a reduction in the numbers or volumes of glial cells. (155) Lastly, the changes in thickness may be due to reversal of myelin loss in the cortex. (156) The data from this thesis do not address any of these possibilities.

Anatomical consequences: Yes. But are there functional consequences?
If the observed changes in cortical thickness are indeed caused by the loss and gain of neuroglial tissue, the structural changes may have direct consequences on brain function, especially in the patho-physiology of vascular cognitive impairment. Patients, in whom neuronal activity is no longer met with a commensurate augmentation of cerebral blood flow, are believed to be at a higher risk of an acute ischemic stroke, (66,97,98) even in the absence of acute ischemia. Experimental animal models simulating a state of non-ischemic chronic hypoperfusion demonstrate a decline in neuronal structure and viability. (99,100) In humans, vascular cognitive impairment is associated with the loss of cortical gray matter, (102-104) whereas steno-occlusive disease without stroke has been associated with neurocognitive decline. (105-107) Looking at it from another perspective, neurodegenerative disorders such as Alzheimer disease (139) and Huntington disease (101,140) are associated with reduced vascular function. These studies indicate that there may well be a patho-physiological association among vascular impairment, structural changes in the brain, and neurocognitive dysfunction.

White matter is not immune to these effects although the mechanism may be different. Mandell et al. (147) have demonstrated that in young, healthy subjects (age range, 22 to 42 years), the presence of steal physiology in the deep white matter precisely matches with frequency maps of leukoaraiosis. Addendum chapters I & II describe Apparent Diffusion Coefficient (ADC) measurements in the white matter of subjects with chronic cerebrovascular steno-occlusive disease exhibiting unilateral steal physiology and cortical thinning, but without structural abnormalities on conventional imaging. ADC values in the hemisphere with steal physiology were significantly elevated compared to the normal hemisphere suggesting the presence of chronic injury. It remains to be determined if the findings represent degeneration secondary to injury of neuronal cell bodies on the side of the thinner cortex, or due to the direct effects of steal physiology and episodic ischemia on the axons themselves. In animal models of chronic hypoperfusion, WM is particularly susceptible to ischemic changes including glial activation, axonal damage, and disturbed synthesis and metabolism of myelin. (217,218) ADC elevation in WM of patients with carotid occlusive disease is consistent with the demyelination, axonal loss, and resulting rarefaction observed in experimental models. (219) Although the observed ADC elevations are small in both of our studies they are similar in magnitude to WM changes previously reported in both large vessel (220,221) and small vessel (222) cerebrovascular disease. In some (221,222) but not all (220) of these studies, the degree of ADC elevation correlated to

the degree of cognitive dysfunction. Interestingly, the one study, which did not report a correlation between WM ADC and cognitive function, selected WM ROIs manually, without reference to the presence or spatial distribution of CVR impairment. (220) Use of CVR mapping in patient selection and ROI generation allows identification of precise regions where ADC elevation would be expected as a result of CVR impairment, and may improve the correlation between WM ADC and neuropsychological outcome measures. Like cortical thinning, leukoaraiosis and elevated apparent diffusion coefficient values in white matter tissue have been associated with vascular cognitive impairment. (149,150) The distributions of the cortical changes elucidated in the present studies correspond anatomically to those involved in vascular cognitive impairment. Furthermore, a steno-occlusive etiology causing chronic hypoperfusion has been related to a decline in neurocognitive performance in humans. (106-107)

CVR as indicator of autoregulatory reserve

Pressure autoregulation is located in the pial arteries with a diameter > 50 um, whilst CO_2 reactivity involves smaller pial arterioles. The assumption that the response of the BOLD MR signal to an increase in arterial PCO_2 can be considered a measure of cerebrovascular perfusion reserve can be challenged. It may be argued that the response to CO_2 is not an indicator of perfusion reserve or of autoregulatory reserve, but simply CO_2 reactivity. In other words, if pressure autoregulation and CO_2 reactivity occur in different vessel sizes, they may act in series and thus independently. Indeed, Lundar et al. (223) found that patients on cardiopulmonary bypass did not have evidence of cerebral autoregulation but still responded to CO_2. Kazumata et al. (224) showed that acetazolamide and CO_2 correlate poorly in eliciting CBF responses, suggesting the possibility that their different mechanisms of cerebral vasodilatation may not reflect the same autoregulatory reserve.

However, Harper et al. (225) in a dog model of CO_2 response in whole brain showed that progressive reductions in blood pressure and the elicitation of autoregulatory vasodilatory changes, progressively dampens the constrictor and dilatory responses to CO_2. At a critically reduced blood pressure, the vessels become totally unresponsive to CO_2 indicating that autoregulatory exhaustion of vasodilatory reserve can be shown by lack of dilatory response to CO_2. Extrapolated to a vascular bed that contains a region upstream from a stenotic vessel in parallel to normally responsive vessels, a hypercapnic stimulus would result in vasodilation in vessels with retained perfusion pressure and a degree of vasodilation commensurate with the remaining vasodilatory reserve distal to the stenosis. Regional measures of blood flow would show a distribution of blood flow away from the territory distal to the stenosis. Indeed, this was described by Ringelstein et al. (51) in humans with unilateral occlusion of the internal carotid artery. Furthermore, CO_2 response has been shown to be a good indicator for autoregulation exhaustion by comparing it to the most direct stimulus, hypotension. (226) Lastly, CVR in response to CO_2 (97,227,228) and acetazolamide (14,69,78,79,229,230) are highly predictive of stroke, supporting the assumption that they are related to reductions in cerebrovascular reserve."

The Long-Term Consequences of Chronic Steal Physiology on the Brain: "The Neurovascular Uncoupling Syndrome"

The chronic exposure of neuronal networks to the impending adverse effects of vascular beds that have already responded to proximal vascular stenosis with maximal smooth muscle relaxation, i.e. vascular beds that are already operating at the extreme vasodilatory endpoint of the autoregulatory reserve capacity, may lead to this observed tissue injury. In effect, these vascular beds are unable to respond to a neuronal signal for augmentation of blood flow. In severe cases, this condition may lead to a "paradoxical" reduction in cerebral blood flow, the so-called "steal phenomenon". Furthermore, increases in PCO_2 reduce markedly the gain of the myogenic response thereby also reducing the smooth muscle tone. If the smooth muscle tone is already reduced due to reduction in upstream pressure, obviously there is less tone to be lost due to day-to-day physiological variability in blood pressure and $PaCO_2$.

The vascular deficit may also have a direct effect on glial cells. Astrocytes play a supporting role in the neurovascular unit. (231) When the autoregulatory reserve is exhausted, astrocyte metabolism may be impaired increasing vulnerability of the neurons to injury. Inversely, or more likely in tandem, is the potential loss of these supporting cells due to pruning of neuronal complexity. Metabolic stress on oligodendrocytes resulting in "decay" of myelin may be an alternative explanation for elevated white matter water diffusion.

Overall, the underlying pathophysiology is complex and not well understood. Nevertheless, these studies demonstrate the first indication that areas with steal physiology show structural changes in brain tissue. Neurons in the affected brain regions are operating in an environment where inadequate blood flow is present during activation leading to diminished delivery of nutrients and diminished removal of waste products. We now believe that this condition should be referred to as true neurovascular uncoupling since the normal increase in blood flow during neuronal activation is no longer occurring. If cortical thinning and increased white matter diffusion correlate with deterioration in neurocognitive and functional performance measures specific to the affected vascular territory, it would be appropriate to consider defining the disorder as true "*neurovascular uncoupling syndrome*". Neurovascular uncoupling was introduced by Fox & Raichle (232) after they had observed a decrease in OEF following neuronal activity. We now know that during increased neuronal activity, the regional CBF increases much more than the $CMRO_2$, in fact leading to a decrease in OEF. As a result of the increase in flow, the amount of oxygen consumed is only about one third of the amount delivered. (233) Using the definition of neurovascular uncoupling to describe this observation would be erroneous since it appears to be a physiological condition.

2) Patients with severe chronic cerebrovascular steno-occlusive disease, as gauged by brain tissue exhibiting impaired cerebrovascular reserve with steal physiology on BOLD-MRI, demonstrate subclinical fluctuations in cerebrovascular reserve (i.e. brain tissue perfusion), even after successful surgical revascularization.

With secondary analysis methods developed from the BOLD-MRI sCVR technique (see background section) I was able to derive more sensitive CVR information from the 'conventional' quantitative CVR data as described in chapters 3, 4, and 5. By using the application of the standardized vasodilatory blood flow stimulus, sCVR, in a cohort of normal subjects, an atlas of normal cerebrovascular reactivity could be created. Comparison of sCVR data from a patient to that of the normal atlas enabled the quantitation of the deviation of the subject's sCVR that of the reference cohort. This data can be derived on a voxel-by-voxel basis and in absolute values as well as in terms of probability of occurring by chance (Chapter 2). In chapter 2, I used this method to follow the changes in microvascular perfusion of the brain over the course of progressive stenosis of large cerebral vessels in two patients with severe chronic cerebrovascular steno-occlusive disease. Interestingly was that when the patients were symptomatic, the CVR showed marked reduction in microvascular reserve, however, CVR seemed to also fluctuate subclinically, even after revascularization in one patient. Nevertheless, the total blood flow in both patients apparently remained above the threshold required to sustain neuronal function and cellular integrity preventing an acute stroke. This phenomenon has also been reported by Ringelstein et al. (51) where they state: "*patients with severely reduced vasomotor reactivity who remain asymptomatic may in fact be stroke-prone but may not have experienced critical challenges of their marginal cerebral blood supply yet*." Considering my study, bypass revascularization transiently improved microvascular reserve (but not to normal values) in patient A. Thereafter, the degree and extent of CVR progressively deteriorated with each succeeding scan. The patient remained asymptomatic till the last follow-up scan 1-year after the intervention. It may be very well possible that the progressive nature of the moyamoya vasculopathy, will exceed the rate of compensatory collateralization therefore initiating ischemic symptoms again in this patient. With the last follow-up scan I may have observed this process unfolding subclinically, i.e. the patient was neurologically asymptomatic at that point, but the sensitive 'secondary' sCVR analyses demonstrated a decrease in cerebrovascular reserve again. The course of disease as revealed by sCVR scans in patient B (chapter 2) was that of progressive improvement of the microvascular reserve up until the fourth examination followed by progressive deterioration in studies 5 and 6. Important to note is that this patient had an idiopathic unilateral intracranial stenosis but did not receive surgical revascularization therapy. During asymptomatic periods, the balance of vascular reserve as indicated by the functional imaging was not ascertainable from structural imaging and clinical examination alone. Progressive vessel obliteration on structural imaging would suggest worsening of the patients' clinical condition, even ischemia. However, collateralization undetectable on

structural imaging but demonstrated by sCVR (i.e. improvement in cerebrovascular reserve) may have resulted in sufficient tissue perfusion. The recurrence of symptoms during the last follow-up sCVR scan correlated well with the progressive decrease in cerebrovascular reserve on the last two scans (Chapter 2). Although the decreased CVR was detected subclinically during study 5, the symptoms recurred 3 months later, where the CVR was worsened progressively. Longitudinal follow-up of such patients may teach us more about the significance of subclinical deviations in cerebrovascular reserve and the accuracy of the sCVR analysis methods.

Using functional imaging methodologies, in particular BOLD-MRI sCVR, to select the right patient cohort and moment of surgical revascularization

After the failure of the EC-IC bypass trail in 1985 (234) to prove a reduced risk of ischemia, many studies have proposed that with proper selection of a subgroup of patients (i.e. those with severe hemodynamic failure) surgical revascularization may play a role indeed in prevention of future ischemia. Also from a clinical point of view, given the invasiveness and risk of peri-operative ischemia with surgical revascularization, it is important to select the right cohort of patients and moment of intervention. There is mounting evidence that these decisions cannot be guided by clinic alone since changes in brain hemodynamics not necessarily correlate with onset of ischemic symptoms and degree of stenosis. (12,16,17,9) As illustrated in chapter 2 and by others (51,66,97,98,235,258) it becomes more evident that imaging modalities may assist or may even guide decision making with respect to patient selection and timing of bypass revascularization as subclinical changes in hemodynamics may predict risk of ischemia.

For example, Mandell et al. (236) has recently validated the BOLD-MRI sCVR exam as a robust test to identify such patients and suggested that preoperative results derived from the sCVR exam may predict the success of the EC-IC bypass revascularization. The advantage of this particular imaging method over other existing methods, such as Xe-CT and ^{15}O-PET, is the wide availability, low cost, and noninvasive nature making this test very eligible for diagnostic purposes.

A different treatment consideration for moyamoya vasculopathy?

Moyamoya vasculopathy holds a unique place within the group of chronic cerebrovascular diseases. Considering what is currently known about the patho-physiology, a different approach to treatment might be considered. A strategy designed to form robust collaterals by intervening in the process of neovascularization and angiogenesis. This approach may realize sufficient tissue perfusion over time despite progression of the vasculopathy. Currently, the EC-IC bypass procedure remains the only effective treatment for brain revascularization in moyamoya vasculopathy.

From a hemodynamic point of view, however, bypass revascularization may not provide a finite cure in preventing brain ischemia. In Chapter 2, sequential follow-up sCVR exams

demonstrated that although sub-acute relief can be gained from an EC-IC bypass procedure, brain perfusion may fall short again over time. Considering the vascular anatomy of the circulation that is affected by this disease, it becomes apparent that brain tissue, especially the white matter, may not benefit from collateral supply or a bypass procedure. Vessel obliteration of the supraclinoid ICA, and M1 segment of the MCA, may leave no vascular lumen in severe and/or chronic progression of the disease. Consequently, collateral supply, either via the communicating arteries or pial collaterals, cannot provide blood flow to these vessels. The moyamoya collaterals may be too fragile or outnumbered for ample tissue perfusion. Considering the lenticulo-striate vessels supplying (deep) white matter: these vessels originate from the M1 segment, and cannot benefit from a physiological collateral network. Although an EC-IC revascularization can provide blood flow, either by direct revascularization of existing vessels or improve flow through collaterals, only the gray matter may benefit form this intervention. (236) But when the revascularization falls short, either due to an unsuccessful anastomosis or progression of disease, there is as of yet no adequate treatment option left to prevent ischemia in these severely affected patients. Therefore, future research avenues for treatment may involve a strategy that stimulates (collateral) vessel growth that complements surgical revascularization providing a vascular network restoring blood flow to all parts of the affected brain. Several studies have investigated the stimulation of vasculogenesis and angiogenesis in animal models, mostly by studying the effects of vascular endothelial growth factor (VEGF), (237,238) Granulocyte Colony Growth Factor (GCGF), (239) and fibroblast growth factor (FGF). (240-242) Also, since the “de novo” formed moyamoya-type collaterals by the process of neo-revascularization are very fragile and at high risk for rupture new efforts should be made to influence this process and strengthen these collaterals thereby reducing the risk of hemorrhage.

3) Seizure-prone brain arteriovenous malformations exhibit peri-nidal impaired cerebrovascular reserve and venous congestion

There is a strong association between, impaired peri-nidal cerebrovascular reserve, venous congestion and seizure presentation in patients with bAVM. However, the exact patho-physiological mechanisms underlying this association remain to be determined. With a follow-up study (unpublished work, not included in this thesis) I have investigated the relationship between impaired cerebrovascular reserve and venous outflow restriction. The hypothesis was that high pressure in the venous system caused by an outflow restriction, i.e. stenosis, may also stress the smooth muscle tone in the pre-capillary smooth muscle sphincter, as occurs with an arterial stenosis. In the case of a venous outflow restriction, however, instead of a decrease in vascular resistance (as would occur with an arterial stenosis) there is an increase in vascular resistance, quite possibly causing improper functioning of the flow control system. Figure 30 is a simple illustration of this proposed mechanism. This work shows that cervical venous outflow restriction in healthy subjects

leads to globally impaired cerebrovascular reserve. All specific tissue segmentations, such as gray matter, white matter and individual vascular territory CVR, all exhibited a mean decrease of 24% when venous outflow constriction of the internal jugular veins was applied (unpublished work). Another hypothesis resulting from these findings is dilution of neurons due to increased extracellular water content, which may occur due to venous congestion. Since the default neuronal network is based on inhibition of signals (243) onset of seizure activity may be established when neurons become less successful inhibiting electrical activity. This distortion may occur due to increase water content that prevent effective synaptic signaling.

An interesting additional observation for the CVR examinations related to bAVM, is that steal physiology could not be confirmed for the cohort presented in chapter five. This was also not confirmed for patients with cerebral proliferative angiopathy (CPA), which is considered a more ischemic disease. For functional MRI, steal physiology is thought to demonstrate a 'paradoxical' decrease in BOLD response to hypercarbia during the sCVR exam. (138) The measured impaired peri-lesional cerebrovascular reserve in seizure-prone patients with bAVM has been related to venous congestion, a finding that was not detected in our cases with CPA. Furthermore in the four patients studied there appears to be a greater degree of impairment of cerebrovascular reserve distributed in a unique, but consistent pattern, however, again no steal physiology on average. Being prone to seizures seems to be common to both groups; however it is not clear what role, if any, chronic or repetitive hypoperfusion plays in these symptoms. Currently, arterial steal has been a controversial observation during investigations of AVM hemodynamics, (159,162,163) and evidence remains to be established with empirical data.

Figure 30: *Schematic representation of venous congestion leading to impaired cerebrovascular reserve*

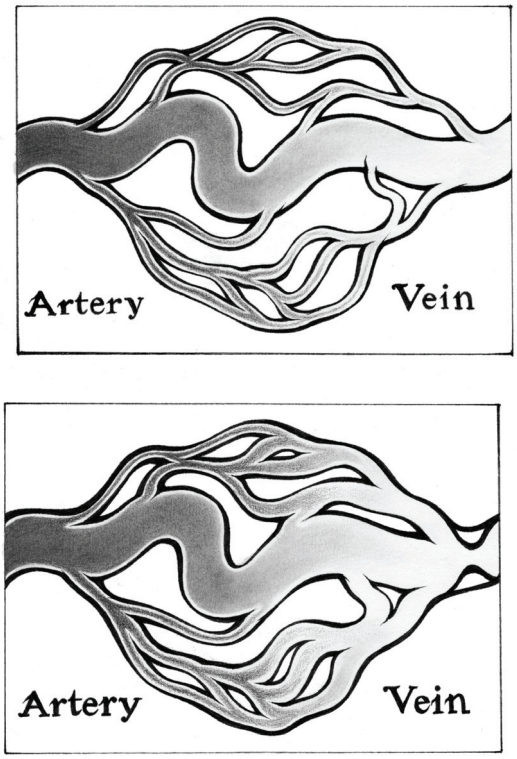

Caption figure 30: *(Upper illustration) Schematic representation of an arteriovenous shunt; the arterial blood directly drains into the low-pressure venous system in absence of an intervening capillary bed. (Lower illustration) In the case of a venous outflow restriction (schematic stenosis in the right draining vein), instead of a decrease in vascular resistance (as would occur with an arterial stenosis in the situation of an "inflow" problem) there is an increase in vascular resistance, quite possibly causing improper functioning of the flow control system. Here, arterial flow overwhelms the autoregulatory flow control system, which may in fact be responsible for impaired cerebrovascular reserve in such instances*

4) With a modified re-breathing circuit, compatible with positive inspiratory pressure, the method of end-inspiratory rebreathing is also compatible with mechanical ventilation.

In order to apply the standardized end-inspiratory rebreathing method for more critically ill patients, i.e. patients that require mechanical ventilation, we employed an animal model to test a modified breathing circuit compatible with that of positive inspiratory pressure (chapter 6). Using the same protocol the breathing circuit was also designed and tested for use in pediatric patients (chapter 7). These two studies of the end-inspiratory rebreathing technique in a ventilated animal model, $P_{ET}CO_2$ was found to be interchangeable with $PaCO_2$ throughout the full range of PCO_2 and PO_2 tensions of the protocols, regardless of the $\dot{V}/\dot{Q}$ (as measured by the A-a O_2 gradient) of the animals.

Although both studies demonstrated an excellent agreement between $P_{ET}CO_2$ and $PaCO_2$, several considerations have to be taken into account. The animals had various combinations and severity of underlying pulmonary disease and cardiac shunts. Indeed, the animals may also have had undetermined changes in cardio-pulmonary pathophysiology as a result of the severe hypoxia, hypercarbia and hypocarbia induced in Protocol 3 (see methods section Chapter 6 & 7). Nevertheless, Bland-Altman analysis of our data indicated that the agreement between $P_{ET}CO_2$ and $PaCO_2$ was within measurement of clinical error, an agreement not due to chance ($p < 0.0001$). (200) The consistently small P_{ET}-aCO_2 in our study contrasts with those of most other studies in which P_{ET}-aCO_2 varies widely between subjects and in the same subjects over time. McDonald (182) studied 1708 sample pairs of $P_{ET}CO_2$ and $PaCO_2$ in 129 children in an intensive care unit; P_{ET}-aCO_2 ranged between 0 to > -30 mmHg and only 74% of samples changed in the same direction. Tobias and Meyer (195) reported a range of P_{ET}-aCO_2 of 5 to -22 mmHg in 100 sample sets in 25 infants and toddlers. Nevertheless, both studies suggested that even the broad P_{ET}-aCO_2 in their studies of -4.7 ±8.2 mmHg and - 6.8 ± 5.1 mmHg respectively were still within a "clinically acceptable" range. Yamanaka and Sue, (180) in a study of 17 ventilated adults in a critical care unit, found that the correlation between $P_{ET}CO_2$ and $PaCO_2$ was too poor for $P_{ET}CO_2$ to be used even as an indicator of direction of changes of $PaCO_2$. Others too have found poor, or no correlations between $P_{ET}CO_2$ and $PaCO_2$ in adults with multi-system disease, (201) trauma, (183) undergoing neurosurgery, (202,203) as well as in dogs with healthy lungs (191) or lungs with oleic acid-induced ARDS. (192) That our findings differ from those in the literature is likely due to the simple expedient of administering previously exhaled gas at the end of each inspiration, thereby reducing mean P_{ET}-aCO_2 within clinical measurement error despite considerable pulmonary and circulatory pathology. End-inspiratory rebreathing has previously been shown to reduce P_{ET}-aCO_2. In a study by Bowie and group, (185) the exhaled gas was diluted with fresh gas during exhalation and once more during inspiration. Nevertheless, the authors showed that the extent of reduction of the P_{ET}-aCO_2 was related to the degree of rebreathing. In the study by Ito, (58) spontaneously breathing subjects rebreathed gas with PCO_2 that matched previously exhaled gas more closely. The result was a reduction in P_{ET}-aCO_2 to that of the difference

in $PaCO_2$ between two successively drawn blood samples. However, it was not clear that this method would remain robust with positive pressure ventilation, which causes increased intra-thoracic pressure, changes in alveolar deadspace (186,197) and affects the distribution of pulmonary blood flow. (198) Furthermore, Bowie et al. (185) studied animals at only one $P_{ET}CO_2$ and one $P_{ET}O_2$.Whether P_{ET}-aCO_2 remain small over a wide range of $P_{ET}O_2$ and $P_{ET}CO_2$ tensions, both of which affect V&Q matching (187,188) was unknown. In our animal model, we found that with positive pressure ventilation, end-inspiratory rebreathing resulted in low P_{ET}-aCO_2 differences over a wide range of combinations of $P_{ET}CO_2$ and $P_{ET}O_2$, despite the potentially confounding presence of widespread severe lung pathology and cardiac shunting. (179)

Analysis of the animal model

Alveolar deadspace. Of the several pathologic conditions that increase the P_{ET}-aCO_2 gradient, increases in alveolar deadspace have the greatest effect. (180) Elevated mean airway pressures increase the proportion of high ventilation to perfusion ratios (V/Q) in non-dependent lung regions, (244,245) increasing alveolar deadspac (192) and thereby increasing P_{ET}-aCO_2. This can be viewed from the perspective of the Bohr physiologic deadspace equation $VD/VT = (PaCO_2 - P_{ET}CO_2) / PaCO_2$, where $P_{ET}CO_2$ is the PCO_2 of mixed exhaled gas. In our experiment where $P_{ET}CO_2$ is nearly equal to $PaCO_2$, the calculated Bohr deadspace approaches 0.

Effect of right-to-left shunt. Blood can bypass the lung and enter the systemic circulation at the level of the heart or through atelectatic lung regions, increasing P_{ET}-aCO_2. (179) However, a massive right-to-left shunt sufficient to reduce SaO_2 by 10% would change $PaCO_2$ by only 2-4 mmHg with no change in minute ventilation, (179) and a small increase in minute ventilation can abolish this increase in $PaCO_2$ without affecting SaO_2.

Why end-inspiratory rebreathing reduces P_{ET}-aCO_2

The concept of rebreathing previously exhaled gas to bring the $P_{ET}CO_2$ towards the $PaCO_2$ is well established. The rebreathing methods of Read (184) and Duffin (204,205) for measuring ventilatory response are based on the premise that rebreathing eliminates the gradient between $P_{ET}CO_2$, $PaCO_2$ and mixed venous PCO_2. Rebreathing has also been used to reduce the P_{ET}-aCO_2 for monitoring purposes (185) and for controlling end-tidal gases. (58) Our study is the first to demonstrate that end-inspiratory rebreathing, first described by Sommer, (206) or its rebreathing equivalent, (207) maintains a P_{ET}-aCO_2 gradient to within the error of measurement in a ventilated neonatal animal model. $PaCO_2$ reflects the flow-averaged perfusion of the various zones of the lung, whereas the PCO_2 of expired gas reflects the proportion of gases from these various zones in exhaled gas, as well as the extent of their equilibration with the blood. As a result, the relation between expired and $PaCO_2$ is too complex to deconvolve. Nevertheless, adding previously exhaled gas to the inspired gas at the end of inspiration (57,127) brings the PCO_2 of high $\dot{V}/\dot{Q}$ alveoli towards that of alveoli that are well equilibrated with arterial blood. This addition also

eliminates the dilution effect of alveolar deadspace on the PCO_2 of expired gas and, to the extent that rebreathing equalizes the PCO_2 in all lung zones, the distribution of perfusion ceases to affect the $PaCO_2$. Thus, rebreathing results in the PCO_2 of exhaled gas being equal to the PCO_2 of alveolar gas, which, by definition, has equilibrated with arterial blood. Advances in ventilator technology provide choices for different ventilation modes inspiratory flow profiles and compensates for compressible gas, but they cannot mitigate the effects of alveolar deadspace. Our data suggest that end-inspiratory rebreathing may be the first ventilation feature to do so. Although our experiments used a complicated breathing circuit in order to control the $P_{ET}CO_2$ and $P_{ET}O_2$ tensions over a considerable range, a simpler approach can be employed to enable rebreathing at end inspiration alone if such control is not required. Figure 22 illustrates one example of a simple principle that would enable rebreathing at the end of inspiration. We successfully tested a model based on this approach; however it was not used for these animal studies as it did not allow control of $P_{ET}CO_2$ and $P_{ET}O_2$.

Study limitations of the animal models

Range of lung pathology in subjects. In this proof of concept study we included all subjects, even those with gross lung pathology. This pathology may differ from that commonly seen in patients in an ICU, who often have a component of obstructive lung disease and inflammation such as acute respiratory distress syndrome (ARDS). Our subject cohort was too small, and the extent of lung disease was insufficiently investigated for us to comment about the robustness of our method beyond the observations in this study. However, statistical analysis did indicate that our results were independent of subject. Nevertheless, the ability of the end-inspiratory rebreathing technique to reduce the P_{ET}-aCO_2 gradient in various lung pathologies will require further investigation. The piglets in our study were ventilated near their ventilator capacity. Increasing peak airway pressures risked pneumothorax, and greater ventilator frequencies risked breath stacking. We note that piglets are bred specifically for rapid muscle growth to reduce their time to market (http://www.thepigsite.com/stockstds/17/growth-rate), which markedly increases their CO_2 production to 2-5 times that of a human of comparable weight, but their ventilatory capacity remains proportional to their body size. Further reducing their ventilatory reserve was the presence of extensive atelectasis. PEEP was not used in this study in order to isolate the effects of our intervention (end-inspiratory rebreathing) and to maintain a "worst case scenario".

Quantifying the extent of rebreathing. Only the presence, rather than the extent, of end-inspiratory rebreathing could be identified in these experiments by observing a rise in the recorded PCO_2 trace at the end of the inspiratory phase. As a result, the extent of end-inspiratory rebreathing likely varied across the protocols. Despite this variation, the measured P_{ET}-aCO_2 gradients remained uniformly small. This finding implies that the threshold for effective end-inspiratory rebreathing is low. Nevertheless, there may be

identifiable thresholds for rebreathing that vary with the underlying lung pathology, and ventilator settings.

Sampling from the trachea vs. from the proximal endotracheal tube. Small tidal volumes, high respiratory frequencies, and high ratios of equipment deadspace to tidal volume contribute to the sampling error with sidestream capnography. Badgewell (177,213) studied this issue in considerable detail and concluded that for children less than 12 kg, accurate end-tidal measurements can only be obtained from the distal endotracheal tube. We placed the gas sampling catheter beside, rather than inside, the endotracheal tube in order to provide the least resistance for the high minute ventilations required to ventilate piglets compared to those required to ventilate humans of the same weight (see above).

Considerations for the sCVR exam

I have performed CVR mapping using a BOLD MRI acquisition during a controlled hypercapnia challenge. The automatic gas blender and rebreathing circuit employed in this study insured that a well-defined, reproducible hypercapnic stimulus was achieved for each patient, independent of the subject's minute ventilation and $P_{ET}CO_2$. Despite the availability of quantitative MR-based measures of cerebrovascular reserve, including the aforementioned advantages over other dynamic functional imaging modalities (see background section), several limitations have to be taken into consideration, however. MR signal loss due to susceptibility effects may cause unreliable BOLD signal in certain brain areas. Given the wide expertise gained at the University of Toronto with sCVR examinations (we have performed over 500 sCVR studies as of September 2011), it became apparent certain brain areas, the frontal lobes and cerebellum, do not produce reliable CVR measurements with the acquisition parameters as set out in section "*MR protocol for sCVR test*". These susceptibility artifacts mainly arise from the frontal aerated sinuses and skull base, respectively. Further advances and improvements in scanning parameters, and MR field-strength may generate sufficient signal-to-noise for reliable CVR measures over the entire brain.

The greatest concern with BOLD related CVR measurements has been that BOLD contrast depends on CBF, and to an unknown extent on other factors, such as $CMRO_2$, CBV, PaO_2, and hematocrit. Recent validation studies employing the same technique (88,89) provided empirical data showing good between-session reproducibility, thereby indicating that these factors are not major issues. Furthermore others have demonstrated the accuracy of the sCVR examination versus the 'gold standard' acetazolamide challenged SPECT (111) and ASL. (90)

The latter, demonstrated a good correlation. Ultimately, ASL may be used in combination with end-inspiratory rebreathing to provide a standardized exam directly measuring changes in CBF. Yet, the current ASL sequences cannot match the signal-to-noise ratio and spatial resolution as for BOLD acquisitions.

Functional neurovascular imaging may be performed with modalities such as ^{15}O-positron emission tomography (^{15}O –PET), single-photon emission computed tomography (SPECT), or perfusion CT/MRI measuring changes to acetazolamide challenge. These tests have been used to provide information about the cerebral hemodynamics that may address indications for surgical revascularization and predict prognosis. (114,235) However, they are invasive and carry a degree of complexity that precludes their use in routine clinical assessment. In contrast, BOLD CVR MRI is non-invasive and the BOLD sequence is available for every MR system. Standardization of the vasodilatory provocation allows for comparability of MR signal values from follow-up examinations whereas the high spatial resolution of the MR data indicates more accurately the extent of the brain tissue at risk. Lastly, this method has also been proven safe and of diagnostic value in pediatric patients with steno-occlusive disease. (94)

8.1 Future research avenues

For chronic cerebrovascular steno-occlusive disease, two very interesting questions emerge from this thesis, that remain unanswered

1) Is the observed cortical thinning indeed related to neuronal injury that can be reversed after revascularization? And,

2) If these processes are indeed unfolding on neuronal level, how does this influence neurocognitive performance?

These questions may be addressed by studying patients with moyamoya vasculopathy, usually representing the severe end of the spectrum for cerebrovascular disease. Imaging modalities other than MRI may assist in targeting the functioning of neurons. Iodine-IMZ-SPECT and ^{11}C-Flumazenil PET are sensitive techniques to assess the integrity of the neurons. Targeting the benzodiazepine receptors on the neurons surface, information about the receptor density, as a surrogate for neuronal density, is provided. Magnetic encephalography (MEG) or emerging Electro-encephalography EEG) techniques (246) may assist to further investigate neuronal activity in brain areas with severely impaired cerebrovascular reserve.

Currently, one of the most impending goals in neurovascular research is gathering empirical evidence for the relationship between chronic hypoperfusion and neurocognitive performance, i.e. the vascular component in dementia. Although more evidence is mounting, as nicely set out in a comprehensive review by drs. Marshall and Lazar, (247) more definitive answers have to be found.

Building on findings emerging from this thesis, a neurocognitive testing battery may address decline in cognitive performance and possible improvement after bypass surgery. Currently, there is one exciting publication that reports about neurocognitive decline before and improvement after bypass revascularization in patients with carotid artery disease. The caveats for this study were the small number of subjects (n=20) and the non-standardized testing of CVR with TCD. Improved results from such projects may be achieved with BOLD-MRI sCVR, where CVR can be quantified and mapped so that outcomes can be specifically matched with brain areas that exhibit (severely) impaired cerebrovascular reserve, as spatially identified with the sCVR exam. Improving the MR acquisition may result in more robust spatial CVR maps, especially in the frontal pole an area of great interest from a neuropsychological perspective.

Altered hemodynamics versus clinical presentation for brain arteriovenous malformations
Future investigations to learn more about the relationship of seizure activity, impaired peri-nidal cerebrovascular reserve, and venous outflow restriction may focus on ADC measurements in the peri-nidal tissue of seizure-prone bAVMs to test the "neuronal dilution" hypothesis (see previous paragraph about bAVM). Also, pre- and post embolization studies should be instigated to investigate whether seizure-prone bAVMs will demonstrate normalized cerebrovascular reserve after successful embolization and whether this may correlate with decrease or even absence of epileptic seizure activity.

End-inspiratory rebreathing method for mechanical ventilation; going beyond the animal model
Application of this technique for clinical investigations will be the next avenue to explore. Studies assessing the cerebrovascular reserve, either with MRI or TCD, may prove useful in determining cerebrovascular autoregulation in aneurysmal subarachnoid hemorrhage patients and patients with (severe) traumatic brain injury, Also, noninvasive and continuous evaluation of $PaCO_2$ may replace invasive methods for acquiring blood gasses, this may have a major utility in pediatric patients where the blood volumes are small. The interchangeability of $PaCO_2$ and $PETCO_2$ measures in these ill, ventilated animals is a unique finding. If the end-inspiratory rebreathing technique works as well in mechanically ventilated humans it would be of great clinical value.

The $PET\text{-}aCO_2$ gradients we found in the ventilated pig experiments are in marked contrast to those from studies in humans. Large $PET\text{-}aCO_2$ differences are found in healthy ventilated patients undergoing surgery, (193) and in patients on ventilator support in intensive care units—both children (209,210) and adults. (180-183) The magnitudes of $PET\text{-}aCO_2$ gradients are affected by the type and severity of primary pulmonary disease, the presence of other organ failure, (180,183,209,210) or a history of trauma. (180) The gradient magnitude is also related to alveolar deadspace, (183) hemoglobin concentration and saturation, (195) level of positive end-expiratory pressure (PEEP), (180) respiratory

frequency, fractional inspiratory concentration of O_2, pH, blood pressure, level of left-to-right shunt, and type of surgery, both singly and in combination. (180)

Implementation of end-inspiratory rebreathing in humans:
In our study we used sequential gas delivery circuit to target various combinations of $P_{ET}CO_2$ and $P_{ET}O_2$, as well as to implement rebreathing at the end of each breath. Reducing the P_{ET}-aCO_2 in human studies would require only the end-inspiratory rebreathing. The device shown in Figure 21 is a simple passive shuttle valve that when interposed in an ICU ventilator circuit or a circle anesthetic circuit, can be adjusted to give a fixed amount of end-inspiratory rebreathing with each breath. This amount can theoretically be titrated to provide an optimum reduction in the P_{ET}-aCO_2 gradient, while still controlling $P_{ET}CO_2$ by adjusting ventilator tidal volume and frequency. Indeed, careful ventilator adjustments may allow end-inspiratory rebreathing to be employed even in patients with increased intra-cranial pressures. We also anticipate that it may still be possible to implement the end-inspiratory rebreathing technique in patients ventilated with low tidal volume strategies, albeit at the expense of increases in $PaCO_2$.

8.2 Summary

In this thesis I have applied a quantitative MR-based test to assess cerebrovascular reserve, with a view to investigate the consequences of impaired cerebrovascular reserve in patients with chronic cerebrovascular disease. Furthermore, I successfully translated the end-inspiratory rebreathing technique towards clinical studies with severely ill patients that require mechanical ventilation.

The main findings resulting from this thesis are that seizure-prone brain arteriovenous malformations exhibit impaired peri-nidal cerebrovascular reserve with concomitant venous congestion, and that non-ischemic steno-occlusive patients with severely impaired cerebrovascular reserve associated with steal physiology exhibit thinning of the cortex that can be reversed following successful surgical revascularization. The consequences of possible neuronal involvement in these patho-physiological processes, as well as neurocognitive performance, should be considered for future in-depth investigation.

Addendum

Chapter I

Impaired cerebrovascular reactivity with steal phenomenon is associated with increased diffusion in white matter of patients with moyamoya disease

Abstract

Introduction

Reduced cerebrovascular reactivity (CVR) with steal or is an independent predictor for stroke, and may indicate tissue exposed to episodic low-grade ischemia. The Apparent Diffusion Coefficient (ADC) calculated using diffusion-weighted MRI is effective in characterizing focal brain ischemia and subtle structural changes in normal-appearing white matter (WM). We hypothesized that regions of steal phenomenon are associated with increased ADC in normal-appearing WM of patients with moyamoya disease.

Methods

Twenty-two patients with unilateral CVR impairment secondary to moyamoya disease and 12 healthy controls underwent diffusion-weighted MRI and functional MRI mapping of the cerebrovascular response to hypercapnia. Parametric maps of ADC and CVR were calculated, co-registered, and segmented using automated image processing methods. ADC of normal-appearing WM was compared between hemispheres, and between WM with negative CVR (i.e., steal phenomenon) and WM with positive CVR.

Results

In patients, ADC of normal-appearing WM was elevated in the hemisphere ipsilateral to the CVR impairment compared to the contralateral hemisphere ($P < 0.005$), and in WM with negative CVR compared to WM with positive CVR ($P < 0.001$). WM in regions of steal phenomenon within the affected hemisphere had higher ADC than homologous contralateral WM ($P < 0.005$). In controls, negative CVR in WM was not associated with elevated ADC.

Conclusions

Regions of steal phenomenon are spatially correlated with elevated ADC in normal-appearing WM of patients with moyamoya disease. This structural abnormality may reflect low-grade ischemic injury following exhaustion of the cerebrovascular reserve capacity.

Introduction

Cerebrovascular reactivity (CVR) can be defined as the increase in cerebral blood flow (CBF) in response to a vasodilatory stimulus. Negative CVR, also known as steal phenomenon, occurs when a stimulus results in the redistribution of blood flow from regions of exhausted cerebrovascular reserve to areas with preserved vasodilatory capacity. Steal phenomenon is a risk factor for future ischemic stroke. (66,248) In patients with moyamoya disease, a progressive narrowing of the supraclinoid internal carotid artery (ICA) and its proximal branches, negative or severely reduced CVR has been used to identify patients who may benefit from surgical revascularization. However, the impact of steal phenomenon on normal-appearing brain tissue (i.e., in the absence of overt infarction) has not been previously investigated.

Diffusion-weighted MRI is useful in characterizing focal brain ischemia in the acute and chronic stages, diffuse and focal leukoaraiotic changes, and normal brain structures. (149,249,250) In chronic hypoperfusion, ischemic injury to white matter (WM) is associated with axonal destruction and glial proliferation, (251) resulting in the hyperintense lesions on T2-weighted MRI referred to as leukoaraiosis. These lesions are associated with an increase in the apparent diffusion coefficient (ADC), likely reflecting increased water diffusivity due to axonal loss. (249) ADC changes are not confined to ischemic lesions however, and may occur in WM that appears normal on conventional MRI. Increased ADC in otherwise normal-appearing WM occurs for example in patients with atherosclerotic ICA stenosis, (252) previous stroke, (149,222) to some extent in normal aging. (253)

In the present study, we sought to determine whether regions of steal phenomenon are associated with ADC changes in normal-appearing WM of patients with moyamoya disease. We assessed CVR by measuring changes in the BOLD MRI response to hypercapnia. (88,147,254) This semi-quantitative approach to CVR mapping is reproducible, provides high spatial resolution, and has been validated against alternative methods of CVR assessment. (90,111,147) We hypothesized that the ADC of WM in regions of steal phenomenon would be elevated compared to WM with normal reactivity. This hypothesis was tested in a group of patients with unilateral CVR impairment, allowing comparison between regions of steal phenomenon in the affected hemisphere and homologous WM in the contralateral hemisphere.

Methods

Subjects

Subjects were participants in an ongoing study of CVR in cerebrovascular disease, for which institutional ethics review board approval and informed patient consent had been obtained. Images from 252 patients who underwent CVR studies between June 2005 and December 2009 were screened by an experienced neuroradiologist using the following inclusion criteria: (1) angiographically confirmed diagnosis of moyamoya disease or

moyamoya syndrome; (2) a CVR map showing impaired reactivity within one hemisphere and normal reactivity within the contralateral hemisphere (a minimum 30% mean CVR reduction in the affected hemisphere compared to the contralateral hemisphere was required for inclusion), and; (3) no evidence of cerebral infarction or intracranial hemorrhage on anatomic MR images (T1-weighted images, T2-weighted Fluid-Attenuated Inversion Recovery (FLAIR) images, and diffusion-weighted images). The presence of focal white matter hyperintensities (WMHs) on FLAIR images was permitted. Patients with obvious motion artifacts on any image series were excluded. Twenty-two patients (age 30 ± 12 years) met the inclusion criteria and were considered in subsequent analysis. Twelve healthy control subjects (age 31 ± 7 years) with no history of any neurologic or systemic disease underwent an identical imaging protocol.

MRI Acquisition

Imaging was performed using a Signa HDx 3.0-T scanner with an 8-channel phased array head coil (GE Healthcare, Milwaukee, WI). T1-weighted anatomical images were acquired using a 3-dimensional inversion-recovery prepared spoiled gradient-echo sequence (field of view (FOV) = 22×22 cm; matrix = 256×256; slice thickness = 1 mm; flip angle = 12°; TR/TI/TE = 8000/450/3 ms). BOLD images were acquired using a $T2^*$-weighted echo-planar imaging (EPI) gradient-echo sequence (FOV = 24×24 cm; matrix = 64×64 cm; slice thickness = 5 mm; flip angle = 85°; TR/TE = 2000/30 ms; number of frames = 254). Diffusion-weighted images were acquired using an EPI spin-echo sequence with diffusion gradients of $b = 0$, and $b = 1000$ s/mm^2 along each of the 3 principal axes (FOV = 24×24 cm; matrix = 256×256; slice thickness = 5 mm; flip angle = 90°; TR/TE = 6000/80 ms). Conventional T2-weighted FLAIR images were also obtained.

Vasodilatory Stimulus

An automated gas blender adjusted the composition and flow to a sequential gas delivery mask and breathing circuit according to the method described by Slessarev et al. (57) (RespirAct; Thornhill Research, Toronto, Canada). This apparatus enables prospective control of the patient's end-tidal PCO_2 ($PETCO_2$) and PO_2 ($PETO_2$) independently of each other and of minute ventilation. During the BOLD MRI acquisition, a vasodilatory stimulus was provided by alternating between iso-oxic states of normocapnia and hypercapnia. $PETCO_2$ values were selected as the maxima of the continuously sampled PCO_2 waveform during exhalation.

Image Reconstruction

MRI and $PETCO_2$ data were imported to AFNI (95) for analysis. BOLD images were slice time corrected and volume registered. BOLD images and diffusion-weighted images were then aligned to the anatomical dataset using the Local Pearson Correlation cost functional. (96)

CVR maps were constructed as follows. To compensate for temporal error resulting from the pulmonary to cerebral circulation time, the $P_{ET}CO_2$ waveform was time-shifted to the point of maximum correlation with the whole brain average BOLD signal. To minimize the effect of task correlated motion (i.e., head motion correlated to the $P_{ET}CO_2$ (waveform), the BOLD time series at each voxel was orthogonalized to the 6 motion parameters estimated by the volume registration. A voxel-wise linear least-squares fit of the BOLD time series to the $P_{ET}CO_2$ waveform was then performed. CVR was defined as the percent BOLD signal change per unit change in $P_{ET}CO_2$.

ADC maps were constructed by computing the ADC along 3 orthogonal directions using the equation:

$$\mathrm{ADC}_i = -\ln[S_i^{b=1000} / S^{b=0}] / \Delta b, \qquad [1]$$

where ADC_i is the ADC along direction i, $S_i^{b=1000}$ is the signal intensity in the diffusion-weighted image with diffusion gradient along direction i, $S^{b=0}$ is the signal intensity in the image without diffusion gradients, and Δb = 1000 mm^2/s. The average ADC (ADC_{av}) was calculated as the mean of the ADC values along the 3 principal axes.
Anatomical images as well as co-registered CVR and ADC maps were transformed to Tailarach space and resampled to a 1 mm isotropic grid to facilitate subsequent analysis.

Regions-of-Interest
Foci of WMH were identified on T2-weighted FLAIR images by a neuroradiologist and manually traced onto the T2-weighted (b = 0) diffusion images.

Next, a tissue probability map for WM was generated from the anatomical dataset (SPM5; Wellcome Department of Imaging Neuroscience, University College, London, UK) and thresholded at a probability of 0.9 to produce an initial WM ROI. The initial ROI was then masked to exclude regions of WMH, as well as any voxels with ADC_{av} greater than 1.5×10^{-3} mm^2/s (threshold selected between the ADC of cerebrospinal fluid (CSF) and normal brain tissue). (249) To minimize contamination with grey matter (GM) or CSF, the WM ROI underwent binary erosion using a spherical structuring element of 4 mm diameter (Matlab, Image Processing Toolbox; Mathworks, Natick, MA). The result was a conservative WM ROI that appeared well separated from GM and CSF when overlaid on the co-registered ADC map.

The WM ROI was divided into left and right hemispheres, and a categorical CVR mask was used to subdivide the WM within each hemisphere into regions of positive and negative CVR.

Lastly, we defined a set of homologous WM ROIs to allow interhemispheric ADC comparison while controlling for within-hemisphere ADC variation.[9] For WM with negative CVR in the affected hemisphere, ahomologous contralateral ROI was defined by reflecting the categorical CVR mask about the mid-sagittal plane, and then combining the negative CVR region with the WM mask of the contralateral hemisphere using a logical 'and' operation. For WM with positive CVR in the affected hemisphere, a similar procedure was used to generate a homologous contralateral ROI.

Statistical Analysis

The following comparisons were performed using a Student's *t*-test for dependent or independent samples as appropriate. ADC_{av} values in patients were compared between: affected hemisphere versus unaffected hemisphere (all WM); negative CVR versus positive CVR (all WM); negative CVR versus positive CVR (affected hemisphere only); negative CVR vs positive CVR (unaffected hemisphere only); negative CVR (affected hemisphere) versus homologous contralateral WM, and; positive CVR (affected hemisphere) versus homologous contralateral WM. ADC_{av} was also compared between positive CVR and negative CVR in controls (all WM). For patients with WMHs detected on FLAIR images, mean CVR was compared between WMHs and the mean CVR for all WM. Finally, mean WM CVR in the patient's affected hemisphere was compared to that of the contralateral hemisphere, and to that of healthy controls. Results were considered significant if the per comparison *P*-value was less than 0.05 / (10 comparisons) = 0.005, i.e., Bonferroni correction for multiple comparisons.

Results

All CVR values are given in units of percent BOLD signal change per mmHg change in $P_{ET}CO_2$ (mean ± standard deviation). Mean WM CVR in patients was 0.027 ± 0.032 in the affected hemisphere, compared to 0.064 ± 0.031 in the unaffected hemisphere ($P< 10^{-6}$ between hemispheres) and 0.062 ± 0.038 in controls ($P< 0.005$ vs patient's affected hemisphere).

ADC_{av} was higher in the affected hemisphere than the unaffected hemisphere ($P< 0.005$), and higher in all WM with negative CVR than all WM with positive CVR ($P< 0.001$). Within the affected hemisphere, ADC_{av} was higher in WM with negative CVR compared to WM with positive CVR ($P< 0.001$). Within the unaffected hemisphere, there was no significant difference in ADC_{av} between WM with negative and positive CVR, although there was a trend toward increased ADC_{av} in WM with negative CVR. ADC_{av} was increased in WM with negative CVR in the affected hemisphere compared to homologous contralateral WM ($P< 0.005$). ADC_{av} in WM with positive CVR in the affected hemisphere was not significantly different than ADC_{av} in homologous contralateral WM. In controls, ADC_{av} was not significantly different between WM with positive and negative CVR.

Ten of 22 patients had small foci of WMH on FLAIR images, with more foci in the affected hemisphere (median 3, range 0 to 9) than the unaffected hemisphere (median 1, range 0 to 6). For these patients, mean CVR within WMHs was lower than the average for all WM (−0.008 ± 0.041 versus 0.036 ± 0.028, $P < 0.005$).

Discussion

Our results demonstrate that steal phenomenon is associated with increased ADC in normal-appearing WM of patients with moyamoya disease. While diffusion-weighted imaging has been used to monitor progression of focal ischemic lesions in patients with moyamoya disease, (255) increased ADC within the normal-appearing WM has not been previously reported. Soinne et al. (219) studied patients with unilateral atherosclerotic ICA stenosis, and reported increased ADC of ipsilateral WM compared to contralateral WM. However, moyamoya disease differs from atherosclerosis in the development of numerous parenchymal, leptomeningeal, and transdural collateral vessels supplying the hemodynamically compromised brain parenchyma. (24) Thus, the results reported by Soinne et al. (219) cannot be generalized to this population. Further, 14 of 45 patients in the study by Soinne et al. (252) had lacunar infarcts, while we excluded patients with cortical or lacunar infarction to minimize the reported influence of such pathology on the ADC of normal-appearing WM. (149,222) Even in the absence of focal infarction, we found an ADC increase in ipsilateral WM compared to contralateral WM. The use of high-resolution CVR mapping method allowed us to further localize the increased ADC to regions of negative CVR.

Elevated ADC is consistent with structural damage to tissue, resulting in increased water diffusivity. In experimental models of chronic hypoperfusion, WM appears particularly vulnerable, undergoing rarefaction with demyelination, axonal loss, and gliosis. Our results suggest that subtle ischemic changes may be present in regions of steal phenomenon in the normal-appearing WM of patients with moyamoya disease, leading to increased ADC in these areas. We also found increased ADC within foci of WMH on FLAIR images, in agreement with previous studies. (149,222,250) Mean CVR within these WMHs was negative and significantly lower than the mean CVR of normal-appearing WM, supporting the hypothesis that CVR impairment plays a role in the pathogenesis of these lesions. (147)

Steal phenomenon was also observed both in controls and in the hemisphere of normal reactivity in patients, suggesting that CVR impairment cannot be the sole determinant of ADC elevation. Negative CVR in the WM of healthy young adults has been previously documented in the centrum semiovale, corpus callosum and periventricular WM. (147) This raises the question: how might steal phenomenon be a normal physiologic response in some brain areas, and yet lead to ischemic injury in others? One explanation for our findings would be a spatial variation in vulnerability to CVR impairment within the WM. The aforementioned areas that are chronically exposed to physiologic steal may be better able to tolerate negative CVR, while WM that normally exhibits robust positive CVR (e.g.,

subcortical WM) may be more adversely affected when exposed to pathological negative reactivity, and more likely to undergo ischemic changes with concomitant ADC elevation. Although negative CVR in controls was not associated with increased ADC, it may not be an entirely benign phenomenon. The distribution of steal phenomenon in healthy young adults is spatially concordant with the development age-related WM disease, (147) which is in turn associated with ADC elevation (250) and cognitive decline. (252)

Regional variation in normal WM ADC has also been reported, (255) although not all studies found such variation to be statistically significant. (249,253) Nonetheless, it is possible that increased ADC in regions of steal phenomenon could reflect a tendency for steal to occur in areas that naturally have higher ADC. We took two steps to rule out this possibility. First, we compared the ADC of WM with negative CVR in the affected hemisphere to the ADC of homologous contralateral WM. ADC was significantly elevated in the ipsilateral WM with negative CVR ($P< 0.005$). Second, we compared ADC between regions of negative CVR and positive CVR in WM of healthy controls. This comparison was powered to detect an ADC difference of approximately 1.7×10^{-5} mm^2/s (using Eq. 2 in Ref. 256) with $\alpha = 0.05$, $\beta = 0.2$, $n = 12$ and σ^2 estimated from the control subjects). However, ADC of WM in controls was virtually identical when compared between regions of positive and negative CVR.

We constructed CVR maps using the BOLD MRI response to hypercapnia, and must consider the limitations of this technique. First, BOLD signal changes do not directly reflect changes in CBF, but rather a complex interaction of CBF, cerebral blood volume, arterial PO_2, hematocrit, and cerebral metabolic rate of oxygen consumption. (257) However, empirical evidence suggests that the BOLD response to hypercapnia is dominated by CBF effects in healthy subjects (111,147) and in patients with steno-occlusive cerebrovascular disease. (90) Second, the EPI readouts typically used for BOLD MRI are associated with signal loss and geometric distortion near the interfaces of aerated sinuses and adjacent tissue. These artifacts had little effect on our measurements because we excluded cortical GM, and eroded the underlying WM by approximately one full BOLD voxel, leaving a WM ROI sufficiently distant from regions of signal loss and distortion. However, these artifacts may impede the future comparison of ADC and CVR within the cortex.

Our study is also limited by the relatively small number of patients. Unilateral CVR impairment was found to be rare among patients with moyamoya disease, particularly in the complete absence of infarction. Despite the small sample size, the ADC differences were highly significant, and similar in magnitude to ADC increases in the normal-appearing WM of patients with previous lacunar strokes. (149,222) In that context, ADC has been correlated with cognitive dysfunction, suggesting that ADC elevation may in part reflect a neurodegenerative process induced by chronic hypoperfusion (see Ref. 258) for a review of the relationship between vascular

insufficiency and neurodegeneration). The discovery that ADC increases are localized to regions of negative CVR may prove useful for future investigations of cognitive function in patients with moyamoya disease. For example, CVR maps could be used to automatically identify WM regions where increased ADC would be expected due to negative CVR. ADC of these ROIs may correlate more closely with cognitive dysfunction than ADC of ROIs chosen without knowledge of the spatial distribution of CVR impairment. (194,222)

In summary, we compared parametric maps of CVR and ADC in patients with unilateral CVR impairment secondary to moyamoya disease. ADC of normal-appearing WM was increased in the hemisphere ipsilateral to the CVR deficit, and in WM with negative CVR compared to WM with positive CVR. ADC changes were present despite the complete absence of cortical or lacunar infarction. These findings suggest that in addition to its prognostic implications for stroke, steal phenomenon is associated with subtle abnormalities in WM structure, consistent with low-grade ischemic injury. Further study is recommended to extend this analysis to patients with bilateral CVR impairment, and to determine the relationship between WM ADC and cognitive function before and after surgical revascularization.

Chapter II

Mapping white matter diffusion and cerebrovascular reactivity in carotid occlusive disease

Abstract

Introduction

To characterize the relationship between cerebrovascular reactivity (CVR) and white matter (WM) diffusion in patients with internal carotid artery (ICA) occlusive disease.

Methods

In this exploratory observational study, 41 patients with severe stenosis or occlusion of the extracranial ICA and 12 healthy controls underwent CVR mapping using the functional MRI response to hypercapnia. Conventional anatomic and diffusion-weighted MRI sequences were used to calculate maps of the apparent diffusion coefficient (ADC), and to exclude areas of previous ischemic injury. In all subjects, ADC was compared between WM with positive and negative CVR. In 27 patients with unilateral ICA involvement, ADC and CVR were compared between ipsilateral and contralateral WM while co-varying for relevant clinical risk factors.

Results

In patients with bilateral disease, and in the ipsilateral hemisphere of patients with unilateral disease, negative CVR was associated with increased WM ADC ($P< 0.01$ and $P< 0.005$ respectively). In patients with unilateral disease, the ipsilateral CVR deficit was correlated to the degree of hemispheric WM ADC elevation ($P< 0.005$). ADC elevation remained significant after correction for potential confounding risk factors.

Conclusions

CVR impairment is associated with ADC elevation in normal-appearing WM of patients with severe stenosis or occlusion of the extracranial ICA. This finding is consistent with the presence of early, low-grade ischemic injury.

Introduction

Atherosclerotic disease of the internal carotid artery (ICA) is common in elderly patients and in the presence of vascular risk factors. (259) When luminal narrowing becomes hemodynamically significant, dependent arterioles undergo compensatory vasodilation to maintain cerebral perfusion pressure. Cerebrovascular reactivity (CVR) is a convenient marker of hemodynamic impairment, and can be defined as the increase in cerebral blood flow (CBF) following a vasodilatory stimulus. Hemodynamically compromised brain tissue may exhibit reduced CVR, or a "steal phenomenon" in which a vasodilatory stimulus results in redistribution of blood flow to adjacent vascular beds with preserved vasodilatory capacity (i.e., negative CVR). Reduced CVR (260,261) and steal phenomenon (66,248) are predictors of stroke in patients with carotid occlusive disease. However, little is known regarding the direct effect of impaired CVR on otherwise normal-appearing brain tissue.

The apparent diffusion coefficient (ADC) calculated using diffusion-weighted MRI measures the degree to which tissue water is free to diffuse. ADC is elevated in both chronic stroke and leukoaraiosis. (250,262) Further, patients with a variety of cerebrovascular pathologies have ADC elevation in otherwise normal-appearing WM, (136,219,222,250) which may represent low-grade ischemic injury.

Here, we sought to characterize the relationship between CVR impairment and ADC elevation in normal-appearing WM of patients with carotid occlusive disease. CVR was assessed using the blood oxygenation level dependent (BOLD) MRI response to a standardized hypercapnic stimulus. (57,84) We hypothesized that regions of severely impaired CVR would exhibit increased ADC compared to regions of normal CVR, and that patients with greater hemispheric CVR deficits would have greater increases in WM ADC.

Methods

Standard Protocol Approvals, Registrations, and Patient Consents

Subjects were participants in an ongoing prospective observational study of CVR in cerebrovascular disease, for which informed consent and institutional research ethics board (REB) approval had been obtained.

Subjects

Patients with carotid occlusive disease were recruited through the Neurology and Neurosurgery services at the Toronto Western Hospital. Imaging and clinical data for 77 consecutive patients with extracranial carotid disease were screened using the following inclusion criteria:

1. Severe stenosis (>70%) or occlusion of the extracranial segment of one or both ICAs;
2. Absence of acute or subacute infarction on diffusion-weighted MRI;
3. Successful acquisition of the complete MRI protocol described below;

4. Head motion < 3 mm translation and < 3° rotation during BOLD MRI acquisition;
5. Availability of complete clinical data regarding major stroke risk factors.

Severity of stenosis was assessed using either: catheter angiography (6 of 41 patients) using NASCET criteria, MR angiography (21 of 41 patients) or CT angiography (8 of 41 patients) using NASCET-like measurements, or duplex ultrasound (6 of 41 patients) using standard Doppler velocimetry criteria. Patients were classified as 'bilateral' in the presence of severe stenosis or occlusion of both carotid arteries, and 'unilateral' in the absence of hemodynamically significant contralateral stenosis (i.e., contralateral stenosis < 70%). Forty-one patients met the inclusion criteria and were considered in subsequent analysis. Twelve healthy adult controls with no history of neurological disease underwent an identical imaging protocol as part of a previous study of WM CVR, (136; see also addendum chapter I) and were included in the analysis below.

Image Acquisition
All imaging was performed on a Signa HDx 3.0-T MRI system using an 8-channel phased array receiver coil. BOLD MRI data were acquired using a 2D echo-planar imaging (EPI) gradient-echo sequence (TR/TE = 2000/30 ms, matrix = 64×64, field of view (FOV) = 24×24 cm, slice thickness = 5 mm, slice gap = 2 mm, flip angle (FA) = 85°, number of frames = 254). High-resolution anatomic images were acquired using a 3D inversion-recovery prepared spoiled gradient-echo imaging sequence (TR/TI/TE = 8000/450/3 ms, matrix = 256×256, FOV = 22×22cm, slice thickness = 1 mm, FA = 12°). Diffusion-weighted images were acquired using a 2D EPI fast spin-echo sequence with diffusion gradients of b = 0, and b = 1000 s/mm^2 applied along 3 orthogonal directions (TR/TE = 6000/80 ms, matrix = 256×256, FOV = 24×24 cm, slice thickness = 5 mm, FA = 90°). Conventional T2-weighted FLAIR images and T2*-weighted gradient-echo images were also obtained.

End-tidal Gas Manipulation
During the BOLD MRI acquisition, end-tidal PO_2 ($P_{ET}O_2$) andPCO_2 ($P_{ET}CO_2$) were prospectively targeted using a custom built sequential gas delivery circuit and automated gas sequencer (RespirAct; Thornhill Research Inc, Toronto, Canada). This system enables rapid and precise changes in the end-tidal gas concentrations of spontaneously breathing subjects, and has been described in detail elsewhere. (57) A controlled hypercapnia challenge was provided by alternating between iso-oxic states of normocapnia and hypercapnia. $P_{ET}CO_2$ and $P_{ET}O_2$ values were automatically selected as the maximum and minimum values of the PCO_2 and PO_2 waveforms, respectively, during exhalation.

Image Reconstruction
All images and $P_{ET}CO_2$ data were imported to AFNI. (95) BOLD time series data were volume registered, and the 6 associated rigid body motion parameters were used to exclude

subjects with head motion greater than 3 mm translation or 3° rotation. The local Pearson correlation method (96) was used to co-register BOLD images, diffusion-weighted images, and FLAIR images to the high-resolution anatomical dataset. All images were then converted to Talairach space (263) and resampled to a 1 mm isotropic grid to facilitate further analysis.

CVR maps were reconstructed from the BOLD MRI data as follows. To compensate for temporal uncertainty associated with the end-tidal gas sampling, the $P_{ET}CO_2$ waveform was time shifted to the point of maximal correlation with the whole-brain average BOLD signal. To minimize the effect of sub-voxel head movements on the BOLD signal, the BOLD data were orthogonalized to the previously estimated rigid body motion parameters. Finally, the BOLD signal at each voxel was fitted to the $P_{ET}CO_2$ waveform using a linear least-square regression, and CVR was defined as the percent BOLD signal change per unit change in $P_{ET}CO_2$.
ADC maps were calculated by applying the following equation (264) at each voxel:

$$\mathrm{ADC}_{\mathrm{av}} = -\ln[S^{b=1000} / S^{b=0}] / \Delta b, \qquad [1]$$

where $\mathrm{ADC}_{\mathrm{av}}$ is the average of the ADC values along the scanner's 3 principal axes, $S^{b=1000}$ is the geometric mean of the signal intensity in the 3 images with applied diffusion gradients, $S^{b=0}$ is the signal intensity in the image without diffusion sensitizing gradients, and Δb = 1000 s/mm^2.

Tissue Segmentation
Clinical images were assessed by a neuroradiologist to determine the presence and stage of ischemic injury. Patients demonstrating acute or subacute infarction were excluded. Regions-of-interest (ROIs) for chronic infarction and leukoaraiosis were manually traced on FLAIR images by a single rater blinded to all clinical data including presence and laterality of ICA stenosis or occlusion. These lesion ROIs were then transferred to the coregistered ADC map.

An ROI consisting purely of normal-appearing WM was then generated as follows. First, WM segmentation was performed (SPM 8; Wellcome Department of Imaging Neuroscience, University College, London, UK) using the previously defined areas of ischemic injury as a masking image (i.e., these areas were excluded from the segmentation). The resulting WM probability map was thresholded at a level of 0.9 to produce an initial WM ROI. Next, all voxels with ADC greater than 1.2×10^{-3} mm^2/s were automatically removed from the initial WM ROI (threshold chosen above the ADC of normal WM (249) but below the ADC of cerebrospinal fluid (CSF) (249) and chronic infarction (250,262)). Finally, the WM ROI was subjected to a morphological erosion using a spherical structuring element of 4 mm diameter (Matlab, Image Processing Toolbox;

Mathworks, Natick, Mass). The result was a conservative WM ROI that appeared well separated from GM, CSF, and ischemic pathology.

The WM ROI was then subdivided into regions of positive and negative CVR based on the values of the co-registered CVR map, and into left and right hemispheres on the basis of the Talairach coordinate system. Finally, image data below the level of the mid-thalamus was excluded from the analysis to avoid regions of signal loss and geometric distortion associated with the EPI gradient-echo acquisition.

Statistical Analysis

In all subjects, ADC was compared between WM with positive CVR and WM with negative CVR using dependent samples Student *t*-tests. In controls and patients with bilateral disease, normal-appearing WM in both hemispheres was included in a single comparison. In patients with unilateral disease, a separate comparison was performed for each of the ipsilateral and contralateral hemispheres.

In patients with unilateral disease, we investigated the relationship between inter-hemispheric changes in ADC and CVR. We defined the ipsilateral CVR deficit as $\Delta CVR = CVR_{ipsilateral} - CVR_{contralateral}$, and the ipsilateral ADC increase as $\Delta ADC = ADC_{ipsilateral} - ADC_{contralateral}$. Univariate tests (linear regression for continuous variables and unpaired *t*-tests for binary variables) were used to identify significant relationships between clinical risk factors and imaging findings and ADC increase (ΔADC). A multi-variate linear regression of ΔADC on ΔCVR was then performed, including all risk factors that yielded $P < 0.10$ in univariate analyses as covariates in the regression model.

According to a Bonferroni correction for multiple comparisons, the threshold for statistical significance was set at 0.05 / (5 comparisons) = 0.01.

Results

Throughout this section, ADC values are reported in units of $mm^2/s \times 10^{-3}$ and CVR values are reported in units of % BOLD signal change per mmHg increase in $P_{ET}CO_2$ (mean ± sd). Normal-appearing WM CVR values were 0.045 ± 0.036 for controls, 0.045 ± 0.040 for contralateral WM in patients with unilateral disease, 0.023 ± 0.042 for ipsilateral WM in patients with unilateral disease, and 0.018 ± 0.025 for patients with bilateral disease. In control subjects, small regions of negative CVR were consistently observed in the corpus callosum, centrum semiovale, and periventricular WM, but did not typically involve subcortical WM, cerebral cortex, or deep GM. In patients, negative CVR was observed in a wide distribution of WM and GM regions within affected cerebral hemispheres, although not all patients exhibited visibly obvious CVR impairment relative to controls.

In patients with bilateral disease and in the ipsilateral hemisphere of patients with unilateral disease, ADC was increased in WM with negative CVR compared to WM with positive CVR ($P < 0.01$ and $P < 0.005$ respectively). In healthy controls and in the contralateral

hemisphere of patients with unilateral disease, there was no significant difference in ADC between WM with positive CVR and WM with negative CVR.

Greater magnitude of CVR deficit was associated with larger ADC increase ($P< 0.005$). Of the risk factors, male sex, age, ICA occlusion and previous infarct were significantly associated with ΔADC. The relationship between CVR deficit and ADC increase remained statistically significant after inclusion of these variables as covariates in the multi-variate linear regression model.

Discussion

We have shown that negative CVR is spatially associated with increased ADC in WM of patients with severe stenosis or occlusion of the extracranial ICA. Further, in patients with unilateral disease the degree of ipsilateral ADC elevation was well correlated to the magnitude of the hemispheric CVR deficit. A previous study reported WM ADC elevation in this population, but did not directly correlate this anomaly with decreased CVR. (219) Another recent investigation revealed a spatial association between increased ADC and negative CVR in patients with unilateral moyamoya disease. (136) The present study extends these results to the larger population of patients with extracranial carotid disease, and includes patients with both unilateral and bilateral ICA involvement.

The association between ADC and CVR remained statistically significant after correcting for potential confounding variables, including presence of neurological symptoms, vascular risk factors, previous infarct, and ICA occlusion. Combined with previous results, (136) this suggests that the observed ADC increase is a general result of chronic exposure to reduced CVR, independent of the anatomic location and etiology of the steno-occlusive lesion. We thus predict that a similar relationship may exist in other pathologies that cause chronic CVR impairment in normal-appearing brain tissue, for example in patients with epileptogenic brain arteriovenous malformations. (111)

In animal models of chronic hypoperfusion, WM is particularly susceptible to ischemic changes including glial activation, axonal damage, and disturbed synthesis and metabolism of myelin, (218,265) ADC elevation in WM of patients with carotid occlusive disease is consistent with the demyelination, axonal loss, and resulting rarefaction observed in experimental models. (219)

Although the observed ADC elevations are small (absolute change of up to 0.1×10^{-3} mm^2/s), they are similar in magnitude to WM changes previously reported in both large vessel (221,252) and small vessel (222) cerebrovascular disease. In some (221,222) but not all (252) of these studies, the degree of ADC elevation correlated to the degree of cognitive dysfunction. Interestingly, the one study which did not report a correlation between WM ADC and cognitive function selected WM ROIs manually, without reference to the presence or spatial distribution of CVR impairment. (252) Further, the mean degree of ICA

stenosis was 77%, which may not have resulted in significant CVR reduction to WM. Many patients with unilateral disease do not show significant WM CVR reduction (i.e., $\Delta CVR \approx 0$). Use of CVR mapping in patient selection and ROI generation allows identification of precise regions where ADC elevation would be expected as a result of CVR impairment, and may improve the correlation between WM ADC and neuropsychological outcome measures.

It is noteworthy that regions of negative CVR were also present in the WM of healthy adults and in the contralateral hemisphere of patients with unilateral ICA occlusive disease. As has been previously observed using both BOLD and arterial spin labeling MRI methods, (147) this effect was typically confined to specific anatomic regions including the corpus callosum, centrum semiovale, and periventricular WM. Although no ADC change was present, these areas have been reported to spatially correspond with the development of leukoaraiosis, suggesting that this phenomenon may not be entirely benign. (147) Longitudinal evaluation with CVR mapping in addition to conventional imaging techniques would be required to clarify the etiologic role of chronic CVR impairment in leukoaraiosis. A detailed discussion of the significance of negative CVR in WM of healthy adults is provided elsewhere. (147)

We performed CVR mapping using a BOLD MRI acquisition during a controlled hypercapnia challenge. The automatic gas blender and rebreathing circuit employed in this study insured that a well-defined, reproducible hypercapnic stimulus was achieved for each patient, independent of the subject's minute ventilation and $P_{ET}CO_2$. However, there are a number of limitations associated with BOLD MRI in this context. The BOLD signal is sensitive to a variety of hemodynamic parameters in addition to CBF, including cerebral blood volume, oxygen saturation, and the cerebral metabolic rate of oxygen consumption. (266) Although the BOLD response to controlled hypercapnia is well correlated with CBF changes in both healthy adults and patients with steno-occlusive disease, the resulting CVR parameter provides relative reactivity (% signal change per unit stimulus) rather than quantitative flow reactivity (absolute CBF change per unit stimulus). Further, the EPI gradients commonly used to maximize temporal resolution during BOLD acquisition are associated with characteristic artifacts near the interface between aerated sinuses and adjacent brain parenchyma. Most relevant to the present study are T2* mediated signal drop-out, and geometric distortion due to off-resonance effects. (267) To minimize the influence of these artifacts on our measurements, we excluded image data below the level of the mid-thalamus, and eroded the initial WM segmentation by 1 full BOLD voxel width. Partial volume contamination was avoided through use of an optimized image registration technique, (96) the aforementioned erosion of the initial WM ROI, and an additional ADC threshold to exclude voxels with ADC greater than 1.2×10^{-3} mm^2/s (eliminating both CSF and any chronic infarct that was not excluded by the manually traced lesion ROIs). Bias in the manual tracing of lesion ROIs was minimized by blinding the rater to all clinical data, and relying predominantly upon automated methods in the segmentation of normal-

appearing WM. We are thus confident that these results represent valid ADC and CVR measurements from normal-appearing WM only.

The present findings demonstrate that impaired CVR is associated with increased ADC in the normal-appearing WM of patients with severe stenosis or occlusion of the extracranial ICA. This abnormality was observed in patients with both unilateral and bilateral steno-occlusive disease. In patients with unilateral disease, the degree of ipsilateral CVR impairment was correlated with the mean hemispheric increase in WM ADC. The relationship between CVR impairment and ADC elevation remained significant after correction for the presence of previous infarction, ischemic symptomaticity, complete ICA occlusion, and major clinical risk factors. In addition to prognostic implications for future ischemic events, chronically impaired CVR is associated with abnormal WM structure, which may represent low-grade ischemic injury.

Bibliography

1. Martini FH. Anatomy and physiology. 2007 ed. Pearson Education Inc: Singapore; 2007. p. 531–76.
2. Johnson LR, Byrne JH. Essential medical physiology. 2nd ed. Philadelphia: Lippincott-Raven; 1998. p. 225–33.
3. Jones SE, Buchbinder BR, Aharon I. Three-Dimensional Mapping of Cortical Thickness Using Laplace's Equation. Hum Brain Mapp 2000;11(1):12-32.
4. Luders E, Narr KL, Thompson PM, Rex DE, Jancke L, Toga AW. Hemispheric Asymmetries in Cortical Thickness. Cereb Cortex 2006;16980:1232-8.
5. Rhoton AL. Rhoton's cranial anatomy and surgical approaches. 2007 1st ed. Lippincott Williams & Wilkins.
6. Ye OF, Yang Y, Duyn J, et al. Quantitation of regional cerebral blood flow increases during motor activation: a multislice, steady-state, arterial spin tagging study. Magn Reson Med. 1999;42:404–7.
7. Edvinsson L, MacKenzie ET, McCulloch J. Cerebral Blood Flow and Metabolism, 1993 (57-91) Raven Press: New York.
8. Aaslid R, Lindegaard KF, Sorteberg W, Nornes H. Cerebral Autoregulation Dynamics in Humans. Stroke 1989;20:45-52.
9. Squire LR, Bloom FE, Spitzer LE, et al. Fundamental neuroscience. 3rd ed. London: Elsevier Inc; 2008. p. 41–296.
10. Koehler RC, Roman RJ, Harder DR. Astrocytes and the regulation of cerebral blood flow. Trends Neurosci 2009;32:160–9.
11. Hamel E. Perivascular nerves and the regulation of cerebrovascular tone. J Appl Physiol 2006;100:1059–64.
12. Powers WJ. Cerebral hemodynamics in ischemic cerebrovascular disease. Ann Neurol 1991;29(3):231-40.
13. Derdeyn CP, Videen TO, Yundt KD, Fritsch SM, Carpenter DA, Grubb RL, Powers WJ. Variability of cerebral blood volume and oxygen extraction: stages of cerebral haemodynamic impairment revisited. Brain 2002;125(Pt 3):595-607.
14. Yonas H, Smith HA, Durham SR, Pentheny SL, Johnson DW. Increased stroke risk predicted by compromised cerebral blood flow reactivity. J Neurosurg 1993;79(4):483-9.
15. Nemoto EM, Yonas H, Kuwabara H, et al. Identification of hemodynamic compromise by cerebrovascular reserve and oxygen extraction fraction in occlusive vascular disease. J Cereb Blood Flow Metab 2004;24:1081-89.
16. North American Symptomatic Carotid Endarterectomy Collaborators. Beneficial effect of carotid endarterectomy in symptomatic patients with high-grade carotid stenosis. N Eng J Med 1991;325(7):445-53.
17. Barnett HJ, Taylor DW, Eliasziw M, Fox AJ, Ferguson GG, Rankin RN, Clagett GP, hachinski VC, Sackett DL, Thorpe KE, Meldrum HE, Spence JD. Benefit of carotid endarterectomy in patients with symptomatic moderate or severe stenosis. North American Symptomatic Carotid Endarterectomy Trial Collaborators. N Eng J Med 1998;339(20):1415-25.

18. Inzitari D, Eliasziw M, Gates P, Sharpe BL, Chan RK, Meldrum HE, Barnett HJ. The causes and risk of stroke in patients with asymptomatic internal-carotid-artery stenosis. North American Symptomatic Carotid Endarterectomy Trial Collaborators. N Eng J Med 2000;342(23):1693-700.
19. Executive committee for the Asymptomatic Carotid Atherosclerosis Study. Endarterectomy for asymptomatic carotid artery stenosis. JAMA 1995;273(18):1421-8.
20. Halliday A, Mansfield A, Marro J, Peto C, Peto R, Potter J, Thomas D for MRC Asymptomatic Carotid Surgery Trial (ACST) Collaborative Group. Prevention of disabling and fatal strokes by successful carotid endarterectomy in patients without recent neurological symptoms: randomised controlled trial. Lancet 2004;363(9430):1491-502.
21. Brott TG, Hobson RW 2nd, Howard G, Roubin GS, Clark WM, Brooks W, Mackey A, Hill MD, Leimgruber PP, Sheffet AJ, Howard VJ, Moore WS, Voeks JH, Hopkins LN, Cutlip DE, Cohen DJ, Popma JJ, Ferguson RD, Cohen SN, Blackshear JL, Silver FL, Mohr JP, Lal BK, Meschia JF; CREST Investigators. Stenting versus endarterectomy for treatment of carotid-artery stenosis. N Eng J Med 2010;363(1):11-23.
22. Eckstein HH, Ringleb P, Allenberg JR, Berger J, Fraedrich G, Hacke W, Hennerici M, Stingele R, Fiehler J, Zeumer H, Jansen O. Results of the Stent-Protected Angioplasty versus Carotid Endarterectomy (SPACE) study to treat symptomatic stenoses at 2 years: a multinational, prospective, randomised trial. Lancet Neurol 2008;7(10):893-902.
23. International Carotid Stenting Study Investigators. Carotid artery stenting compared with endarterectomy in patients with symptomatic carotid stenosis (International Carotid Stenting Study): an interim analysis of a randomised controlled trial. Lancet 2010;375(9719):985-97.
24. Scott RM, Smith ER. Moyamoay disease and moyamoya syndrome. N Eng J Med 2009;360:1226-37.
25. Fukui M. Current statae of study on moyamoya disease in Japan. Surg Neurol 1997;47:138-43.
26. Burke GM, Burke AM, Sherma AK, Hurley MC, Batjer HH, Bendok BR. Moyamoya disease: a summary. Neurosurg Focus 2009;26:E11.
27. Karzmark P, Zeifert PD, Bell-Stephens TE, Dorfman LJ, Steinberg GK. Effect of moyamoya diseae on neuropsychological functioning in adults. Neurosurgery 2008;62:1048-51.
28. Karzmark P, Zeifert PD, Bell-Stephens TE, Steinberg GK, Dorfman LJ. Neurocognitive impairment in adults with moyamoya disease without stroke. Neurosurgery 2011 [Epub ahead of print]
29. Takahashi JC, Mitamoto S. Moyamoya disease: recent progress and outlook. Neurol Med Chir (Tokyo) 2010;50;824-32.

30. Han DH, Kwon OK, Byun BJ, Choi BY, Choi CW, Choi JU, Choi SG, Doh JO, Han JW, Jung S, Kang SD, Kim DJ, Kim HI, Kim HD, Kim MC, Kim SC, Kim SC, Kim Y, Kwun BD, Lee BG, Lim YJ, Moon JG, Park HS, Shin MS, Song JH, Suk JS, Yim MB. A co-operative study: clinical characteristics of 334 Korean patients with moyamoya disease treated at neurosurgical institutes (1976-1994). The Korean society for Cerebrovascular disease. Acta Neurochir (Wien) 2000;142:1263-73.
31. Kim SK, Cho BK, Phi JH, Lee JY, Chae JH, Kim KJ, Hwang YS, Kim IO, Lee DS, Lee J, Wang KC. Pediatric moyamoya disease: An analysis of 410 consecutive cases. Ann Neurol 2010;68:92-101.
32. Baba T, Houkin K, Kuroda S. Novel epidemiological features of moyamoya diseae. J Neurol Neurosurg Psychiatry 2008;79:900-4.
33. Uchino K, Johnston SC, Becker KJ, Tirschwell DL. Moyamoya disease in Washington State and California. Neurology 2005;65:956-58.
34. Yonekawa Y, Ogata N, Kaku Y, Taub E, Imhoff HG. Moyamoya diseae in Europe, past and present status. Clin Neurol Neurosurg 1997;99 (Suppl 2):S58-S60.
35. Stieg P, Batjer HH, Samson D. Intracranial arteriovenous malformations. 1st edn., New York: Informa Healthcare USA, Inc; 2007. Chapter 5, natural history; p. 73–9. Chapter 16, supratentorial lobar arteriovenous malformations; p. 215–37.
36. Berenstein A, Lasjaunias P, Ter Brugge K. Surgical neuroangiopathy, 2.2. 2nd ed. Berlin: Springer-Verlag; 2003. Chapter 9, cerebral vascular malformations; p. 609-91
37. Moftakhar P, Hauptman JS, Malkasian D, Martin NA. Cerebral arteriovenous malformations. Part 2: Physiology. Neurosurg Focus 2009;36(5):E11.
38. Davidson AS, Morgan MK. The embryologic basis for the anatomy of the cerebral vasculature related to arterionvenous malformations. J Clin Neurosci 2011;18(4):464-9.
39. Jeffree RL, Stoodley MA. Postnatal development of arteriovenous malformations. Pediatr Neurosurg 2009;45:296–304.
40. Moftakhar P, Hauptman JS, Malkasian D, Martin NA. Cerebral arteriovenous malformations. Part 1: cellular and molecular biology. Neurosurg Focus 2009;26:E10.
41. Dehdashti AR, Thines L, Willinsky RA, terBrugge KG, Schwartz ML, Tymianski M, Wallace MC. Multidisciplinary care of occipital arteriovenous malformations: effect on nonhemorrhagic headache, vision, and outcome in a series of 135 patients. J Neurosurg. 2010;113:742–748.
42. Mohr JP, Moskowitz AJ, Stapf C, Hartmann A, Lord K, Marshall SM, Mast H, Moquete E, Moy CS, Parides M, Pile-Spellman J, Al-Shahi Salman R, Weinberg A, Young WL, Estevez A, Kureshi I, Brisman JL. The ARUBA trial: current status, future hopes. Stroke. 2010;41:e537–540.

43. Spetzler RF, Hargraves RW, McCormick PW, et al. Relationship of perfusion pressure and size to risk of hemorrhage from arteriovenous malformations. J Neurosurg 1992; 76: 918-23.
44. Taylor CL, Selman WR, Ratcheson RA. Steal affecting the central nervous system. Neurosurgery 2002; 50: 679-89.
45. Norris JS, Valiante TA, Wallace MC, et al. A simple relationship between radiological arteriovenous malformation hemodynamics and clinical presentation: a prospective blinded analysis of 31 cases. J Neurosurg 1999;90:673-79.
46. Willinsky R, Goyal M, Ter Brugge K, Montanera W. Tortuous, engorged pial veins in intracranial dural arteriovenous fistulas: correlations with presentation, location, and MR findings in 122 patients. AJNR Am J Neuroradiol 1999;20: 1031-6.
47. Geibprasert S, Pongpech S, Jiarakongmin P, et al. Radiologic assessment of brain arteriovenous malformations: what clinicians need to know. Radiographics 2010; 30: 483-501.
48. Lanzino G, D'Urso PI, Tymianski M. Advances in vascular neurosurgery 2010. Stroke 2011;42:288-90.
49. Colombo F, Cavedon C, Casentini L, Francescon P, Causin F, Pinna V. Early results of Cyberknife radiosurgery for arteriovenous malformations. J Neurosurg. 2009;111:807– 19.
50. Powers WJ, Press GA, Grubb RL Jr, et al. The effect of hemodynamically significant carotid artery disease on the hemodynamic status of the cerebral circulation. Ann Intern Med 1987;106(1):27-43.
51. Ringelstein EB, Sievers C, Ecker S, Schneider PA, Otis SM. Noninvasive assessment of CO2-induced cerebral vasomotor response in normal individuals and patients with internal carotid artery occlusions. Stroke 1988; 19(8):963-969.
52. Robbins PA, Conway J, Cunningham DA, Khamnei S, Paterson DJ (1990) A comparison of indirect methods for continuous estimation of arterial PCO2 in men. J Appl Physiol 68:1727-31.
53. Wilkinson HA. Cerebral blood flow response to acetazolamide. J Neurosurg 1989; 70(1):156.
54. Leaf DE, Goldfarb DS. Mechanisms of action of acetazolamide in the prophylaxis and treatment of acute mountain sickness. J Appl Physiol 2007;102:1313-22.
55. Parkes MJ. Breath-holding and its breakpoint. Exp Physiol 2006: 91:1-15.
56. Floyd TF, Clark JM, Gelfand R, et al. Independent cerebral vasoconstrictive effects of hyperoxia and accompanying arterial hypocapnia at 1 ATA. J Appl Physiol 2003;95:2453–61.
57. Slessarev M, Prisman E, Han J, et al. Prospective targeting and control of end-tidal CO2 and O2 concentrations. *J Physiol* 2007; 581.3: 1207–19.
58. Ito S, Mardimae A, Han J, et al. Non-invasive prospective targeting of arterial PCO_2in subjects at rest. *J Physiol* 2008; 586.15: 3675–82.

59. Robbins PA, Swanson GD & Howson MG. A prediction-correction scheme for forcing alveolar gases along certain time courses. J Appl Physiol 1982;52:1353–57.
60. Howard LS, Barson RA, Howse BP, McGill TR, McIntyre ME, O'Connor DF & Robbins PA. Chamber for controlling end-tidal gas tensions over sustained periods in humans. J Appl Physiol 1995;78:1088–91.
61. Huber P, Handa J. Effect of contrast material, hypercapnia, hyperventilation, hypertonic glucose and papaverine on the diameter of the cerebral arteries. Angiographic determination in man. Invest Radiol 1967; 2(1):17-32.
62. Bradac GB, Simon RS, Heidsieck CH. Angiographically verified transient alteration of the intracranial arteries and veins in dependence of different CO2 tensions. Neuroradiology 1976;10(5):257-62.
63. Kirkham FJ, Padayachee TS, Parsons S, Seargeant LS, House FR, Gosling RG. Transcranial measurement of blood velocities in the basal cerebral arteries using pulsed Doppler ultrasound: velocity as an index of flow. Ultrasound Med Biol 1986;12(1):15-21.
64. Bishop CCR, Powell S, Rutt D, Browse NL. Transcranial Doppler measurement of middle cerebral artery blood flow velocity: a validation study. Stroke 1986;17(5):913-15.
65. Dahl A, Lindegaard KF, Russel D, et al. A comparison of transcranial Doppler and cerebral blood flow studies to assess cerebral vasoreactivity. Stroke 1992;23(1):15-19.
66. Yonas H, Smith HA, Durham SR, Pentheny SL, Johnson DW. Increased stroke risk predicted by compromised cerebral blood flow reactivity. J Neurosurg 1993; 79(4):483-89.
67. Gooskens I, Schmidt EA, Czosnyka M et al. Pressure-autoregulation, CO2 reactivity and asymmetry of haemodynamic parameters in patients with carotid artery stenotic disease. A clinical appraisal. Acta Neurochir (Wien) 2003;145(7):527-32.
68. Herold S, Brown MM, Frackowiak RS, Mansfield AO, Thomas DJ, Marshall J. Assessment of cerebral haemodynamic reserve: correlation between PET parameters and CO2 reactivity measured by the intravenous 133 xenon injection technique. J Neurol Neurosurg Psychiatry 1988;51(8):1045-50.
69. Vorstrup S, Brun B, Lassen NA. Evaluation of the cerebral vasodilatory capacity by the acetazolamide test before EC-IC bypass surgery in patients with occlusion of the internal carotid artery. Stroke 1986;17(6):1291-98.
70. Gibbs JM, Wise RJ, Leenders KL, Jones T. Evaluation of cerebral perfusion reserve in patients with carotid-artery occlusion. Lancet 1984;1(8372):310-14.
71. Grubb RL Jr, Derdeyn CP, Fritsch SM, et al. Importance of hemodynamic factors in the prognosis of symptomatic carotid occlusion. JAMA 1998;280(12):1055-60.

72. Yamauchi H, Fukuyama H, Nagahama Y, et al. Evidence of misery perfusion and risk for recurrent stroke in major cerebral arterial occlusive diseases from PET. J Neurol Neurosurg Psychiatry 1996;61(1):18-25.
73. Yamauchi H, Fukuyama H, Nagahama Y, et al. Significance of increased oxygen extraction fraction in five-year prognosis of major cerebral arterial occlusive diseases. J Nucl Med 1999;40(12):1992-98.
74. Norrving B, Nilsson B, Risberg J. rCBF in patients with carotid occlusion. Resting and hypercapnic flow related to collateral pattern. Stroke 1982;13(2):155-62.
75. Rogg J, Rutigliano M, Yonas H, et al. The acetazolamide challenge: imaging techniques designed to evaluate cerebral blood flow reserve. Am J Roentgenol 1989;153:605-12.
76. Kety SS, Schmidt CF. The effects of altered arterial tensions of carbon dioxide and oxygen on cerebral blood flow and cerebral oxygen consumption of normal young men. J Clin Invest 1948;27:484-92.
77. Ogasawara K, Ogawa A, Terasaki K, et al. Use of cerebrovascular reactivity in patients with symptomatic major cerebral artery occlusion to predict 5-year outcome: comparison of xenon-133 and iodine-123-IMP single-photon emission computed tomography. J Cereb Blood Flow Metab 2002;22(9):1142-48.
78. Ogasawara K, Ogawa A, Yoshimoto T. Cerebrovascular reactivity to acetazolamide and outcome in patients with symptomatic internal carotid or middle cerebral artery occlusion: a xenon-133 single-photon emission computed tomography study. Stroke 2002;33(7):1857-62.
79. Ogawa S, Lee TM, Kay AR, Tank DW. Brain magnetic resonance imaging with contrast dependent on blood oxygenation. Proc Natl Acad Sci USA. 1990;87:9868–72.
80. Kwong KK, Belliveau JW, Chesler DA, et al. Dynamic magnetic resonance imaging of human brain activity during primary sensory stimulation. Proc Natl Acad Sci USA. 1992;89:5675–79.
81. Roy CS, Sherrington CS. On the regulation of the blood supply of the brain. J Physiol. 1890;11:85–108.
82. Buxton RB, Uludag K, Dubowitz DJ, Liu TT. Modeling the hemodynamic response to brain activation. Neuroimage 2004;23:S220–33.
83. Rostrup E, Larsson HB, Toft PB, Garde K, Henriksen O. Signal changes in gradient echo images of human brain induced by hypo and hyperoxia. NMR Biomed 1995;8:41–7.
84. Vesely A, Sasano H, Volgyesi G, Somogyi R, Tesler J, Fedorko L, Grynspan J, Crawley A, Fisher JA, Mikulis D. MRI mapping of cerebrovascular reactivity using square wave changes in end-tidal PCO2. Magn Reson Med. 2001;45(6):1011-3.
85. Mark CI, Fisher JA, Pike GB. Improved fMRI calibration: precisely controlled hyperoxic versus hypercapnic stimuli. Neuroimage 2011;24(2):1102-11.

86. Mark CI, Slessarev M, Ito S, Han J, Fisher JA, Pike GB. Precise control of end-tidal carbon dioxide and oxygen improves BOLD and ASL cerebrovascular reactivity measures. Magn Reson Med 2010;64(3):749-56.
87. Prisman E, Slessarev M, Han J, Poublanc J, Mardimae A, Crawley A, Fisher JA, Mikulis D. Comparison of the effects of independently controlled end-tidal PCO2 and PO2 on blood oxygen level-dependent (BOLD) MRI. J Magn Reson Im 2008;27:185-91.
88. Goode SD, Krishan S, Alexakis C, Mahajan R, Auer DP. Precision of cerebrovascular reactivity assessment with use of different quantification methods for hypercapnia functional MR imaging. AJNR Am J Neuroradiol 2009;30:972-77.
89. Kassner A, Winter JD, Poublanc J, Mikulis DJ, Crawley AP. Blood-oxygen level dependent MRI measures of cerebrovascular reactivity using a controlled respiratory challenge: reproducibility and gender differences. J Magn Reson Imaging 2010;31(2):298-304.
90. Mandell DM, Han JS, Poublanc J, Crawley AP, Stainsby JA, Fisher JA, Mikulis DJ. Mapping cerebrovascular reactivity using blood oxygen level-dependent MRI in patients with arterial steno-occlusive disease: comparison with arterial spin labeling. Stroke 2008; 39(7):2021-8.
91. Heyn C, Poublanc J, Crawley A, Mandell D, Han JS, Tymianski M, terBrugge K, FisherJA, Mikulis DJ. Quantification of cerebrovascular reactivity by blood oxygen level dependent MR imaging and correlation with conventional angiography in patients with moyamoya disease. AJNR AM J Neuroradiol 2010;31:862-67.
92. Mikulis DJ, Krolczyk G, Desal H, Logan W, Deveber G, Dirks P, Tymianski M, Crawley A, Vesely A, Kassner A, Preiss D, Somogyi R, Fisher JA (2005) Preoperative and postoperative mapping of cerebrovascular reactivity in moyamoya disease by using blood oxygen level-dependent magnetic resonance imaging. J Neurosurg 103:347-55.
93. Han JS, Mandell DM, Poublanc J, Mardimae A, Slessarev M, Jaigobin C, Fisher JA, Mikulis DJ (2008) Cocaine-induced cerebral vasculitis: high resolution vessel wall MRI and BOLD MR cerebrovascular reactivity findings. Nat Clin Pract Neurol 2008;4(11):628-32.
94. Han JS, Mikulis DJ, Mardimae A, Kassner A, Poublanc J, Crawley AP, deVeber GA, Fisher JA, Logan WJ. Measurement of cerebrovascular reactivity in pediatric patients with cerebral vasculopathy using blood oxygen level-dependent MRI. Stroke 2011;42: 1261-69.
95. Cox RW. AFNI: software for analysis and visualization of functional magnetic resonance neuroimages. Comput Biomed Res. 1996;29:162-73.
96. Saad ZS, Glen DR, Chen G, Beauchamp MS, Desai R, Cox RW. A new method for improving functional-to-structural MRI alignment using local Pearson correlation. Neuroimage 2009;44(3):839-48.

97. Silvestrini M, Vernieri F, Pasqualetti P, et al. Impaired cerebral vasoreactivity and risk of stroke in patients with asymptomatic carotid artery stenosis. JAMA 2000;26;283(16):2122-7.
98. Schoof J, Lubahn W, Baeumer M, Kross R, Wallesch CW, Kozian A, Huth C, Goertler M. Impaired cerebral autoregulation distal to carotid stenosis/occlusion is associated with increased risk of stroke at cardiac surgery with cardiopulmonary bypass. J Thorac Cardiovasc Surg 2007;134(3):690-6.
99. Sehkon LH, Morgan MK, Spence I, Weber NC. Chronic cerebral hypoperfusion and impaired neuronal function in rats. Stroke 1994;25(5):1022-7.
100. Hai J, Wan JF, Lin Q, Wang F, Zhang L, Li H, Zhang L, Chen YY, Lu Y. Cognitive dysfunction induced by cerebral hypoperfusion in a rat model associated with arteriovenous malformations. Brain Res 2009;1301:80-9.
101. Rosas HD, Liu AK, Hersch S, Glessner M, Ferrante RJ, Salat DH, van der KA, Jenkins BG, Dale AM, Fischl B. Regional and progressive thinning of the cortical ribbon in Huntington's disease. Neurology 2002;58(5):695-701.
102. Muller M, Van der Graaf Y, Algra A, Hendrikse J, Mali WP, Geerlins MI. Carotid atherosclerosis and progression of brain atrophy: The SMART-MR Study. Ann Neurol 2011;70(2):237-44.
103. Seo SW, Ahn J, Yoon U, Im K, Lee JM, Tae KS, Ahn HJ, Chin J, Jeong Y, Na DL. Cortical thinning in vascular mild cognitive impairment and vascular dementia of subcortical type. J Neuroimaging. 2010;20:37– 45.
104. Vermeer SE, Prins ND, den Heijer T, Hofman A, Koudstaal PJ, Breteler MM. Silent brain infarcts and the risk of dementia and cognitive decline. N Engl J Med. 2003;348:1215–1222.
105. Bakker FC, Klijn CJ, Jennekens-Schinkel A, Van der Tweel I, Tulleken CA, Kapelle LJ. Cognitive impairment in patients with carotid artery occlusion and ipsilateral transient ischemic attacks. J Neurol 2003;250(11):1340-7.
106. Festa JR, Schwarz LR, Pliskin N, Cullum CM, Lacritz L, Charbel FT, Mathews D, Starke RM, Connolly ES, Marshall RS, Lazar RM. Neurocognitive dysfunction in adult moyamoya disease. J Neurol. 2010;25:806–815.
107. Kim SK, Cho BK, Phi JH, Lee JY, Chae JH, Kim KJ, Hwang YS, Kim IO, Lee DS, Lee J, Wang KC. Pediatric moyamoya disease: an analysis of 410 consecutive cases. Ann Neurol. 2010;68:92–101.
108. Suzuki J, Kodama N. Moyamoya disease--a review. Stroke 1983;14:104-9.
109. Shiino A, Morita Y, Tsuji A, Maeda K, Ito R, Furukawa A, Matsuda M, Inubushi T. Estimation of cerebral perfusion reserve by blood oxygenation level-dependent imaging: comparison with single-photon emission computed tomography. J Cereb Blood Flow Metab 2003;23:121-35.
110. Webb J, Guimond A, Eldridge P, Chadwick D, Meunier J, Thirion JP, Roberts N. Automatic detection of hippocampal atrophy on magnetic resonance images. Magn Reson Imaging 1999;17:1149-61.

111. Fierstra J, Conklin J, Krings T, Slessarev M, Han JS, Fisher JA, terBrugge K, Wallace MC, Tymianski M, Mikulis DJ. Impaired peri-nidal cerebrovascular reserve in seizure patients with brain arteriovenous malformations. Brain 2011;134:100-9.
112. Ashburner J, Friston KJ. Nonlinear spatial normalization using basis functions. Hum Brain Mapp 1999;7:254-66.
113. Ashburner J, Friston K. Multimodal image coregistration and partitioning –a unified framework. Neuroimage 1997;6:209-17.
114. Nakagawara J. Functional neuroimagings: "overview". In: Moyamoya Disease Update (Cho BK, Tominaga T, eds), Tokyo: Springer, 2010, pp 171-80.
115. Saito H, Ogasawara K, Suzuki T, Kuroda H, Kobayashi M, Yoshida K, Kubo Y, Ogawa A. Adverse Effects of Intravenous Acetazolamide Administration for Evaluation of Cerebrovascular Reactivity Using Brain Perfusion Single-Photon Emission Computed Tomography in Patients With Major Cerebral Artery Steno-occlusive Diseases. Neurol Med Chir (Tokyo) 2011;51:479-83.
116. Kemp PM, Houston AS, Macleod MA, Pethybridge RJ. Cerebral perfusion and psychometric testing in military amateur boxers and controls. J Neurol Neurosurg Psychiatry 1995;59:368-74.
117. Laliberte JF, Meunier J, Mignotte M, Soucy JP. Detection of diffuse abnormal perfusion in SPECT using a normal brain atlas. Neuroimage 2004;23:561-68.
118. Commowick O, Fillard P, Clatz O, Warfield SK. Detection of DTI white matter abnormalities in multiple sclerosis patients. Med Image Comput Comput Assist Interv 2008;11:975-82.
119. Markus HS, Harrison MJ. Estimation of cerebrovascular reactivity using transcranial Doppler, including the use of breath-holding as the vasodilatory stimulus. Stroke 1992;23:668-73.
120. Van der Zande FH, Hofman PA, Backes WH. Mapping hypercapnia-induced cerebrovascular reactivity using BOLD MRI. Neuroradiology 2005;47:114-20.
121. Silvestrini M, Vernieri F, Troisi E, Passarelli F, Matteis M, Pasqualetti P, Rossini PM, Caltagirone C. Cerebrovascular reactivity in carotid artery occlusion: possible implications for surgical management of selected groups of patients. Acta Neurol Scand 1999;99:187-91.
122. Sasse SA, Berry RB, Nguyen TK, Light RW, Mahutte CK. Arterial blood gas changes during breath-holding from functional residual capacity. Chest 1996;110:958-64.
123. Hoskin PJ, Abdelath O, Phillips H, Gilligan S, Saunders MI, Broderick P, Baddeley H. Inspired and expired gas concentrations in man during carbogen breathing. Radiother Oncol 1999;51:175-77.
124. Guadagno JV, Jones PS, Aigbirhio FI, Wang D, Fryer TD, Day DJ, Antoum N, Nimmo-Smith I, Warburton EA, Baron JC. Selective neuronal loss in rescued penumbra relates to initial hypoperfusion. Brain. 2008;131 (Pt 10):2666-78.

125. Yamauchi H, Kudoh T, Kishibe Y, Iwasaki J, Kagawa S. Selective neuronal damage and borderzone infarction in carotid artery occlusive disease: a ^{11}C-flumazenil PET study. J Nucl Med. 2005; 46:1973–79.
126. Saur D, Buchert R, Knab R, Weiller C, Rother J. Iomazenil-Single-Photon Emission Computed Tomography Reveals Selective Neuronal Loss in Magnetic Resonance-Defined Mismatch Areas. Stroke. 2006;37:2713-19.
127. Somogyi RB, Vesely AE, Preiss D, Prisman E, Volgyesi G, Azami T, Iscoe S, Fisher JA, Sasano H. Precise control of end-tidal carbon dioxide levels using sequential rebreathing circuits. Aneasth Intensive Care. 2005 Dec;33(6):726-32.
128. Sailer M, Fischl B, Salat D, Tempelmann C, Schonfield MA, Busa E, Bodammer N, Heinze HJ, Dale A. Focal thinning of the cerebral cortex in multiple sclerosis. Brain. 2003;126:1734-44.
129. Dale AM, Sereno MI. Improved localization of cortical activity by combining EEG and MEG with MRI cortical surface reconstruction: a linear approach. J Cogn Neurosci. 1993;5:162-76.
130. Fischl B, Sereno MI, Dale AM. Cortical Surface-Based Analysis. II: Inflation, Flattening, and a Surface-Based Coordinate System. Neuroimage. 1999; 9(2):195-207.
131. Salat DH, Buckner RL, Snyder AZ, Greve DN, Desikan RSR, Busa E, Morris JC, Dale AM, Fischl B. Thinning of the Cerebral Cortex in Aging. Cereb Cortex. 2004;14(7):721-30.
132. Richards BA, Chertkow H, Singh V, Robillard A, Massoud F, Evans AC, Jehan Kabani N. Patterns of cortical thinning in Alzheimer's disease and frontotemporal dementia. Neurobiology of Aging. 2009;30:1626–36.
133. Luders E, Narr KL, Thompson PM, Rex DE, Jancke L, Toga AW. Hemispheric Asymmetries in Cortical Thickness. Cereb Cortex. 2006; 16980:1232-8.
134. Jones SE, Buchbinder BR, Aharon I. Three-Dimensional Mapping of Cortical Thickness Using Laplace's Equation. Hum Brain Mapp. 2000;11(1):12-32.
135. Good CD, Johnsrude I, Ashburner J, Henson RN, Friston KJ, Frackowiak RS. Cerebral asymmetry and the effects of sex and handedness on brain structure: a voxel-based morphometric analysis of 465 normal adult human brains. Neuroimage 2001;14(3):685-700.
136. Conklin J, Fierstra J, Crawley AP, Han JS, Poublanc J, Mandell DM, Silver FL, Tymianski M, Fisher JA, Mikulis DJ. Impaired cerebrovascular reactivity with steal phenomenon is associated with increased diffusion in white matter of patients with Moyamoya disease. Stroke 2010;41(8):1610-6.
137. Conklin J, Fierstra J, Crawley AP, Han JS, Poublanc J, Silver FL, Tymianski M, Fisher JA, Mandell DM, Mikulis DJ. Mapping white matter diffusion and cerebrovascular reactivity in carotid occlusive disease. Neurology 2011;77(5):431-8.

138. Fierstra J, Poublanc J, Han JS, Silver F, Tymianski M, Crawley AP, Fisher JA, Mikulis DJ. Steal physiology is spatially associated with cortical thinning. J Neurol Neurosurg Psychiatry 2010;81(3):290-3.
139. Ongali B, Nicolakakis N, Lecrux C, Aboulkassim T, Rosa-Neto P, Papadopoulos P, Tong XK, Hamel E. Transgenic Mice Overexpressing APP and Transforming Growth Factor-{beta}1 Feature Cognitive and Vascular Hallmarks of Alzheimer's Disease. Am J Pathol 2010;177(6):3071-80.
140. Querfurth HW, LaFerla FM. Alzheimer's disease. N Engl J Med 2010;362(4):329-44.
141. Bearden CE, Thompson PM, Dalwani M, Hayashi KM, Lee AD, Nicoletti M, Trakhtenbroit M, Glahn DC, Brambilla P, Sassi RB, Mallinger AG, Frank E, Kupfer DJ, Soares JC. Greater cortical gray matter density in lithium-treated patients with bipolar disorder. Biol Psychiatry 2007;62(1):7-16.
142. Carmichael ST. Themes and strategies for studying the biology of stroke recovery in the poststroke epoch. Stroke 2008;39(4):1380-8.
143. Taguchi A, Soma T, Tanaka H, Kanda T, Nishimura H, Yoshikawa H, Tsukamoto Y, Iso H, Fujimori Y, Stern DM, Naritomi H, Matsuyama T. Administration of CD34+ cells after stroke enhances neurogenesis via angiogenesis in a mouse model. J Clin Invest 2004;114(3):330-8.
144. Nadareishvili Z, Hallenbeck J. Neuronal regeneration after stroke. N Engl J Med 2003;348(23):2355-6.
145. Arvidsson A, Collin T, Kirik D, Kokaia Z, Lindvall O. Neuronal replacement from endogenous precursors in the adult brain after stroke. Nat Med 2002;8(9):963-70.
146. Jan YN, Jan LY. Branching out: mechanisms of dendritic arborization. Nat Rev Neurosci 2010 May;11(5):316-28.
147. Mandell DM, Han JS, Poublanc J, Crawley AP, Kassner A, Fisher JA, Mikulis DJ. Selective reduction of blood flow to white matter during hypercapnia corresponds with leukoaraiosis. Stroke 2008;39(7):1993-8.
148. Sachdev P, Wen W, Chen X, Brodaty H. Progression of white matter hyperintensities in elderly individuals over 3 years. Neurology 2006;68(3):214-22.
149. O'Sullivan M, Summers PE, Jones DK, Jarosz JM, Williams SC, Markus HS. Normal-appearing white matter in ischemic leukoaraiosis: a diffusion tensor MRI study. Neurology 2001;57(12):2307-10.
150. Black S, Gao F, Bilbao J. Understanding white matter disease: imaging-pathological correlations in vascular cognitive impairment. Stroke 2009;40(3 Suppl):S48-S52.
151. Bulte D, Chiarelli P, Wise R, Jezzard P. Measurement of cerebral blood volume in humans using hyperoxic MRI contrast. J Magn Reson Imaging 2007 October;26(4):894-9.
152. Jinnouchi J, Toyoda K, Inoue T, Fujimoto S, Gotoh S, Yasumori K, Ibayashi S, Iida M, Okada Y. Changes in brain volume 2 years after extracranial-intracranial

bypass surgery: A preliminary subanalysis of the Japanese EC-IC trial. Cerebrovasc Dis 2006;22(2-3):177-82.
153. Duning T, Kloska S, Steinstrater O, Kugel H, Heindel W, Knecht S. Dehydration confounds the assessment of brain atrophy. Neurology 2005;64(3):548-50.
154. Horner CH, Davies HA, Brown J, Stewart MG. Reduction in numerical synapse density in chick (Gallus domesticus) dorsal hippocampus following transient cerebral ischaemia. Brain Res 1996;735(2):354-9.
155. Tomimoto H, Ihara M, Wakita H, Ohtani R, Lin JX, Akiguchi I, Kinoshita M, Shibasaki H. Chronic cerebral hypoperfusion induces white matter lesions and loss of oligodendroglia with DNA fragmentation in the rat. Acta Neuropathol 2003;106(6):527-34.
156. Kurumatani T, Kudo T, Ikura Y, Takeda M. White matter changes in the gerbil brain under chronic cerebral hypoperfusion. Stroke 1998;29(5):1058-62.
157. Hoh BL, Chapman PH, Loeffler JS, et al. Results of multimodality treatment for 141 patients with brain arteriovenous malformations and seizures: factors associated with seizure incidence and seizure outcomes. Neurosurgery 2002:51(2);303-9.
158. Wilkins RH. Natural history of intracranial vascular malformations: a review. Neurosurgery 1985:16;421-30.
159. Hacein-Bey L, Nour R, Pile-Spellman J, et al. Adaptive changes of autoregulation in chronic cerebral hypotension with arteriovenous malformations: an acetazolamide-enhanced single-photon emission CT study. AJNR Am J Neuroradiol 1995;16:1865–74.
160. Turjman F, Massoud TF, Sayre JW, et al. Epilepsy associated with cerebral arteriovenous malformations: a multivariate analysis of angioarchitectural characteristics. AJNR Am J Neuroradiol 1995;16:345-50.
161. Stein BM, Wolpert SM. Arteriovenous malformations of the brain: I. current concepts and treatment. Arch Neurol 1980;37:1-5.
162. Mast H, Mohr JP, Osipov A, et al. 'Steal' is an unestablished mechanism for the clinical presentation of cerebral arteriovenous malformations. Stroke 1995;26:1215-20.
163. Mast H, Mohr JP, Thompson JLP, et al. Transcranial Doppler Ultrasonography in cerebral arteriovenous malformations. Diagnostic sensitivity and association of flow velocity with spontaneous hemorrhage and focal neurological deficit. Stroke 1995;26:1024-27.
164. Kosnik EJ, Hunt WE, Millar CA. Dural arteriovenous malformations. J Neurosurg 1974;40:322-9.
165. Lasjaunias P, Chiu M, TerBrugge K, et al. Neurological manifestations of intracranial dural arteriovenous malformations. J Neurosurg 1986;64:724-30.
166. Hurst RW, Hackney DB, Goldberg HI, Davis RA. Reversible arteriovenous malformation-induced venous hypertension as a cause of neurological deficits. Neurosurgery 1992;30:422-5.

167. Krings T, Hans FJ, Geibprasert S, Terbrugge K. Partial "targeted" embolisation of brain arteriovenous malformations. Eur Radiol 2010;20(11):2723-31.
168. Varelas P. Seizures in critical care. A guide to diagnosis and therapeutics. 2nd ed. Totowa: Humana Press Inc; 2010. Chapter 3.7, cerebral vein and dural sinus thrombosis; p.101-6.
169. Van Roost D, Schramm J. What factors are related to impairment of cerebrovascular reserve before and after arteriovenous malformation resection? A cerebral blood flow study using Xenon-enhanced computed tomography. Neurosurgery 2001:48;709-16.
170. Robbins PA, Conway J, Cunningham DA, Khamnei S, Paterson DJ. A comparison of indirect methods for continuous estimation of arterial PCO2 in men. J Appl Physiol 1990;68:1727-31.
171. Tenney S, Miller RM. Dead space ventilation in old age. J Appl Physiol 1956;9:321-7.
172. Barr PO. Pulmonary gas exchange in man as affected by prolonged gravitational stress. Acta Psychiatr Scand Suppl 1963;207:1-46.
173. Jones NL, Robertson DG, Kane JW. Difference between end-tidal and arterial PCO2 in exercise. J Appl Physiol 1979;47:954-60.
174. Liu Z, Vargas F, Stansbury D, Sasse SA, Light RW. Comparison of the end-tidal arterial PCO2 gradient during exercise in normal subjects and in patients with severe COPD. Chest 1995;107:1218-24.
175. Prause G, Hetz H, Lauda P, Pojer H, Smolle-Juettner F, Smolle J. A comparison of the end-tidal-CO2 documented by capnometry and the arterial pCO2 in emergency patients. Resuscitation 1997;35:145-48.
176. Matell G. Time-courses of changes in ventilation and arterial gas tensions in man induced by moderate exercise. Acta Physiol Scand 1963;58:1-47.
177. Badgwell JM, McLeod ME, Lerman J, Creighton RE. End-tidal PCO2 measurements sampled at the distal and proximal ends of the endotracheal tube in infants and children. Anesth Analg 1987;66:959-64.
178. Rich GF, Sconzo JM. Continuous end-tidal CO2 sampling within the proximal endotracheal tube estimates arterial CO2 tension in infants. Can J Anaesth 1991;38:201-03.
179. Fletcher R. The relationship between the arterial to end-tidal PCO2 difference and hemoglobin saturation in patients with congenital heart disease. Anesthesiology 1991;75:210-16.
180. Yamanaka MK, Sue DY. Comparison of arterial-end-tidal PCO2 difference and dead space/tidal volume ratio in respiratory failure. Chest 1987;92:832-35.
181. Grenier B, Verchere E, Mesli A, Dubreuil M, Siao D, Vandendriessche M, Cales J, Maurette P. Capnography monitoring during neurosurgery: reliability in relation to various intraoperative positions. Anesth Analg 1999;88:43-8.

182. McDonald MJ, Montgomery VL, Cerrito PB, Parrish CJ, Boland KA, Sullivan JE. Comparison of end-tidal CO2 and Paco2 in children receiving mechanical ventilation. Pediatr Crit Care Med 2002;3:244-49.
183. Russell GB, Graybeal JM. Reliability of the arterial to end-tidal carbon dioxide gradient in mechanically ventilated patients with multisystem trauma. J Trauma 1994;36:317-22.
184. Read DJ. A clinical method for assessing the ventilatory response to carbon dioxide. Australas Ann Med 1967;16:20-32.
185. Bowie JR, Knox P, Downs JB, Smith RA. Rebreathing improves accuracy of ventilatory monitoring. J Clin Monit 1995;11:354-57.
186. Fletcher R, Jonson B. Deadspace and the single breath test for carbon dioxide during anaesthesia and artificial ventilation. Effects of tidal volume and frequency of respiration. Br J Anaesth 1984;56:109-19.
187. Larson C, Severinghaus JW. Postural variations in dead space and CO2 gradients breathing air and O2. J Appl Physiol 1962;17:417-20.
188. Anderson KJ, Harten JM, Booth MG, Kinsella J. The cardiovascular effects of inspired oxygen fraction in anaesthetized patients. Eur J Anaesthesiol 2005;22:420-5.
189. Preiss DA. A new method for measurement of carbon dioxide flux in the lungs during breathing. Toronto: Graduate Department of Chemical Engineering and applied Chemistry, University of Toronto, 2003.
190. Bland JM, Altman DG. Statistical methods for assessing agreement between two methods of clinical measurement. Lancet 19861:307-10.
191. Neto FJ, Carregaro AB, Mannarino R, Cruz ML, Luna SP. Comparison of sidestream capnograph and a mainstream capnograph in mechancally ventilated dogs. J Am Vet Med Assoc 2002;221:1582-5.
192. Murray IP, Modell JH, Gallagher TJ, Banner MJ. Titration of PEEP by the arterial minus end-tidal carbon dioxide gradient. Chest 1984;85:100-4.
193. Hillier SC, Badgwell JM, McLeod ME, Creighton RE, Lerman J. Accuracy of end-tidal PCO2 measurements using a sidestream capnometer in infants and children ventilated with the Sechrist infant ventilator. Can J Anaesth 1990;37:318-21.
194. Berkenbosch JW, Lam J, Burd RS, Tobias JD. Noninvasive monitoring of carbon dioxide during mechanical ventilation in older children: end-tidal versus transcutaneous techniques. Anesth Analg 2001;92:1427-31.
195. Tobias JD, Meyer DJ. Noninvasive monitoring of carbon dioxide during respiratory failure in toddlers and infants: end-tidal versus transcutaneous carbon dioxide. Anesth Analg 1997;85:55-8.
196. Short JA, Paris ST, Booker PD, Fletcher R. Arterial to end-tidal carbon dioxide tension difference in children with congenital heart disease. Br J Anaesth 2001;86:349-53.

197. Tusman G, Suarez-Sipmann F, Bohm SH, Pech T, Reissmann H, Meschino G, Scandurra A, Hedenstierna G. Monitoring dead space during recruitment and PEEP titration in an experimental model. Intensive Care Med 2006;32:1863-71.
198. Wahba RW, Tessler MJ. Misleading end-tidal CO2 tensions. Can J Anaesth 1996;43:862-6.
199. Dejours P. Respiration. New York: Oxford University Press, 1966.
200. Preiss D, Fisher J: A measure of confidence in Bland-Altman analysis for the interchangeability of two methods of measurement. J Clin Monit Comput 2008;22:257-9.
201. Hoffman RA, Krieger BP, Kramer MR, Segel S, Bizousky F, Gazeroglu H, Sackner MA: End-tidal carbon dioxide in critically ill patients during changes in mechanical ventilation. Am Rev Respir Dis 1989;140:1265-8.
202. Russell GB, Graybeal JM: The arterial to end-tidal carbon dioxide difference in neurosurgical patients during craniotomy. Anesth Analg 1995;81:806-10.
203. Russell GB, Graybeal JM: End-tidal carbon dioxide as an indicator of arterial carbon dioxide in neurointensive care patients. J Neurosurg Anesthesiol 1992;4:245-9.
204. Casey K, Duffin J, McAvoy GV: The effect of exercise on the central-chemoreceptor threshold in man. Journal of Physiology 1987;383:9-18.
205. Mohan RM, Amara CE, Cunningham DA, Duffin J: Measuring central-chemoreflex sensitivity in man: rebreathing and steady-state methods compared. Respir Physiol 1-1-1999;115:23-33.
206. Sommer LZ, Iscoe S, Robicsek A, Kruger J, Silverman J, Rucker J, Dickstein J, Volgyesi GA, Fisher JA: A simple breathing circuit minimizing changes in alveolar ventilation during hyperpnoea. Eur Respir J 1998;12:698-701.
207. Banzett RB, Garcia RT, Moosavi SH. Simple contrivance "clamps" end-tidal PCO2 and PO2 despite rapid changes in ventilation. Journal of Applied Physiology 2000;88:1597-1600.
208. Meida-Junior AA, da Silva MT, Almeida CC, Ribeiro JD: Relationship between physiologic deadspace/tidal volume ratio and gas exchange in infants with acute bronchiolitis on invasive mechanical ventilation. Pediatr Crit Care Med 2007;8:372-7.
209. Burrows FA: Physiologic dead space, venous admixture, and the arterial to end-tidal carbon dioxide difference in infants and children undergoing cardiac surgery. Anesthesiology 1989;70:219-25.
210. Hedenstierna G, McCarthy G: The effect of anaesthesia and intermittent positive pressure ventilation with different frequencies on the anatomical and alveolar deadspace. Br J Anaesth 1975;47:847-52.
211. Moss AJ, Emmanouilides G, Duffie Jr ER: Closure of the ductus arteriosus in the newborn infant. Pediatrics 1963;32:25-30.

212. Emmanouilides GC, Moss AJ, Duffie Jr ER, Dams FH: Pulmonary arterial pressure changes in human newborn infants from birth to 3 days of age. J Pediatr 1964;65:327-33.
213. Badgwell JM, Heavner JE, May WS, Goldthorn JF, Lerman J: End-tidal PCO2 monitoring in infants and children ventilated with either a partial rebreathing or a non-rebreathing circuit. Anesthesiology 1987;66:405-10.
214. Fierstra J, Machina M, Battisti-Charbonney A, Duffin J, Fisher JA, Minkovich L: End-inspiratory rebreathing reduces the end-tidal to arterial PCO(2) gradient in mechanically ventilated pigs. Intensive Care Med 2011;37:1543-50.
215. Garcia JH, Lassen NA, Weiller C, et al. Ischemic stroke and incomplete infarction. Stroke 1996;27:761–5.
216. Nakagawara J, Sperling B, Lassen NA. Incomplete brain infarction of reperfused cortex may be quantitated with iomazenil. Stroke 1997;28:124–32.
217. Kurumatani T, Kudo T, Ikura Y, Takeda M. White matter changes in the gerbil brain under chronic cerebral hypoperfusion. Stroke. 1998;29: 1058–62.
218. Shibata M, Ohtani R, Ihara M, Tomimoto H. White matter lesions and glial activation in a novel mouse model of chronic cerebral hypoperfusion. Stroke. 2004;35:2598 –603.
219. Soinne L, Helenius J, Saimanen E, et al. Brain diffusion changes in carotid occlusive disease treated with endarterectomy. Neurology 2003;61:1061–5.
220. Soinne L, Helenius J, Tikkala I, et al. The effect of severe carotid occlusive disease and its surgical treatment on cognitive functions of the brain. Brain Cogn 2009;69:353–9.
221. Viana-Baptista M, Bugalho P, Jordao C, et al. Cognitive function correlates with frontal white matter apparent diffusion coefficients in patients with leukoaraiosis. J Neurol 2008;255:360 –6.
222. O'Sullivan M, Morris RG, Huckstep B, Jones DK, Williams SC, Markus HS. Diffusion tensor MRI correlates with executive dysfunction in patients with ischaemic leukoaraiosis. J Neurol Neurosurg Psychiatry 2004;75:441– 7.
223. Lundar T, Lindegaard KF, Froysaker T, Aaslid R, Grip A, Nornes H. Dissociation between cerebral autoregulation and carbon dioxide reactivity during nonpulsatile cardiopulmonary bypass. Ann Thorac Surg 1985;40:582-7.
224. Kazumata K, Tanaka N, Ishikawa T, Kuroda S, Houkin K, Mitsumori K. Dissociation of vasoreactivity to acetazolamide and hypercapnia. Comparative study in patients with chronic occlusive major cerebral artery disease. Stroke 1996:27:2052-8.
225. Harper AM, Glass HI. Effect of alterations in the arterial carbon dioxide tension on the blood flow through the cerebral cortex at normal and low arterial blood pressures. J Neurol Neurosurg Psychiatry 1965;28:449-52.
226. Nishimura S, Suzuki A, Hatazawa J, Nishimura H, Shirane R, Yasui N, Yoshimoto T. Cerebral blood-flow responses to induced hypotension and to CO2

inhalation in patients with major cerebral artery occlusive disease: a positron-emission tomography study. Neuroradiology 1999;41:73-9.
227. Kleiser B, Krapf H, Widder B. Carbon dioxide reactivity and patterns of cerebral infarction in patients with carotid artery occlusion. J Neurol 1991;238:392-4.
228. Markus H, Cullinane M. Severely impaired cerebrovascular reactivity predicts stroke and TIA risk in patients with carotid artery stenosis and occlusion. Brain 2001;124:457-67.
229. Kuroda S, Houkin K, Kamiyama H, Mitsumori K, Iwasaki Y, Abe H. Long-term prognosis of medically treated patients with internal carotid or middle cerebral artery occlusion: can acetazolamide test predict it? Stroke 2001;32:2110-16.
230. Ogasawara K, Ito H, Sasoh M, Okuguchi T, Kobayashi M, Yukawa H, Terasaki K, Ogawa A. Quantitative measurement of regional cerebrovascular reactivity to acetazolamide using 123I-N-isopropyl-p-iodoamphetamine autoradiography with SPECT: validation study using H2 15O with PET. J Nucl Med 2003;44:520-5.
231. Blanco VM, Stern JE, Filosa JA. Tone-dependent vascular responsesto astrocyte-derived signals. Am J Physiol Heart Circ Physiol 2008;294:2855–63.
232. Fox PT, Raichle ME. Focal physiological uncoupling of cerebral blood flow and oxidative metabolism during somatosensory stimulation in human subjects. Proc Natl Acad Sci USA 1986;83: 1140–4.
233. Davis TL, Kwong KK, Weisskoff RM, Rosen BR. Calibrated functional MRI: mapping the dynamics of oxidative metabolism. Proc Natl Acad Sci USA 1998;95(4):1834–9.
234. The EC/IC Bypass Study Group: Failure of extracranial-intracranial arterial bypass to reduce the risk of ischemic stroke. N Eng J Med 1985;313:1191-1200.
235. Wintermark M, Sesay M, Barbier E, Borbely K, Dillon WP, Eastwood JD, Glenn TC, Grandin CB, Pedraza S, Soustiel JF, Nariai T, Zaharchuk G, Caille JM, Dousset V, Yonas H. Comparative overview of brain perfusion imaging techniques. Stroke 2005;36(9):e83-99.
236. Mandell DM, Han JS, Poublanc J, Crawley AP, Fierstra J, Tymianski M, Fisher JA, Mikulis DJ.Quantitative measurement of cerebrovascular reactivity by blood oxygen level-dependent MR imaging in patients with intracranial stenosis: preoperative cerebrovascular reactivity predicts the effect of extracranial-intracranial bypass surgery. AJNR Am J Neuroradiol 2011;32(4):721-7.
237. Shibuya M. Brain angiogenesis in developmental and pathological processes: therapeutic aspects of vascular endothelial growth factor. FEBS J 2009;276(17):4636-43.
238. Lim M, Cheshier S, Steinberg GK. New vessel formation in the central nervous system during tumor growth, vascular malformations, and Moyamoya. Curr Neurovasc Res 2006;3(3):237-45.
239. Duelsner A, Gatzke N, Glaser J, Hillmeister P, Li M, Lee EJ, Lehmann K, Urban D, Meyborg H, Stawowy P, Busjahn A, Nagorka S, Persson AB, Buschmann IR.Acetylsalicylic acid, but not clopidogrel, inhibits therapeutically induced

cerebral arteriogenesis in the hypoperfused rat brain. J Cereb Blood Flow Metab 2011 Aug 10 [Epub ahead of print].
240. Hoshimaru M, Takahashi JA, Kikuchi H, Nagata I, Hatanaka M. Possible roles of basic fibroblast growth factor in the pathogenesis of moyamoya disease: an immunohistochemical study. J Neurosurg 1991;75(2):267-70.
241. Yoshimoto T, Houkin K, Takahashi A, Abe H. Angiogenic factors in moyamoya disease. Stroke 1996;27(12):2160-5.
242. Cho BK, Tominaga T. Moyamoya disease update. Tokyo: Springer; 2010. Part IV: Pathophysiolgoy I: Protein, Cell, and Immunology; p. 63-99
243. Arbib MA. The handbook of brain theory and neural network. 2nd ed. Massachussets Institute of Technology; 2003. Part I: Background, Part II: Road map. p. 3-78.
244. Bynum LJ, Wilson JE, III, Pierce AK. Comparison of spontaneous and positive-pressure breathing in supine normal subjects. J Appl Physiol 1976; 41: 341-7.
245. Moens Y, Lagerweij E, Gootjes P, Poortman J. Influence of tidal volume and positive end-expiratory pressure on inspiratory gas distribution and gas exchange during mechanical ventilation in horses positioned in lateral recumbency. Am J Vet Res 1998; 59: 307-12.
246. Protzner AB, Valiante TA, Kovacevic N, McCormick C, McAndrews MP. Hippocampal signal complexity in mesial temporal lobe epilepsy: a noisy brain is a healthy brain. Arch Ital Biol 2010;148(3):288-97.
247. Marshall RS, Lazar RM. Pumps, aqueducts, and drought management: vascular physiology in vascular cognitive impairment. Stroke 2011;42(1):221-6.
248. Webster MW, Makaroun MS, Steed DL, Smith HA, Johnson DW, Yonas H. Compromised cerebral blood flow reactivity is a predictor of stroke in patients with symptomatic carotid artery occlusive disease. J Vasc Surg. 1995;21:338 - 4;discussion 344–5.
249. Helenius J, Soinne L, Perkio J, Salonen O, Kangasmaki A, Kaste M, Carano RA, Aronen HJ, Tatlisumak T. Diffusion-weighted MR imaging in normal human brains in various age groups. AJNR Am J Neuroradiol. 2002;23:194 –9.
250. Helenius J, Soinne L, Salonen O, Kaste M, Tatlisumak T. Leukoaraiosis, ischemic stroke, and normal white matter on diffusion-weighted MRI. Stroke. 2002;33:45–50.
251. Pantoni L, Garcia JH. Pathogenesis of leukoaraiosis: a review. Stroke. 1997;28:652–9.
252. Soinne L, Helenius J, Saimanen E, Salonen O, Lindsberg PJ, Kaste M, Tatlisumak T. Brain diffusion changes in carotid occlusive disease treated with endarterectomy. Neurology. 2003;61:1061–5.
253. Engelter ST, Provenzale JM, Petrella JR, DeLong DM, MacFall JR. The effect of aging on the apparent diffusion coefficient of normal-appearing white matter. AJR Am J Roentgenol. 2000;175:425– 30.

254. Rostrup E, Larsson HB, Toft PB, Garde K, Thomsen C, Ring P, Sondergaard L, Henriksen O. Functional MRI of CO2 induced increase in cerebral perfusion. NMR Biomed. 1994;7:29 –34.
255. Yamada I, Himeno Y, Nagaoka T, Akimoto H, Matsushima Y,Kuroiwa T, Shibuya H. Moyamoya disease: evaluation with diffusion weighted and perfusion echo-planar MR imaging. Radiology. 1999; 212:340 –7.
256. Wittes J. Sample size calculations for randomized controlled trials. Epidemiol Rev. 2002;24:39 –53.
257. Ogawa S, Lee TM, Barrere B. The sensitivity of magnetic resonance image signals of a rat brain to changes in the cerebral venous blood oxygenation. Magn Reson Med. 1993;29:205–10.
258. Costantino I. Atherosclerosis and neurodegeneration: unexpected conspiratorsin Alzheimer's dementia. Arterioscler Thromb Vasc Biol. 2003;23:1951–3.
259. de Weerd M, Greving JP, Hedblad B, et al. Prevalence of asymptomatic carotid artery stenosis in the general population: an individual participant data meta-analysis. Stroke 2010;41:1294 –7.
260. Markus H, Cullinane M. Severely impaired cerebrovascular reactivity predicts stroke and TIA risk in patients with carotid artery stenosis and occlusion. Brain 2001;124: 457–67.
261. Vernieri F, Pasqualetti P, Passarelli F, Rossini PM, Silvestrini M. Outcome of carotid artery occlusion is predicted by cerebrovascular reactivity. Stroke 1999;30:593–8.
262. Marks MP, de Crespigny A, Lentz D, Enzmann DR, Albers GW, Moseley ME. Acute and chronic stroke: navigated spinecho diffusion-weighted MR imaging. Radiology 1996;199: 403–8.
263. Talairach J, Tournoux P. Co-Planar Stereotaxic Atlas of the Human Brain. New York: Thieme Medical Publishers; 1988.
264. Le Bihan D, Breton E, Lallemand D, Grenier P, Cabanis E, Laval-Jeantet M. MR imaging of intravoxel incoherent motions: application to diffusion and perfusion in neurologic disorders. Radiology 1986;161:401–7.
265. Kurumatani T, Kudo T, Ikura Y, Takeda M. White matter changes in the gerbil brain under chronic cerebral hypoperfusion. Stroke 1998;29:1058 –62.
266. Ogawa S, Lee TM, Barrere B. The sensitivity of magnetic resonance image signals of a rat brain to changes in the cerebral venous blood oxygenation. Magn Reson Med 1993;29:205–10.
267. Jezzard P, Clare S. Sources of distortion in functional MRI data. Hum Brain Mapp 1999;8:80–5.

Nederlandse samenvatting

Aangenomen wordt dat hersengebieden met verminderde cerebrovasculaire reserve een verhoogd risico hebben voor ischemische weefsel schade in situaties waar de cerebrale doorbloeding ontoereikend is voor de metabole behoefte. Anders dan voor acute ischemie, met duidelijk (irreversibel) verlies van hersenweefsel en functie, zijn de consequenties voor chronisch intermitterend hemodynamisch falen minder goed begrepen. In deze gevallen kan perfusie van het hersenweefsel nog net genoeg zijn om ernstige ischemie te voorkomen maar valt het tekort bij verhoogde behoefte wat normaal gezien wordt gedurende neuronale activiteit. Tot op heden zijn er geen studies gepubliceerd betreffende de anatomische en functionele uitkomsten van niet-ischemische chronische intermitterende hypoperfusie in mensen, echter, vanuit dier experimentele studies, met een niet-ischemische chronische hypoperfusie simulatie, is er een afname van neuronale structuur en functie geobserveerd.

Om de aanwezigheid van chronische hypoperfusie te onderzoeken, kan de integriteit van de cerebrovasculaire autoregulatie worden gemeten door middel van cerebrovasculaire reactiviteit (CVR), een maat voor de verandering in cerebrale doorbloeding als reactie op een vasodilatoire stimulus. Reducties in CVR kunnen variëren van een suboptimale toename van de doorbloeding als reactie op een stimulus in milde gevallen, tot "paradoxale" vermindering in regionale doorbloeding wijzende op "steal fysiologie", in ernstige gevallen. Bestaande beeldvormende technieken om cerebrovasculaire reactiviteit spatieel te meten, zoals ^{133}Xe-CT en Single Photon Emission Computed Tomography (SPECT), brengen nadelen met zich mee gezien deze technieken duur zijn en klinisch beperkt inzetbaar.

In dit proefschrift maak ik extensief gebruik van een niet-invasieve op MR gebaseerde methode om de anatomische en klinische consequenties van verminderde cerebrovasculaire reserve te besluiten. Deze methode gebruikt functionele vervaardigingen van een Bloed Zuurstof-Gehalte Afhankelijk (BOLD) contrast met gestandardiseerde iso-oxische veranderingen in eind tidale PCO_2 als de vasoactieve stimulus. In het bijzonder onderzoek ik de nadelige effecten van chronisch verminderde doorbloeding op het welzijn van het hersenweefsel om dit te vergelijken met het ontstaan van klinische symptomen in patiënten met ernstige chronische cerebrovasculaire steno-occlusieve ziekten en brein arterioveneuze malformaties.

Gezien MRI-CVR gerelateerde metingen precieze veranderingen vergen in eind tidale PCO_2, zal ik in het tweede deel van dit proefschrift in een diermodel, de translatie van de gestandardiseerde PCO_2 stimulus bestuderen voor patiënten die mechanische ventilatie (oftewel een positieve inspiratoire druk) behoeven. Deze methode kan nieuwe potentiële onderzoekswegen openen voor ernstig zieke patiënten die baat kunnen hebben bij MRI-CVR studies, zoals patiënten met traumatisch hersenletsel of een subarachnoidale bloeding door een aneursymale ruptuur.

Acknowledgments

This thesis is the result of a wide collaborative effort that I was fortunate to have been a part of, and involved several authors from a variety of departments and institutions. I feel privileged to have worked with so many inspiring people, many of them world leaders within their field of expertise, during my time at Toronto Western Hospital.

I would like to express my sincerest gratitude to everyone that has assisted and supported me during my time in Toronto. However, to some I am particularly indebted:

Dr. Michael Tymianski: To grant a meeting to a foreign medical student who literally knocked on your door one day, and based on this one meeting, to agree to supervise, accommodate and support his full PhD thesis, represents an incredible generosity that I cannot thank you enough for. Your input into this thesis has been of extraordinary assistance, and your confidence in me has enabled me to aspire for a career within (vascular) neurosurgery.

Professor Luca Regli: Professor, it is a great honour to obtain my PhD within your department. I share in your international perspective and belief that by collaborating one can achieve greater things, and anticipate with great enthusiasm our upcoming joint research projects.

Dr. David Mikulis: Being a part of an fMRI team that has such innovative ideas and that collaborates with such ease and efficiency has been inspiring. I thank you very much for assisting in launching my PhD projects, as well as for your outstanding ability to come up with truly unique hypotheses and MRI applications. There is no doubt in my mind that Toronto will continue to be a world leader in neurovascular MR-based research, thanks to your (and Drs. Tymianski and Fisher's) invaluable contributions to the field.

Dr. Joseph Fisher: Joe, it is forbidden to call you "Dr. Fisher" and that illustrates who you are; despite your achievements you are the most humble and open physician-scientist that I know. Your ideas and insights are truly exceptional. Working within your research group has taught me a great deal about human physiology, animal research and thinking outside the box.

Dr. Anne-Marie Guerguerian: You have played an essential role in teaching and showing me how clinical research should be done and how great it can be. Your endless support and advice during my first stay in Toronto gave me the confidence to contact Dr Tymianski and start a PhD abroad. I would not have succeeded without your help. I thank you from the bottom of my heart.

The medical imaging (Mikulis') lab: **Julien, Adrian, Danny, Jay, Dave MacLean, Jesse, Stephie, Kevin, Aneta,** and **Hui.** I appreciate all the teaching, support and collaboration throughout the three years it took to produce this thesis. Thank you for creating such a

tranquil and friendly atmosphere. You truly are a unique group, and I am very grateful to have been part of it.

John Conklin & Joe Barfett: Two very talented men with whom I had the pleasure working. The way that you perform research is impressive and I am glad that I had the chance to participate, and to learn from each of you. I wish you the best of luck with your future careers in academic neuroradiology.

All administrative assistants and research coordinators from the departments of Medical Imaging and Neurosurgery: **Gail, Reann, Alex, Yang, Ursula, Carolyn, Liz, Stacey, Sherry, Ghazelle, Ruth, Nathalie, Amanda** and **Sandy.** Thank you for all the help, the daily chats, and the memorable holiday parties.

A special thanks to **Janet:** From the first time that I walked into Dr. Tymianski's office, you have made me feel at home and have helped me to make my time at TWH a success. I have very much enjoyed our conversations and your great sense of humor, as well as the free food in the kitchen.

From Toronto Western Hospital I would like to thank **Mary-Pat** and **Mel** for their interest in my projects and willingness to collaborate. I truly hope that what we have started will continue in my absence. Thanks also to **Dr. Karin Davis**, **Massieh, Geoff**, **Sarah**, **Kerry, Dave Kideckel,** and **Monica** for fruitful discussions during imaging rounds and great talks during lunch or after-work beers. Thank you, **Ronit,** for all the great conversations on our coffee breaks, and **Dr. Christopher Wallace**, **Dr. Leanne Casaubon** and **Dr. Frank Silver** for collaborating on CVR and NOVA projects. Also a great thanks to all the MRI-technicians, in particular **Eugen, Kiet, Dave Johnstone, Colleen, Hien, Maggie, Magda,** and **Christine.** Without your help and flexibility, I would have never been able to acquire the patient MRI data necessary to create this publication. It was a pleasure working with all of you.

Professor Karel TerBrugge and **professor Timo Krings:** Professors, I am deeply grateful for your support in allowing me to develop my research projects within your department, and for the opportunities to speak at various conferences.

Dr. Andrea Kassner and **Dr. Leodante DaCosta:** Another great example of the spirit of collaboration that is alive in Toronto. Andrea, thank you for allowing me to carry out projects at SickKids and to learn more about pediatric neurovascular pathology. Leo, you are an inspiring man, with a great sense of humour. I am very glad that I was able to assist in starting your CVR research at Sunnybrook. I apologize again that I missed out on the dinner in Rome.

CVR Research team Sunnybrook: **Dr. Michael Schwartz, Dave Houlden, Allison, Samantha, Diem** and **Dave Crane:** It was a pleasure to spend the Fridays and weekends at Sunnybrook with all of you to get CVR research started.

Thornhill Research Inc. (Fisher lab): Dear **Dr. Duffin, Cliff, Mary-Anne,** and **Ron:** Thank you for adopting me into the TRI family and for your contributions towards making the research a success. **Matt, Anais, Olivia, Tracey, Leonid,** and **Mike:** The animal studies were a thrill to be part of. You are a great and knowledgeable team. I have very much enjoyed working with all of you, and am glad some of us are still able to collaborate; there are some very exciting projects yet to finish.

Professor Gabriel Rinkel: Gabriel, ik wil je erg danken voor je hulp en advies omtrent mijn komst naar het UMC Utrecht. Het was helaas niet mogelijk om je als co-promotor voor te dragen, maar ik hoop dat je het wel zo ervaart.

Dr. Marc van Dijk: Marc, voordat ik überhaupt naar Toronto afreisde heb ik erg veel aan je advies gehad. Dit heeft me gesterkt om aanvankelijk zonder "universitaire ondersteuning" aan mijn promotie te beginnen.

Dr. Peter Willems: Peter, we begonnen op hetzelfde moment met onze werkzaamheden in Toronto. Ik zal de tijd dat jij er was nooit vergeten en ben erg blij dat we samen terug kunnen kijken op een jaar vol hoogtepunten.

Andreas Tiel Groenestege: Jij kwam Peter aflossen en het bleef een schitterend tijd. De meest onuitwisbare herinneringen moeten toch wel onze zeiltochtjes zijn.

Dr. Mervyn Vergouwen: Hilarisch dat het kwartje pas viel toen we als enige aanwezigen, als "hockeyfans", het home stadium betraden terwijl de Toronto Marlies een uitwedstrijd speelden. Als geluk bij een ongeluk hebben we die avond onder het genot van een biertje alwel de opening van de Olympische Winterspelen Vancouver 2010 kunnen zien.

Dr. Patrick Brouwer: Alhoewel ik het niet besefte toen ik naar Toronto kwam, is het toch fantastisch om te zien hoe sterk de banden zijn tussen Toronto en Nederland(ers). Ik ben daarvoor ook erg dankbaar dat ik je daar heb mogen ontmoeten en wil je erg bedanken voor je steun en inspiratie. Een congress in Kaapstad had ik nooit durven dromen, maar ook daar we hebben elkaar de hand mogen schudden.

Ad van der Meer: Maestro, wel heel bijzonder dat je ook in Toronto Western Hospital aan een onderzoeksproject werkte. Dank je voor de voortzetting van onze memorable avonden, ditmaal in Toronto en NYC.

Vanuit het UMC Utrecht wil ik graag **Dr. Hans Hoogduin** bedanken voor de herhaaldelijke uitnodigingen om mijn werk te mogen presenteren in het UMC Utrecht gedurende mijn halfjaarlijkse visite aan Nederland. Ik hoop dat we in de toekomst veel gaan samenwerken. Ook wil ik mijn hartelijke dank geven aan **Albi** en **Barbara** voor alle begeleiding en advies sinds mijn terugkomst maar voornamelijk tijdens het afronden van het promotietraject.

Dr. Ernst Delwel en **John Soria Van Hoeve:** De uren die we samen hebben doorgebracht in het (neurochirurgische) skillslab van het Erasmus MC alsmede de fantastische reis naar Tokio hebben mede de basis gelegd voor deze promotie. Ik wil jullie beiden erg bedanken voor de leerzame ervaringen.

Sara Crawley: Thank you for creating such wonderful illustrations for this thesis. You are very talented and I am sure that this is only the beginning of a fantastic creative career.

The reading committee: **Professors Mali, Derdeyn, Kalkman, Moll,** and **Dr. Biessels,** I am grateful for the privilege of having my thesis evaluated by such great experts.

A special thank you to all my friends from Canada and The Netherlands. Thanks for making me feel at home and exposing me to the ideas and subtler details of what makes Canada great. And for those who visited me in Toronto from The Netherlands, thank you: you have given me wonderful memories for life.

Mijn paranimfen **Ruben de Bliek** en **Bas Mathot:** Heren, fantastisch dat ik dit met jullie heb kunnen delen. Bedankt voor de hechte vriendschap en prachtige tijd in Rotterdam.

Heit, mem, Berber, Djurre, pake & beppe en **femylje:** Tige tank foar alle stipe en leafde. Ik haw alles oan jim te tanken. Ik hâld fan jim.

Fabia: Dear Fay, you truly are exceptional and I'm very proud of what you have accomplished in The Netherlands in such a short time. Thank you for all your love and support.

List of publications

Foundational manuscripts

Fierstra J, Mikulis DJ, Regli L, Tymianski M, Fisher JA. Measuring cerebrovascular reactivity: a review of various functional imaging methods and vasoactive stimuli. *Submitted for publication*

Fierstra J, Pucci O, Battisti-Charbonney A, Duffin J, Poublanc J, Crawley, AP, Regli L, Rinkel GJ Van Dijk JMC, Mandell DM, Tymianski M, Mikulis DJ, Fisher JA. Sequential standardized fMRI assessment of cerebrovascular reserve in chronic intracranial steno-occlusive disease with two illustrative case studies. *Submitted for publication*

Fierstra J, Poublanc J, Han JS, Silver F, Tymianski M, Crawley AP, Fisher JA, Mikulis DJ. Steal physiology is spatially associated with cerebral cortical thinning. J Neurol Neurosurg Psychiatry 2010;81(3):290-3

Fierstra J, MacLean DB, Fisher JA, Han JS, Mandell DM, Conklin J, Poublanc J, Crawley AP, Regli L, Mikulis DJ, Tymianski M. Surgical revascularization reverses cerebral cortical thinning in patients with severe cerebrovascular steno-occlusive disease. Stroke 2011;42(6):1631-7

Fierstra J, Conklin J, Krings T, Slessarev M, Han JS, Fisher JA, Terbrugge K, Wallace MC, Tymianski M, Mikulis DJ. Impaired peri-nidal cerebrovascular reserve in seizure patients with brain arteriovenous malformations. Brain 2011;134(Pt 1):100-9

Fierstra J, Machina M, Battisti-Charbonney A, Duffin J, Fisher JA, Minkovich L. End-inspiratory rebreathing reduces the end-tidal to arterial PCO_2 gradient in mechanically ventilated pigs. Intensive Care Med 2011;37(9):1543-50

Fierstra J, Winter JD, Machina M, Lukovich J, Duffin J, Kassner A, Fisher JA. Non-invasive accurate measurement of $PaCO_2$ in a pediatric animal model. *Submitted for publication*

Conklin J, Fierstra J, Crawley AP, Han JS, Poublanc J, Mandell DM, Silver F, Tymianski M, Fisher JA, Mikulis DJ. Impaired cerebrovascular reactivity with steal phenomenon is associated with increased diffusion in white matter of patients with moyamoya disease. Stroke 2010;41(8):1610-6

Conklin J, Fierstra J, Crawley AP, Han JS, Poublanc J, Mandell DM, Silver F, Tymianski M, Fisher JA, Mikulis DJ. Mapping white matter diffusion and cerebrovascular reactivity in carotid occlusive disease. Neurology 2011;77)5):431-8

Fierstra J, Spieth S, Tran LE, Conklin J, Tymianski M, Terbrugge K, Fisher JA, Mikulis DJ, Krings T. Severely impaired cerebrovascular reserve in patients with cerebral proliferative angiopathy. J Neurosurg Pediatr 2011;8(3):310-5

MacLean DB, Fierstra J, Pucci O, Battisti-Charbonney A, Conklin J, Fisher JA, Mikulis DJ. Restriction of cerebral venous outflow decreases cerebrovascular reserve in healthy subjects. *Submitted for publication*

Winter JD, Fierstra J, Dorner S, Fisher JA, St-Lawrence KS, Kassner A.Feasibility and precision of cerebral blood flow and cerebrovascular reactivity MRI measurements using a computer-controlled gas delivery system in an anesthetised juvenile animal model. J Magn Reson Imaging 2010;32(5):1068-75

Mandell DM, Han JS, Poublanc J, Crawley AP, Fierstra J, Tymianski M, Fisher JA, Mikulis DJ. Quantitative measurement of cerebrovascular reactivity by blood oxygen level-dependent MR imaging in patients with intracranial stenosis: preoperative cerebrovascular reactivity predicts the effect of extracranial-intracranial bypass surgery. AJNR Am J Neuroradiol 2011;32(4):721-7

Foundational book chapters

Fierstra J, Mikulis DJ. Neurovascular uncoupling in functional MR imaging; chapter 20 in "Functional Neuroradiology: Principles and Clinical Applications" By Faro S, Mohamed F. 1st ed. 2011. Springerlink Verlag

Editorials by peers related to foundational manuscripts

Marshall RM. On the trail of chronic ischemia. J neurol Neurosurg Psychiatry 2011;81(3):240

Sturiale CL, Puca A, Albanese A, Maira G, Colicchio B. A comment on Impaired peri-nidal cerebrovascular reserve in seizure patients with brain arteriovenous malformations. Brain [Epub ahead of print, May 26 2011]

Other manuscripts

Barfett JJ, Fierstra J, Willems PW, Mikulis DJ, Krings T. Intravascular functional maps of common neurovascular lesions derived from volumetric 4D CT data. Invest Radiol 2010;45(7):370-7

Barfett JJ, Fierstra J, Mikulis DJ, Krings T. Blood velocity calculated from volumetric dynamic computed tomography angiography. Invest Radiol 2010;45(12):778-81

Patents resulting from this thesis

United States Provisional Patent Application No. 61/439,731 For: NON-INVASIVE ARTERIAL BLOOD GAS DETERMINATION (EQUALIZER) Filed: February 4, 2011

Curriculum Vitae

Jorn Fierstra was born on 15 May 1983, in Leeuwarden, The Netherlands. After studying one year of biomedical sciences at Utrecht University, he commenced medical school at the Erasmus Medical Center in Rotterdam in 2003. During this time, as an extracurricular pursuit, he collaborated with Dr. Jos Van der Geest (Neuroscience) in projects related to fMRI research. He also worked with Dr. Ernst Delwel (Neurosurgery) and fellow medical student John Soria Van Hoeve in the neurosurgical skills-lab by studying neuro-anatomy and by improving neurosurgical skull-base techniques. These activities led to a month-long research internship in December 2006 at the KEIO University Medical Center in Tokyo, Japan under the supervision of professor Takeshi Kawase (Neurosurgery). From February to May 2007, during a research elective at the Emergency Medicine Department of the Erasmus MC, he co-founded a student organisation for emergency medicine. Subsequently he completed a 7.5-month research internship at the Hospital for Sick Children in Toronto, Canada under the guidance of Dr. Anne-Marie Guerguerian (Pediatric Critical Care Medicine) and Dr. James Rutka (Pediatric Neurosurgery), to study the outcome of pediatric patients with traumatic brain injury after decompressive craniectomy.

During this internship, he decided to postpone his medical clerkships, with a view to spending the next 3 years on his PhD (June 2008-March 2011) at the departments of Neurosurgery (supervisor Dr. Michael Tymianski) and Neuroradiology (supervisor Dr. David Mikulis) at the University Health Network (UHN), Toronto, Canada. He also joined Thornhill Research Inc. (TRI), a spin-off company of the University Health Network charged with developing medical devices invented within this institution (supervisor Joseph Fisher, Department of Anesthesia of UHN and senior-scientist of TRI).

In April 2011, he was welcomed at the department of neurosurgery by Professor Luca Regli (Neurosurgery) and professor Gabriel Rinkel (Neurology) to finish his thesis at Utrecht University. During his PhD research the author published work in a wide variety of peer-reviewed journals within the field of vascular neurosurgery and neurology and was an invited speaker at various international conferences. He is an MD candidate for 2013 at Utrecht University.